

Università degli Studi di Napoli “Federico II”



Centro Interdipartimentale di Ricerca Ambiente
C.I.R.A.M.

Dottorato di ricerca in
ANALISI DEI SISTEMI AMBIENTALI
XXVIIICICLO

PhD Thesis

**From site-scale to large areas monitoring of
ground deformation phenomena by integration
of different DInSAR techniques in Crotone
Province (Southern Italy)**

by

Pierluigi Confuorto

Advisor:

Prof. Domenico Calcaterra

Co-Advisors:

Dr. Massimo Ramondini

Prof. Kurosch Thuro

PhD Coordinator:

Prof. Maurizio Fedi

Academic Year 2015/2016

Contents

List of Figures.....	IV
List of Tables	VIII
List of Abbreviations	IX
CHAPTER 1: INTRODUCTION.....	1
1.1 Structure of the thesis	3
1.2 Objectives of the research	3
CHAPTER 2: LANDSLIDES	5
2.1 Landslides: Definition and main features.....	5
2.1.1 Landslide definition and classifications	6
2.1.2 Landslide features.....	14
2.1.3 Landslide causes	17
2.2 Landslides in Italy	18
2.3 Landslides mapping and inventory.....	22
2.3 Landslides monitoring.....	26
CHAPTER 3: SUBSIDENCE	30
3.1 Definition and main types	30
3.2 Subsidence investigation	34
CHAPTER 4: SYNTHETIC APERTURE RADAR.....	35
4.1 Remote sensing.....	35
4.2 Synthetic Aperture Radar (SAR): introduction	37
4.3 SAR data acquisition	38
4.4 SAR parameters.....	40
4.5 SAR distortions	41
4.6 Spaceborne SAR missions.....	44
4.7 SAR interferometry	49
4.7.1 Geometry of acquisition and baseline	50
4.7.2 Interferometric phase.....	51
4.7.3 Interferometric chain	52
4.8 Differential SAR interferometry (DInSAR).....	54
4.8.1 Differential SAR interferometry applications	54
4.8.2 Differential SAR interferometry algorithms.....	55

4.8.2.1 Persistent Scatterers SAR Interferometry SAR (PSInSAR)	57
4.8.2.2 Small Baseline Subset (SBAS)	58
4.8.2.3 Coherent Pixels Technique (CPT)	59
4.9 SAR Dataset	59
CHAPTER 5: STUDY AREA.....	61
5.1 Geographical setting.....	61
5.2 Geological setting.....	62
5.3 Geomorphological setting	66
5.4 Landslide inventory map of Crotone Province.....	69
CHAPTER 6: APPLICATION OF DINSAR METHODS ON LANDSLIDE CASES	72
6.1 Cirò case study	72
6.1.1 The February 2011 landslide	73
6.1.2 DInSAR analysis	79
6.1.2.1 CPT	79
6.1.2.2 PSInSAR.....	83
6.1.2.3 SBAS	87
6.1.2.4 R-Index	89
6.2 Papanice case study	92
6.2.1 Setting of the landslide area.....	94
6.2.2 Rainfall analysis	96
6.2.3 Instrumental campaign	99
6.2.4 2008-2010 DInSAR analysis	101
6.2.4.1 SUBSOFT processing	102
6.2.4.2 SARscape processing	104
6.2.5 Summary of the 2008-2010 Papanice results	107
6.2.6 2013-2014 DInSAR results	108
6.2.6.1 SARscape processing	109
6.2.6.2 SUBSOFT processing	110
6.2.7 Slope stability analysis	110
6.2.8 Considerations on the results obtained	114
6.3 Update of the landslide inventory map.....	117
6.3.1 Results	128
6.3.1.1 Crucoli	128
6.3.1.2 Carfizzi	131
6.3.1.3 Melissa	135

6.3.1.4 S. Nicola dell'Alto	140
6.3.1.5 Casabona	144
6.3.1.6 Strongoli	147
6.3.1.7 Rocca di Neto	150
6.3.1.8 Santa Severina	154
6.3.1.9 San Mauro Marchesato	157
6.3.1.10 Scandale	160
6.3.1.11 Cutro	163
6.3.2 Summary of the results	166
CHAPTER 7: SUBSIDENCE CASE STUDIES	171
7.1 Belvedere di Spinello case study.....	171
7.1.1 Belvedere di Spinello setting.....	171
7.1.2 Description of the mining activities.....	173
7.1.3 Hazards related to the mining activities	174
7.1.4 DInSAR results.....	174
7.1.4.1 PSInSAR	175
7.1.4.2 SBAS	177
7.1.4.2 Considerations on the results obtained	179
7.2 Capo Colonna case study	180
7.2.1 Capo Colonna setting.....	181
7.2.2 DInSAR results.....	183
7.2.3 Future outlooks	190
CHAPTER 8: CONCLUSIONS	192
8.1 Future perspectives.....	197
References	199
Acknowledgments	220

List of Figures

Figure 2.1 Impact of the 2014 natural disasters vs. 2004-2013 annual average.....	5
Figure 2.2 Spatial distribution of fatal landslides.....	6
Figure 2.3 a) Cruden and Varnes classification of landslides.....	8
Figure 2.4 a) Scheme of the state of activity of a landslide.....	9
Figure 2.5 Scheme of the distribution of activity of a landslide.....	10
Figure 2.6 Scheme of the style of activity of a landslide.....	11
Figure 2.7 Velocity of a landside according to Cruden and Varnes classification.....	12
Figure 2.8 Hutchinson classification of landslides.....	13
Figure 2.9 Features of a landslide.....	14
Figure 2.10 Landslide dimensions.....	16
Figure 2.11 Maps of the landslide and flood events with “victims” between 1 January and 30 June 2015.....	20
Figure 2.12 Maps of the landslide events with “victims” between 1965 and 2014.....	21
Figure 2.13 a) Frames of stereo-photogrammetry; b) Photographs through airborne acquisition.....	23
Figure 2.14 a) LiDAR DEM for landslide mapping; b) DEM obtained from Regional Technical Cartography of Campania region; c) DEM with GPS showing vectors of displacement.....	25
Figure 2.15 a) Inclinometer configuration; b) Inclinometer operation; c) & d) Inclinometric readings; e) Inclinometric data.....	27
Figure 2.16 a) Open standpipe piezometer; b) scheme of a piezometer installation.....	28
Figure 2.17 a) Scheme of realization of a b) tipping bucket type rain gauge.....	29
Figure 3.1 Summarizing scheme of the different types of subsidence.....	32
Figure 3.2 a) Subsiding sinkholes due to limestone dissolution; b) Cross section of mining subsidence.....	32
Figure 3.3 a) San Joaquin Valley Subsidence caused by water withdrawal; Conceptual diagram of subsidence due to gas/oil extraction from the ground.....	33
Figure 4.1 Electromagnetic wave and its main features.....	36
Figure 4.2 Wavelength, amplitude and frequency of an electromagnetic.....	36
Figure 4.3 Electromagnetic spectrum.....	37
Figure 4.4 SAR imaging geometry and main features.....	38
Figure 4.5 SAR acquisition modes by TerraSAR-X satellite.....	40
Figure 4.6 Geometric model for SAR system.....	41
Figure 4.7 a) Nadir looking radar; b) one-side looking radar.....	41
Figure 4.8 Geometric distortion in SAR imaging.....	42
Figure 4.9 Radar speckle of a SAR image.....	43
Figure 4.10 Interferogram of the 2009 M= 6.3, L’Aquila earthquake.....	49
Figure 4.11 Geometry of acquisition of SAR images.....	50
Figure 4.12 Representative scheme of PSInSAR and of SBAS.....	58
Figure 5.1 a) Location of the study area; b) track of the TerraSAR-X images acquired over ascending and c) descending orbit	61
Figure 5.2 a) Structural map of the Calabrian Arc and location of the Crotone Basin; b) Tectonic sketch map of the Crotone basin	63
Figure 5.3 Geological map of Crotone province	66
Figure 5.4 a) Hilly landscape; b) Rocky cliff made of evaporitic deposits	67
Figure 5.5 Typical badland forms in Cutro. On the background, on the left side, a marine terrace ..	68
Figure 5.6 a) Rocky coastline; b) straight and sandy coastline	69
Figure 5.7 Percentage of the landslide typologies and their occurrence in Crotone province	70
Figure 5.8 Map showing the landslides in Crotone province individuated in the Hydro-geomorphological Setting Plan.....	71
Figure 5.9 Percentage of the landslides state of activity in Crotone province	71

Figure 6.1 Location of Cirò	73
Figure 6.2 Geological map of Cirò town	73
Figure 6.3 HSP of Cirò	74
Figure 6.4 Geological map of the landslide area	75
Figure 6.5 a) Panoramic view of Cirò landslide; b) oblique air view of the main scarp	75
Figure 6.6 Geomorphological map of the landslide area. In blue, the cross section A-A'	76
Figure 6.7 Geological cross section A-A'	77
Figure 6.8 a) View of the sandstone rock on which Cirò historical center is founded; b) particular of the rock, with also protective gabions; c) particular of the excavated foundation system of a house; d) damages on the road and on the houses in occurrence of the main scarp; e) view of Via de Gasperi from above; f) lateral view of Via de Gasperi	77
Figure 6.9 Plots of the antecedent rainfalls measured at the Crucoli rain gauge	78
Figure 6.10 Map showing the displacement rate identified with CPT on the TSX ascending dataset (2008-2010)	80
Figure 6.11 a) Measured displacement rate map of Cirò area, exploiting the descending stack; b) Surface morphol-ogy of the main active landslide along the SW slope, according to the HSP; c) Main active landslide along the SW slope, according to field survey and interferometric results ..	81
Figure 6.12 Comparison between significant points - rainfall data: a) P1 (more than 10mm/yr; b) P2 (between 5 and 7 mm/yr); c) P3 (between 3 and 5 mm/yr; d) P4 (stable point); e) Detail of the comparison be-tween P1 and rainfall data	82
Figure 6.13 Scheme of the procedure adopted for the PSInSAR analysis	83
Figure 6.14 Displacement rate map obtained through PSInSAR application on the ascending dataset (1st period of analysis)	84
Figure 6.15 Displacement rate map obtained through PSInSAR application on the ascending dataset (2nd period of analysis)	85
Figure 6.16 Displacement rate map obtained through PSInSAR application on the descending dataset (1st period of analysis)	86
Figure 6.17 Displacement rate map obtained through PSInSAR application on the descending dataset (2nd period of analysis)	87
Figure 6.18 Displacement rate map obtained through SBAS application on the descending dataset ..	88
Figure 6.19 Displacement rate map obtained through SBAS application on the ascending dataset ..	89
Figure 6.20 R-Index map for the ascending dataset	90
Figure 6.21 R-Index map for the descending dataset	91
Figure 6.22 a) Location of Papanice settlement; b) Geological sketch map of Papanice area; c) Urban evolution of Papanice settlement during 1953-2014	93
Figure 6.23 HSP Landslide inventory map of Papanice (2006)	94
Figure 6.24 a) Field survey landslide inventory map; b) Oblique view of the landslide involving Pironte neighborhood; c) Landslide main scarp	95
Figure 6.25 Damage reported along the landslide main scarp and within the landslide body	96
Figure 6.26 Second Generation InfraRed 10.8 Meteosat image	97
Figure 6.27 Localization of the measurement stations of the Multi-hazard Functional Center of the ARPACAL and relative rainfall heights for the period 21-23 February 2012	97
Figure 6.28 a) Localization of Papanice rain gauge. b) Rainfall diagram for the year 2012, in blue columns daily values, in red cumulative values; c) Rainfall diagram for February 2012; d) Rainfall diagram for the week 19-25 February 2012	98
Figure 6.29 Rainfall duration vs. cumulated event rainfall	99
Figure 6.30 Geolithological section A-A'	101
Figure 6.31 a) Inclinometric data of the inclinometer I1; b) Comparison between piezometric data from piezometer S1 (blue line) and daily ranfall from Papanice rain gauge (red)	101
Figure 6.32 R-Index computation for ascending (left side) and descending (right side) orbits	102

Figure 6.33 Phase standard deviation vs. TSC plot on the top; Phase standard deviation vs. TSE (Temporal subblock entropy) plot on the bottom.....	103
Figure 6.34 Final pixel selection with the TSC method	103
Figure 6.35 Displacement rate map obtained with the TSC application for the time interval 2008-2010	104
Figure 6.36 Displacement rate map obtained through the PSInSAR application to the 1st period of analysis	105
Figure 6.37 Displacement rate map obtained through the PSInSAR application to the 2nd period of analysis	105
Figure 6.38 Displacement rate map obtained with the SBAS method for the time interval 2008-2010	106
Figure 6.39 Comparison between time series of the displacement and the 15-days cumulated rainfall.....	107
Figure 6.40 Comparison between time series of displacement obtained with PSI and CPT (TSC pixel selection method).....	108
Figure 6.41 Displacement rate map obtained through the SBAS application for the time interval 2013-2014.....	109
Figure 6.42 Displacement rate map obtained with the CPT-TSC method for the time interval 2013-2014	110
Figure 6.43 Profiles of the slope of analysis: a) pre-event configuration (red line), b) post-event configuration (black line)	111
Figure 6.44 Simulation with the back-analysis, in red line are represented the three hypothetical slip surfaces	112
Figure 6.45 Stability analysis on the post-event profile	113
Figure 6.46 Comparison between piezometric and rainfall data with time series obtained with the CPT-TSC algorithm.....	115
Figure 6.47 Pie-chart showing the state of activity of the landslides in the 11 municipalities selected, according to the HSP	117
Figure 6.48 Frequency of the distribution of the velocities.....	119
Figure 6.49 Scheme adopted for the identification of the anomalous areas	121
Figure 6.50 R-Index computation on the whole Crotone Province on the ascending dataset	123
Figure 6.51 R-Index computation on the whole Crotone Province on the descending dataset	124
Figure 6.52 Map of the anomalous areas obtained with PSInSAR processed data: Cutro case	125
Figure 6.53 Map of the anomalous areas obtained with PSInSAR processed data: Strongoli case	126
Figure 6.54 Flow Diagram of the procedure adopted for the update of the landslide inventory map	127
Figure 6.55 Geological map of Crucoli	128
Figure 6.56 HSP map of Crucoli	129
Figure 6.57 Displacement rates map obtained through the SBAS application to Crucoli	130
Figure 6.58 Landslide inventory map resulting from the joint application of DInSAR and field survey at Crucoli	130
Figure 6.59 Evidences of the redefined landslide in the South-facing slope of Crucoli	131
Figure 6.60 Geological map of Carfizzi	132
Figure 6.61 HSP map to Carfizzi	133
Figure 6.62 Displacement rates map obtained through the SBAS application at Carfizzi	133
Figure 6.63 Landslide inventory map resulting from the joint application of DInSAR and field survey for Carfizzi	134
Figure 6.64 Evidences of the sport center landslide in Carfizzi	134
Figure 6.65 Geological map of Melissa	135
Figure 6.66 HSP map of Melissa, on the top, and Torre Melissa, on the bottom	136

Figure 6.67 Displacement rates map obtained through the SBAS application on Melissa, on the top, and Torre Melissa, on the bottom	138
Figure 6.68 Landslide inventory map resulting from the joint application of DInSAR and field survey for Melissa, on the top, and Torre Melissa, on the bottom	139
Figure 6.69 Evidences of the northern landslide in Melissa, on the top, and of the continuous landslide in Torre Melissa, on the bottom	140
Figure 6.70 Geological map of S. Nicola dell'Alto	141
Figure 6.71 HSP map of S. Nicola dell'Alto	141
Figure 6.72 Displacement rates map obtained through the SBAS application on S. Nicola dell'Alto	142
Figure 6.73 Landslide inventory map resulting from the joint application of DInSAR and field survey to S. Nicola dell'Alto	143
Figure 6.74 Evidences of the SE landslide in S. Nicola dell'Alto	143
Figure 6.75 Geological map of Casabona, on the top, and Zinga, at the bottom	144
Figure 6.76 HSP map of Casabona	145
Figure 6.77 Displacement rates map obtained through the SBAS application to Casabona	146
Figure 6.78 Landslide inventory map resulting from the joint application of DInSAR and field survey to Casabona	146
Figure 6.79 Landslide inventory map resulting from the joint application of DInSAR and field survey to Zinga area	147
Figure 6.80 Geological map of Strongoli	147
Figure 6.81 HSP map of Strongoli	148
Figure 6.82 Displacement rates map obtained through the SBAS application to Strongoli	149
Figure 6.83 Landslide inventory map resulting from the joint application of DInSAR and field survey to Strongoli	149
Figure 6.84 Evidences of the landslides in Strongoli	150
Figure 6.85 Geological map of Rocca di Neto	151
Figure 6.86 HSP map of Rocca di Neto	151
Figure 6.87 Displacement rates map obtained through the SBAS application on Rocca di Neto	152
Figure 6.88 Landslide inventory map resulting from the joint application of DInSAR and field survey to Rocca di Neto	153
Figure 6.89 Evidences of the northern landslide in Rocca di Neto	153
Figure 6.90 Evidences of the landslides in Rocca di Neto	154
Figure 6.91 Geological map of S. Severina	154
Figure 6.92 HSP map of Santa Severina	155
Figure 6.93 Displacement rates map obtained through the SBAS application to S. Severina	156
Figure 6.94 Landslide inventory map resulting from the joint application of DInSAR and field survey to S. Severina	156
Figure 6.95 Evidences of the landslides in Santa Severina	157
Figure 6.96 Geological map of S. Mauro Marchesato	158
Figure 6.97 HSP map of San Mauro Marchesato	158
Figure 6.98 Displacement rates map obtained through the SBAS application to S. Mauro Marchesato	159
Figure 6.99 Landslide inventory map resulting from the joint application of DInSAR and field survey to S. Mauro Marchesato	160
Figure 6.100 Geological map of Scandale	160
Figure 6.101 HSP map of Scandale	161
Figure 6.102 Displacement rates map obtained through the SBAS application to Scandale	162
Figure 6.103 Landslide inventory map resulting from the joint application of DInSAR and field survey to Scandale	162
Figure 6.104 Evidences of the landslides in Scandale	163

Figure 6.105 Geological map of Cutro	163
Figure 6.106 HSP map of Cutro	164
Figure 6.107 Displacement rates map obtained through the SBAS application to Cutro	165
Figure 6.108 Landslide inventory map resulting from the joint application of DInSAR and field survey to Cutro	165
Figure 6.109 Evidences of the landslides in Cutro	166
Figure 6.110 State of activity of landslides in the 11 test sites, according to SBAS elaboration and field activity	168
Figure 6.111 Active landslides detected by the overlap between SBAS and field, only in the field, and only through SBAS	168
Figure 6.112 Landslides undetected by the satellite	169
Figure 6.113 Active landslides detected by both SBAS and field activities	169
Figure 6.114 Landslides detected with and without coincidence between SBAS and field survey	170
Figure 7.1 a) Mining area of Belvedere di Spinello; b) and c) salty crust emersions	172
Figure 7.2 Geological and geomorphological map of the mining area of Belvedere di Spinello	173
Figure 7.3 Displacement rate maps obtained through the PSInSAR processing of the 1st period of analysis	176
Figure 7.4 Displacement rate maps obtained through the PSInSAR processing of the 2nd period of analysis	177
Figure 7.5 Displacement rate maps obtained through the SBAS processing	178
Figure 7.6 Capo Colonna promontory	180
Figure 7.7 a) Roman ruins in Capo Colonna archaeological site. Nao Tower and the Sanctuary on the background; b) prism of rock isolated by systems of fractures; c) and d) ruins located along the coastline	181
Figure 7.8 On the top, geological map of Capo Colonna. On the bottom, typical stratigraphic sequence of Capo Colonna	182
Figure 7.9 Damage reported during a field survey in November 2015	183
Figure 7.10 Displacement rate map through SBAS on the descending dataset	184
Figure 7.11 Displacement rate map with SBAS on the descending dataset	185
Figure 7.12 Displacement rates map: a) ERS descending data; b) ENVISAT ascending data	186
Figure 7.13 Map of the total vertical displacements occurring in Capo Colonna area between April 2008 and June 2010	188
Figure 7.14 Location of the corner reflectors installed. All around, photos of some of the corners	189
Figure 7.15 On the left, COSMO-SkyMed HR image; on the right, Pixel selection with COSMO-SkyMed products	189
Figure 7.16 CosmoSKY-MED HR image	190

List of Tables

Table 4.1 SAR bands and frequency and wavelength associated.....	39
Table 4.2 Main features of each SAR satellite mission.....	46
Table 4.3 Main DInSAR approaches.....	56
Table 5.1 Number of landslides for each type.....	70
Table 6.1 Main parameters for the SBAS application to the Cirò case study	87
Table 6.2 Main parameters for the SBAS application on Papanice case study	106
Table 6.3 Main parameters for the SBAS application on Papanice case study	109
Table 7.1 Main parameters for the SBAS application on Belvedere di Spinello case study	177
Table 7.2 Main parameters for the SBAS application to Capo Colonna case study	183
Table 7.3 Amplitude value of each point with the available imagery	190

List of Abbreviations

- AADE: area affected by deep erosion
AADSD: Area Affected by Deep Slow Deformation/movement
AASSD: Area Affected by Shallow Slow Deformation/movement
ALOS: Advanced Land Observing Satellite
ARPACAL: Calabrian Regional Agency for the Environmental Protection
ASI: Italian Space Agency
AVI: Vulnerable Areas in Italy
BMBF: German ministry of Education and Science
CARG: CARtografia Geologica
COSMO-SkyMed: COnstellation of small Satellites for Mediterranean basin Observation
CP: Coherent Point
CPT: Coherent Pixels Technique
CRED: Centre for Research on the Epidemiology of Disasters
CSA: Canadian Space Agency
CSK: COSMO-SkyMed
DEM: Digital Elevation Model
DInSAR: Differential SAR Interferometry
DLR: German Aerospace Center
DSGSD: Deep-Seated Gravitational Slope Deformation
EEA: European Environmental Agency
ENI: Ente Nazionale Idrocarburi
ENVISAT: Environmental Satellite
EO: Earth Observation
EPOCH: European Programme On Climate and Natural Hazards
ESA: European Space Agency
ESD: Enhanced Spatial Differences
GBSAR: Ground-Based SAR
GIS: Geographical Information System
GNDCI: National Group for the Hydro-geological Catastrophes Defense
GPS: Global Positioning System
HR: High Resolution
HSP: Hydro-geomorphological Setting Plan
IAEG: International Association for Engineering Geology and the Environment
IFFI: Inventario dei Fenomeni Frangosi in Italia
IFSAR/InSAR: Interferometric Synthetic Aperture Radar
IPTA: Interferometric Point Target Analysis
IRPI: Italian Research Institute for Geo-Hydrological Protection
ISBAS: Intermittent Small Baseline Subset
ISPRA: Institute for Environmental Protection and Research
ISTAT: Italian Institute of Statistics
JAXA: Japan Aerospace eXploration Agency
JPL: Jet Propulsion Laboratory
LEWIS: Landslide Early Warning Integrated System
LiDAR: Light Detection And Ranging
LOS: Line Of Sight
MORFEO: Monitoring Landslide Risk Through Earth Observation Technology
MTI: Multi-Temporal Interferometry
NASA: National Aeronautics and Space Administration
NASDA: National Space Development Agency of Japan

PS: Permanent Scatterers
PSInSAR: Persistent Scatterer InSAR
PSP-DIFSAR: Persistent Scatterers Pairs- DIFFerential InSAR
RADAR: RAdio Detection And Ranging
SAR: Synthetic Aperture Radar
SBAS: Small BAseLine Subset
SLAM: Service for LAndslide Monitoring
SLC: Single Look Complex
SNR: Signal Noise Ratio SPN: Stable Point Network
STUN: Spatio-Temporal Unwrapping Network
TOPSAR: Terrain Observation with Progressive Scans SAR
TSC: Temporal Sublook Coherence
TSX: TerraSAR-X
VHR: Very High Resolution
UNESCO: United Nations Educational, Scientific and Cultural Organization
UPC: Universitat Politecnica de Catalunya
USGS: United States Geological Survey
WGS 84: World Geodetic System 1984
WP/WLI: Working Party on World Landslide Inventory

CHAPTER 1: INTRODUCTION

Ground deformation and instability represent globally one of the most remarkable and widespread natural hazards. They also determine very often a considerable number of casualties and huge economic losses. Among ground instabilities, landslides are a significant natural hazard involving mountainous and hilly regions as well as along riverbanks and coastlines. Italy is severely affected by landslide phenomena and it is one of the European countries most affected by this kind of events. According to recent studies made by Superior Institute for the Environmental Protection and Research (ISPRA, 2014), more than 1000 landslides occurred in 2014 on the Italian territory, causing severe damage to urban areas and infrastructures. Moreover, according to the Italian Research Institute for Geo-Hydrological Protection (IRPI), landslides in Italy are “recurrent, widespread and dangerous phenomena”, counting, only in the first half year of 2015, three victims and nine casualties. The reasons should be addressed to several factors: The geological and geomorphological context of the Italian territory is very prone to such phenomena, in addition, a wrong land management following the economic miracle of the early 60s’ surely influenced and still influences the frequency of landslides occurrence and the exposure of the Italian settlements to them. Fast-moving landslides and flash floods are the most “evocative” for the violence and the number of casualties caused, however it should not be underrated the contribution of landslides characterized by very slow to slow kinematic, according to Cruden and Varnes classification (1996). Slow-moving landslides are extremely widespread especially in Southern Italy: Recent cases can be mentioned, among which the most significant examples are represented by the case histories of Agnone (Berti et al., 2003; Fortuna, 2006; Calcaterra et al., 2008), Montaguto (Guerriero et al., 2013), Moio della Civitella (Calcaterra et al., 2008; Calò et al., 2009; Di Martire et al., 2014), San Fratello (Bardi et al., 2014; Bianchini et al., 2014) and Montescaglioso (Manconi et al., 2014). Such examples are very peculiar and illustrative for the belonging category, being characterized by a long evolutionary history, and by several reactivations of the already deformed mass, due to several reasons such as intense and prolonged rain events, earthquakes, and sometimes to human activities. The area of interest of this PhD project is located in Southern Italy, more precisely in Calabria region: The deformation events in Crotone province (located along the Ionian coast), in fact have been individuated and analyzed. This area is affected both by slow-moving landslides and by subsidence, involving terrains characterized by weak materials, such as Pliocene clays, located in a peculiar tectonic setting. Therefore, the monitoring of these deformation phenomena is of utmost importance, not only for the scientific community, but also for the public administrations, in order to prevent and reduce their effects and consequences. The technology embodies nowadays a very helpful and relevant supporting tool for the monitoring of areas affected by ground displacements, being able to follow the evolution of the above-mentioned

typology of events, and to provide useful information for the stakeholders. Among the recent technological advancements, remote sensing tools have become one of the most important and valuable methods for the prevention and investigation of instabilities, thanks to their rapidity of acquisition, the easy management of the data and for the relative low costs as well. The Differential Synthetic Aperture Radar Interferometry (DInSAR) is a worthwhile remote sensing device for the mapping and the monitoring of landslides (Colesanti & Wasowski, 2006; Cascini et al., 2010; Di Martire et al., 2011; Calò et al., 2012; Herrera et al., 2013; Ciampalini et al., 2014; Wasowski & Bovenga, 2014; Bianchini et al., 2014; Notti et al., 2015; Novellino et al., 2015; Di Martire et al., 2016); in the last 15 years, many DInSAR techniques have been developed, becoming able to analyze large datasets of Synthetic Aperture Radar (SAR) imagery acquired on the same area, at different dates. Moreover, the development of the so-called Multi Temporal Interferometry (MTI), which overcome some of the limitations of conventional DInSAR (Wasowski & Bovenga, 2014), successfully improved the analysis and the monitoring of the landslide events. The availability of Very High Resolution (VHR) images, acquired by modern sensors, also contributed to improve analyses on areas affected by diffuse instability, allowing to obtain better-quality results thanks to a higher accuracy of such data. For this PhD project datasets of VHR images, acquired by the TerraSAR-X (2007-ongoing) satellite mission, operated by the German Aerospace Center (DLR) were exploited. These stacks cover almost the whole Crotone province, except for a band of territory in the inner part, toward the Sila sector. Several MTI approaches have been applied here, in order to investigate and analyze displacements present in the area. The integration with “conventional” methods, such as inclinometers, piezometers and geomorphological surveys, turned out to be relevant for these purposes, providing very precise information about the nature and causes of ground deformation. The general idea of the project has been to assess the landslide hazard in selected areas of the Crotone province and to update the related landslide inventory map of the area, dated back to 2006, by means of DInSAR techniques. These goals have been reached through the comprehension and the understanding of the movements, on one hand on a very local scale (slope), and on the other hand, on a wide-area scale (the whole Crotone province). Thanks to this consideration, it is possible to analyze movements observable by the satellite, and update the existing landslide inventory map of the Crotone province, where it is covered by the available SAR imagery. Additionally, two other case studies of subsidence, caused by different sources, have been studied with MTI techniques, showing the suitability of such methods for other types of ground deformation.

1.1 Structure of the thesis

The thesis is structured in nine sections. The first paragraph introduces and motivates the work carried out in the three years of the project, providing information about the issues affecting the Italian territory and the role of this research in a wider framework. The second chapter gives an illustration concerning landslides, starting from the simple description and classification, to the landslide overview in Italy, and at last highlighting the most common methods for mapping and monitoring such events. In the third chapter, a description of subsidence phenomena and their monitoring will be given. Afterwards, in the fourth chapter, a general overview about the SAR technology is presented. In addition, in this case, the first objective is to define such methodology, also illustrating the various SAR missions performed in the last 20 years, and the development of some of the algorithms available in the scientific community, also describing the range of applications of DInSAR for natural hazards monitoring and investigation. A particular focus is given on landslide monitoring by means of DInSAR techniques, showing benefits and constraints of each methodology. In the last paragraph of the SAR chapter, a short description on the data available and exploited is given. The following chapter, the fifth, deals with the study area: The objective in this chapter has been to depict the geographical, geological and geomorphological features of the study area, also providing information on the cartography available. The sixth chapter describes the methodology conceived and applied for the DInSAR monitoring on the whole study area, through an in-depth focusing on the case-histories selected, meanwhile in the following section the results of the two subsidence cases will be shown. The last two chapters deal with the discussions and the conclusions of this research, critically analysing the role of such work in the general panorama of the scientific community, and illustrating the possible future perspectives.

1.2 Objectives of the research

One of the most significant aims of this thesis is to apply SAR methods for the monitoring, the investigation and the evaluation of ground deformation phenomena in the Crotone province. The intention is to show the potential of such techniques for the detection, the estimation of the velocities and of the deformation of surface displacements, both on very local scale (slope scale) and on wide areas (kilometre-size extension). Moreover, it will be verified if the comparison with “traditional” ground techniques will provide reliable results, showing analogous rates of displacement and good connections, and if it will be possible to confirm the efficacy of these tools for geoscientific applications, in spite of some of the most common limitations, such as temporal decorrelation of the interferometric signal or atmospheric noises, for instance.

The main highlights of this thesis are:

- The exploitation of DInSAR methodologies for the monitoring and the analysis of slow-moving landslides in the Crotone province study area, starting from the implementation of MTI, (Wasoski & Bovenga, 2014) on a site scale, aiming at the comprehension and the prediction of slope failures. Moreover, extending the SAR monitoring on the entire study area, it is possible to update the official landslide inventory map available, dated back to the year 2006. The case study selected for the local scale analysis is a landslide occurred in 2011 in Cirò town, while further analysis have been done on Papanice settlement (2012 event).
- The application of DInSAR methods also for the subsidence monitoring, although caused by different sources. Two cases have been selected: Belvedere di Spinello, where the ground subsidence was triggered by the 30 years-activity of extraction of salt in a mining area, and Capo Colonna, where the subsidence in this case was originated by the gas extraction and by the normal tectonic activity of the area, affecting, besides, a significant heritage site of Greek origin.
- The inquiry of the benefits and the constraints of the two packages used (SUBSOFT processor, developed by the Remote Sensing Lab of the *Universitat Politecnica de Catalunya*, Barcelona, Spain, and the SARscape® software, a commercial software ran by the SARMAP team and available on the ENVI® suite). Additionally, also an evaluation of the different algorithms employed has been performed: On the SUBSOFT processor the CPT (Coherent Pixels Technique, Mora et al., 2003; Blanco et al., 2008) is implemented, with two different methods for the final pixel selection, one by coherence and another one by the temporal sublook coherence (Iglesias et al., 2015); in the SARscape software two fundamental techniques are available, the PSInSAR (Ferretti et al., 2001) and the SBAS (Berardino et al., 2002).

CHAPTER 2: LANDSLIDES

2.1 Landslides: definition and main features

Landslides are one of the main natural hazards, for extent, impact on man-made infrastructures and properties and number of casualties, accounting every year severe damage, in terms of direct and indirect costs. In general, the theme of natural triggered disasters gained significant awareness in the last years. Many annual reports and databases have been developed: The Centre for Research on the Epidemiology of Disasters (CRED) every year publishes an “Annual Disaster Statistical Review”, focusing on the emergency situations with a major impact on human health. In 2014, globally 324 natural disasters have been registered, killing 7823 people; however, in the year 2014 the third lowest number of disaster of the last decade has been reported. It is worth to point out that hydrological disasters still represents one of the major hazards, counting in 2014 153 reported events, 47.2 % of the natural disasters, and also the number of victims is the highest compared to meteorological, climatological and geophysical disasters, as observable in Figure 2.1.

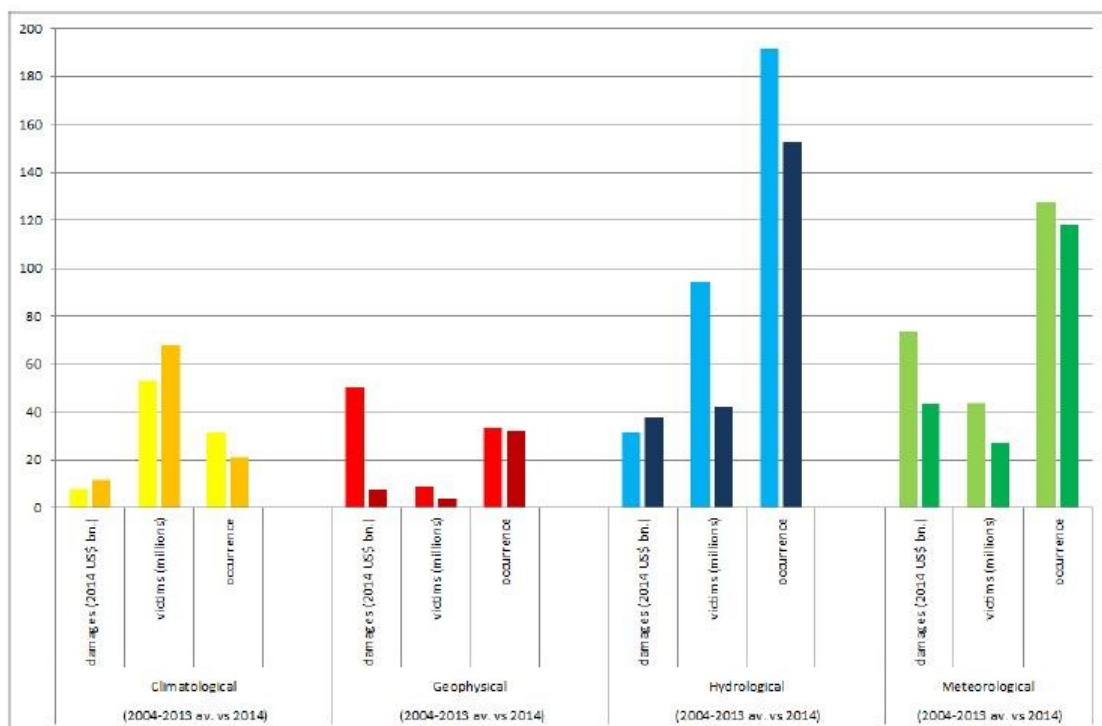


Figure 2.1 Impact of the 2014 natural disasters vs. 2004-2013 annual average (modified from CRED, 2014). In yellow climatological, in red geophysical, in blue hydrological and in green meteorological disasters. In bright colors 2004-2013 average, in dark colors 2014 number of events.

For “hydrological disasters” it is intended floods, landslides and wave action, the meteorological

events are represented by storms and extreme temperatures, the climatological group summarizes events as drought and wildfires, and at last geophysical disasters include earthquakes and volcanic activity. Obviously, landslides represent one of the most impactful events affecting human activities and, globally, the costs of their exposure to hazard are quite significantly relevant. Moreover, the growth of the urbanization increased the damage and the related costs for restoration and reparation. The spatial distribution of fatal landslides (events with loss of lives reported) present a strongly heterogeneous pattern, as shown in Petley et al. (2012), being located in all the continents (Fig. 2.2). In order to prevent casualties and damage due to natural disasters such as landslides, the monitoring and the mapping of landslides assume a paramount role. In the following, a general overview of the main topics related to landslides is presented, along with information on landslide mapping and monitoring.

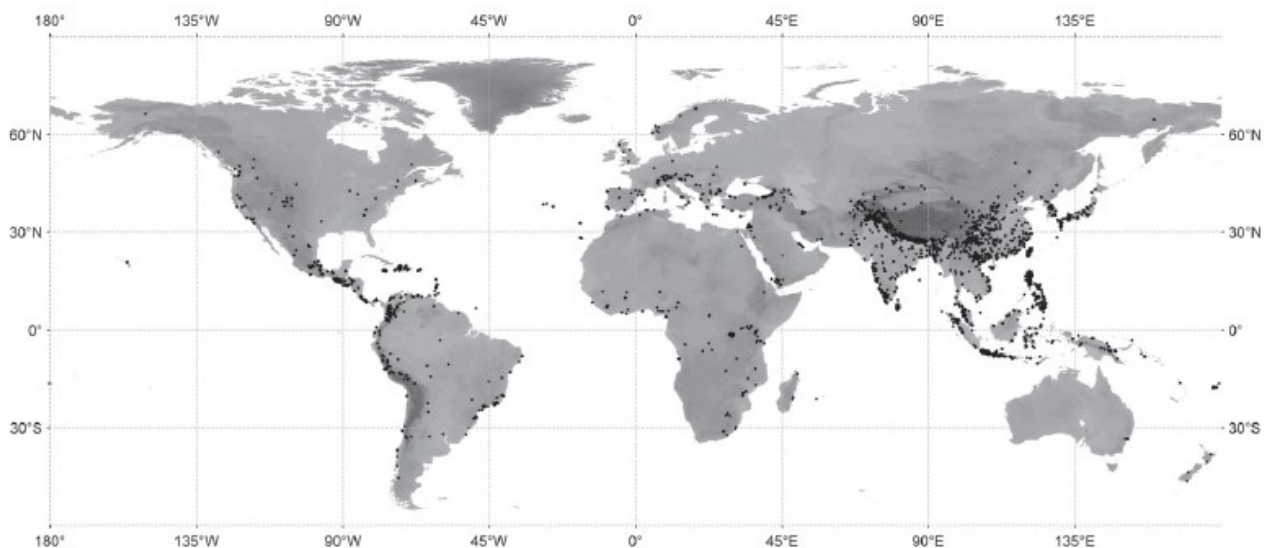


Figure 2.2 Spatial distribution of fatal landslides (modified from Petley et al., 2012).

2.1.1 Landslide definition and classifications

A definition given by Cruden (1991) for the UNESCO Working Party on Landslide Inventory (1990) describes the term landslide as “the movement of a mass of rock, debris or earth down a slope”. Landslide is a North American word, meanwhile in the British vocabulary a common term used in the early 1900’ is “landslide”, definable as “the sliding down of a mass of land on a mountain or a cliffside: land which has so fallen”, according to the Oxford English Dictionary (Onions, 1933). Although any dispute on the term used to describe these phenomena, the term landslide is the most recognizable and employed in literature, thus the one that will be used in this thesis. Varnes (1978)

indicated landslides as “downward and outward movement of slope forming materials under the influence of gravity”; further definitions have been provided by Brunsden (1984), preferring the term mass movement, and distinguishing this from mass transport as being a process non requiring a transporting medium such as water, air or ice (Dikau et al., 1996). Taking into account the significantly increase of devastating landslide events, the UNESCO Working Party on World Landslide Inventory claimed for an establishment of a detailed list of the World’s landslides. One of the first tasks has been to set up a Working Party, to suggest methods of classifying the rates of movement of landslides, their causes, the geology and activity and distribution of movement within landslides (WP/WLI, 1993). One of the most diffused classifications for landslides is based on the kind of materials involved and the type of movement (Varnes, 1978). Such classification is thus based on two terms: The first concerns the material involved, the second describes the type of movement. Five different materials have been included:

- **Rock:** is “a hard or firm mass that was intact and in its natural place before the initiation of movement”.
- **Soil:** is “an aggregate of solid particles, generally of minerals and rocks, which either was transported or was formed by the weathering of rock in place. Gases or liquids filling the pores of the soil form part of the soil”.
- **Earth:** “describes material in which 80% or more of the particles are smaller than 2 mm, the upper limit of sand sized particles”.
- **Mud:** “describes material in which 80% or more of the particles are smaller than 0.06 mm, the lower limit of silt sized particles”.
- **Debris:** “contains a significant proportion of coarse material; 20% to 80% of the particles are larger than 2 mm, and the remainder are less than 2 mm”.

As regards the movements, seven different types have been classified and depicted (Fig. 2.3):

- **Falls:** movements composed by masses detached from steep slopes or cliffs, with little or no shear displacement, and going downward through air (free fall) or bouncing and rolling.
- **Topples:** movements of masses of different materials made of a forward rotation about a fulcrum point.
- **Rotational slides:** in this case the masses slide downwards and outwards on one or more concave surfaces, sinking at the back and heaving at the toe.
- **Translational slides:** in this case the movements occur along a planar failure surface and it may continue parallel to the slope.

- **Spreads:** involve the fracturing and the lateral extension of coherent rocks or soils, after the liquefaction of the subjacent materials.
- **Flows:** they can be a slow to rapid movement of saturated or dry material, advancing like a viscous fluid.
- **Complex landslides:** they consist in the composition of one or more types of movements, one following the others.

However, the importance of providing significant information concerning the age, the mechanism and the style of the movement has been more and more acknowledged by earth scientists and governments. Starting from the experiences of the various WP/WLI, and especially within the WP/WLI of 1993, a glossary on the terminology to use in order to univocally describe landslides has been drafted. Such glossary provided a rationalization of the terms, starting from Varnes 1978's classification, and finalized into the Cruden and Varnes classification of 1996. First of all, just five of the former seven categories of typology of movement have been distinguished, referring only to falls, topples, slides, flows and spreads, then including rotational and translational slides into one category, and eliminating the complex typology.

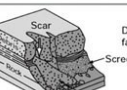
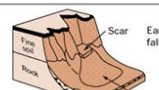
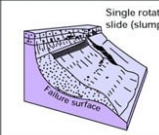
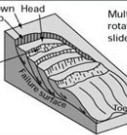
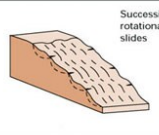
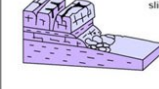
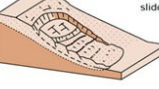
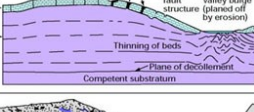
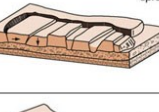
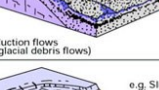
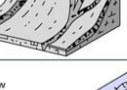
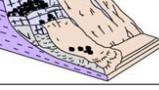
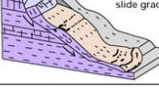
Material Movement type	ROCK	DEBRIS	EARTH
FALLS	 Rock fall	 Debris fall Scree Debris cone	 Scar Rock Colluvium Debris cone
TOPPLES	 Rock topple	 Debris topple Debris cone	 Cracks Debris cone
SLIDES	 Single rotational slide (stump) Failure surface	 Crown Scarp Head Scarp Minor Scarp Failure surface Top	 Successive rotational slides
	 Rock slide	 Debris slide	 Earth slide
SPREADS	 Gap rock Clay shale Normal sub-horizontal structure Gully Camber slope Dip and fold structure Valley bulge (planed off by erosion) e.g. cambering and valley bulging Plane of disconnection Competent substratum		 Earth spread
FLLOWS	 Solifluction flows (Periglacial debris flows)	 Debris flow	 Earth flow (mud flow)
COMPLEX	 e.g. Slump-earthflow with rockfall debris		 e.g. composite, non-circular part rotational/part translational slide grading to earthflow at toe

Figure 2.3 Cruden and Varnes classification of landslides (modified from Cruden and Varnes, 1996).

Moreover, the state of activity, which describes, through geomorphological information, the temporal evolution characteristics of a landslide, has been defined, selecting eight different types (Fig., 2.4):

- 1. Active:** landslides are active when are actually moving;
- 2. Suspended:** when landslides moved within the last seasonal cycle, but they are not currently active;
- 3. Reactivated:** landslides are reactivated when they are again active after being inactive;
- 4. Inactive:** when landslides moved for the last time before the last seasonal cycle. Besides the inactive landslides can be further divided in the following states:
- 5. Dormant:** inactive landslide which could be reactivated following instability;
- 6. Stabilized:** inactive landslides protected after human intervention;
- 7. Abandoned:** inactive landslides protected from their original causes;
- 8. Relict:** inactive landslide developed in a geomorphological and climatic condition completely different from the actual situation.

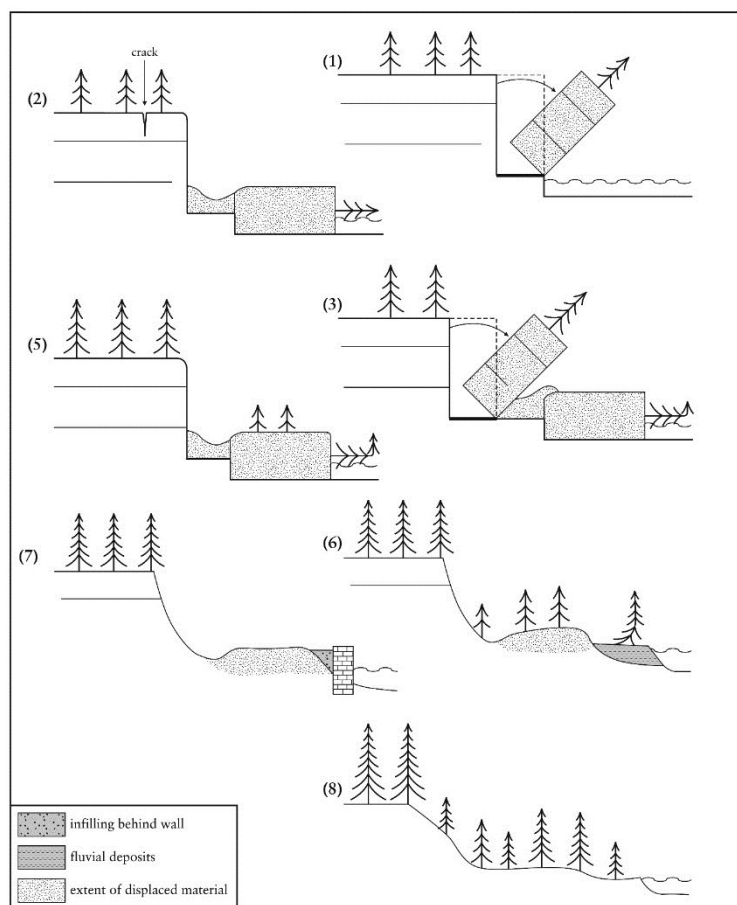


Figure 2.4 Scheme of the state of activity of a landslide, modified from WP/WLI (1993). 1) Active landslide; 2) Suspended landslide; 3) Reactivated landslide; 5) Dormant landslide; 6) Abandoned landslide; 7) Stabilized landslide; 8) Relict landslide. State 4 (inactive) comprehends states 5-8.

Another important task which has been defined by the WP/WLI (1993) is the delineation of the distribution of activity, which refers to how and where the landslide is moving. It can be (Fig. 2.5):

- 1. Advancing:** the rupture surface of a landslide extends towards the direction of the movement;
- 2. Retrogressive:** the rupture surface is extending in the opposite direction respect to the movement direction;
- 3. Enlarging:** the rupture surface is extending in two or more directions;
- 4. Diminishing:** the volume of mobilized material decreases;
- 5. Confined:** there is the presence of a scarp, but no rupture surface is clearly visible;
- 6. Moving:** the mobilized material continues to move without any visible change in the rupture surface and in the volume;
- 7. Widening:** in this case the rupture surface extends into one or both flanks of the landslide.

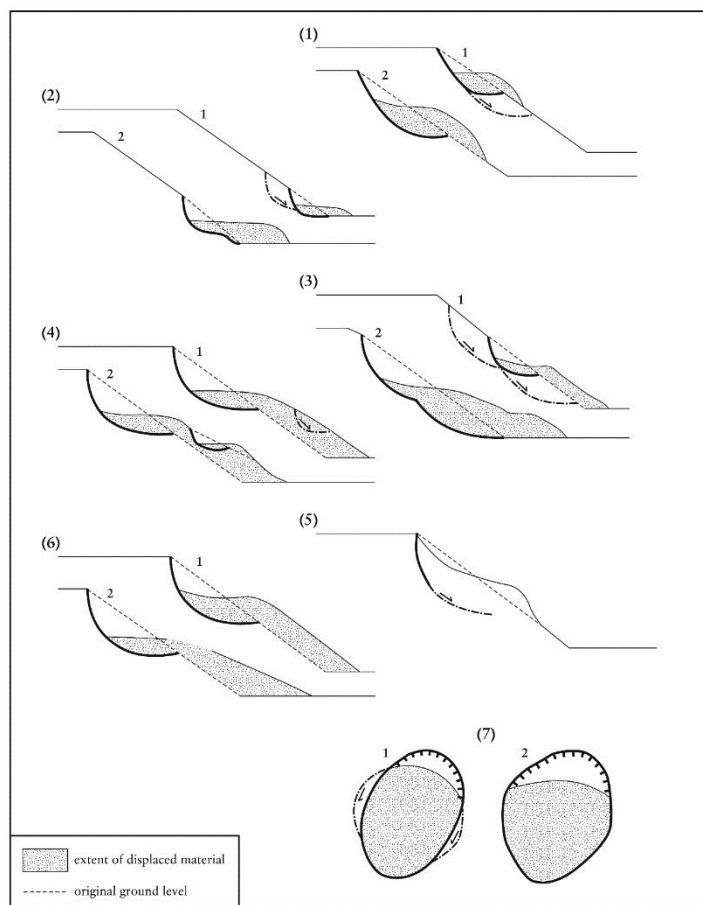


Figure 2.5 Scheme of the distribution of activity of a landslide, modified from WP/WLI (1993). 1) Advancing landslide; 2) Retrogressive landslide; 3) Enlarging landslide; 4) Diminishing landslide; 5) Confined landslide; 6) Moving landslide; 7) Widening landslide.

Finally, also the style of a landslide activity has been defined and described, consisting in the contribution of different movements within a single landslide and their relationship. Several styles have been identified (Fig. 2.6):

- **Complex:** a complex landslide is made of at least two different types of movement (e.g., sliding and flowing) in sequence;
- **Composite:** a composite landslide shows at least two types of simultaneous types of movements, but located in different parts of the landslide;
- **Successive:** it is a similar type as a nearby, earlier landslide, but not sharing mobilized material or a rupture surface with it;
- **Single:** a single landslide is a single movement of displaced material;
- **Multiple:** a multiple landslide shows repeated movements of the same kind.

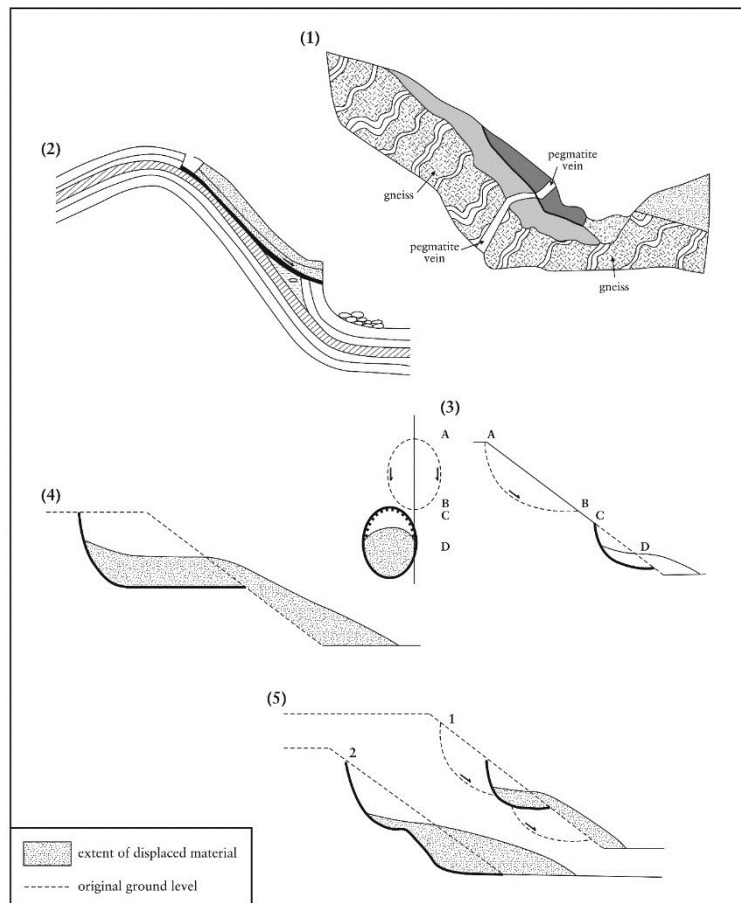


Figure 2.6 Scheme of the style of activity of a landslide, modified from WP/WLI (1993). 1) Complex landslide; 2) Composite landslide; 3) Successive landslide; 4) Single landslide; 5) Multiple landslide.

Finally, Cruden & Varnes (1996) introduced a velocity scale, rationalizing all the previous scale. For a landslide, velocity is intended as the highest speed achieved after the slope failure. It represents a very important parameter for the risk assessment in hazardous areas and especially for DInSAR analysis, where, due to several technical aspects, only a range varying from extremely slow to very slow movements (from 15 mm/year up to 1.6 m/year) (Cigna et al., 2013) can be observed and detected by the satellite. Figure 2.7 shows this classification and the related probable destructive significance.

Velocity Class	Description	Velocity (mm/sec)	Typical Velocity	Probable Destructive Significance
7	Extremely Rapid	5×10^3	5 m/sec	Catastrophe of major violence; buildings destroyed by impact of displaced material; many deaths; escape unlikely
6	Very Rapid	5×10^1	3 m/min	Some lives lost; velocity too great to permit all persons to escape
5	Rapid	5×10^{-1}	1.8 m/hr	Escape evacuation possible; structures; possessions, and equipment destroyed
4	Moderate	5×10^{-3}	13 m/month	Some temporary and insensitive structures can be temporarily maintained
3	Slow	5×10^{-5}	1.6 m/year	Remedial construction can be undertaken during movement; insensitive structures can be maintained with frequent maintenance work if total movement is not large during a particular acceleration phase
2	Very Slow	5×10^{-7}	15 mm/year	Some permanent structures undamaged by movement
	Extremely SLOW			Imperceptible without instruments; construction POSSIBLE WITH PRECAUTIONS

Figure 2.7 Velocity of a landside according to Cruden and Varnes classification (modified from Cruden and Varnes, 1996).

From the abovementioned classification, other movements defined in the scientific literature have been excluded but can be cited and monitored by satellite techniques: first, the so-called Deep-Seated Gravitational Slope Deformation (DSGSD) (IAEG, 1977; Dramis, 1994; Soldati, 2013), which could be divided into three basic types, sacküng (Zischinsky, 1966), lateral spread of ridges (Jahn, 1964; Varnes, 1978; Hutchinson, 1988) and lateral spread of thrust fronts (Varnes, 1978); the other movement not ascribable to landslides is the soil creep (Sharpe, 1938; Terzaghi, 1950; Kirkby, 1967), very slow form of mass wasting, adjustment of soil, hardly noticeable by eyes, but recognizable by evidences, like fencepost shifted or tilting of poles and trees.

It is worth to mention that other classifications have been proposed in engineering geological studies, starting from Balzer (1875) onward, but Varnes (1978), ideating a classification based on type of material involved and type of movement, has given a first modern approach. Successively, Pierson and Costa (1987) focused their attention to classify the flow type landslide, based on velocity and sediment concentration. Hutchinson (1988) proposed a geomorphological and geotechnical approach, shown in Figure 2.8, and then the European Programme On Climate and Natural Hazards, (EPOCH, 1993) focused their efforts on classifying landslides on the base of the European experiences and conditions. Dikau et al. (1996) suggested a classification of landslide mechanisms compatible with Hutchinson (1988) and EPOCH (1993), and finally, Hungr et al. (2001) analyzed and re-organized the flow-type landslides, based on the genetic and the morphological aspects, and in the year 2014 attempted to revise several aspects of the well-known classification of Varnes (1978), modifying the definition of landslide-forming materials and providing compatibility with accepted geotechnical and geological terminology of rocks and soils, and in conclusion individuating 32 landslide types.

A	Rebound	
	1	Movements associated with man-made excavations
	2	Movements associated with naturally eroded valleys
B	Creep	
	1	Superficial, predominantly seasonal creep; mantle creep
	2	Deep-seated, continuous creep; mass creep
	3	Pre-failure creep; progressive creep
	4	Post-failure creep
C	Sagging of mountain slopes	
	1	Single-sided sagging associated with the initial stages of landsliding
	2	Double-sided sagging, associated with the initial stages of double landsliding, leading to ridge spreading
	3	Sagging associated with multiple toppling
D	Landslides	
	1	Confined failures
	2	Rotational slips
	3	Compound failures (markedly non-circular, with listric or bi-planar slip)
	4	Translational slides
E	Debris movements of flow-like form	
	1	Mudslides (non-periglacial)
	2	Periglacial mudslides (gelification of clays)
	3	Flow slides
	4	Debris flows, very to extremely rapid flows of wet debris
	5	Sturzstroms, extremely rapid flows of dry debris
F	Topples	
	1	Topples bounded by pre-existing discontinuities
	2	Topples released by tension failure at rear of mass
G	Falls	
	1	Primary, involving fresh detachment of material; rock and soil falls
	2	Secondary, involving loose material, detached earlier; stone falls
H	Complex slope movements	
	1	Cambering and valley-bulging
	2	Block-type slope movements
	3	Abandoned clay cliffs
	4	Landslides breaking down into mudslides or flows at the toe
	5	Slides caused by seepage erosion
	6	Multi-tiered slides
	7	Multi-storeyed slides

Figure 2.8 Hutchinson classification of landslides (Modified from Hutchinson, 1988).

In this thesis the Cruden and Varnes (1996) classification has been followed.

2.1.2 Landslide features

A more complete knowledge about landslides passes compulsorily through the individuation and the definition of the main features that characterize landslides in their totality (Fig. 2.9). The following terminology is based on Cruden & Varnes (1996).

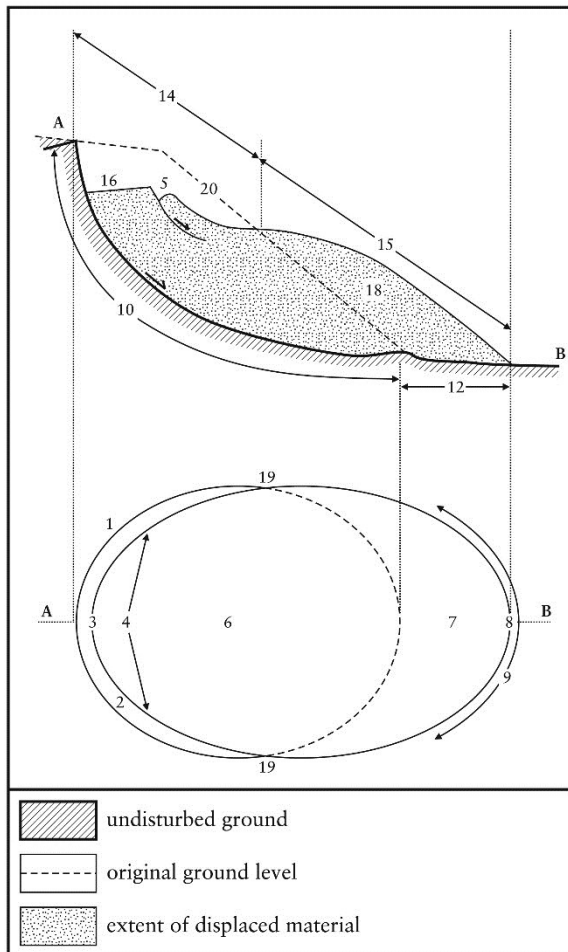


Figure 2.9 Features of a landslide (modified from WP/WLI, 1993).

- 1. Crown:** The non-mobilized material still in place and adjacent to the highest parts of the main scarp.
- 2. Main Scarp:** A steep surface on the undisturbed ground at the upper edge of the landslide, caused by movement of the displaced material away from the undisturbed ground.
- 3. Top:** The highest point of contact between the displaced material and the main scarp.

- 4. Head:** The upper parts of the landslide along the contact between the displaced material and the main scarp.
- 5. Minor Scarp:** A steep surface on the displaced material of the landslide produced by differential movements within the displaced material.
- 6. Main Body:** The part of the displaced material of the landslide that overlies the surface of rupture between the main scarp and the toe of the surface of rupture.
- 7. Foot:** The portion of the landslide that has moved beyond the toe of the surface of rupture and overlaid the original ground surface.
- 8. Tip:** The point of the toe farthest from the top of the landslide.
- 9. Toe:** The lower, usually curved margin of the displaced material of a landslide, it is the most distant from the main scarp.
- 10. Surface of Rupture:** The surface which forms (or which has formed) the lower boundary of the displaced material below the original ground surface.
- 11. Toe of the Surface of Rupture:** The intersection (usually buried) between the lower part of the surface of rupture of a landslide and the original ground surface.
- 12. Surface of Separation:** The part of the original ground surface overlain by the foot of the landslide.
- 13. Displaced Material:** Material displaced from its original position on the slope by movement in the landslide. It forms both the depleted mass and the accumulation.
- 14. Zone of Depletion:** The area of the landslide within which the displaced material lies below the original ground surface.
- 15. Zone of Accumulation:** The area of the landslide within which the displaced material lies above the original ground surface.
- 16. Depletion:** The volume bounded by the main scarp, the depleted mass and the original ground surface.
- 17. Depleted Mass:** The volume of the displaced material, which overlies the rupture surface but underlies the original ground surface.

18. Accumulation: The volume of the displaced material, which lies above the original ground surface.

19. Flank: The undisplaced material adjacent to the sides of the rupture surface. Compass directions are preferable in describing the flanks but if left and right are used, they refer to the flanks as viewed from the crown.

20. Original Ground Surface: The surface of the slope that existed before the landslide took place.

Important as well is to define the landslide dimensions, as provided by WP/WLI (1993). In Figure 2.10 the main characteristics are shown.

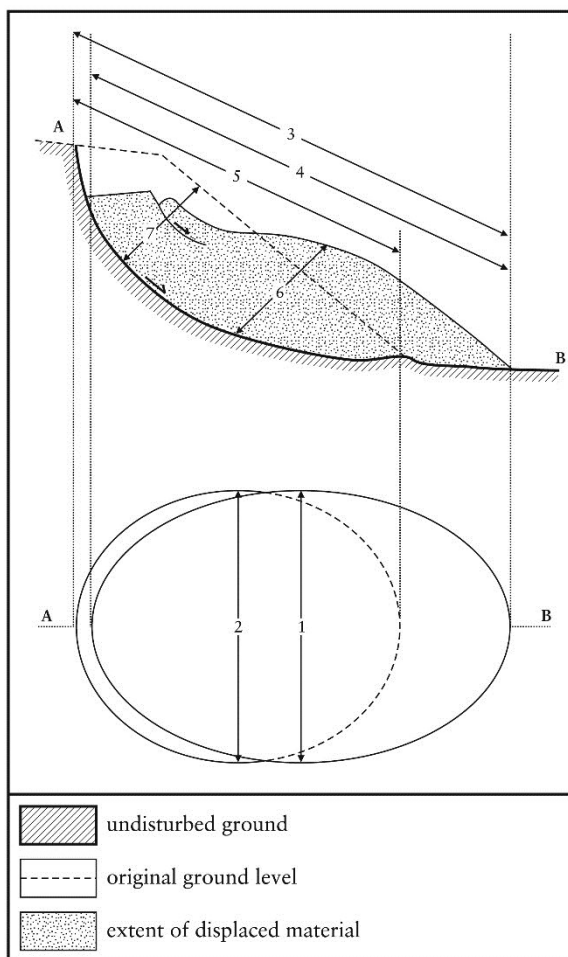


Figure 2.10 Landslide dimensions (modified from WP/WLI, 1993).

- 1. Width of the Displaced Mass:** The width of the displaced mass, W_d , is the maximum width of the displaced mass perpendicular to the length of the displaced mass, L_d .
- 2. Width of the Rupture Surface:** The width of the rupture surface, W_r , is the maximum width between the flanks of the landslide, perpendicular to the length of the rupture surface, L_r .
- 3. Total length:** The total length, L , is the minimum distance from the tip of the landslide to the crown.
- 4. Length of the Displaced Mass:** The length of the displaced mass, L_d , is the minimum distance from the tip to the top.
- 5. Length of the Rupture Surface:** The length of the rupture surface, L_r , is the minimum distance from the toe of the surface of rupture to the crown.
- 6. Depth of the Displaced Mass:** The depth of the displaced mass, D_d , is the maximum depth of the displaced mass, measured perpendicular to the plane containing W_d and L_d .
- 7. Depth of the Rupture Surface:** The depth of the rupture surface, D_r , is the maximum depth of the rupture surface below the original ground surface measured perpendicular to the plane containing W_r and L_r .

2.1.3 Landslide causes

The trigger of a landslide can have several causes and reasons, which may act singularly or in combination between them. The mechanisms which lead to generate a landslide can be discretized in several categories:

- Geological causes: Weak and weathered materials involved, sheared, jointed or fissured lithotypes, presence of discontinuity (bedding, schistosity, fault, unconformity, etc.), contrast of permeability.
- Morphological causes: Tectonic or volcanic uplift, erosion, vegetation removal, deposition loading on slopes, etc.

- Human causes: Excavation of slope or its toe, deforestation, irrigation, mining, loadin of slope, artificial vibration, water leakage, etc.

Although the multitude of elements which may represent a trigger for slope failures activation, three are the main factors that caused the most of the landslides around the world, and they are water, earthquakes and volcanism.

Water surely represents the main trigger for landslide activation; in particular, the slope saturation by water is the primary reason (Iverson et al., 1997). Very often, this is an effect after prolonged and intense rainfalls (Iverson, 2000), snowmelts (Cardinale et al., 2000) or generally changes in the groundwater levels, also along coastlines, earth dams, reservoirs and canals and rivers. Also earthquakes and in general seismic activity increase the instability of mountainous areas, and consequently the likelihood of slopes to landslide occurrence (Yin et al., 2009). Many are the examples of slides, lateral spreadings and other types following large earthquakes. As a final point, the volcanic activity embodies one of the most destructive types of trigger for landslides, whereas the lava can melt snow and ice, and facilitate flooding on the slopes of volcanoes and surrounding mountains, generating the so-called lahars, volcanic debris flows (Scott et al., 2005).

2.2 Landslides in Italy

Historically, Italy has always been a country severely affected by landslide events. Therefore, the role of the Italian nature scientists has been to acquire the right knowledge and awareness of such phenomena. A first attempt to conduct a census of the landslides was done by the geographer Roberto Almagià (1910), on behalf of the Italian Geological Society. The final result was a complete knowledge of the landslides occurred between the 19th and 20th century on the whole national territory (excluding the Alps and the islands), carried on after several field surveys (Palmieri, 2004). Successively, another census has been done by the Minister of Public Works during the 60's, publishing, in 1965 a volume with all the inventory collected between 1957 and 1963. More recently a more complete survey on areas hit by landslides and floods between 1918 and 1990 has been carried out by the National Group for the Hydro-geological Catastrophes Defense (GNDCI) in 1998. In 1992 the Geological National Service published an important study on the "Geological and Geo-environmental instability in Italy, from postwar to 1990", curated by V. Catenacci, collecting qualitative and quantitative information on the main devastating events occurred on the national territory. Another archive of landslide in Italy is within the Vulnerable Areas in Italy project (AVI), developed with the aim of make a census of the areas historically

affected by landslides and floods (between 1918 and 2001). It is only after the disaster of Sarno (1998 involving also the municipality of Siano, Quindici, Bracigliano and S.Felice a Cancello) that the Government felt the need of a complete and homogeneous analysis of the distribution of landslides on the national territory. Hereafter started the IFFI project, providing for an accurate landslide inventory on the Italian territory, based on photointerpretation and geological field surveys. The IFFI project represents the first homogeneous and updated landslide inventory of the Italian territory. More than 300 among geologists, ITs and bureaucrats collaborated for the realization of this project. The archive is published on the Web, in order to promote the accessibility of information to as much people as possible. The archive, up to the end of 2014, counted 499.511 landslide phenomena involving an area of about 1.182 km², equal to the 7% of the national territory. The two main products of the IFFI project are the online cartography service, allowing to visualize the landslides and the main parameters associated, and the Report on landslides in Italy (ISPRA), published each year, and summarizing the information on the national and regional situation. According to this, ca. the 12% of the landslide individuated caused damage to objects and population. In parallel, the law 183/1989 on the soil defense, established the “Basin plan” as a cognitive, normative and technical instrument for the planning of the actions and the rules for the conservation, the defense and the development of the soil and the correct use of the water, on the base of the physical and environmental characteristics of the area of interest (Law 183/1989). In this case, the hydrographic basin has been chosen as scope in all the studies and elaborations. Accordingly, the new-established Basin’s Authorities are the agencies predisposed for such aims. The Hydro-geomorphological Setting Plan (HSP) is the tool which the Basin’s Authorities use to understand and determine a territorial setting capable to ensure a balance between the hydrogeological dynamics and the growing urbanization. One of the tasks of the Basin’s Authorities deal with the slope instabilities, starting from a census of the landslides present on the given territory, in order to identify landslide hazard and risk and eventually define the intervention in some cases. Obviously, the above-mentioned numbers point out the necessity of a correct land management and the implementation and the improvements of instruments like Landslide Inventory Maps. Also recently it is possible to count every year more than one thousand events on the national territory (ISPRA, 2014). According to Research Institute for Geo-Hydrological Protection (CNR-IRPI), landslides in Italy are “recurrent, widespread and dangerous phenomena”. The most significant recent cases in Italy which provoked damage to urban centres and communication infrastructures are in Parma and Reggio Emilia province in 2013, Cinque Terre and Lunigiana in October 2011 (Cevasco et al., 2013), Massa (MS) in October 2010, Montaguto (AV) in March 2010 (Giordan et al., 2013; Guerriero et al., 2013), Maierato (VV) in February 2010 (Gattinoni et al.,

2012), San Fratello (ME) in February 2010 (Bardi et al., 2014; Bianchini et al., 2014), Giampilieri (ME) in October 2009 (Aronica et al., 2012), Borca di Cadore (BL) in July 2009 and Altilia (CS) in January 2009. Among the main events in the last 60 year, with catastrophic consequences it is possible to cite Genova (1970), Ancona (1982) (Coltorti et al., 1985; Cotecchia, 2006), Stava (1985) (Chandler et al., 1995; Sammarco, 2004), Sarno (1998) (Del Prete et al., 1998; Calcaterra et al., 2000; Zanchetta et al., 2004), Nocera Inferiore (2005) (Revellino et al., 2013). According to ISPRA 211 main landslide events have been counted in Italy in 2014, causing 14 victims, casualties and evacuees as well as damage to buildings and infrastructures of primary importance. Meanwhile, according to CNR-IRPI, which for more than 20 years is collecting, organizing and analyzing information on the impact of instability events on the people, in the first half year of 2015 twelve landslide events were identified, that provoked the death of 3 people and 9 casualties (Fig. 2.11). IRPI also collected and organized an archive of the events between 1965-2014, arranged in a map, and calculating 1279 deaths, 1702 casualties and 158.923 evacuees (Fig. 2.12). A noteworthy parameter to quantify the number of people potentially involved by instability phenomena has been set by ISPRA, thus calculating a number of people exposed to landslides of ca 1.001.174 inhabitants. This estimation has been obtained intersecting in a GIS (Geographic Information System) environment the ISTAT (Italian Institute of Statistics) census sections with landslides individuated during the IFFI (Landslide phenomena inventory in Italy) project. On a regional scale, the Calabria region has the highest number of population exposed to landslide (159.611 inhabitants).



Figure 2.1 Maps of the landslide and flood events with “victims” between 1 January and 30 June 2015 (modified from CNR IRPI, 2015).

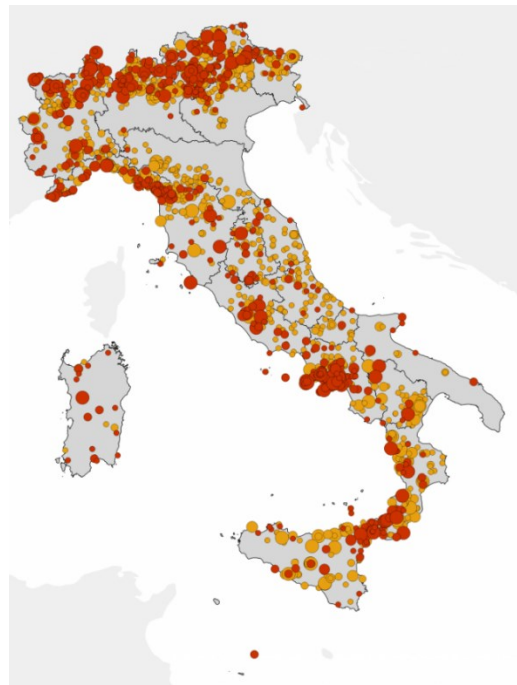


Figure 2.2 Maps of the landslide events with “victims” between 1965 and 2014 (modified from CNR IRPI, 2015).

2.3 Landslide mapping and inventory

Landslide mapping is a fundamental tool for the assessment of landslide hazard, even with the differences that characterize their generation, due to variability of scale and procedure existing, the requirements of the end user and the purpose of the investigation (Varnes, 1974, 1978; Rockaway, 1976; Cotecchia, 1978). The landslide inventory is an essential part of any landslide zoning and understanding of the evolution of landscapes. It involves the location, classification, volume, travel distance, state of activity and date of occurrence of landsliding in an area (Fell et al., 2008). Furthermore, it is a map useful for the record of the location and, where possible, the date of occurrence and the types of mass movements which have left discernable traces in an area (Pašek, 1975; Hansen, 1984a, 1984b; McCalpin, 1984; Wieczorek, 1984; Guzzetti et al., 2000). The representation of a landslide can be achieved through a point or a polygon, according to the scale of the map. An inventory can also include information on past documented activity of landslides, but does not provide any information about their temporal evolution, or the changes that may have occurred with time (Parise, 2001). This instrument basically embodies the base of further maps, such as landslide susceptibility or hazard maps. Landslide inventory maps are prepared for different purposes (Brabb, 1991; Galli et al., 2008; Guzzetti et al., 2012), like: 1) showing the location and type of landslides in a region (Antonini et al., 1993; Cardinali et al., 2001; Antonini et al., 2002); 2) showing the effects of single landslide triggering events, such as an earthquake (Harp & Jibson, 1995, 1996), an intense rainfall event (Bucknam et al., 2001) or rapid snowmelt event (Cardinali et al., 2000); 3) showing the abundance of mass movements (DeGraff, 1985; DeGraff & Canuti, 1988; Guzzetti et al., 2000); 4) determining the frequency area statistics of slope failures (Hovius et al., 1997, 2000; Guzzetti et al., 2002; Brardinoni et al., 2003; Guthrie & Evans, 2004a,b; Malamud et al., 2004); and 5) providing relevant information to construct landslide susceptibility (Soeters & van Westen, 1996; Guzzetti et al., 1999; Chung & Fabbri, 1999, 2003, 2005) or hazard (Guzzetti et al., 2005, 2006a,b) models.

Several methodologies have been developed in the last years to better locate and define landslides in a given area: one of the most exploited is the photogrammetry, an instrument which allows the user to study and to interpret landslides, visualizing all their morphological features and modifications through aerial or satellite stereoscopic photos. Usually they are taken by fixed focus cameras, mounted on aircrafts. Every frame reports on the edge the so-called data-strip (Fig. 2.13), where the altimetry, the level, the clock and the counter necessary for the identification of the flight are shown.

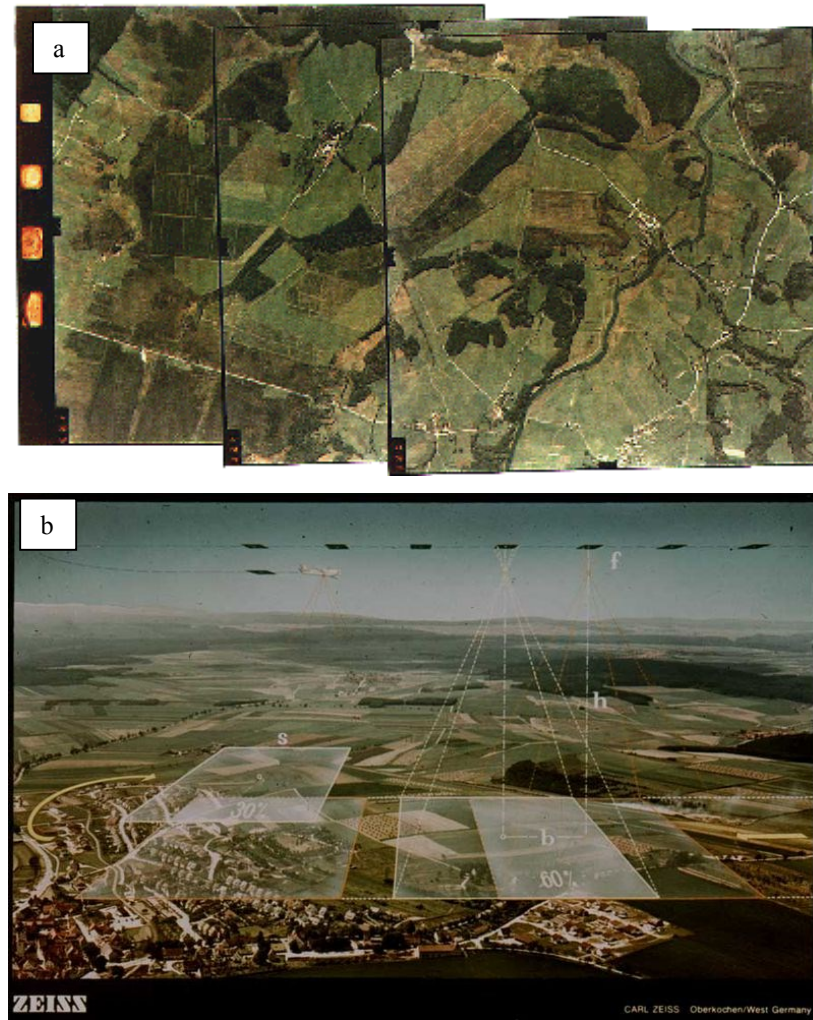


Figure 2.3 a) Frames of stereo-photogrammetry (www.regione.veneto.it); b) Photographs through airborne acquisition (www.treccani.it).

The photos are acquired in sequence, so that every frame covers at least the 60% of the previous one. After the acquisition, the photos are analyzed through the stereoscope, an instrument that permits the 3D vision of the shot area. The recognition of landslides through the visual stereoscopic analysis, anyway, requires experience, training and a certain methodology, as well as defined interpretation criteria (Speight, 1977; Rib and Liang, 1978; van Zuidam, 1985; Antonini et al., 2002a, 2002b). Unfortunately, the capacity of visualization through aerial photointerpretation can be influenced by the presence of the vegetation, especially when dense and growing rapidly. With the improvement of the technologies, thanks to the use of Digital Elevation Models (DEMs), that reconstruct the Earth surface, it is possible to make temporal comparisons in order to observe and analyze modifications of the topography caused by instability phenomena. Basically a DEM is a pixel-based raster (Fig 2.14), where at every pixel the height of the ground level is associated. DEMs can be generated

by means of remote sensing techniques, like satellites, airplanes or earth-based stations. Even with the help of many technologies like the ones explained before, the individuation and the study of ground displacements for the generation of landslide inventory maps passes through classical geomorphological ground surveys, aiming at the inspection of the morphology and of the main features of a landslide (i.e. main scarp, flanks, toe, etc.), the identification of the geo-lithological setting of the study area, as well as of the state of activity and the possible evolution and the infrastructures involved in landslides. The implementation of airborne laser profilers and Light Detection and Ranging (LiDAR) represents an innovation for the generation of very-high resolution DEMs.

Above all, the airborne LiDAR is a consistent remote sensing technique useful for the digital reproduction of topographic surfaces (Shan & Toth, 2009). The laser is mounted on the aircraft for measuring the distance from the instrument to the Earth surface. LiDAR can be very useful for the detection of landslides in vegetated areas, thanks to its ability to penetrate canopy (Haugerud et al., 2003; Schulz, 2007; Van den Eeckhaut et al., 2007; Booth et al., 2009; Razak et al., 2011). Also satellite sensors are valuable instruments to recognize and map landslides: initially (since the early 70's) the adoption of new sensors able to acquire optical image like Landsat and SPOT were fundamental for investigators (e.g., Gagnon, 1975; McDonald & Grubbs, 1975; Sauchyn & Trench, 1978; Stephens, 1988; Scanvic & Girault, 1989; Scanvic et al., 1990; Huang & Chen, 1991; Vargas, 1992). Obviously the improvement and the development of new technologies simplified and made landslide investigation easier, like the availability of High Resolution (HR) and VHR imagery, as well as improvements in computer hardware and software for the processing and analysis of images. In addition, SAR sensors have been exploited for landslide detection: It is the case of the SAR. Further details about SAR principles and techniques can be found in the fourth chapter. In the last two decades, several technologies have been developed, helping geologists and geomorphologist in landslide mapping in the field, but one of the most valuable is the satellite-based GPS (Guzzetti et al., 2012). GPS simplifies the location of features on the Earth surface with an accuracy which often exceeds the needs for landslide mapping (Malamud et al., 2004; Fiorucci et al., 2011). The role of GIS is clearly significant for the collection and analysis of the acquired data. One of the limitation of the Inventory Maps are due to a lack of standards for the preparation and update, and no agreement exists on how to obtain or validate a landslide map (Guzzetti et al., 2012).

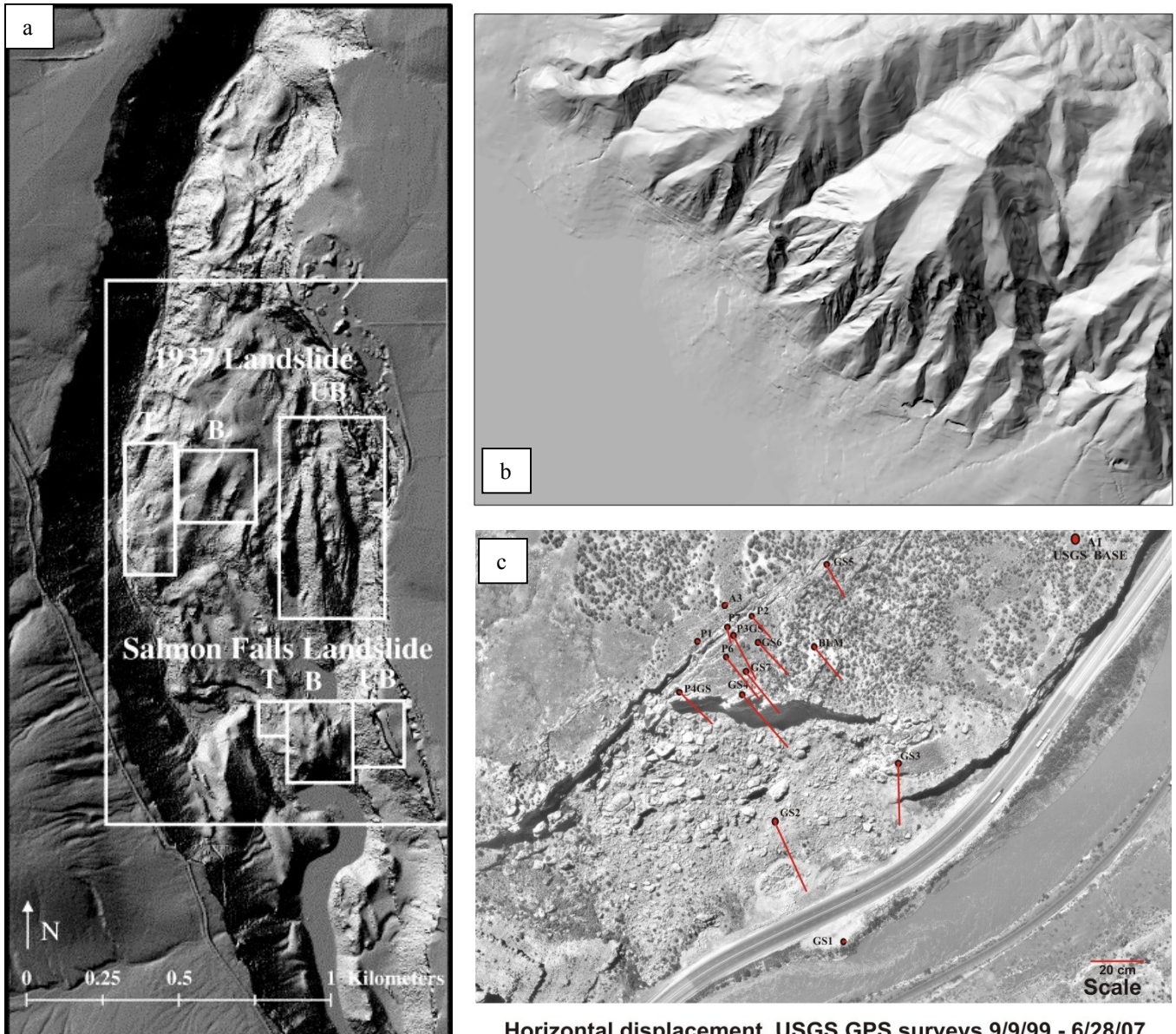


Figure 2.4 a) LiDAR DEM for landslide mapping (modified from Glenn et al., 2006); b) DEM obtained from Regional Technical Cartography of Campania region; c) DEM with GPS showing vectors of displacement (modified from Colorado Geological Survey).

2.4 Landslide monitoring

Landslide mapping is essential for the investigation on causes and effects of such phenomena, but landslide monitoring is fundamental, too. After the mapping, the regular observation and recording of the evolution of landslides, especially for the events characterized by slow and intermittent kinematic assumes a paramount role, in order to prevent eventually damage to structures and to preserve buildings. The monitoring of natural phenomena has acquired relevance also due to the improvement in technology, allowing more detailed analyses and interpretations. A correct monitoring is achieved through the observation of the kinematic, the hydrological and the climatic parameters in order to (Angeli et al., 2000):

- Identify movements before important morphological changes at the surface have taken place;
- Define the geometry of the moving mass with precision;
- Quantify the principal kinematic parameters (velocity, acceleration, etc.) and their possible correlation with hydrological and climatic characteristics;
- Carry out constant surveillance for events that put inhabited areas at risk;
- Propose reasonable plans to help people in risk areas.

Obviously a correct monitoring makes the implementation of appropriate instrumentations mandatory: Specific instruments installed within landslides can provide useful information regarding possible landslide movements and the potential for increased hazards (Wieczorek & Snyder, 2009). A first step can be achieved with the landslide mapping, as showed in the previous paragraph; for a more accurate analyses instruments of various nature are necessary.

For instance, for the study of deep deformations of the mass and for the individuation of the slip surface, one of the best-suited instruments is the inclinometer. It consists of a hollow metal tube (Fig. 2.15 a, c and d), which is installed within a drilled hole. Such installation registers the deformation of the surrounding terrain, determining the variation of the original inclination of the tube. The inclinometer monitors deformation normal to the axis of the casing and the depth detected for the shear movement is the depth of the failure surface. The acquisition of the deformation are executed periodically using an inclinometric probe, the inclinometer indeed, even if nowadays real-time transmission of measurement data to data loggers are much more widespread. The probe usually contains two perpendicular accelerometers, for the measurement of the inclination of the casing with respect to the vertical; therefore, it is possible to quantify the movement in the four different directions. Displacement measurements are obtained multiplying the lecture pace (usually 50 cm) for the sinus of the inclination measured by the probe (Fig. 2.15 b). The slope inclinometer installation and interpre-

tation processes involve several important factors or steps, so the resulting measurements and difference between the zero and subsequent readings are meaningful (Stark & Choi, 2008). The inclinometer must be located below the slip surface. Moreover, the same probe and the electrical cable used for the zero readings should be used for subsequent readings, in order to calibrate the measurement, and it is also preferable that the same person performs all the readings, so avoiding any difference from the zero reading. In addition, the measurement of the rate of the movement is important, because it determines whether the slide is accelerating, decelerating or keeping constant (Fig. 2.15 e), in order to take decisions on possible evacuation of the area of interest (Stark & Choi, 2008).

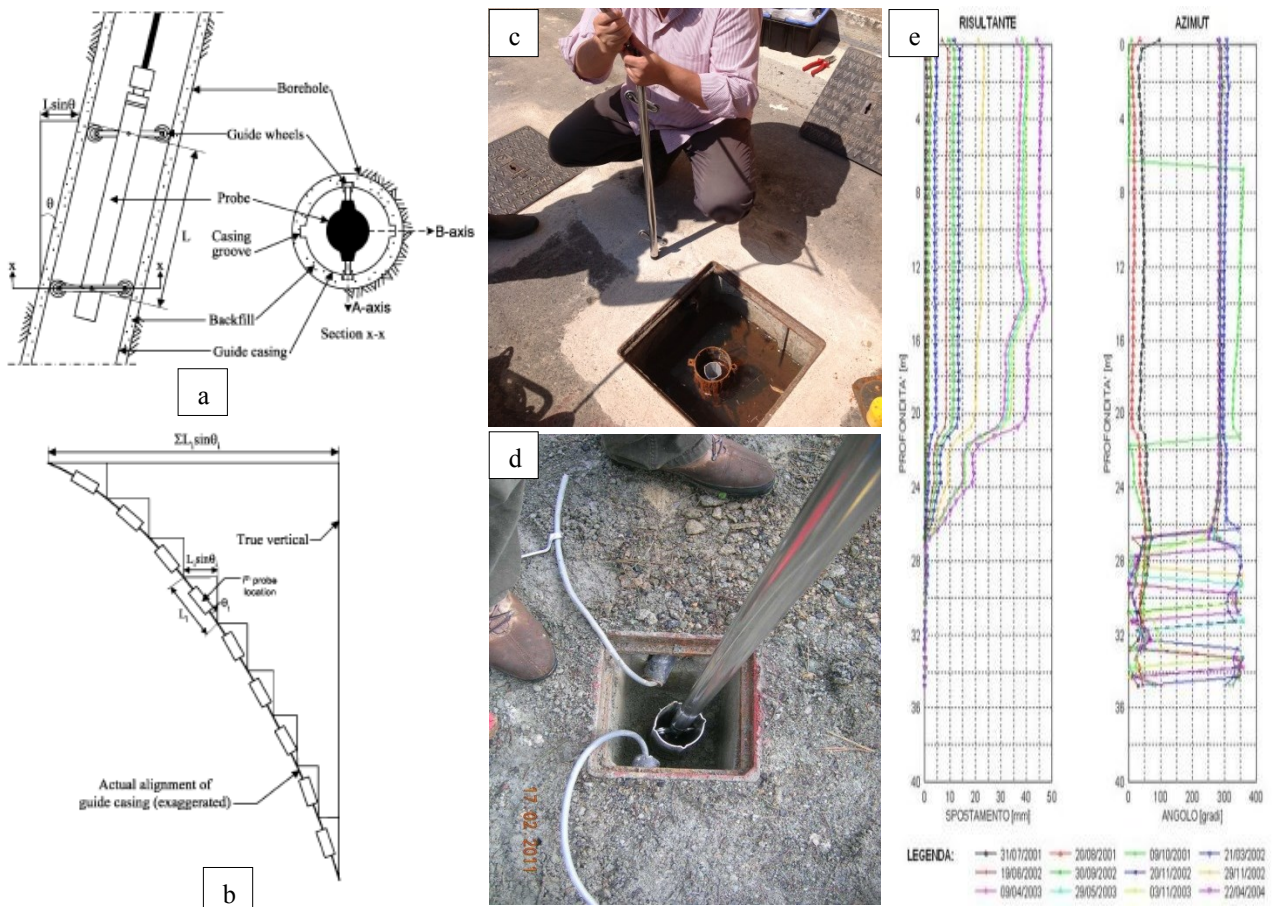


Figure 2.5 a) Inclinometer configuration; b) Inclinometer operation (Stark & Choi, 2008); c) & d) Inclinometric readings; e) Inclinometric data.

One of the most significant triggering factors is the pressure of groundwater, related, very often, to precipitations. Piezometers are installation of instruments, within a drill hole, for detecting first the depth of water, but also the groundwater fluctuation and the pressure of groundwater levels at specific depths and the pore pressure (Fig. 2.16). The latter parameter in particular can provide information on the stresses and the strains in a rock or terrain mass. Several types of piezometers have

been invented in the last 80 years, according to the type of terrain to investigate or to the parameters to obtain. For instance, PVC casings down to the depth of interest and slotted or screened casing characterize the open standpipe piezometers, where the water pressure needs to be measured. The casing is sealed into the drill hole with clay or concrete to prevent surface water from outer contamination. Also in this case, a probe, a piezometric probe, is dropped into the borehole for the periodical reading. The transducer of the probe converts the pressure into an electrical signal and can be a vibrating-wire, pneumatic, or strain gauge in operation. The open standpipe piezometer is very suitable for terrain characterized by a mean permeability.

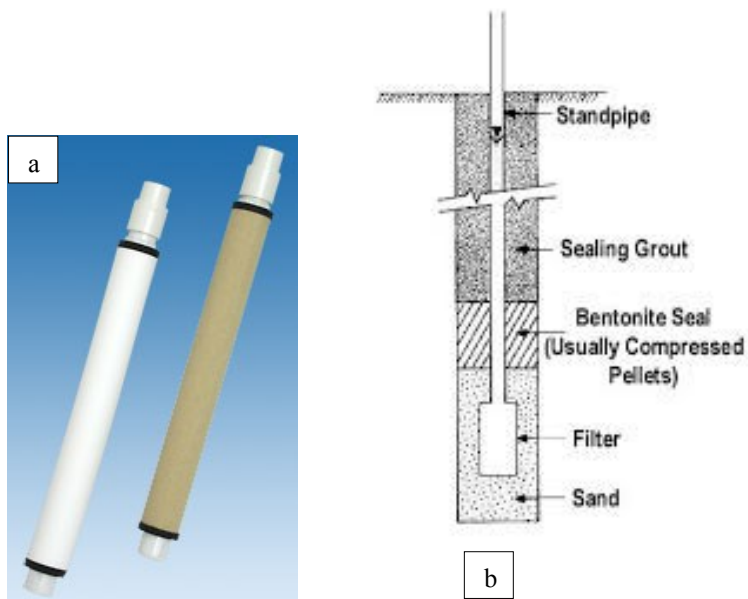


Figure 2.6 a) Open standpipe piezometer (www.slopeindicator.com); b) scheme of a piezometer installation (<http://civcal.media.hku.hk/>).

Rainfall-triggered landslides are, from a quantitative point of view, very significant. In particular, landslides with a slow and intermittent kinematic present acceleration and deceleration according to the intensity of precipitation, especially for the shallow deformations (Caine, 1980). High-resolution temporal rainfall data can be acquired by using specific instruments, like automatic tipping bucket rain gauges, weighing rain gauge, acoustic rain gauge, optical rain gauge, etc., all known as pluviometers (De Luca, 2014). These are instruments to gather and measure the precipitation occurring in a given period of time. Tipping bucket rain gauges are the most popular recording rain gauges used by many national weather and hydrological service agencies. High accuracy of recording low-to-intermediate intensity rainfalls, a superior mechanism for actuating circuits, suitability for remote recording and reliability distinguish tipping bucket rain gauges. This type of gauge produces rainfall data in digital form, which can be readily processed by computers (Vasvári, 2005). A

standard tipping bucket (Fig. 2.17 a and b) rain gauge is composed of three parts arranged on a mounting bracket: A funnel, a measuring tube and an overflow tube. The funnel directs the precipitation into the measuring tube. The measuring tube, when full, pours the excess water in the overflow tube. The process then repeats itself allowing for precise measurement of rainfall intensity and amount (Ahrens, 2007). Despite the huge amount of different rain gauges, precipitation measurements are always expressed as a vertical depth of water.

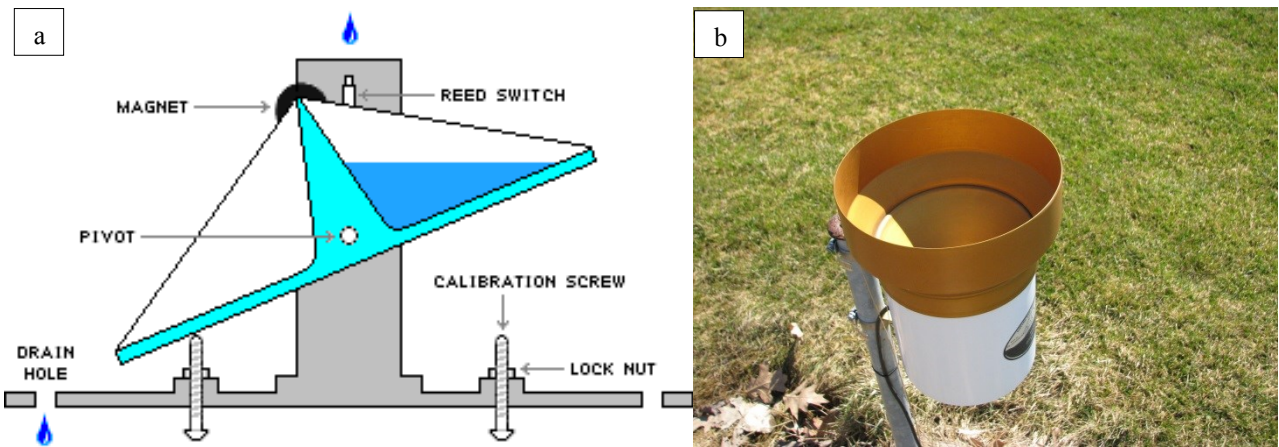


Figure 2.7 a) Scheme of realization of a b) tipping bucket type rain gauge (www.weathershack.com).

These are the instruments used during the experience of this work of thesis, but obviously many other instruments are indicated for landslide monitoring, such as extensometers, topographic measurements, GPSs, etc. Other applications, like remote sensing technologies, will be deeply discuss in the following chapters.

CHAPTER 3: SUBSIDENCE

3.1 Definition and main types

Subsidence is a geological hazardous phenomenon: It consists in the gradual settling, up to the sudden sinking of the Earth surface. The reasons can be various: Scott (1979) grouped the subsidence causes into two main categories, natural and anthropic. Natural causes can be summarized in compaction of soil materials, deep material dissolution, lateral soil creep, deep erosion and tectonic activity, among the anthropic activities generating or contributing to subsidence can be cited fluid withdrawal (oil, water, and gas) and excavation of tunnels or mining galleries. Tomás et al. (2013), following Prokopovich's genetic classification (1979) identified two different types of subsidence:

- “endogenic”, when associated with natural geological processes, such as faulting, folding, isostatic adjustments and volcanism;
- “exogenic”, when related to anthropogenic, sometimes natural, processes involving the creation of cavities and/or the removal of material from the subsurface.

Active subsidence in highly urbanized areas may cause significant damage to human infrastructures, with relatively high costs (Kappel et al., 1999; Autin 2002; Gutiérrez et al., 2009; Mancini et al., 2009; Julio-Miranda et al., 2012). Subsidence is a global and widespread natural phenomenon. Hu et al. (2004) estimated more than 150 cities affected by subsidence due to excessive groundwater withdrawal. The most famous cases are: the Po valley (Carminati and Martinelli, 2002; Teatini, 2011), Venice and Ravenna (Italy) (UNESCO, 1984; Strozzi et al., 2003; Teatini, 2005), Mexico City (UNESCO, 1984; Strozzi and Wegmuller, 1999; Osmanoglu et al., 2008), Antelope (USA) (Galloway et al, 1998; Hoffman et al., 2003), Bangkok (Thailand) (Phien-Wej, 2006), Osaka (Itoh, 2000). Different types of genesis for subsidence have been reported (Fig. 3.1). Subsidence can frequently occur and causes major problems in karst terrains (Fig. 3.2 a), where the piping within limestone formations is made by the creation of voids due to dissolution of limestone by water. The expansion of these voids brings the roof of limestone terrains to collapse. Such type of subsidence can result in sinkholes, sometimes called subsidence sinkholes (Culshaw and Waltham, 1987; Waltham et al., 2007). Subsurface mining, instead, is an invasive methodology, which can intentionally cause the collapse of the surface and then results in surface subsidence. Mining-induced subsidence (Fig. 3.2 b) is relatively predictable in its magnitude, manifestation and extent, except for the rapid collapse of tunnel or cavities (Herrera et al, 2007). Mining-induced subsidence is nearly always much localized to the surface above the mined area, plus a margin around the outside. The impact of mining subsidence on the environment can occasionally be very catastrophic; however, such subsidence gives rise to varying

degrees of structural damage (Bell et al., 2000). When mining activity is planned, mining-induced subsidence can be successfully managed if there is co-operation from all of the stakeholders. Even earthquakes can provoke subsidence: Examples have been observed in Japan (Tohoku earthquake) (Imakiire and Koarai, 2012) or in California (Lee, 1979). Faulting, due to volcanic or tectonic activity is another factor causing subsidence (Holzer et al., 1978; Rubin, 1992; Bartov et al., 2006). When faulting occurs, subsidence may take place in the hanging wall of normal faults, in reverse faults or thrust, relative subsidence may be observed in the footwall. More rapid type of subsidence is the one caused by anthropic activity such as gas or oil extraction (Fig. 3.3 b) (Pratt and Johnson, 1926; Mayuga and Allen, 1970; Vanhasselt, 1992, Fielding and Blom, 1998). Gas withdrawal depends on the depth of burial, thickness of mineralized rocks and overall volumetric production (Gambolati et al., 1991). One of the main causes for subsidence is surely the withdrawal of fluids below the ground surface, in particular water-withdrawal (Fig. 3.3 a). In fact, the principal consequence of pumping groundwater in excess is the subsidence (Hix, 1995). Water used for irrigation in arid areas is very often extracted from groundwater sources, and the groundwater withdrawal results in fluid pressure change in the layers. Land subsidence caused by groundwater pumping is due to compaction of aquitards during the time-dependent and typically slow process of aquitard drainage (Tolmand and Poland, 1940; Galloway et al., 1998). A correct water management, thus, must take into account the subsidence occurring in the area of withdrawal.

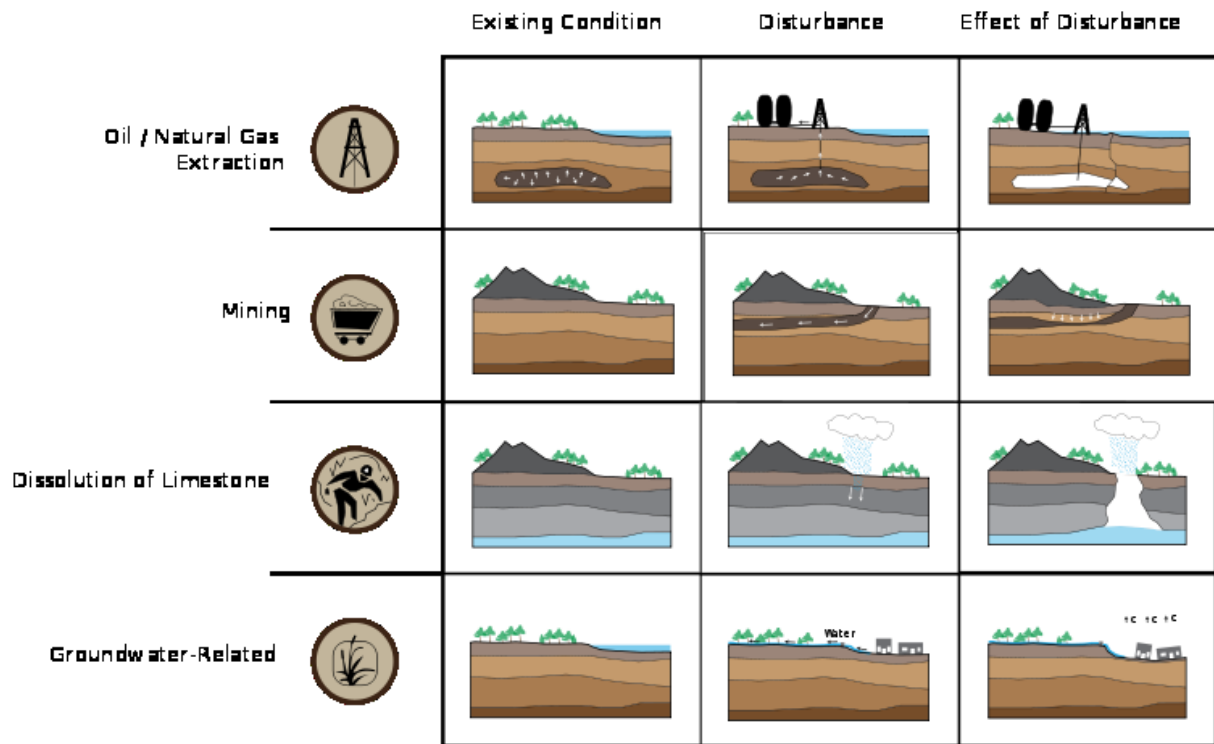


Figure 3.8 Summarizing scheme of the different types of subsidence (<https://en.wikipedia.org/wiki/Subsidence>).

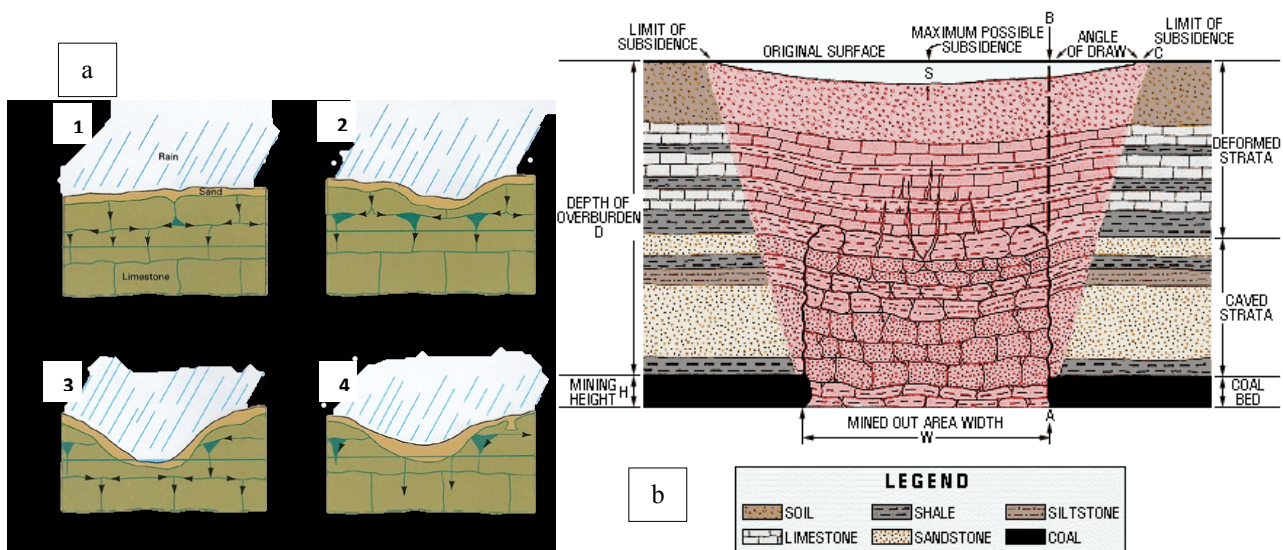


Figure 3.9 a) Subsiding sinkholes due to limestone dissolution, from top left to bottom right, clockwise: 1 Infiltration of rainwater; 2 Depression of surface due to dissolution of limestone; 3 The depression intersect the water table; 4 subsiding sinkhole filled with sediments of surrounding limestone; b) Cross section of mining subsidence. Adapted from S. Tandanand and L. R. Powell, 1982, Assessment of Subsidence Data from

the Northern Appalachian Basin for Subsidence Prediction: U. S. Bureau of Mines Report of Investigations 8630. (Illustration by Ray Strawser).

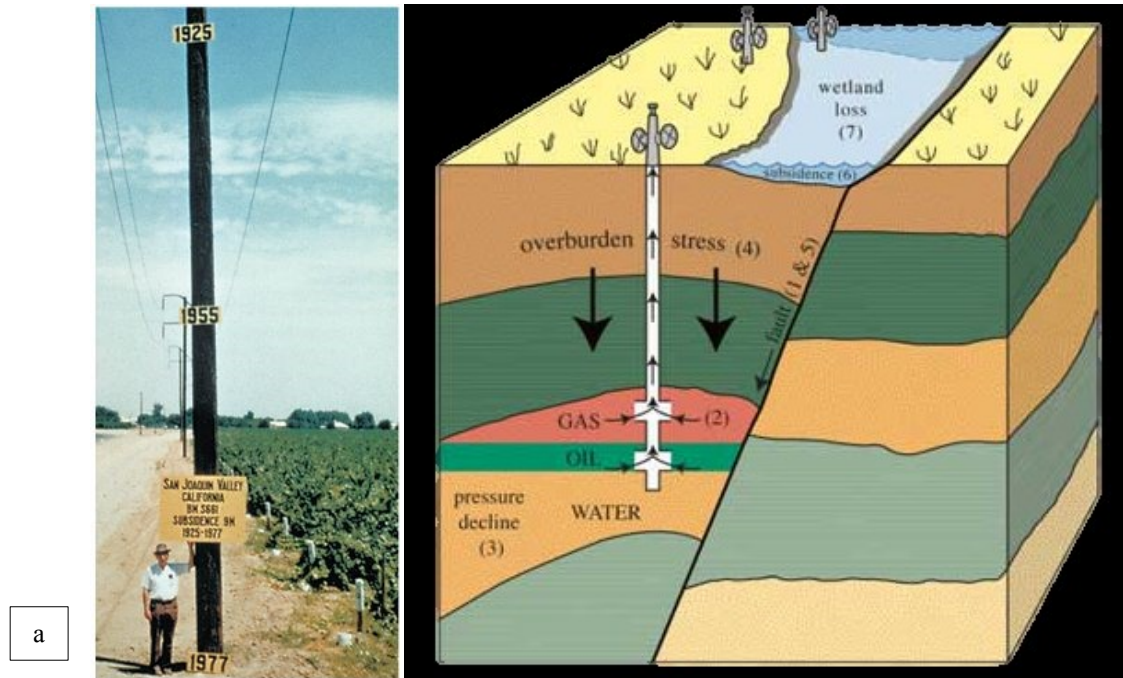


Figure 3.10 a) San Joaquin Valley Subsidence caused by water withdrawal (USGS); b) Conceptual diagram of subsidence due to gas/oil extraction from the ground (USGS).

3.2 Subsidence investigation

The investigation of the subsidence is important to delineate the extent of the affected area, measuring the surface displacements (magnitude, rate and temporal and spatial variability), determining the strain mechanisms and identifying precursory movements indicative of potential catastrophic subsidence events, in order to propose mitigation measures (Tomás et al., 2013). Several techniques are available for the measurement and the mapping of local subsidence (Galloway et al., 1998; Galloway and Burberry, 2011). The approach is generally based on several key factors (Tomás et al., 2008; Galloway and Burberry, 2011): Costs, accuracy and resolution (according to the type of subsidence), type of data and measuring frequency (according to the subsidence pattern), land cover and weather conditions, flexibility of the method (related to the possibility to select time and location of the measurements) and geometry and kinematics of the subsidence. The comprehension of the subsidence phenomena can be obtained by planning a valuable monitoring system, analyzing both the deformations and their causes. Obviously, it is necessary the measure of most significant parameters, for instance relative displacements between two points, inclinations, settlements and their directions, etc. A correct monitoring system must take into account the characteristics and the development of the phenomenon to investigate, like the extension, the magnitude, the frequency of the measures and the economic resources to invest as well. The principal methodologies for the subsidence monitoring can be categorized into two main categories, “*in situ*” technologies and remote sensing applications. In the first group can be mentioned all the instruments capable to measure linear or angular deformations within the area of interest. The most used instruments belonging to such category for the monitoring of subsidence are extensometers, inclinometers, and micrometers. Remote sensing techniques, instead, are capable to obtain quantitative and qualitative information about targets located far from a sensor, through the emission of electromagnetic radiation. Further description of the principles of remote sensing are provided in the Chapter 4.

CHAPTER 4: SYNTHETIC APERTURE RADAR

4.1 Remote sensing

The monitoring of displacement phenomena is a paramount task for Earth observation scientists and for the stakeholders. Remote sensing represents a valuable tool for such aim, because of its rapidity of acquisition, the easy management of the data, and for the relative low costs as well. Observation of the Earth from space is one of the keys to a better understanding of the Earth as a system, and so vital in achieving a comprehensive assessment of the influence of man's activities on his environment (Goldsmith & de Villiers, 1990). Various definitions have been provided since the origin of the appropriate instruments for the Earth observation; one of the most interesting and concise is by Barrett and Curtis (1976) which define Remote Sensing as "the observation of a target by a device separated from it by some distance". The origin of the remote sensing obviously derives from the beginning of the practice of photography. The use of photography to record an aerial view of the Earth surface, from a captive balloon, dates to 1858, then with technological improvements such as the invention of the plane and the development of photography and the discovery of radar, this practice has become worldwide (Campbell, 2011). During World War II, photography and radar remote sensing were used for military applications, with the work of Robert Colwell (1956), such tools were finally exploited for civilian purposes, with the aim of identifying small-grain cereal crops and their diseases through colored infrared film. Therefore, the development of satellites widely improved the Earth observation (and within this context, the term remote sensing was first used): In 1972, the launch of Landsat 1 was one of the most important milestones in this field. Landsat provided, for the first time, systematic repetitive observations of the Earth's land areas. In the 1980s, scientists at the Jet Propulsion Laboratory of Pasadena (California, USA), in cooperation with NASA, developed instruments for collecting data in more precise spectral regions, so began the so-called hyperspectral remote sensing. By the 1990s, satellite systems had been designed specifically to collect remotely sensed data representing the entire Earth (Campbell, 2011). Nowadays, Earth observation techniques are making rapid advances, becoming more effective instruments for geohazards mapping, monitoring and analysis. The monitoring of deformations occurring on the Earth surface works also by means of electromagnetic radiations: All the objects emit electromagnetic radiations, and can also reflect radiations emitted by other objects. The most familiar form of electromagnetic radiation is visible light, which is a part of the complete electromagnetic spectrum. Electromagnetic radiation (Fig. 4.1) consists of an electrical field, varying in magnitude perpendicularly to the direction of propagation, and a magnetic field, propagating in phase with the electrical and oriented at right angles to it. An electromagnetic signal is characterized by the wavelength, which is the distance from one wave crest

to the next, the frequency, consisting in the number of crests in a given period of time and from a certain point, and the amplitude, equivalent to the height of each peak (Fig. 4.2).

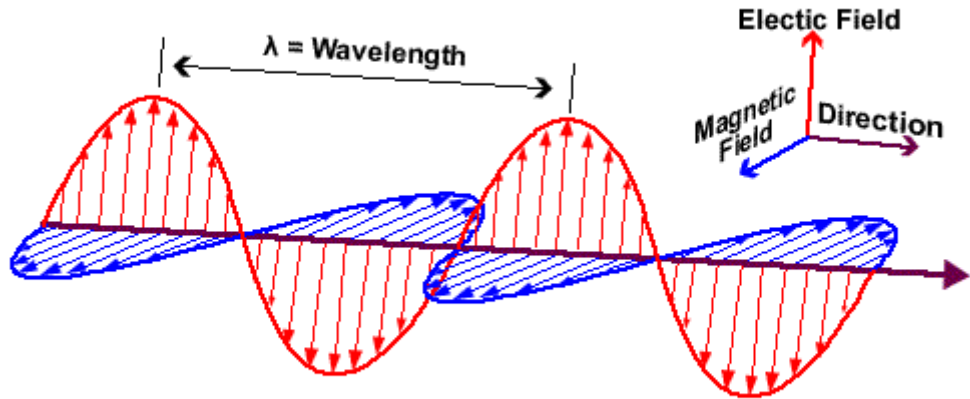


Figure 4.11 Electromagnetic wave and its main features (NOAA).

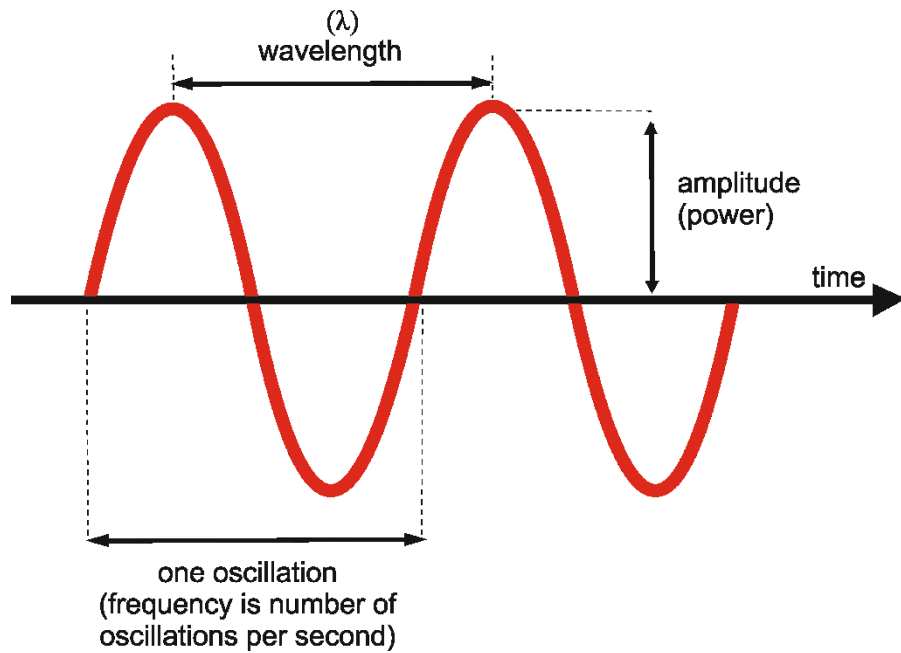


Figure 4.2 Wavelength, amplitude and frequency of an electromagnetic.

Major divisions of the electromagnetic spectrum can be done on the basis of the wavelength (Fig. 4.3). For remote sensing applications, every wavelength has a very important application: Ultraviolet spectrum can be useful to induce fluorescence in some materials, but it is not generally used for remote sensing. The visible spectrum is obviously significant for Earth observation, being the spectrum for optical imagery meanwhile the infrared, also used for optical sensors, in particular the

far infrared radiation, consists of heat or thermal energy. Microwave spectrum is the spectrum for RADAR (Radio Detection And Ranging) applications. The radar is a technique working in all-weather conditions (having a cloud-penetrating capability) and it is able to work day and night, as the instruments transmit a pulse to the Earth and receive its echo, back scattered from the object, independently from the solar radiation used by optical sensors (Gupta, 2013). The radar technique uses the two-ways travel time of the pulse to determine the range to the detected object and its backscatter intensity to gather physical quantities. On the base of such considerations, radar can be classified as an “active sensors”, in spite of the passive ones (optical, thermal, seismic) that gather target data through the detection of vibrations, light, radiation or other phenomena occurring in the subject’s environment.

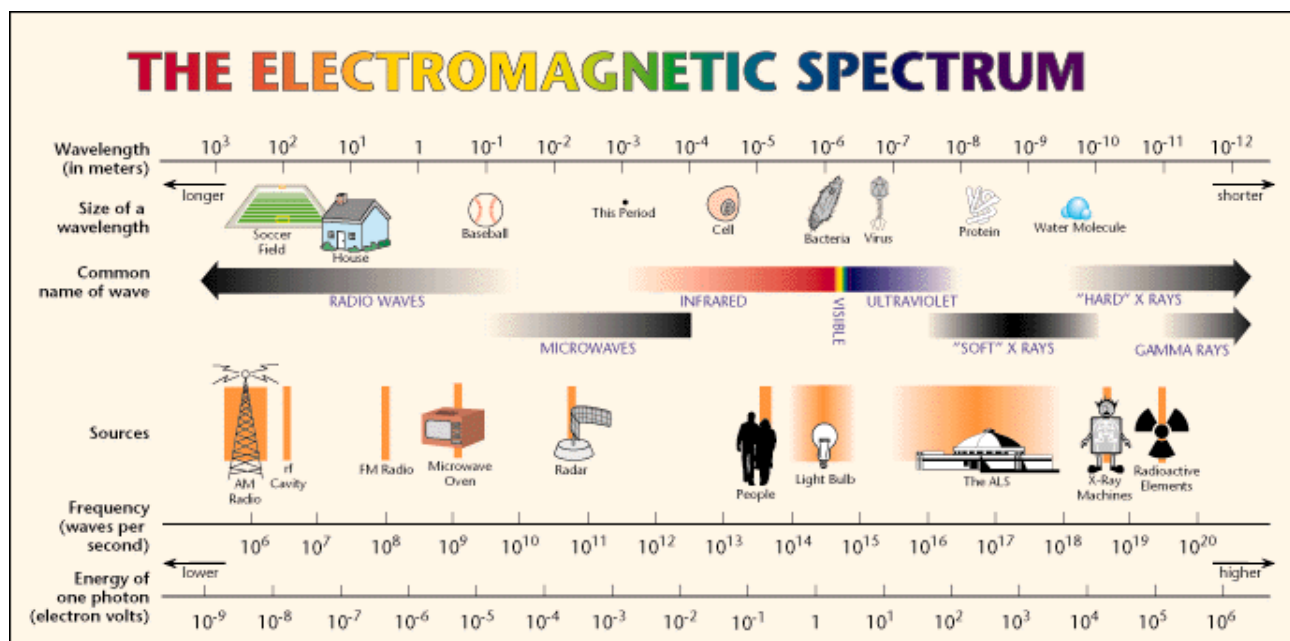


Figure 4.3 Electromagnetic spectrum (modified from <http://www.lbl.gov/MicroWorlds/ALSTool/EMSpec/EMSpec2.html>).

4.2 Synthetic Aperture Radar (SAR): introduction

Synthetic Aperture Radar (SAR) is a microwave imaging system, which sensors consist of an antenna, mounted on a mobile ground, airborne or satellite device, which transmits a radiation reflected by the target and acquired again. Since the beginning of its application, SAR demonstrated to be a valuable tool to acquire information about the physical properties of the Earth surface, and to have a large range of applications, over land, ice and sea surfaces. The most used frequency bands in civilian space-borne SAR missions are the L-band, C-band and X-band (Table 4.1) (Barbieri & Lichtenegger, 2005). Higher frequency sensors, such as C- and X-band enable higher spatial resolutions, while lower frequencies (L-Band), are less influenced by vegetation (Bamler & Hartl, 1998;

Barbieri & Lichtenegger, 2005). Even though the use of SAR interferometry (InSAR) developed in the 1990s, the basic principles are dated back to the early 1970s (Richman, 1971; Graham, 1974), and the first terrestrial applications took place in the 1980s (Gabriel et al., 1988; Gabriel et al., 1989; Goldstein et al., 1989; Prati et al., 1989). All the details about the SAR principle are provided in Gabriel et al. (1989), Bamler & Hartl (1998), Franceschetti & Lanari (1999), Rosen et al. (2000), in the next paragraphs the description of the basic principles and of the main feature are described, according to the aforementioned authors.

4.3 SAR data acquisition

SAR is a two-step procedure. Raw data acquired by a radar require a considerable amount of signal processing for image formation (focusing) (Bamler & Hartl, 1998).

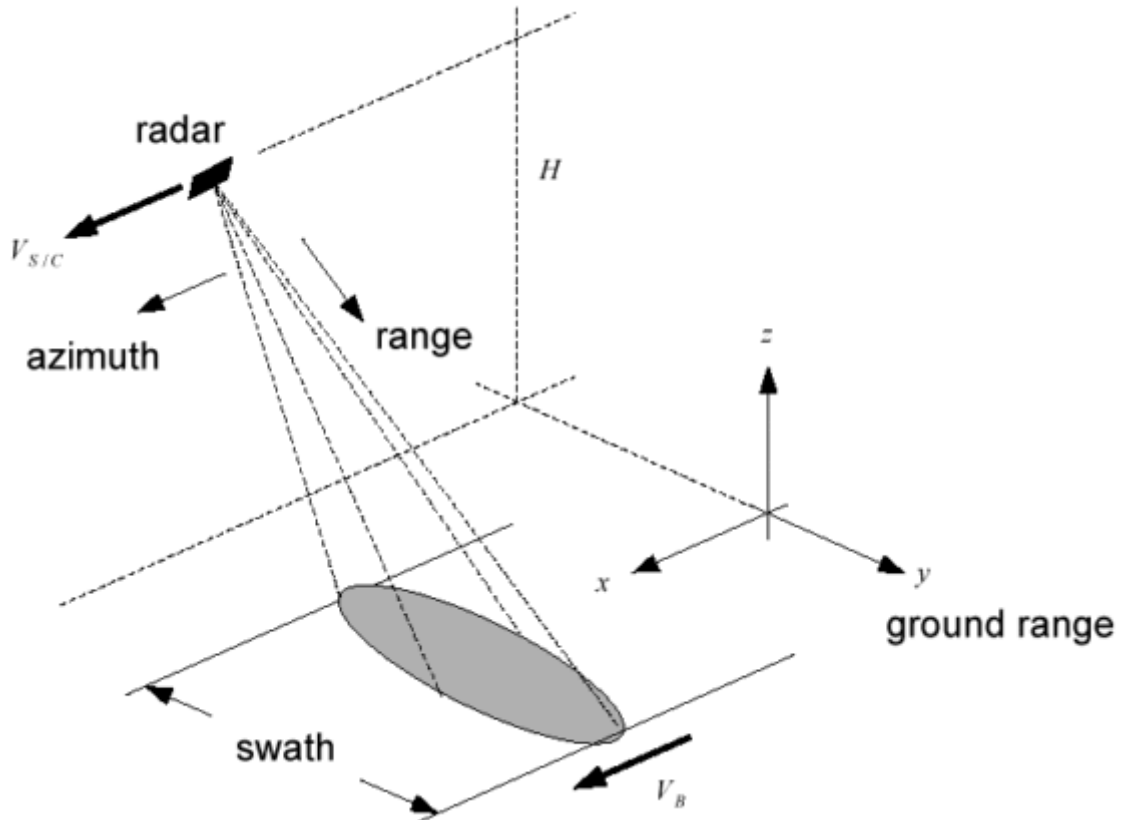


Figure 4.4 SAR imaging geometry and main features (modified from Bamler & Hartl, 1998).

A spaceborne or airborne SAR illuminates the Earth's surface in a side-looking style (Fig. 4.4). The sensor moves along a path at an altitude H over a reference point and transmits microwave pulses, receiving then the echoes of each pulse scattered back from the Earth surface. The SAR receiver detects the stream of echoes coherently and separates it into individual echoes, each corre-

sponding to a transmitted pulse (Bamler & Hartl, 1998). The wavelengths of the pulse or signal characterize the bands of the electromagnetic spectrum. Usually wavelengths and consequent bands are adopted, as shown in Table 4.1.

Table 4.1 SAR bands and frequency and wavelength associated.

Band	Frequency (GHz)	Wavelength (cm)
P-band	0.225 - 0.39	140 - 76.90
L-band	0.39 - 1.55	76.90 - 19.30
S-band	1.55 - 4.00	19.30 - 7.50
C-band	4.00 - 8.00	7.50 - 3.75
X-band	8.00 - 10.90	3.75 - 2.75

SAR imagery can be acquired in different geometries (Fig. 4.5), according to the system configuration:

- Stripmap: Antenna pointing is fixed relative to the flight line (perpendicular to the flight line). In this case, the result of the acquisition is a moving antenna footprint sweeping along a terrain strip parallel to path motion. The stripmap mode is usually applied for the mapping of large areas (however, characterized by coarser resolution of the image);
- ScanSAR: The sensor drives the antenna beam to illuminate a strip of terrain at any angle to path of platform motion. Basically, the assumption is that with the ScanSAR mode, it is possible to share the radar operation time between two or more separate sub-swaths in order to obtain full image coverage of each of them;
- Spotlight: The sensor steers its antenna beam to illuminate continuously a specific spot or terrain patch being imaged while the platform flies by in a straight line. The spotlight mode is very recommended for fine-resolution data from very specific areas. Thanks to the spotlight acquisition, it is possible to have finer azimuth resolution than in the other ways, even using the same physical antenna; moreover, spotlight imagery provides the possibility of imaging a scene at multiple viewing angles during one single pass.

More recently, with the development of the Sentinel-1 mission, a new acquisition mode has been proposed, the TOPSAR mode. With the TOPSAR technique, in addition to steering the beam in range as in ScanSAR, the beam is also electronically steered from backward to forward in the azimuth direction for each burst, avoiding scalloping and resulting in homogeneous image quality throughout the swath (De Zan & Guarneri, 2006).

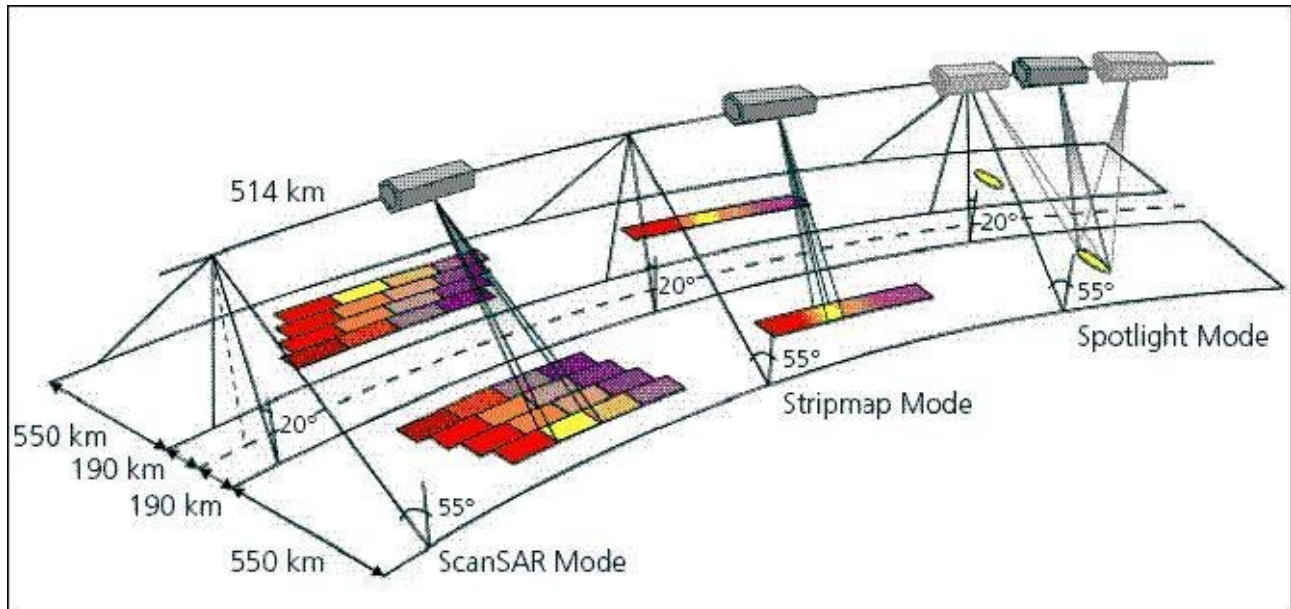


Figure 12.5 SAR acquisition modes by TerraSAR-X satellite (credit: DLR).

4.4 SAR parameters

A SAR antenna (Fig. 4.6) is mounted on a platform moving with velocity V at altitude H , acquiring images through the emission of electromagnetic radiations. The direction of travel is the azimuth direction, meanwhile the distance from the radar track represents the range direction. The range (or across track) is the measure of the “line of sight” distance from the radar to the target; the azimuth direction (or along track) is perpendicular to range and parallel to the flight path of the antenna. The angle between the radar beam and a line perpendicular to the surface is referred to as the off-nadir, or look angle, or incidence angle (θ), and it changes from near-range, the value at the shortest path of radar beam, to far-range, the value at the longest path of radar beam. The distance between antenna and objects on the Earth’s surface is defined as slant range, while the horizontal distance along the ground is called ground range. The closest sector of the image to the radar track is the so-called near range, while the furthest one is the far range. The geometry of acquisition of the spaceborne SAR is side-looking style (Fig. 4.7 b): limiting the radar observation to just one side, the pulse enlighten two points at different times, differently from a nadir-looking radar (Fig. 4.7 a), therefore they are distinguishable from each other.

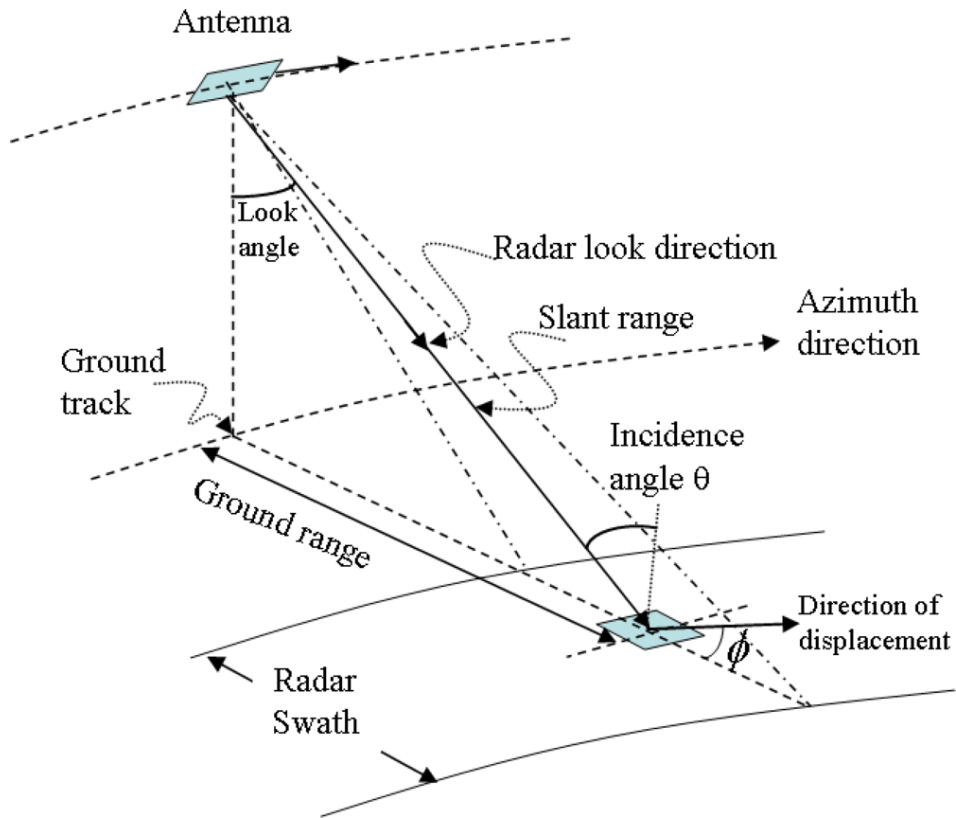


Figure 4.6 Geometric model for SAR system. Slant range is the length between the antenna and ground pixel and ground range is the distance between the ground track and the ground pixel (modified from Zhou et al., 2008).

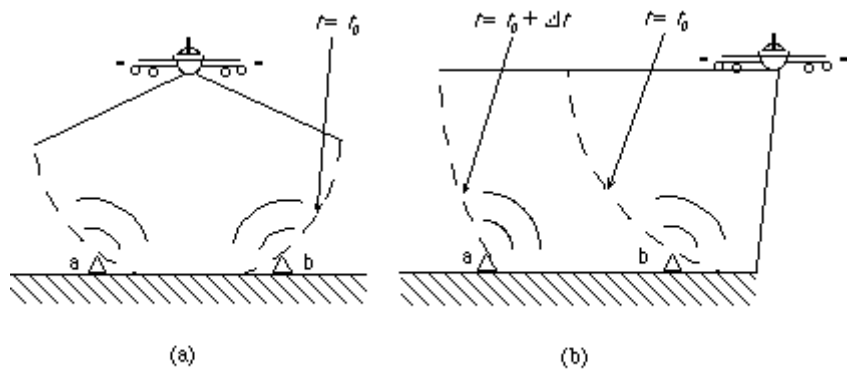


Figure 4.7 Nadir looking radar (a) and one-side looking radar (b) (modified from <http://www.csr.utexas.edu/rs/sensors/active.html>).

4.5 SAR distortions

The acquisition of SAR images is done in slant range coordinates, corresponding to the radar coordinate system. As a consequence, ground elevation will cause geometric distortions in the imagery, in function of the incidence angle respect to the surface morphology. The result is the compression of features in the near-range relative to features in the far range. However, knowing the height of the sensor and assuming a flat area, it is possible to approximate the real positions of the

radar return. Such operation is called slant-to-ground projection. The presence of so-called radiometric distortions, which change the intensity value (or brightness) of the SAR image, may be also cited. The geometric distortions can be subdivided in three types:

- Shadowing: It occurs when the signal is not able to illuminate the ground surface, or certain areas are not reached by the radar pulse. Shadowing occurs at slopes oriented averse to the SAR antenna, hence when the slope angle α is greater than 90 minus the incidence angle θ . The consequence of shadowing on the final image is the darkness on objects on the surface not backscattered.
- Foreshortening: It is caused by the shorter travel time of the radar pulse, as the slant range distance to an object on the inclined slope is shorter than to an object on flat areas. The foreshortened areas appear brighter in the SAR image, due to the compression into a smaller image part of the backscattered slope.
- Layover: It is an extreme form of foreshortening, occurring when the slope angle α is greater of the incidence angle θ . For instance, layover can be observed when, in very steep slopes, the radar pulse first hits the top of a mountain and then its foot. Consequently, the top is imaged in front of the mountain's foot, leading to great geometric distortions in the radar image. Layover areas are usually characterized by very high intensity values.

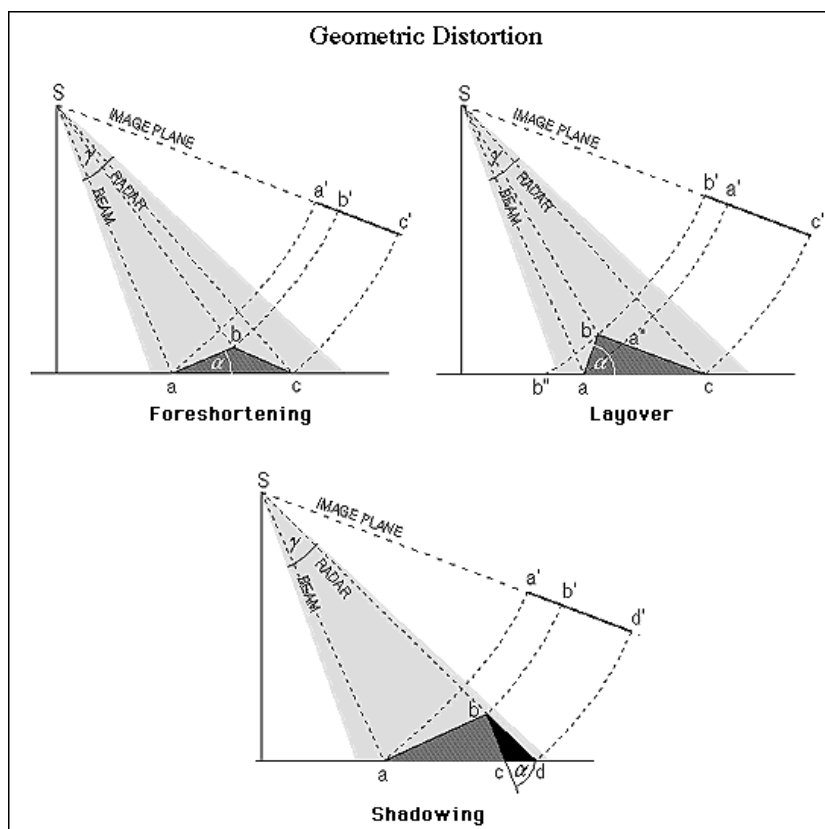


Figure 4.8 Geometric distortion in SAR imaging (<https://earth.esa.int/handbooks/asar/CNTR1-1-2.html>).

Several tools have been developed for the estimation of geometrical distortions, such as in Notti et al. (2010; 2014) or in Plank et al. (2013).

Radiometric distortions, instead, have an influence on the energy received by the sensor. They are very often associated to the geometric ones, as from slopes in foreshortening. The energy coming from distinct objects is combined together, then leading to have brighter points, due to the compression of pixels in a smaller area than the original one. Speckle is the cause of radiometric distortions, due to the casual interference among different backscatterer signals in every cell. Speckle appears as a grainy "salt and pepper" texture in an image (Fig. 4.9). This is caused by random constructive and destructive interference from the multiple scattering returns that will occur within each resolution cell. As an example, a homogeneous target, such as a large grass-covered field, without the effects of speckle would generally result in light-toned pixel values on an image (Fig. 4.9, A). However, reflections from the individual blades of grass within each resolution cell results in some image pixels being brighter and some being darker than the average tone (Fig. 4.9, B), such that the field appears speckled. Speckle is basically the product of the interference among waves coming from different objects inside the pixel. Speckle reduces the quality of the image and its interpretation becomes more complicated. The reduction of the speckle can be done through a multilook process and spatial filtering. The multilooking is a procedure for the re-projection of the image to a geometry comparable to the reality, having a ground range resolution with a square pixel. This operation, however, reduces the spatial resolution. Speckle can be reduced also applying different filters to the image, like the Lee filter (Lee et al., 1994), the Frost filter (Frost et al., 1982), the Gamma filter (Lopes et al., 1993), and others (Hanssen, 2001).

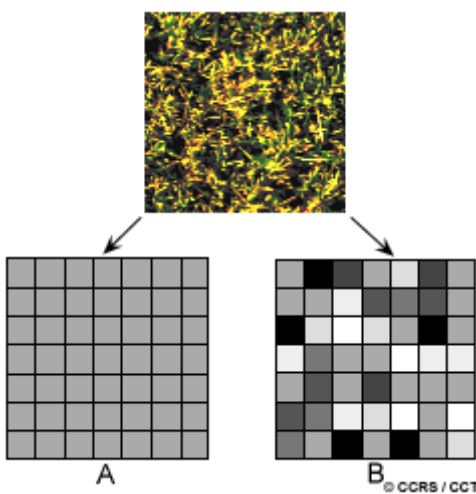


Figure 4.9 Radar speckle of a SAR image (<http://www.nrcan.gc.ca/earth-sciences/geomatics/satellite-imagery-air-photos/satellite-imagery-products/educational-resources/9299>).

4.6 Spaceborne SAR missions

The first satellite designed for the observation and the study of oceans implemented with SAR instruments was SeaSat-1, launched in 1978. SIR-C/X-SAR, in 1994 and SRTM/X-SAR, in 2000, were successive experiences of modern spaceborne SAR systems: The first, covering 230 test sites acquired into two periods of the vegetation growing season, and the latter, producing topographic products, such as DEM in a mosaic format, generated from C- and X-band radar frequencies (Eineder et al., 2000; Werner, 2000). The main spaceborne missions started with the ERS 1/2 experience, carried out by ESA (European Space Agency). ESA launched ERS-1 in July 1991 and ERS-2 in April 1995. These satellites represented the first ESA Earth observation mission, and they were characterized by a Synthetic Aperture Radar (SAR), a radar altimeter and ocean surface temperature and sea winds instruments. Both of them were acquired in C-band and with an incidence angle of 23° and a resolution of 30m x 26m. ERS-1 was deactivated in March 2000, while ERS-2, which had an additional ozone sensor, was deactivated in 2011. The JERS-1 mission, instead, started in February 1992, led by the National Space Development Agency of Japan (NASDA). It was an Earth observation satellite whose task was to cover the global land area for national land survey, agriculture, forestry and fishery, and also for the environmental and disaster protection. It acquired images in L-band and with a westward repeat cycle of 44 days. The JERS-1 mission ended in 1998 due to a malfunction. The RADARSAT-1 satellite was launched in November 1995 and it provided imagery for operational monitoring services on a global basis ever since. It was equipped with a C-band SAR. It was the Canada's first commercial Earth observation satellite. Its peculiarity was the ability to shape and steer its radar beam over a 500-km range, having the possibility to image swaths from 45 to 500 km in width and a resolution from 8 to 100 m. Afterwards, the RADARSAT-2 mission was launched, on December 14, 2007. New features of such mission were higher resolution imaging, flexibility in selection of polarization, left and right-looking imaging options, shortened programming, processing and delivery timelines, superior data storage and more precise measurements of spacecraft position and attitude. On May 9, 2013, the Canadian Space Agency (CSA) reported the end of the RADARSAT-1 mission due to technical issues. RADARSAT-2 is then continuing the Canada's RADARSAT program. EnviSAT, acronym for Environmental Satellite, was an Earth Observation mission of ESA. Its objectives were: Studying and monitoring the Earth's environments on various scales, from local to global, the management of Earth's resources, continuation and improvement of the services provided to the worldwide operational meteorological community, contribution to the understanding of the structure and dynamics of the Earth's crust and interior (<http://envisat.esa.it>). It was ESA's successor to the ERS missions, and it was launched in 2002 with 10 instruments aboard, such as radar

altimeter, temperature-measuring radiometer instruments, medium-resolution spectrometer, two atmospheric sensors for the monitoring of gases traces, etc. On May 9, 2012 ESA declared the end for the EnviSAT mission, due to a loss of contact with the satellite. The Advanced Land Observing Satellite (ALOS) was a Japanese satellite launched in 2006. It followed the JERS-1 mission and was launched in January 2006. The satellite carried three sensors used for cartography and disaster monitoring of Asia and the Pacific. On 12, May 2011, JAXA (Japan Aerospace eXploration Agency) sent a command to the satellite to power down its batteries, and declared it dead in orbit, due to technical problems. In May 2014, the ALOS-2 mission started: it is the successor of the previous mission, with a more advanced radar sensor and with 2 optical cameras in addition.

The TerraSAR-X mission started on June 15, 2007; it is a German SAR satellite mission for scientific and commercial applications. The project is supported by BMBF (German ministry of Education and Science) and managed by DLR (German Aerospace Center). The science objectives were to make multi-mode and high-resolution X-band data available for a wide spectrum of scientific applications in fields as hydrology, geology, climatology, oceanography, environmental and disaster monitoring, and cartography (DEM generation). Its main features are: resolution up to 0.25 m (in-staring spotlight mode), an excellent radiometric accuracy, unique agility (rapid switches between imaging modes and polarizations). On June 21, 2010, the twin mission TanDEM-X started, and since then they fly in a close formation at distances of only few hundred meters and record data synchronously. This peculiar configuration allows the generation of WorldDEM, which is a DEM of the Earth's land surface with a vertical accuracy of 2 m (relative) and 10 m (absolute). COSMO-SkyMed (COntellation of small Satellites for Mediterranean basin Observation) is a satellite mission ran by the ASI (Italian Space Agency) and the Italian Ministry of Defense. The CSK system is made up of four satellites and it is equipped with High-Resolution SAR, in sun-synchronous polar orbits, phased in the same orbital plane. This results in varied intervals between the satellites along the same ground track of between 1 and 15 days. The first two satellites were launched in 2007, the remaining two in 2008 and 2010, respectively. Its main goal is to provide imagery for environmental monitoring and surveillance applications for the management of exogenous, endogenous and anthropogenic risks, but also commercial products. Finally, Sentinel satellites are the last generation of Earth observation satellites of the ESA and the Copernicus group (program of the European Commission). Sentinel-1A satellite was launched on April 3, 2014 and provides all-weather, day and night radar imaging for land and ocean services, such as: monitoring of Arctic sea-ice extent, routine sea-ice mapping, surveillance of the marine environment, including oil-spill monitoring, monitoring land-surface for motion risks, mapping of forests, water and soil management and to support humanitarian aid and crisis situations. The Sentinel-2 satellite has been launched on June 23, 2015, and it is providing high-

resolution optical imaging for land services (i.e. vegetation, soil and water cover, etc.). Sentinel-3 will provide ocean and global land monitoring services, Sentinel-4 and Sentinel-5 will be responsible for data for atmospheric composition monitoring and Sentinel-6 will be implemented for the observation of the topography of the global ocean. The main features of each satellite mission are shown in Table 4.2.

Table 4.2 Main features of each SAR satellite mission.

	ERS-1 and ERS-2		JERS-1 SAR
Agency	European Space Agency	Agency	Japanese Aerospace eXploration Agency
Frequency	C-Band	Frequency	L-Band
Ground Resolution	25 m	Ground Resolution	20 m
Acquisition Mode	Stripmap	Acquisition Mode	Stripmap
Swath	100 km	Swath	70 km
Repeat Cycle	35 days	Repeat Cycle	44 days
Year of Start	1991-2000 (ERS-1); 1995-2011 (ERS-2)	Year of Start	1992-1998

	RADARSAT-1/2
Agency	Canadian Space Agency
Frequency	C-Band
Ground Resolution	10-100 m (Radarsat-1); 3100 m (Radarsat-2)
Acquisition Mode	Stripmap and ScanSAR
Swath	50-500 km
Repeat Cycle	24 days
Year of Start	1995-2013 (Radarsat-1); 2007 - (Radarsat-2)

	ENVISAT
Agency	European Space Agency
Frequency	C-Band
Ground Resolution	15-1000 m
Acquisition Mode	Stripmap and ScanSAR
Swath	100-405 km
Repeat Cycle	35 days
Year of Start	2001-2012

	ALOS-PALSAR
Agency	Japanese Aerospace eXploration Agency
Frequency	L-Band
Ground Resolution	7-1000 m
Acquisition Mode	Stripmap and ScanSAR
Swath	120-350 km
Repeat Cycle	44 days
Year of Start	2006-2011 (ALOS-1) 2014 - (ALOS-2)

	TerraSAR-X
Agency	German Aerospace Center (DLR)
Frequency	X-Band
Ground Resolution	1-16 m
Acquisition Mode	Stripmap, ScanSAR, Spotlight, HR Spotlight, Staring Spotlight and Wide ScanSAR
Swath	15-60 km
Repeat Cycle	11 days
Year of Start	2007 - ongoing

	COSMO-SkyMed		Sentinel-1
Agency	Italian Space Agency (ASI)	Agency	European Spatial Agency (ESA)
Frequency	X-Band	Frequency	C-Band
Ground Resolution	1-100 m	Ground Resolution	15-1000 m
Acquisition Mode	Stripmap, ScanSAR and Spotlight	Acquisition Mode	StripMap, Interferometric Wide Swath, Extra Wide Swath
Swath	20-400 km	Swath	100-405 km
Repeat Cycle	4/8/16 days	Repeat Cycle	12 days (6 with upcoming S1B)
Year of Start	2007 - ongoing	Year of Start	2014 - ongoing

4.7 SAR interferometry

As firstly described by Gabriel et al. (1989), Interferometry SAR (InSAR) is the study of the phase and amplitude difference of the back-scattered signal of two SAR images, observing the same scenes from different points of view (Gabriel et al., 1989; Massonnet & Feigl, 1998). The map describing the phase difference between two SAR images is the so-called interferogram. The first applications of SAR Interferometry can be dated back to the early 1970s, based on the analysis of single or few interferences, allowing to provide information about the topography of the Earth surface (Zebker & Goldstein, 1986; Li & Goldstein, 1987; Gabriel et al., 1989; Prati et al., 1989) or for the generation of DEMs (Digital Elevation Models) of the Earth surface (Franceschetti & Lanari, 1999; Rosen et al., 2000). An example of an interferogram is reported in Figure 4.10.

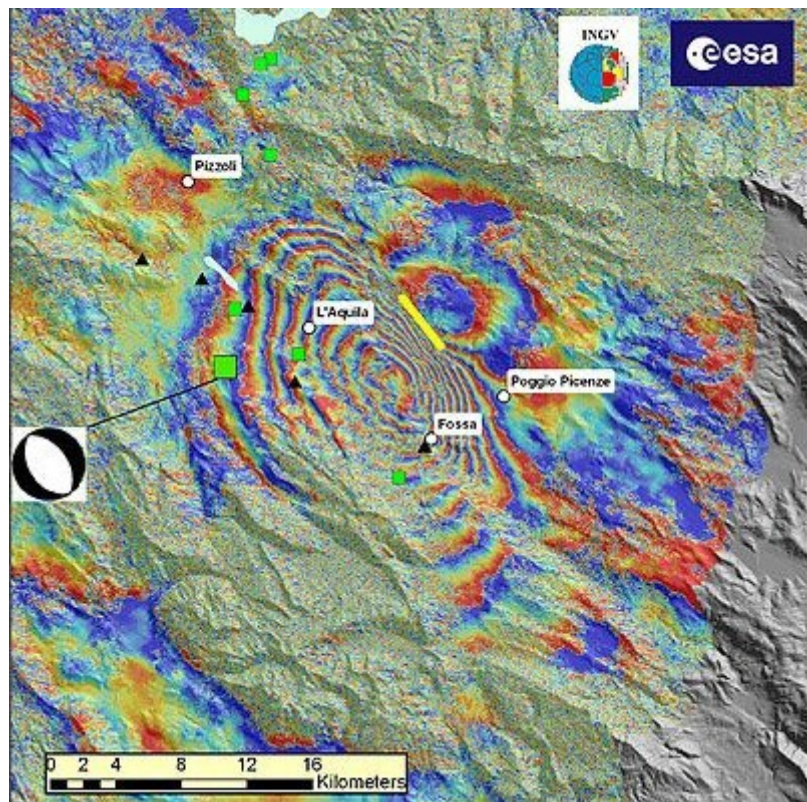


Figure 4.10 Interferogram of the 2009 M= 6.3, L'Aquila earthquake (ESA, 2009).

For the comprehension of the interferometry operation and of its generation, in the next paragraphs the main features, parameters and steps are briefly described.

4.7.1 Geometry of acquisition and baseline

The acquisition of SAR images for interferometric purposes can be done in two different ways, single pass or dual pass. The first is characterized by the simultaneous acquisition with a slight difference in the geometry of acquisition (Fig. 4.11) (e.g. two antennas mounted on the same device); in the latter, instead, images are acquired in dissimilar time intervals (e.g. the same antenna passing on the area of interest two times). In this last case, very peculiar for the spaceborne SAR, the distance between the two-acquisition orbits can vary of several meters. The distance between the two acquisitions on the perpendicular plan to the orbit direction is the interferometer baseline (B_r), while the component projected on the normal direction to the image acquired in the second time interval is called perpendicular baseline (B_n). The time interval between two succeeding is called temporal baseline (B_t).

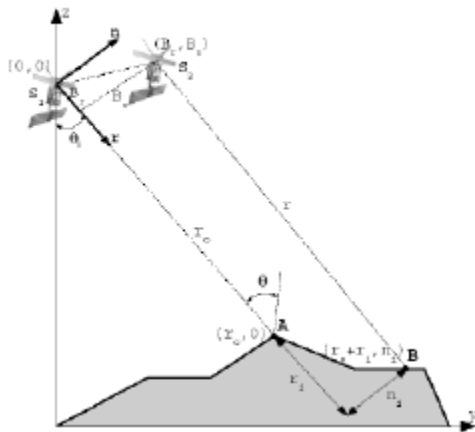


Figure 4.11 Geometry of acquisition of SAR images (modified from Blanco, 2008).

Once a reference point on the surface has been identified, the path difference between the two satellites in the slant-range direction, defined as Δ_r , is equal to the equation (1):

$$\Delta r = -2 \frac{B_n q_s}{R} \quad (1)$$

where: B_n is the perpendicular baseline, R is the distance in slant range between target and sensor and q_s is the distance between two points in perpendicular direction to the slant range. The interferometric phase difference (Δ_ϕ) (Equation 2) between the two observations, corresponding to the path difference Δ_r between two acquisitions, is proportional to the relationship between a complete phase cycle in radians (equal to 2π) and the wavelength λ , which is the distance between the two following peaks, all multiplied for Δ_r .

$$\Delta\varphi = \frac{2\pi\Delta r}{\lambda} = \frac{4\pi}{\lambda} * \frac{B_n q_s}{R}$$
(2)

due to the periodicity of the signal, path differences Δ_r , differing among them of a multiple integer of the wavelength, introduce the same phase difference (Ferretti et al., 2007), for instance equal to 2π , 4π and so on, basically a path difference equal to a phase cycle. Hence, the SAR phase signal is the measurement of the fractions of Δ_r , which is smaller than the wavelength of the signal (Ferretti et al., 2007).

Considering a phase difference equal to a 2π cycle (Equation 3),

$$r = \frac{\Delta\varphi * \lambda}{4\pi} = \frac{2\pi * \lambda}{4\pi} = \frac{\lambda}{2}$$
(3)

so that an interferometric fringe corresponds to a deformation variation of half of the wavelength (Casu et al., 2011).

4.7.2 Interferometric phase

The interferometric phase (φ_{int}) is the difference between two SAR images acquired from different angles of view. It is equal to the sum of several contributions (Equation 4), such as:

$$\varphi_{int} = \varphi_{geom} + \varphi_{topo} + \varphi_{displ} + \varphi_{atm} + \varphi_{err}$$
(4)

where φ_{geom} is the contribution due the slight difference of the geometry of acquisition of two images, φ_{topo} is the phase concerning the topographic information, φ_{displ} is the contribution due to the eventual displacements occurring between the two acquisitions, φ_{atm} is the part of the interferometric phase caused by atmospheric patterns such as humidity, temperature, etc. and φ_{err} is the contribution due to errors in different procedures or due to radiometric distortions. For the calculation of one single contribution, the latter must be isolated from the other ones. This is the base for the calculation, for instance, of the displacements occurring on the Earth surface.

The phase can be influenced by different factors, due to the interferometry or by instrumental sources. Geometrical decorrelation and temporal decorrelation belong to the first category, meanwhile in the second group instability of radar frequency and thermic instrumental noises can be mentioned.

Geometrical decorrelation is caused by the angular variation of the scene acquisition of the two SAR images which form the interferometric couple. The longer the baseline, the higher the spatial decorrelation, because of an increase of the geometry of acquisition difference, causing then a loss of information due to geometrical distortions. For this reason, a critical baseline (B_c) (Equation 5) value is defined for having a significant interferometric phase:

$$B_c = \frac{\lambda * r}{2r_g * \cos^2\theta} \quad (5)$$

The critical baseline is proportional to the wavelength (λ) and to the sensor-objective distance in slant range (r), while it is inversely proportional to the ground range resolution (r_g) and to the incidence angle.

Temporal decorrelations are caused by the modification of the electromagnetic signal due to atmospheric patterns (such as humidity, temperature, pressure), or to human modifications, or to vegetation growth. Coherence is the value of the variation of backscattering property of the target on the surface between two or more satellite passages. It is a parameter which better expresses the quality of the information within an interferogram. It can vary between 0 and 1: Lower values of coherence are due to severe modifications of the area observed; on the contrary, higher values means that the target has not changed.

4.7.3 Interferometric chain

Interferometric processing is composed of various stages. For this project, TerraSAR-X products have been exploited. DLR provides TerraSAR-X images as Single Look Complex (SLC) products, therefore images are already focused. Hence, the first step, within this work of thesis, is coregistration.

Coregistration

Coregistration is a fundamental step, necessary for making two SAR images comparable and in the same slant range geometry. The procedure consists in a precise superimposition of two or more images in the same area, removing scale differences and correcting rotations and translations. A “master” image must be selected, which is the reference image, on which all the “slave” images will be overlapped. Coregistration is also significant for the coherence estimation of a stack of images. Co-registration accuracy must be in sub-pixel scale, because InSAR processing requires sub-pixel accuracy.

Interferogram Generation

The interferogram generation is the basic step of SAR interferometry. Interferograms are generated from the complex product between the single values of the pixels. The final result is the phase difference, the interferometric phase, between the master and the slave images.

Filtering

The filtering step is useful for reducing potential noises in the interferograms. There are several filtering methods, such as the Goldstein method (Goldstein & Werner, 1998), the adaptive windows (Lopes et al., 1993), the boxcar, etc. The Goldstein filter is coherence-based, filtering more the low-coherence areas respect to the high-coherence areas. The adaptive windows filter the interferogram in a window based on the frequency and the homogeneity of the area, the boxcar are low-pass filters that eliminate noises exploiting small windows, in order to preserve the interferometric features.

Flattening

During the flattening phase, DEM is removed, hence is removed the contribution of the topography in the interferometric phase. Also the “flat earth” phase is removed (i.e. fringes due to the range). The result is a levelled interferogram, where the width of the fringes is due to the altimetry residuals and to possible displacements.

Phase Unwrapping

Every color of an interferogram corresponds to a phase cycle equal to 2π , so to a variation in altitude or to the movement of a target. Because of the unwrapping, the phase, explaining the multiple 2π , obtains a value in meters. Several algorithms for the phase unwrapping have been developed, such as the minimum cost flow (Costantini, 1998), the region growing (Xu et al., 1999), the minimum least square (Fried, 1977), etc. The basic assumption of all these algorithms is that adjacent pixels show a not unwrapped phase difference between $-\pi$ and π .

Orbital refinement

After the unwrapping, another necessary operation before obtaining the height or the displacement is the orbital refinement, which is an improvement of the orbital parameters available. In order to further refine the geometry of acquisition, the generation of so-called Ground Control Points (GCPs) can be also useful. They must be located in easy-to-observe areas, such as bridges, crossroads, or peculiar buildings, to get a good correspondence between SAR and geographical coordinates. Moreover, it is

necessary that they are located in high coherence areas and outside from the area of the displacement (if known).

Phase to height/displacement conversion

In this step the value Δr , the difference between the slant-range vectors, is determined and expressed as topographic measurement (InSAR) or as a displacement velocity (DInSAR).

Geocoding

It is the conversion from slant range coordinates to a reference cartographic system (e.g. WGS 84). As regards the displacement information, SAR processing is able to calculate it only in slant range coordinates, and the results is then geocoded. However, deformation is given in Line-of-sight (LOS) geometry.

4.8 Differential interferometry SAR (DInSAR)

As mentioned before, the interferometric processing, besides providing elevation maps, can also be exploited for the measurement of the deformation of different genesis occurring on the Earth surface. The interferometric phase is represented by different contributions; in order to get the displacement contribution (or the topographic one) the other contribution must be removed (or reduced). The exploitation of DInSAR methods, using multi-temporal stacks of SAR images, allows to remove all these other contributions and to isolate the phase related to the displacement. Moreover, analyzing a great number of SAR images acquired in a large time interval, it is also possible to follow long-duration deformation phenomena (with millimeter accuracy). The first differential interferometry application have been developed at the end of the 1990s and at the beginning of the 2000s (Wegmuller et al., 1998; Costantini et al., 2000; Ferretti et al., 2000, 2001; Berardino et al., 2002; Mora et al., 2003), with several applications and algorithms, which will be further discussed in the next paragraphs.

4.8.1 Differential interferometry applications

In the last two decades many applications have been carried out exploiting DInSAR methods, which proved to be an efficient tool in the monitoring and the investigation of several types of natural hazards and deeply contributed to the development of several geosciences. Among the most significant DInSAR application, the following can be mentioned:

- Earthquakes: Seismology is one of the geoscience branches in which interferometry has been most widely implemented. In particular DInSAR approaches have been carried out in the co-seismic phase (Zebker et al., 1994; Peltzer & Rosen, 1995; Tobita et al., 1998; Stramondo et al., 1999; Klinger et al., 2000), post-seismic deformation (Peltezer et al., 1996; Massonnet et al., 1996) and inter-seismic tectonic events (Wright et al., 2001 Colesanti et al., 2003);
- Volcanology: The study of deformations due to volcanic deflation and uplift has been widely analyzed by means of DInSAR techniques, e.g. in Rosen et al., 1996; Lanari et al., 1998; Lu et al., 2000; Lundgren et al., 2003; Hooper et al., 2004;
- Glaciology: The study of glaciers through DInSAR has been led by several authors, whose aim was to detect ice topography measurements (Kwok & Fahnestock, 1996) and ice velocity estimation (Goldstein et al, 1993; Fatland & Lingle, 1998; Strozzi et al., 2002);
- Subsidence: Subsidence due to natural or anthropic causes can be monitored and investigated by DInSAR, being able to follow the long duration of the deformation (Galloway et al., 1998; Ferretti et al., 2000; Mora et al., 2001; Strozzi et al., 2001; Crosetto et al., 2002; Tomás et al., 2005; Fiaschi et al., 2015; Tessitore et al., 2016);
- Landslides: Landslide monitoring with DInSAR methods gained a lot of attention in recent years by the scientific community, even though the detection of gravitational phenomena is limited to slow and very slow movements. Some of the most relevant results are described in Fruneau et al. (1996), Squarzoni et al. (2003), Tarchi et al. (2003), Strozzi et al. (2005), Colesanti & Wasowski (2006), Meisina et al. (2008), Cascini et al. (2010), Herrera et al. (2011), Novellino et al. (2015) and Di Martire et al. (2016).
- Infrastructures: The monitoring of man-made infrastructure can be also conducted by means of DInSAR methods, for the estimation of the deformation and settlements of dams, buildings, highways, bridges, etc., as for instance in Perissin et al. (2009), Proto et al. (2010), Stabile et al. (2012), Sousa & Bastos (2013), Di Martire et al. (2014).
- Heritage sites: The preservation of archaeological and cultural sites can be also monitored by DInSAR methods, as done by Tapete et al. (2011, 2012) or by Zeni et al. (2011).

4.8.2 Differential interferometry algorithms

The first attempts to develop advanced DInSAR methods able to reduce atmospheric artefacts and uncertainties in the sensor orbit information (orbital artefacts) were made by Peltzer et al. (2001), who created the so-called InSAR stacked approach. In this way, the deformation velocity is calculated as a weighted average computed from the single interferograms, allowing then to retrieve the mean deformation rate of the investigated area. By means of developments of more advanced techniques,

aimed at the computation of time series of deformation calculated over several SAR images analysis, a step forward has been done toward an improved Earth observation. Usually such techniques require at least 15-20 SAR images for a reliable analysis (Colesanti et al., 2003, Hanssen, 2005, Crosetto et al., 2010) and can be grouped into two main categories: Techniques exploiting localized targets, the so called Persistent Scatterers (PS) (Ferretti et al., 2000) approaches and those which exploit distributed targets, the so-called Small Baselines Subset (SBAS) (Berardino et al., 2002) methods. Moreover, more recently approaches combining PS and SBAS methods have been proposed (Hooper, 2008). In Table 4.3 the main algorithms belonging to the three approaches are resumed:

Table 4.3 Main DInSAR approaches.

PS Approaches	SBAS approaches	Mixed approaches
<ul style="list-style-type: none"> • Permanent Scatterers (PSInSAR, Ferretti et al. 2001) • Point Target Analysis (IPTA, Werner et al., 2003) • GENESIS-PSI (Adam et al. 2003) • Spatio-Temporal Unwrapping Network (STUN, Kampes, 2006) • DePSI (Kampes, 2006) • Stable Point Network (SPN, Crosetto et al., 2008) • Persistent Scatterers Pairs - DIFFerential InSAR method (PSP-DIFSAR, Costantini et al., 2000) 	<ul style="list-style-type: none"> • Small Baseline Subset (Berardino et al., 2002) • Coherent Pixel Technique (CPT, Mora et al., 2003) • Enhanced Spatial Differences (ESD, Fornaro et al., 2007) • Multidimensional SBAS (MSAS, Samsonov & d'Oreye, 2012) • Intermittent SBAS (ISBAS, Sowter et al. 2013) 	<ul style="list-style-type: none"> • Stanford Method for PS (StaMPS, Hooper, 2006) • SqueeSAR (Ferretti et al., 2011)

In the following paragraphs, the techniques applied in this thesis will be further discussed.

4.8.2.1 Permanent Scatterers Interferometry SAR (PSInSAR)

The Permanent Scatterers Interferometry SAR (PSInSAR, Ferretti et al., 2001) is one of the basic algorithms belonging to the PS category. It is an algorithm successfully used for long series of SAR data, in order to estimate and remove the atmospheric effects (Ferretti et al., 2000, 2001). Phase and amplitude are the main parameters exploited by the PSInSAR method: Amplitude gives information about the reflectivity of the target, while the phase indicate the sensor-target distance; therefore, amplitude allows to individuate the PS and phase to estimate the movement of the PS. Persistent Scatterers (PS) are targets which keep stable the electromagnetic signal (hence, their reflectivity property) during the time span of acquisition of the image. Usually PSs correspond to man-made structures (i.e. buildings, dams, infrastructures, etc.) or to rocky outcrops, while vegetated areas, due to the frequent variation of their electromagnetic properties, cannot be considered as good scatterers. The main concepts of the PS detection are: One is based on the amplitude dispersion D_a (Ferretti et al., 2001)(Equation 6), which is calculated by dividing the temporal standard deviation of the amplitude by the temporal mean of the amplitude of a certain pixel in a stack of SAR images

$$D_a = \frac{\sigma_a}{\mu_a} = \sigma_\phi \quad (6)$$

where D_a is the dispersion index, σ_a is the temporal standard deviation of the amplitude, μ_a is the temporal mean of the amplitude and σ_ϕ is the estimated phase standard deviation. The basic idea of this concept is that a pixel characterized by a high and more or less constant amplitude value is assumed to show a low phase dispersion. The final PS candidates are selected if the value D_a is below a given threshold (Kampes, 2006). The second concept for the detection of PSs exploits the signal-to-clutter ratio (SCR) (Equation 7), originally developed for SAR calibration with corner reflectors (Freeman, 1992). SCR is calculated by dividing the intensity of the signal (S^2) by the clutter (C^2), the intensity of the spatial neighborhood of the pixel. S^2 is equal to the square of the amplitude:

$$\text{SCR} = \frac{S^2}{C^2} \quad (7)$$

According to Adam et al. (2005), a high SCR value corresponds with a low phase error (Equation 8):

$$\sigma_\phi = \frac{1}{\sqrt{2\text{SCR}}} \quad (8)$$

Therefore, pixels exceeding a certain SCR threshold are detected as PS targets.

The final result of the PSInSAR is an accurate measurement of the movements along the SAR Line Of Sight (LOS velocities) of each PS, respect to an assumed reference point (considered as stable), in the time interval considered. Deformation and velocity maps and time series of the displacements are the main final products.

4.8.2.2 Small Baseline Subset (SBAS)

The Small BAseline Subset approach (SBAS, Berardino et al., 2002) is a DInSAR algorithm able to retrieve temporal series of deformation exploiting interferograms characterized by small temporal and spatial baseline. This algorithm aims to limit the spatial decorrelation taking into account the spatial and the temporal information from the SAR data (Berardino et al., 2002). By reducing the spatial separation between SAR images, it is possible to reduce the decorrelation especially due to the large baseline separation and to obtain correlated interferograms. These interferograms are used as inputs to calculate the unwrapping stage, from which the estimation of the topographic contribution and the extraction of the Low Pass (LP) temporal deformation, which will be subtracted from the wrapped interferogram module 2π , is done. Hence, the interferograms will be considered as residual phase and be unwrapped. Therefore, the spatial and temporal filters are applied to the unwrapping residual file which contains the temporal deformation and the topographic phase residual. Finally, the inversion of the stack of interferograms is guaranteed using the singular value decomposition (SVD) method. The advantage of the SBAS technique is represented by the high coherence and the high spatial density of the final product, and the reduction of the errors due to the redundancy of the information (more interferograms for every image), although disadvantages are due to the high computational requests.

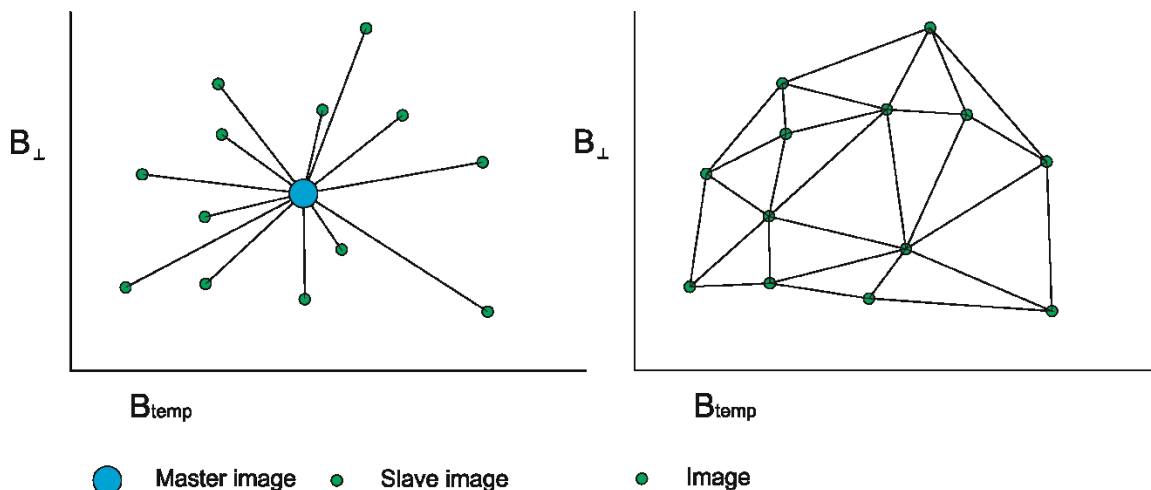


Figure 4.12 Representative scheme of PSInSAR, on the left, of SBAS, on the right.

4.8.2.3 Coherent Pixels Technique (CPT)

The Coherent Pixels Techniques (CPT, Mora et al., 2003), developed at the Remote Sensing Laboratory (RSLab) of Universitat Politècnica de Catalunya (UPC), is an algorithm able to extract from a stack of differential interferograms the deformation evolution during long time spans. The main steps of its processing are: 1) the generation of the best interferogram set among all the available images, 2) the selection of the pixels with reliable phase within the employed interferograms and 3) the phase analysis of the interferograms in order to calculate deformation time series of the period of observation. The selection of the best set of interferograms is done selecting the temporal baseline, the spatial baseline and the Doppler frequency. The interferogram selection is then achieved using the Delaunay method for the triangulation of the available images. The pixel selection is an important step in order to obtain reliable results. Only pixels characterized by a considerable phase quality are selected. There are several criteria for selecting pixels, one based on the coherence stability (Berardino et al., 2002), the other one based on the amplitude dispersion (Ferretti et al., 2001). More recently, also the Temporal Sublook Coherence method (TSC, Iglesias et al., 2015) has been produced. The first one is based on the spatial coherence estimator (Seymour et al., 1994) and the pixel will be selected if it shows a coherence higher than an assigned threshold; the second one, as a PS-like method, exploits the dispersion index, where all the pixels characterized by a D_a value below a certain threshold are selected; the latter is a selection method able to detect point-like scatterer analyzing the spectral properties of the scattered signal. The advantage with respect to the PS selection based on the amplitude dispersion is that there is no need of applying a radiometric calibration. Hence, in this case, pixel selection is carried out exploiting the spectral properties of point-like scatterers. The last step consists in the phase analysis, to calculate their linear deformation time series within the observation period. In this case, the Delaunay triangulation allows to connect neighboring pixels, and, after that, it is possible to evaluate the phase increment between two neighboring pixels. Finally, an integration process is necessary to obtain the velocity values for each pixel: it is necessary to identify a control point (named seed) characterized by linear velocity and height well known.

4.9 SAR Dataset

For this work of thesis, a dataset made of Very High Resolution images, belonging to the TerraSAR-X constellation, was used. Such images have been obtained through the participation to two science proposals, GEO 1589 and GEO 2641. In detail, 66 images have been acquired along the ascending orbit and 67 along the descending one, both covering the time interval between April 2008 and June 2010. Finally, further 34 images, over the ascending orbit, and 8 images, over the descending

one, have been extracted from the available catalogue of DLR, covering the time interval between November 2013 and October 2014.

CHAPTER 5: STUDY AREA

5.1 Geographical setting

The study area of the present research project is located in the southern part of the Italian Peninsula, in the Crotone province. Almost the whole Crotone province is covered by the stack of images mentioned in the previous chapter (Fig. 5.1).

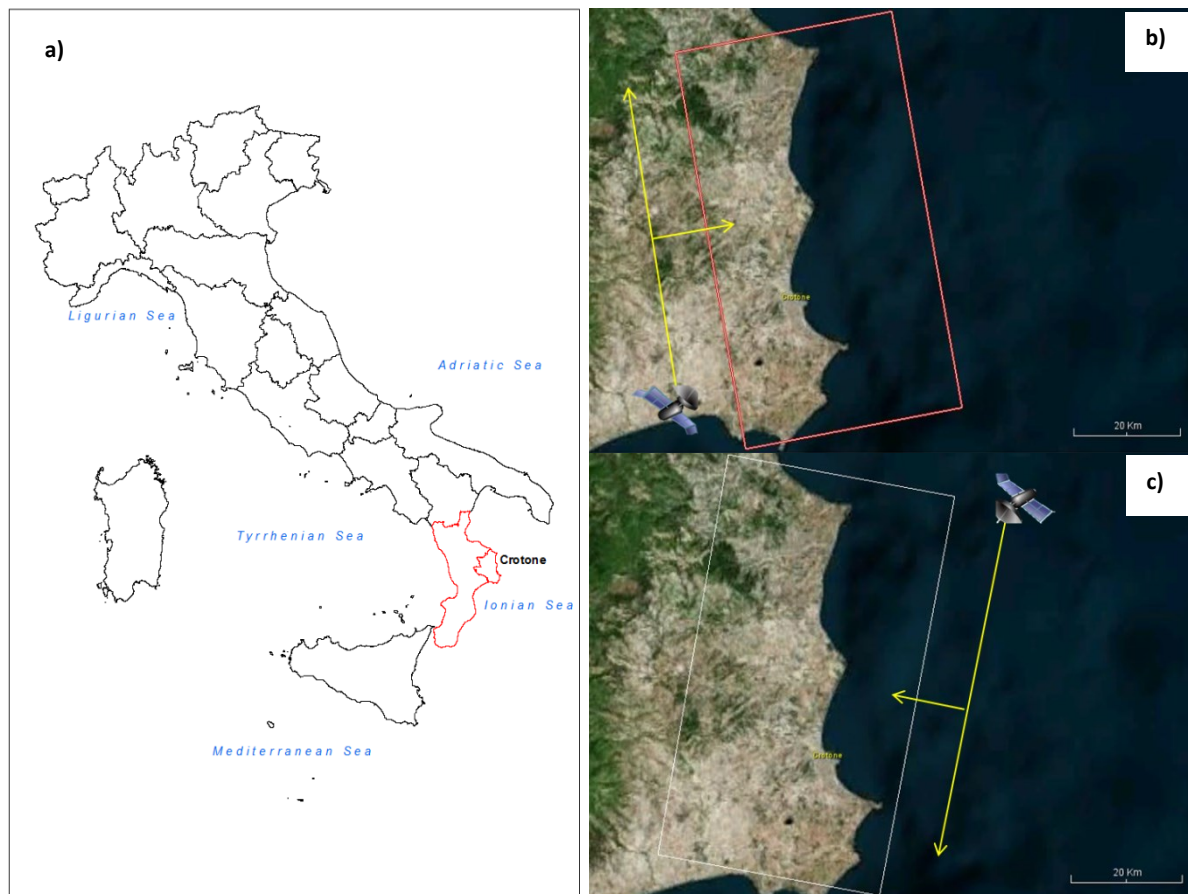


Figure 5.13 Location of the study area (a) (in red Calabria region and Crotone Province); track of the TerraSAR-X images acquired over ascending orbit (b), track of the TerraSAR-X images acquired over descending orbit (c), covering the study area.

Crotone province is located in Calabria region, counting over 171.800 inhabitants and covering a surface of 1.716 km²; it includes 27 municipalities (<http://www.provincia.crotone.it>). It faces to East the Ionian Sea and confines to NW with Cosenza province and to SW with Catanzaro province. The study area is one of the most interesting provinces in the Calabria region, combining peculiar geological characteristics with valuable natural resources both on-land (salt mines and diapers) and underwater (natural gas fields on offshore) (Luca et al., 2011).

5.2 Geological setting

The geodynamic evolution of the central Mediterranean is the result of several generations of interactions between collisional processes and extensional tectonics, controlled by the Cenozoic convergence between African and Eurasian plates (Dewey et al., 1989). The main tectonic elements generated by these processes since the Neogene are the southern Apennine-Maghrebian chain and the Tyrrhenian back-arc Basin, both connected to the westward subduction of the Adriatic and Ionian lithospheres. In this structure, the Calabrian Arc represents an independent arcuate terrane (the Calabria-Peloritani terrane of Bonardi et al., 2001) which connects the NW-trending southern Apennine chain and the E-trending Sicilian Maghrebides, and separates the Ionian and Tyrrhenian basins (Fig. 5.2). It is composed of a pile of pre-Mesozoic polymetamorphic nappes comprising large sheets of an Hercynian crystalline basement (forming the Sila and Aspromonte massifs) and local remnants of a Mesozoic to Cenozoic succession, considered by some authors as a fragment of the Alpine belt over-thrust upon the Triassic-Miocene sedimentary sequence of the Apennine-Maghrebian chain during Miocene (Amodio Morelli et al., 1976). The Calabrian Arc migrated south-eastward from mid-Miocene onwards in response to the subduction of the Ionian oceanic lithosphere along a deep and narrow, W-dipping Benioff zone (Malinverno and Ryan, 1986; Bonardi et al., 2001; Faccenna et al., 2001, 2004; Sartori, 2003; Finetti et al., 2005; Speranza et al., 2011). The movement towards SE caused a fragmentation of the Arc in individual blocks bounded by NW-trending shear zones, which controlled the development of basins located along both the Ionian and Tyrrhenian sides of Calabria (Fig. 5.2) (Knott and Turco, 1991; Lentini et al., 1995). The Neogene Crotone Basin developed along the Ionian side of the Calabrian Arc (Fig. 5.2), and is bounded to the north and to the south by two NW-trending left-lateral shear zones, called Rossano-San Nicola and Petilia-Sosti respectively (Meulenkamp et al., 1986; Van Dijk, 1990, 1991, 1994; Van Dijk and Okkes, 1991). The Crotone basin's tectonic evolution was preliminarily extensional, then it was interrupted periodically by rapid compressional or transpressional phases in mid-Messinian, earliest mid-Pliocene, mid-Pleistocene (Van Dijk, 1990; Zecchin et al., 2012); an uplift, started in middle Pliocene, brought the basin to the rise. The basin lies on a crystalline basement, characterized by lithologies belonging to the Sila Unit (Barone et al., 2008), such as granodiorites, gneisses and phyllites (Fig. 5.3).

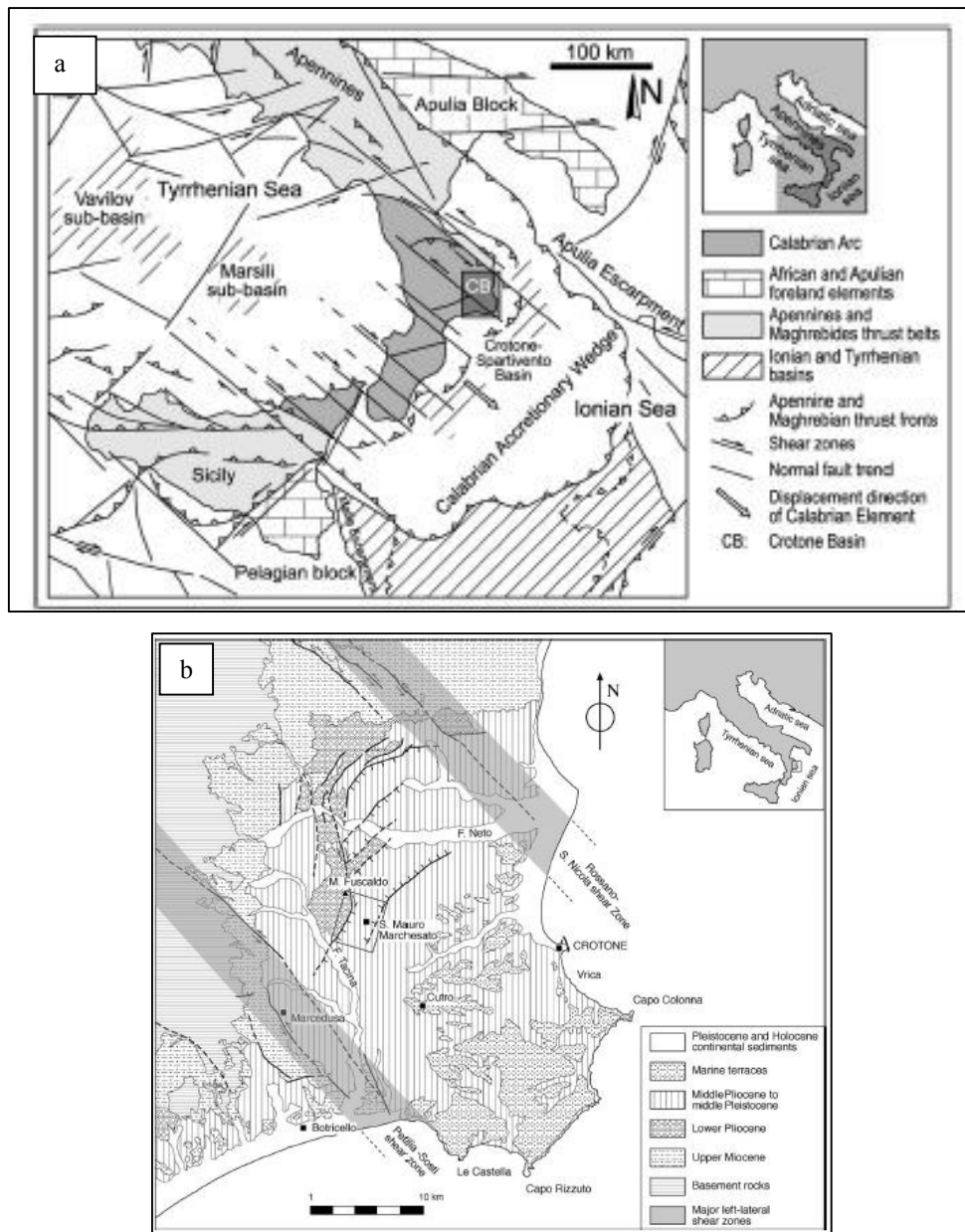


Figure 5.14 a) Structural map of the Calabrian Arc and location of the Crotone Basin (from Zecchin et al., 2013, modified from Van Dijk and Okkes, 1991); b) Tectonic sketch map of the Crotone basin (from Massari et al., 2002).

The basin is composed, according to Roda (1964), by three sedimentary cycles, all of them separated by unconformities, so made:

- The lowest unity is made up of sandstones, conglomerates (San Nicola Unit), marine and turbiditic deposits of Miocene age (Ponda Unit) (Critelli & Le Pera, 1998) and evaporitic Messinian deposits (Roda, 1964);
- The second cycle, from the late Messinian to Lower Pliocene, is made up of conglomerates and sandstones (Carvane Conglomerate) (Roda, 1964);

- The third cycle, Pliocene to Pleistocene in age, shows up marly-clay deposits, with presence of calcarenites and continental clasts (Cavalieri Marls and Cutro Clays) (Zecchin et al., 2012).

The oldest unit is the San Nicola Formation (late Serravallian), about 150 m thick, and composed of stratified conglomerates, passing upward into conglomerates and coarse-grained sandstones (Roda, 1964; Van Dijk, 1990). The unit probably represents a transition from an alluvial to a shallow-marine environment (Van Dijk, 1990; Massari et al., 2010). The San Nicola Formation is overlain by the Ponda Clay Formation (Tortonian), composed of marly claystones and silty sandstones reaching and locally exceeding 300 m of thickness (Ogniben, 1955; Roda, 1964). It is a deep marine unit, locally subjected to turbidite deposition (Barone et al., 2008). Close to Strongoli town, the Ponda Clay is overlain by an olistostrome up to 200 m thick, called “Varicolored Clays” and characterized by a variegated clayey matrix with calcareous, arenaceous and pelitic blocks (Ogniben, 1955; Roda, 1964; Zecchin et al., 2012) (Fig. 5.3). Such chaotic body corresponds to the Sicilide Complex of the Southern Appenines (Ogniben, 1969; Critelli, 1999; Critelli et al., 2011). The Tripoli Formation, of early Messinian age, lies on the Ponda Clay and the olistostrome, reaching a maximum thickness of 60 m (Zecchin et al., 2012). All these formations record a phase of stressed conditions due to water mass stratification which preceded the Messinian salinity crisis of the Mediterranean (Massari et al., 2010). The evaporite is a Messinian unit composed of carbonate breccias grading into gypsrudites, gypsarenites and sandstones containing abundant gypsum clasts, reaching a thickness of about 100 m (Barone et al., 2007; Lugli et al. 2007). At the top of the evaporite Formation a second olistostrome of Varicolored Clays can be found (Zecchin et al., 2012), which in turn is overlain by the Messinian Detritico Salina Formation (300 m thick), composed of alternations of gypsrudites, gypsarenites and gypslutites (Zecchin et al., 2012) (Fig. 5.3). Upward, separated by an unconformity, the late Messinian Upper evaporite Formation follows (Roda, 1964), made of 180 m thick gypsrudites, gypsarenites, gypslutites, sandstones and claystones (Fig. 5.3). The Upper evaporite Formation is erosionally overlain by the late Messinian Carvane Conglomerate (Roda, 1964) formed by conglomerates, sandstones and siltstones and claystones. The Carvane conglomerate closes the second cycle: The Plio-Pleistocene succession of the Crotone Basin overlies the conglomerates. This succession is represented by the deep-marine units of the Cavalieri Marl and Cutro Clay, it is a continuous succession, even if separated by an unconformity. While in the northern part of the basin the Cavalieri Marl and the Cutro Clay both exhibit a thickness which varies between a few tens to a few hundreds of meters, they form a composite succession up to 1200 m thick in the Crotone and Isola di Capo Rizzuto areas to the south (Zecchin et al., 2012). The Cavalieri Marl is Zanclean in age (Roda, 1964; Van Dijk, 1990; Zecchin et al., 2003, 2004a), and crops out in the northern part of the basin,

north of the Mt. Murgie and between the Zinga and Belvedere di Spinello villages (Zecchin et al., 2012). The Cutro Clay (Roda, 1964) is a well-represented formation of the basin, exposed discontinuously in the whole study area excepting the northernmost part (Zecchin et al., 2012). The Cavalieri Marl and the Cutro Clay both consist of gray and light brown claystones and siltstones rich in foraminifera, calcareous nannofossils and mollusc shells, accumulated at distal shelf to slope depth (Fig. 5.3) (Roda, 1964; Zecchin et al., 2003, 2004a; Massari et al., 2010). Locally it is possible to find outcrops of other formations: The Zinga Group, of Zanclean age, is composed of four formations (Zinga Sandstone, Montagnola Clay, Belvedere Formation and Murgie Sandstone, that are present exclusively in the northern and NW parts of the Crotone Basin (Fig. 5.3) and have been extensively described by Zecchin et al. (2003, 2004a, 2006) and Zecchin (2005). This major unit corresponds to both the “Molassa di Zinga” and “Molassa delle Murgie” of previous authors (Ogniben, 1955; Roda, 1964); the Spartizzo Clay (Ogniben, 1955; Roda, 1964; Mellere et al., 2005) is visible nearby the Casabona and Belvedere di Spinello settlements in the northern part of the basin, and its thickness varies from ca 10 to 150 m due to synsedimentary normal faulting. This unit is composed of dark gray and brown layered mudstones. The Spartizzo Clay sharply overlies the Belvedere Formation, and in the Casabona area it interfingers laterally with the shallow-marine deposits of the Scandale Sandstone (Zecchin et al., 2012); the Scandale Sandstone (Ogniben, 1955; Roda, 1964; Mellere et al., 2005; Zecchin et al., 2006) is found in the Casabona, Rocca di Neto, Strongoli and Zinga areas and the units shows a complex architectures that varies according to the location. Finally, the uplift that generally affect the Calabrian Arc since early Pleistocene (relatively later in the Crotone area, according to Zecchin et al., 2012), is accompanied by an extensional tectonic regime. Moreover, glacio-eustatic changes, accompanied by climate variations, are recorded in the Plio-Pleistocene succession of the Crotone Basin (Zecchin et al., 2012). In fact, the relationship between glacio-eustasy and the regional uplift of the study area is testified by the marine terraces present in the area.

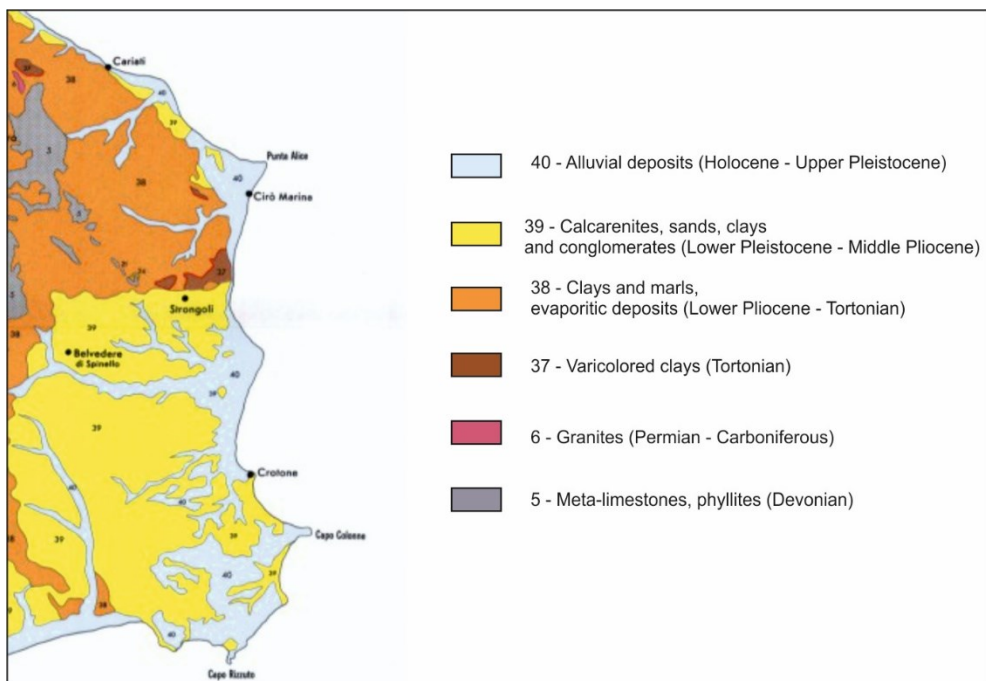


Figure 5.15 Geological map of Crotone province (modified from Bonardi et al., 1976).

5.3 Geomorphological setting

The distribution and the physico-mechanical properties of the lithological units have influenced the slope dynamics and the nature of the geomorphic processes within the area of interest. The western part, in fact, where Paleozoic and Mesozoic rocks crop out, is dominated by a mountainous landscape with steep slopes and narrow V-shaped valleys. The middle sector is characterized by a hilly morphology (Fig. 5.4 a), with low-gradient slopes and sometimes karstic landforms, due to a higher rock erodibility (Luca et al., 2010). The coastal area is characterized by several generations of marine terraces ascribable to the mix of regional uplift and sea level changes.

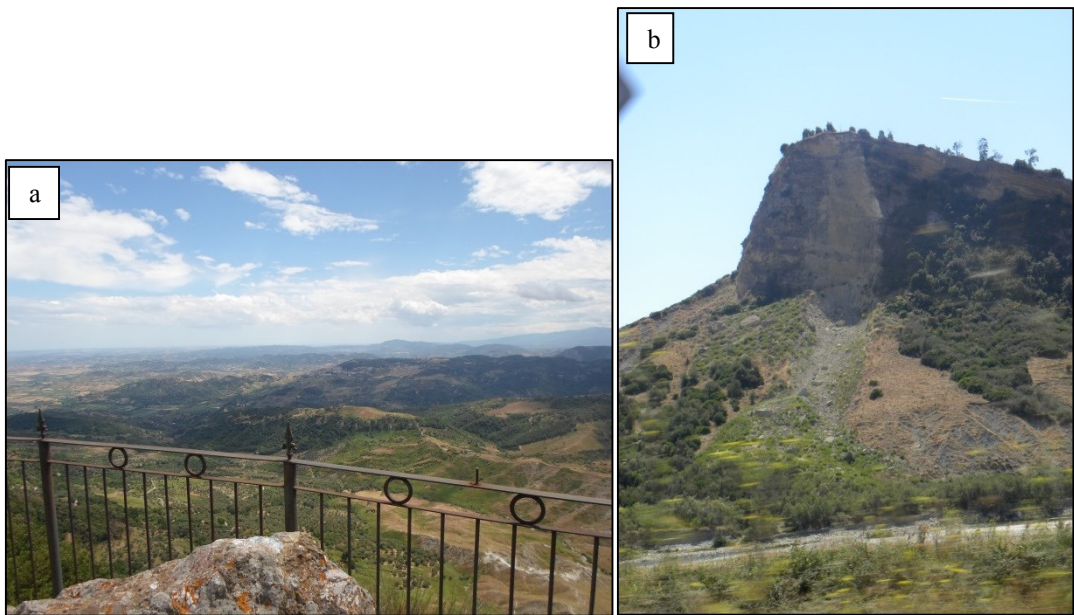


Figure 5.16 a) Hilly landscape (Oblique view from S.Nicola dall'Alto); b) Rocky cliff made of evaporitic deposits (Timpa del Salto, Belvedere di Spinello).

Landforms related to running waters are widespread features in the study area, due to the presence of low permeability and highly erodible lithologies (Luca et al., 2010). The fluvial streams are characterized by a strong seasonal regime, hence by a total absence of water in most parts of the year, and by flooding during wet periods. Only the Nicà, the Neto and Tacina rivers have a perennial nature. Along the valley floor of these three rivers it is possible to observe alluvial terraces, which, sometimes represent relics of dissected alluvial fans. Slope wash forms, such as sheet, rill and gully erosion forms are very highly distributed on the hillslopes, particularly in the non-vegetated areas, due to the presence of clayey and marly-clayey deposits along the slopes. The evolution of these forms is strongly conditioned by the rainfall occurring in the area, but also by the anthropogenic action. Especially in the southern part of Crotone province, the so-called badlands (Fig. 5.5) are a widespread landform: they are very steep valley side slopes carved into clayey deposits.



Figure 5.17 Typical badland forms in Cutro. On the background, on the left side, a marine terrace.

Mass movements and the related forms are widespread in the whole study area, deeply contributing to the landscape evolution and to the increase of geohazards (Iovine et al., 2010; Conforti et al., 2011). Landslide distribution is strictly related to the geological and geomorphological setting of the area (see further). Typical karst form are also widespread, cropping out especially in the Verzino area, with different exokarst and endokarst morphotypes (Parise & Trocino, 2005; Iovine et al., 2010). Blind valleys and dolines, whose presence is underlined by the distribution of the vegetation, are the most typical karst forms present in the study area (Luca et al., 2010). The presence of Messinian gypsum deposits plays a very significant role in the generation of karst forms. On the coastal area of Crotone province, several coastal and transitional forms are very common. The first ones, such as Holocene Aeolian dunes, are visible in the northern sector, in the Cirò Marina area; the latter, instead, represented by fluvial deltas and ephemeral swampy areas, are typical of the Neto delta. The coastline of Crotone province shows differences between the northern and the southern sectors. The northern part, from Torretta di Crucoli to Crotone city, is characterized by sandy beaches and straight coasts (Fig. 5.6 a); conversely, the southern coast is crenulated due to the presence of rocky headlands (Fig. 5.6 b). The crenulation is due to the minor solid input, hence pointing out the role of the marine processes (Luca et al., 2011). Moreover, five orders of marine terraces are also present in the area, deriving from the Middle-Late Pleistocene activity (Fig. 5.5). They show a morphological continuity on the southern part, while they are absent in the northern part. Their deposits are made up of siliciclastic sands and coarse calcarenites. The Crotone terraces are differently interpreted, as regards

their number, distribution and age (Gliozzi, 1987; Palmentola et al., 1990; Zecchin et al. 2004; Nalin et al., 2007).

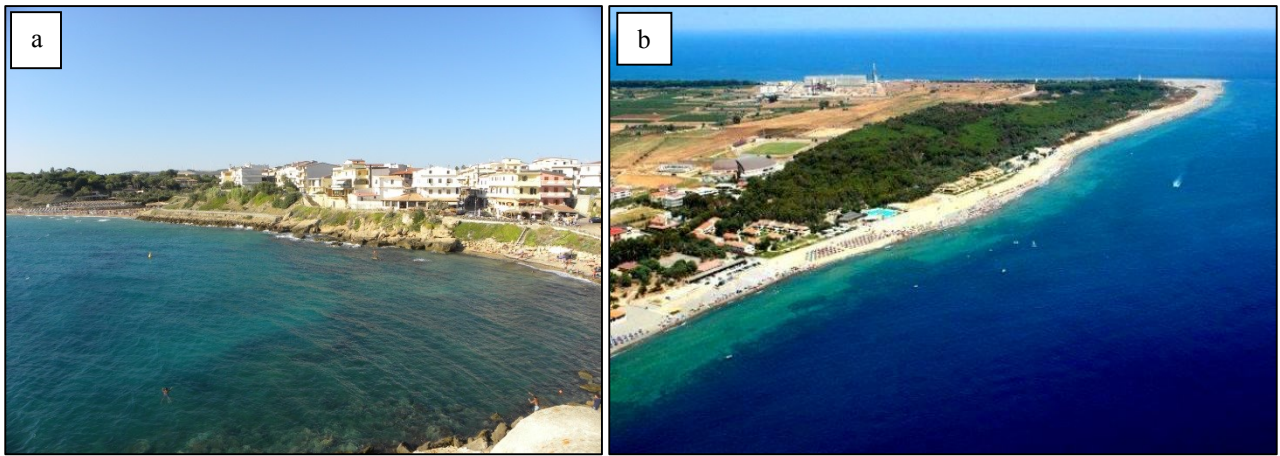


Figure 5.6 a) Rocky coastline (Le Castella, southern sector); b) straight and sandy coastline (Punta Alice, northern sector).

5.4 Landslide inventory map of Crotone Province

As previously mentioned, landslide distribution in Crotone area is strictly related to geological and geomorphological setting and features, such as structural factors (alternation of weak and hard geo-materials), tectonic setting, local relief and fluvial down-cutting (Luca et al., 2011). Moreover, the anthropic impact is increasing in the last decades. The landslide-prone areas or in general the areas involved by instability phenomena have been identified by means of several tools: A first reference has been made through the IFFI Project (Landslide Inventory of Italy), realized by the Italian Institute for Environmental Protection and Research, (ISPRA). Fundamental for the recognition of the landslides in a detailed scale has been the Hydro-geomorphological Setting Plan, produced by the Calabria Basin Authority, along with the Regional Agency for the Environmental Protection of the Calabria (Arpacal). In particular, the Calabria Basin Authority, which developed the first Hydro-geomorphological Setting Plan in 2001 and updated it in the 2006, individuated the landslides, by means of field surveys and aerial photo-interpretation, exclusively in inhabited areas with at least 200 inhabitants. In fact, due to the particularly high concentration of landslides in wild areas, their efforts have been concentrated only in the urban areas. In the 2006 report, in the inhabited areas of Crotone province a total amount of 478 landslides was counted, occupying an area of 44.92 km^2 , about the 2.6% of the whole territory (Table 5.1 and Fig. 5.7). Nine different types of landslides have been identified, following and integrating the Cruden and Varnes classification (1996) and, as shown in Figure 5.7, the

most common type is “slide”, with 140 events recognized, corresponding to 29% of all the landslides. They mainly occur in the northern sector, where the outcrops of sandy and marly-clayey deposits play a significant role. Falls occur mostly on steep slopes made of fractured rock, in the area represented by sandstone cliffs, or along the outer edges of marine and fluvial terraces (Luca et al., 2011). Flow-type landslides have been individuated according to the velocity of the movement: The majority of them are also located in the northern sector of Crotone province. Complex landslides are very common on marly-clayey deposits, typical of the northern sector. Due to difficulties in mapping very small and shallow landslides, or whole sectors affected by widespread instability, four types of areal patterns have been adopted by Calabria Basin’s Authority: Area affected by deep slow deformation/movement; area affected by shallow slow deformation/movement; area affected by deep erosion; slow shallow deformation. Many of such phenomena occur in clayey deposits, as in particular in the southern sector of Crotone province (Fig. 5.8)

Table 5.1 Number of landslides for each type

Flow	Rapid Flow	Complex	Fall	Slide	Slow Shallow deformation	AADE	AADSD	AASSD
23	10	61	12	140	15	63	91	63

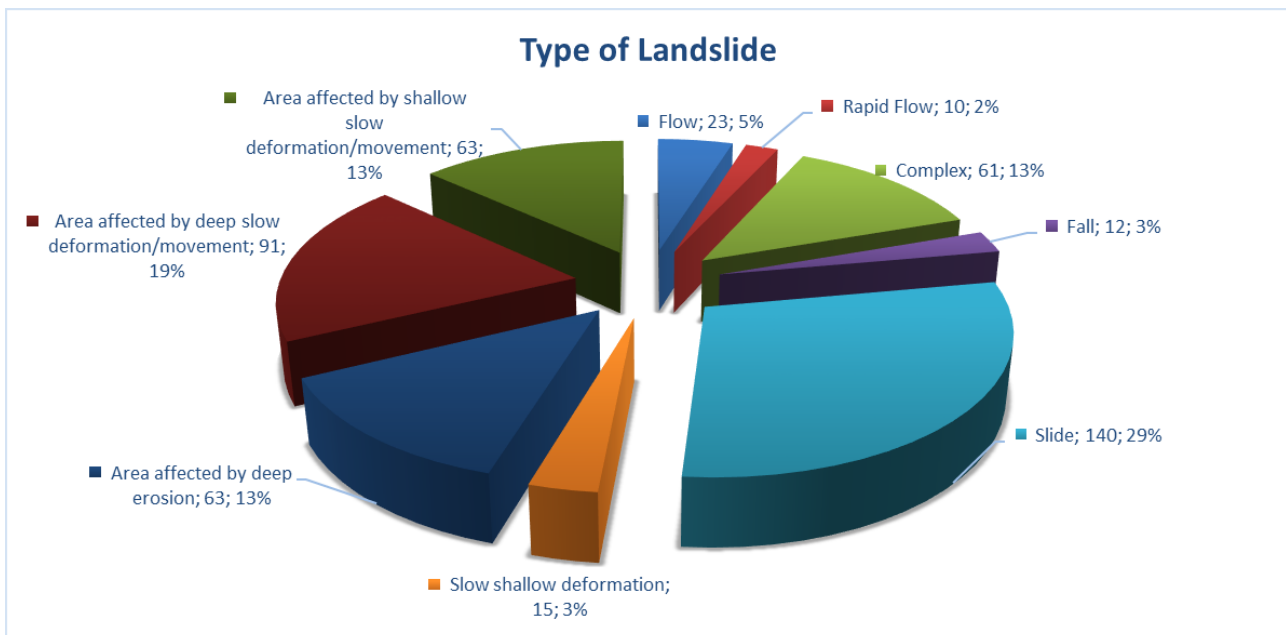


Figure 5.7 Percentage of the landslide typologies and their occurrence in Crotone province.

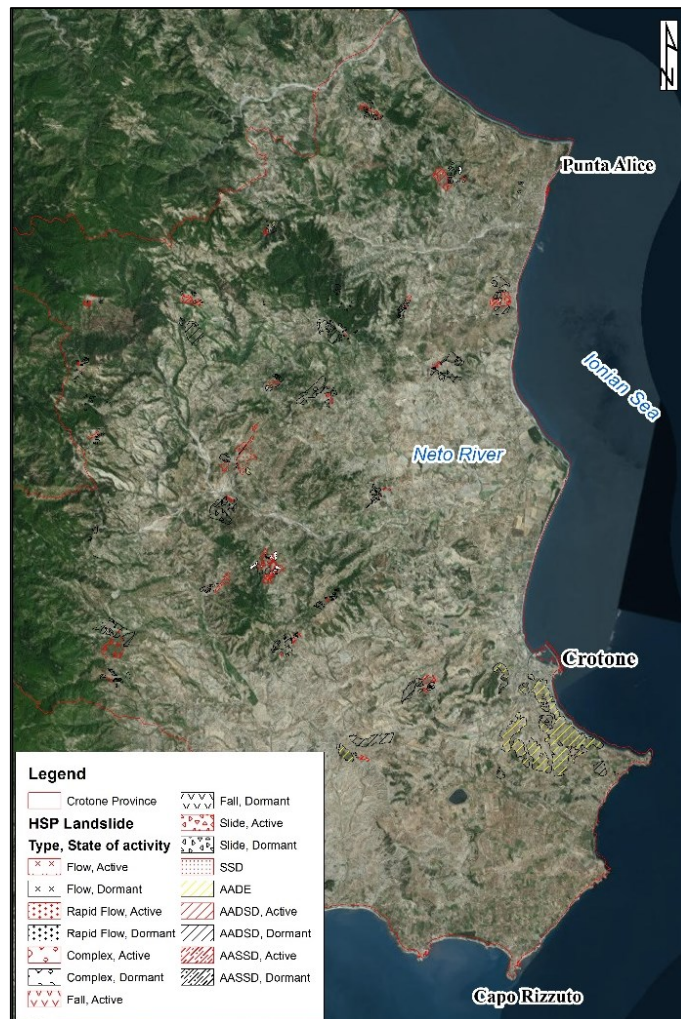


Figure 5.8 Map showing the landslides in Crotone province individuated in the Hydro-geomorphological Setting Plan (Modified from Calabria Basin's Authority, 2006).

As regards the state of activity of the landslides identified during the Hydro-geomorphological Setting Plan, 39% of them were classified as active during the last update of the 2006; conversely, the 61 % turns out to be dormant.

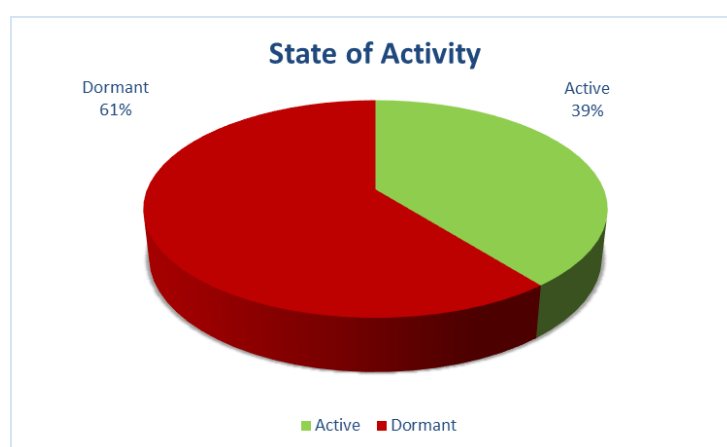


Figure 5.9 Percentage of the landslides state of activity in Crotone province.

CHAPTER 6: APPLICATION OF DINSAR METHODS ON LANDSLIDE CASES

The main focus of this PhD thesis was to monitor, investigate and estimate the landslide hazard in Crotone province. The objective is achievable through the comprehension of the potential of DInSAR methods. On one hand it is remarkable to see the results of their application on a very local scale (slope scale), also analyzing the interaction of observable movements with the local geological and geomorphological setting, on the other hand the assessment of the deformation on wide areas (kilometer-size extension) can assume a paramount role in urban planning, hence of great interest to the local administrations. As concerns the slope scale, two test sites have been chosen according to newspapers consultation, on-line press news, field surveys, and based on the very good suitability of the slopes of interest for the DInSAR application: Cirò and Papanice settlements. The wide scale analysis has been performed following the HSP landslide inventory map, focused on the urban area of each town, and a validation of the methodologies implemented has been done according to field-survey.

6.1 Cirò case study

Cirò is a small village of about 3000 inhabitants, located in the northern part of the Crotone province (Fig. 6.1). Cirò settlement extends on an elongated-shaped hill, NW-SE oriented, at an altitude of 350 m a. s. l. The base of the stratigraphic series at Cirò is made up of Varicoloured Clays, Sandstones of Monte Caciocavallo and Sandstones of Crucoli, all dating to the timespan Eocene-Miocene, while an angular unconformity separates them from the Ponda Clays formation (Serravallian-Tortonian in age). At the top of the series the Scandale Sandstone formation (Pliocene) can be found. The historic centre was established on sandstones, belonging to the Scandale Formation and it presents a very high rate of urbanization. The latter is lithologically composed of shallow-marine, medium-to fine-grained deposits, characterized also by sub-vertical and intensively jointed cliffs (Fig. 6.2).

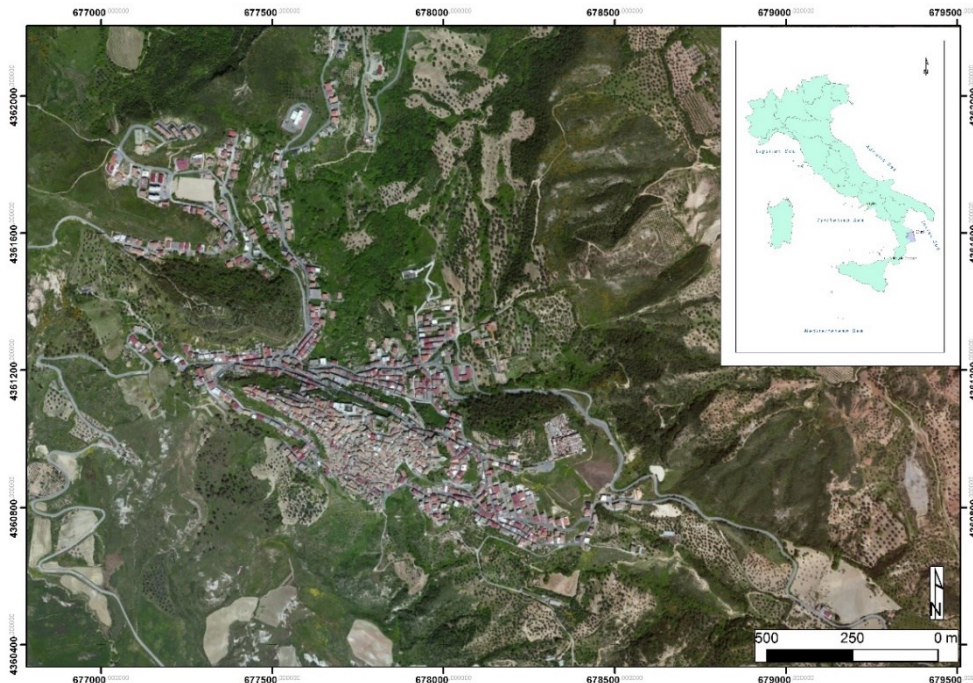


Figure 6.1 Location of Cirò.

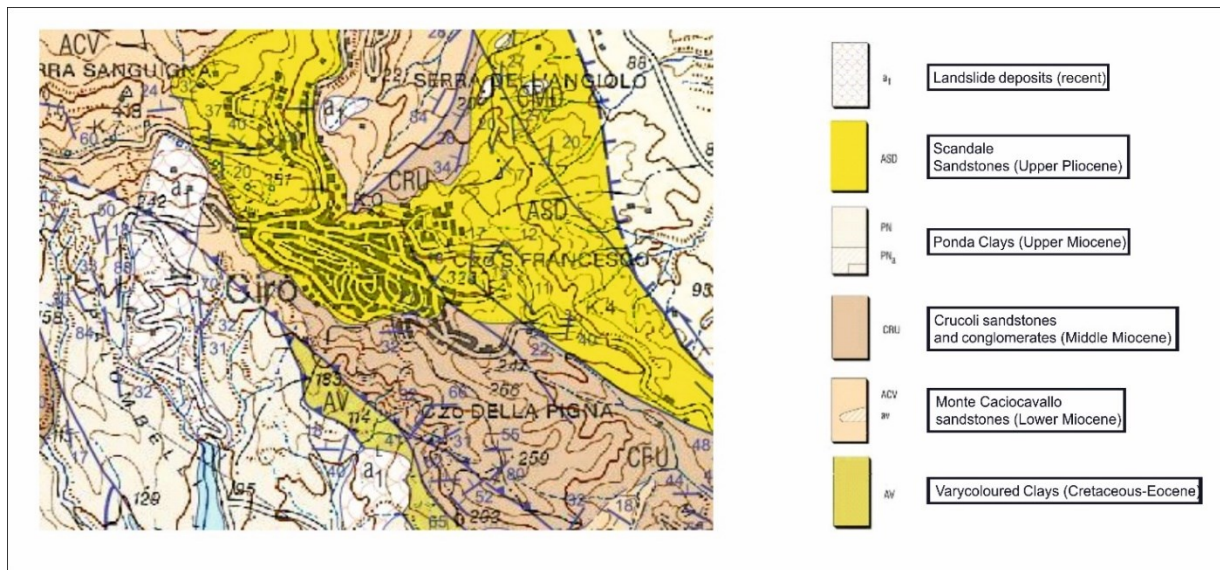


Figure 6.2 Geological map of Cirò town (modified from Geological Map of Italy, 1:50.000, ISPRA, 2006)

All the surrounding slopes are in morphological evolution, due to the presence of a hydrological pattern, whose activation starts in case of intense and prolonged rainfall periods, hence triggering a concentrated erosive action along the slopes and the channels. The HSP (Fig. 6.3) reports in Cirò 23 landslides as unstable areas: In particular 12 of them are documented as dormant, 2 of them are identified as area affected by deep erosion (AADE) and 9 as active, all located in the SW facing slope

(SSD, AADSD and AASSD stand for slow shallow deformation, area affected by deep slope deformation and area affected by shallow slope deformation, respectively). Totally they occupy an area of 1.44 km², while the total extension of Cirò territory is of 71 km².

6.1.1 The February 2011 landslide

As previously stated, the SW slope is particularly interested by active landslides and it is part of a geomorphological setting very prone to erosive actions. Here, in the night of 1st/2nd February 2011, a landslide occurred in one of the main access road to town centre, Via de Gasperi, causing severe damage and also forcing people to abandon five houses (Fig 6.8). Starting from October 2013, the landslide has been mapped and its evolution surveyed until November 2015. According to the Cruden and Varnes classification (1996), the movement can be defined as a rotational slide evolving into an earth flow. The landslide crown is almost vertical, about 5 m high, causing the excavation of the foundation system of three houses, while the landslide body is characterized by a length of about 250 m downslope, and 120 m of width (Fig. 6.5). The morphology of the landslide crown has been strongly influenced by the presence of a supporting wall, on the right flank, and by the presence of the houses, in the central part. This landslide is a reactivation of a well-known phenomenon, included in the entirely unstable SW-facing slope, as reported by the Calabria Basin's Authority in the Hydrogeomorphological Setting-Plan (HSP), realized in 2001 (Fig 6.6).

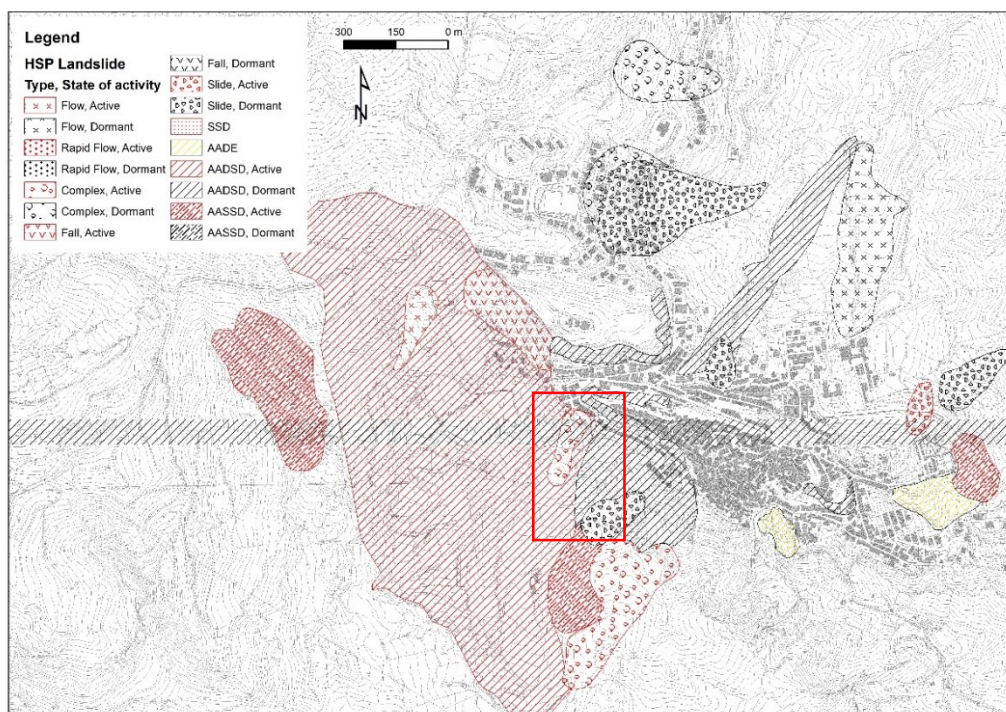


Figure 6.3 HSP of Cirò. The 2011 landslide fall into the red rectangle. Modified from Calabria Basin Authority (2006).

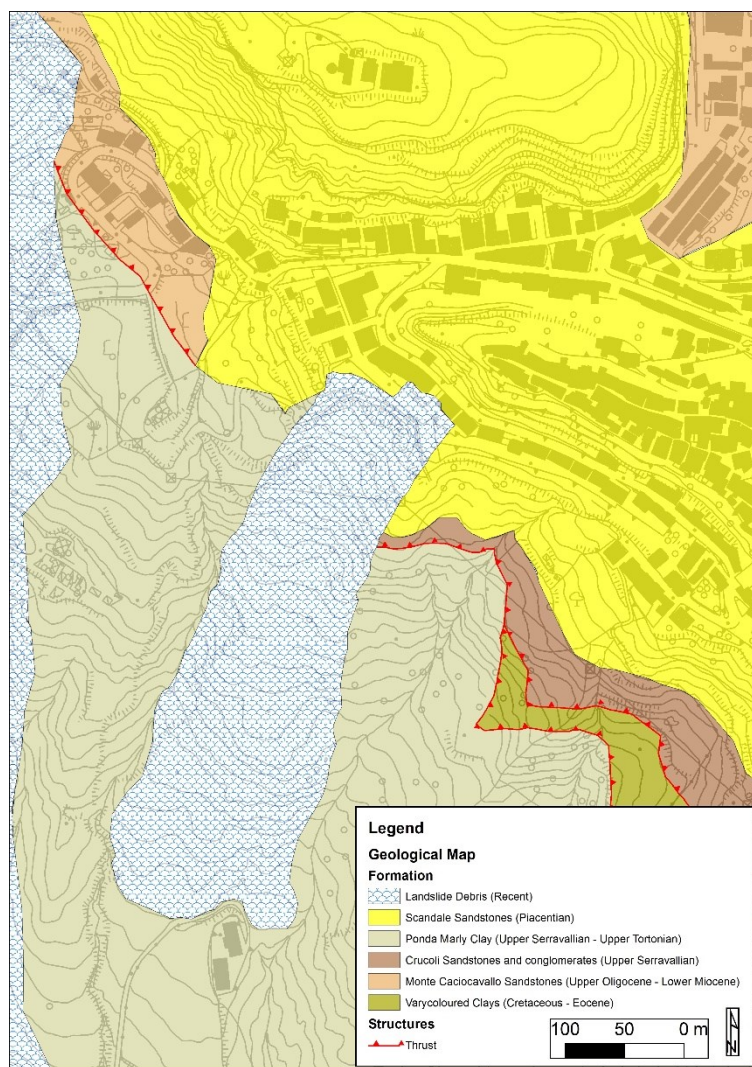


Figure 6.4 Geological map of the landslide area.

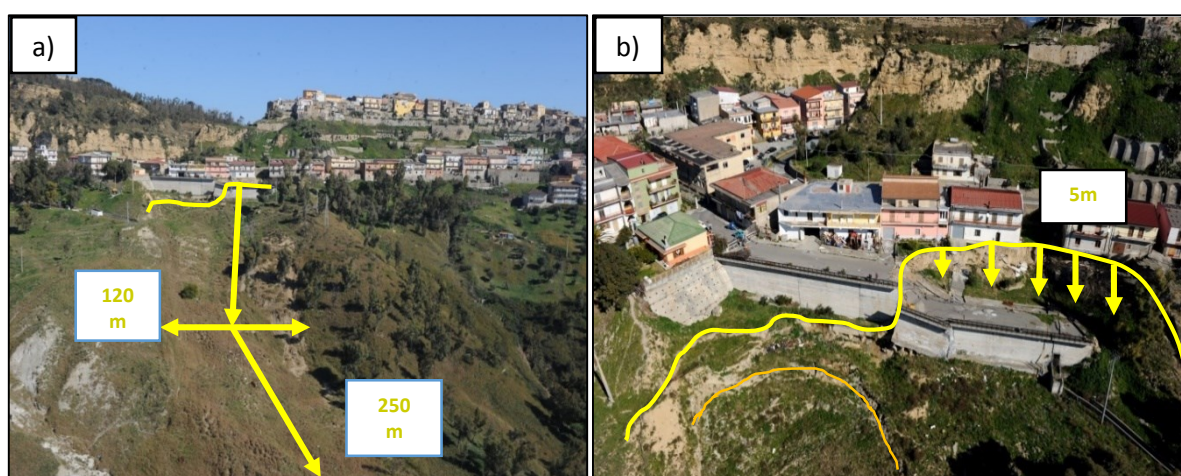


Figure 6.5 a) Panoramic view of Cirò landslide; b) oblique air view of the main scarp. Courtesy of Arpacal (2011).

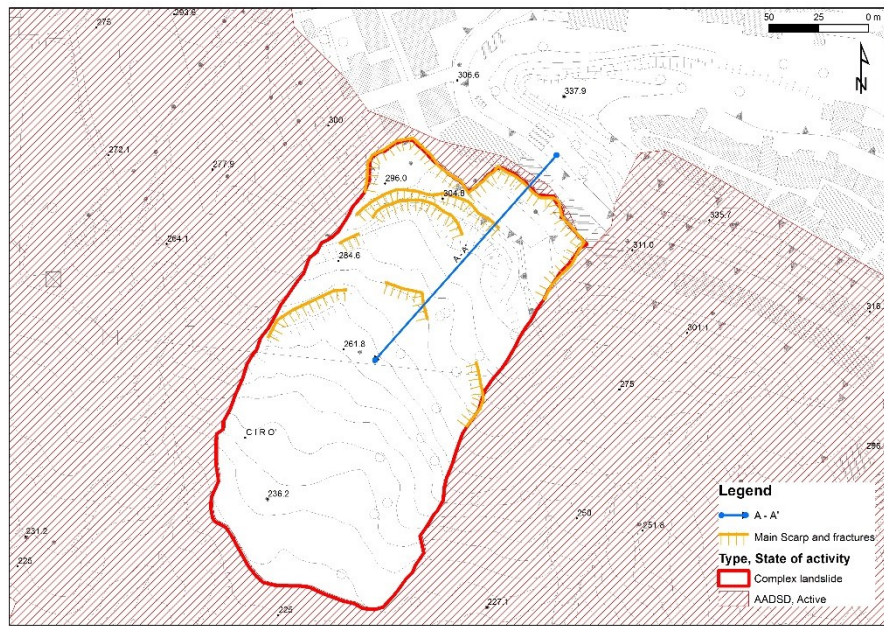


Figure 6.6 Geomorphological map of the landslide area. In blue, the cross section A-A' (Figure 6.7).

The landslide-prone condition, especially in this part, is due to the geological setting (Fig. 6.4), where the basic relationship between sandstones and the underlying Ponda Clays formation, characterized by different permeability, strongly conditioned the water circulation. The movement interested mostly the Scandale Sandstones formation, which shows up with layers with NNW-SSE direction, NE 20° dip and hence anti-dip slope. The arenaceous levels are characterized by a good strength, but the very active water circulation presumably reduces the original geo-mechanic characteristics. An unconformity separates the Scandale formation from the underlying Ponda clays, made of pelagic clays and locally intercalated with sandy levels, few centimeters thick. The landsliding area shows up a chaotic sandy-silty matrix, with lithoid sandstone blocks in the order of tens of centimeters. In the upper part, moreover, it has been possible to recognize end products coming from the overlying houses (Fig. 6.7). This setting, as previously mentioned, strongly conditioned the water circulation in the area. Moreover, the hydrological pattern of the area is strongly influenced by prolonged and concentrated rainfall periods, which start a powerful erosional activity on the slope and along the streams, activating then the deformation. Water circulation is very active in the basin: According to a report made in the aftermath of the landslide event by the ARPACAL (2011), two water springs have been found in the landslide body, registering moreover a constant flow rate during the period of analysis (February-June 2011). In such framework, the presence of a retaining wall along the crest of the slope, without an efficient drainage system, increased the landside propensity.

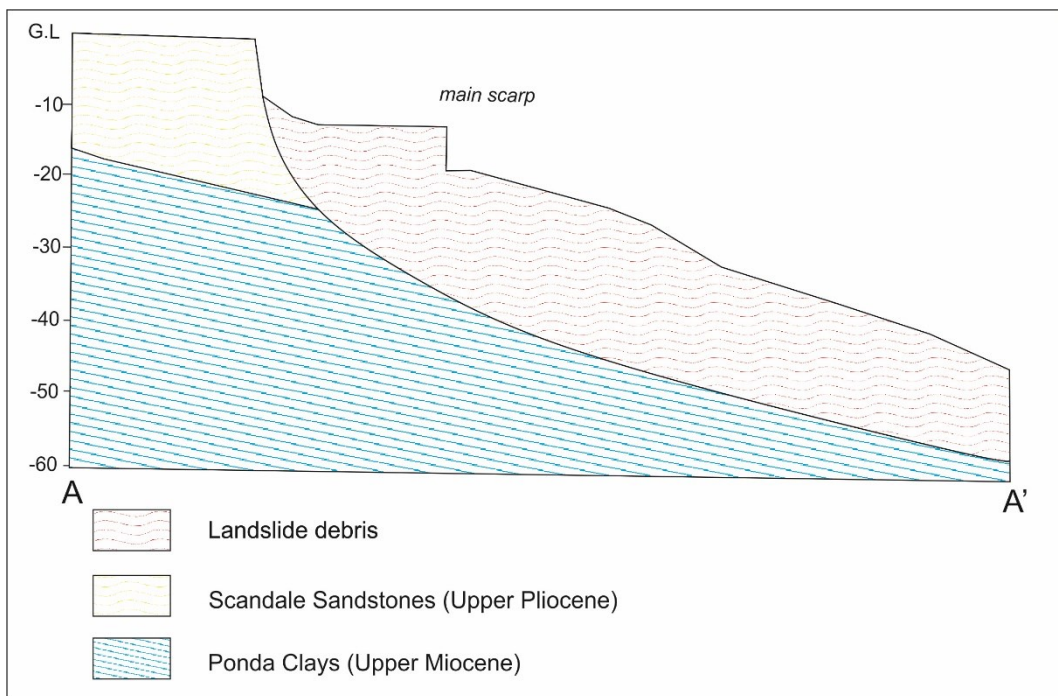


Figure 6.7 Geological cross section A-A'.



Figure 6.8 a) View of the sandstone rock on which Cirò historical center is founded; b) particular of the rock, with also protective gabions; c) particular of the excavated foundation system of a house; d) damages on the road and on the houses in occurrence of the main scarp; e) view of Via de Gasperi from above; f) lateral view of Via de Gasperi (Photos taken during field survey, years 2013-2015).

The most important triggering factor for the February 2011 reactivation is surely represented by the copious rainfall occurred in the area in the previous days. However, the rain gauge in Cirò town has been installed only in June 2011, after the landslide event, so the data collected are from the nearest rain gauge, located in Crucoli, a small village 6 km far from Cirò city center. As it is shown in the rainfall plots (Fig. 6.9), the fall and winter months have been characterized by sporadic but sometimes intense rainfall events, such as the one occurred in the first days of November. However, in the fifteen preceding days of the landslide it is possible to notice the highest rate of precipitation. In fact, the highest precipitation event has been registered on the 28th of January, showing a total amount in the 24 hours of 125 mm, which is an anomalous value for this geographical and geomorphological setting. The cumulative rainfall calculated over the previous 7 days (from 27th of January to the 2nd of February) is of 301 mm. According to this analysis, the movement has been most likely caused by the prolonged rainfall that occurred in Cirò during the days preceding the triggering moment.

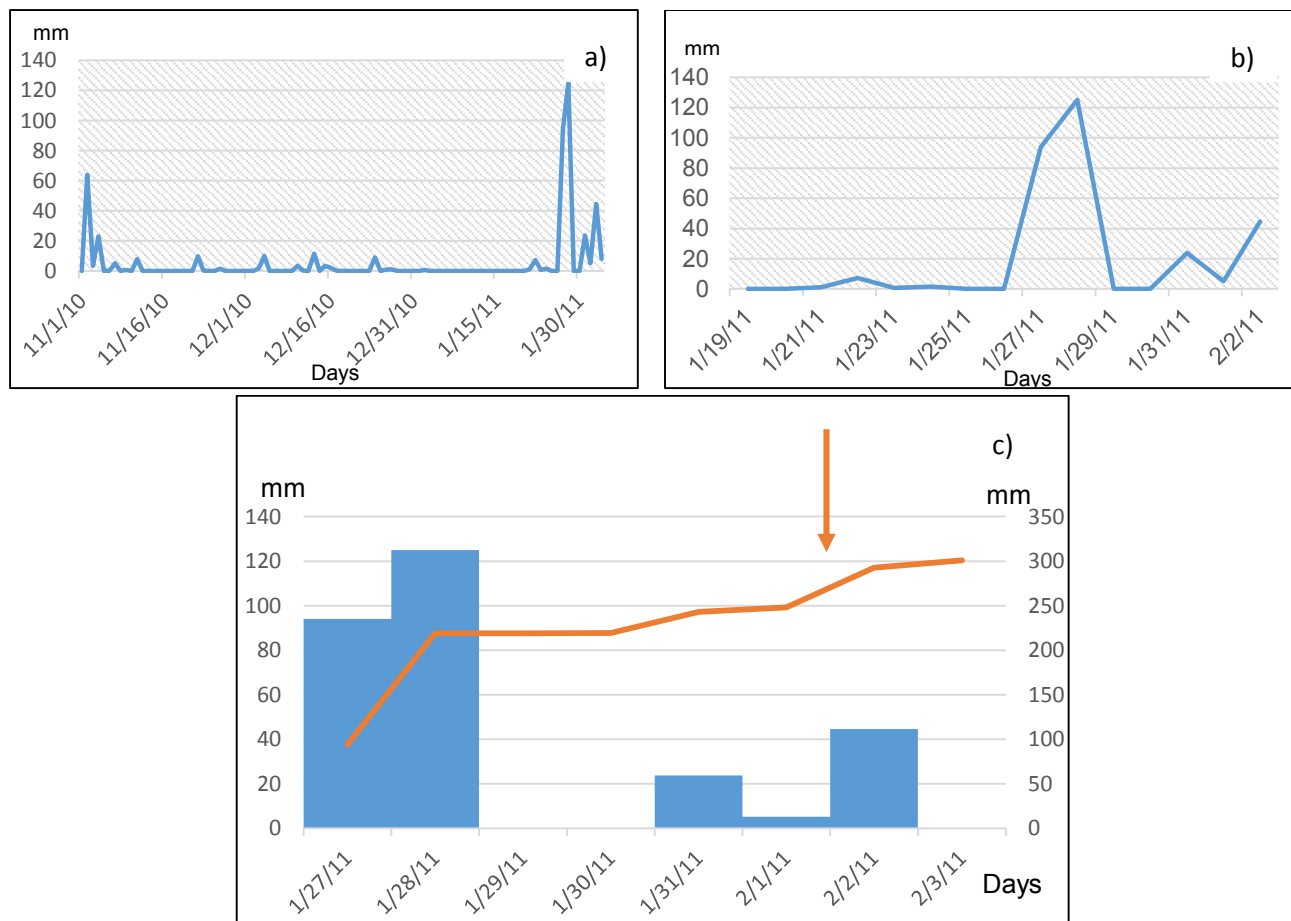


Figure 6.9 Plots of the antecedent rainfalls measured at the Crucoli rain gauge: a) 3 months; b) 15 days; c) 7 days preceding the landslide. The arrow indicates the landslide event.

6.1.2 DInSAR analysis

6.1.2.1 CPT

DInSAR interferometry has been applied to the Cirò case study based on the availability of the original stack of TerraSAR-X images, composed of 35 and 34 images, acquired along the descending and ascending orbit, respectively, in the time span April 2008 - June 2010. The area of interest selected for the SAR analysis is about 10 km² wide. A DEM, extracted from the regional topographic cartography, with resolution cell of 5 x 5 m, has been used in order to remove the effect of the topography on the interferometric phase. The available satellite images have been firstly processed through the SUBSOFT processor (Mora et al., 2003), developed at the Universitat Politècnica de Catalunya of Barcelona. Such software is implemented with the Coherence Pixels Technique (CPT). The results on the ascending dataset (Fig 6.10) did not provide any valuable result: 1.983 CPs have been recorded, but all the CPs identified are characterized by velocities of the displacement below 1 mm, and, moreover, no target has been identified in the 2011 landslide area.

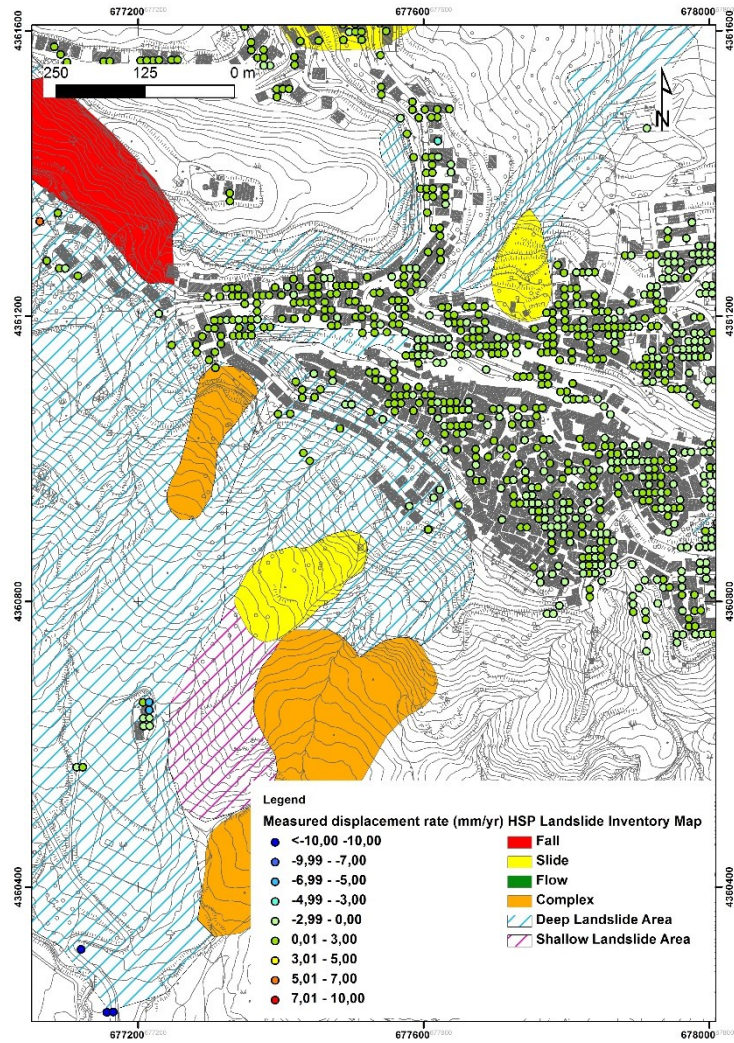


Figure 6.10 Map showing the displacement rate identified with CPT on the TSX ascending dataset (2008-2010).

The implementation on the descending stack (Fig 6.11), instead, turned out to be more remarkable. In this case the CPT identified 3.230 CPs all over the inhabited area of Cirò. Across the landslide area, 14 points located in correspondence of the landslide crest have been recognized, and 8 of them show considerable displacement rates, up to 20 mm/yr along the LOS of the satellite. In this case velocities show a positive sign, but the displacement must be intended as away from the satellite, because the version of the SUBSOFT software used for Cirò case calculated the displacements with reverse signs, with respect to the newer version and the other software. This implies that the positive sign is not a mistake, but a consequence of the software settings. As a result of this elaboration, and jointly with the geological-geomorphological surveys performed between the Fall 2013 and the Summer 2015 it has been possible to confirm the active state of the landslide, as reported in the 2001 HSP. Moreover, DInSAR processing and field survey made also possible to redraw the landslide boundary, which now delimits an area of about 24500 m², a figure almost twice as large

as previously known (Fig. 6.11 c). By comparing the 2001 landslide body and the one resulting from this study, a retrogressive and a widening trend can be recognized.

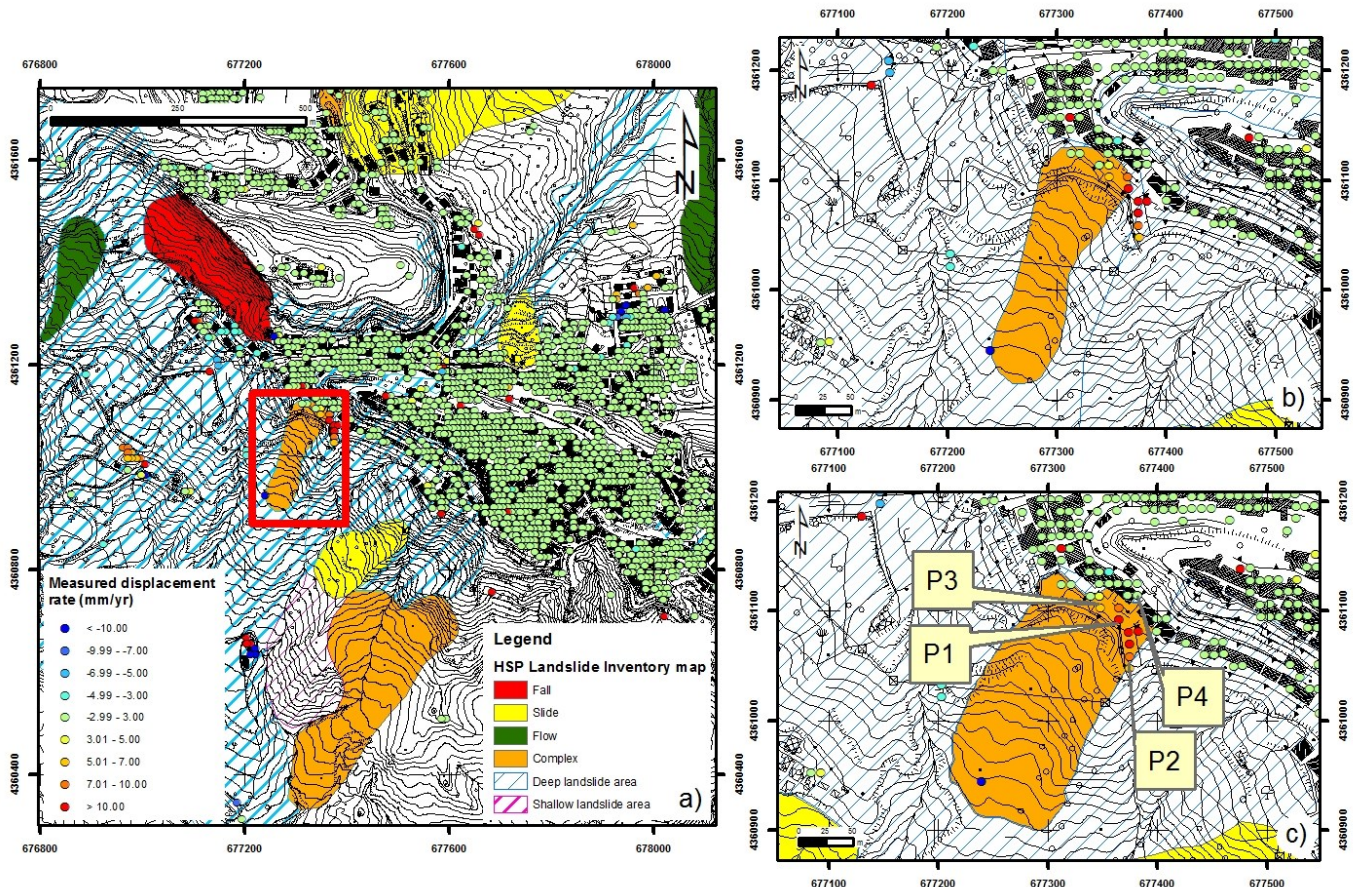


Figure 6.11 a) Measured displacement rate map of Cirò area, exploiting the descending stack; b) Surface morphology of the main active landslide along the SW slope, according to the HSP; c) Main active landslide along the SW slope, according to field survey and interferometric results. P1, P2, P3, P4= significant selected CPs for time series analysis.

Four different classes of velocities have been identified in the area and four representative points have been selected (Fig 6.11). The four classes are:

- Class 1, velocity of displacement higher than 10 mm/yr;
- Class 2, velocity of displacement between 5 and 10 mm/yr;
- Class 3, velocity of displacement between 3 and 5 mm/yr;
- Class 4, velocity of displacement lower than 1 mm/yr.

4 CPs located along the crest belong to Class 1, 4 CPs can be attributed to Class 2, 2 CPs to Class 3 and other 2 CPs to Class 4. The points belonging to the classes 1, 2 and 3 are mostly located

in the SE part of the landslide, then indicating an activation of the displacements in a sector previously not interested by the complex landslide.

As previously stated, rainfalls usually represent a major triggering mechanism for the re-activation of landslides on already unstable slopes. By the comparison between the time-series derived from the CPT analysis on the TerraSAR-X descending stack and the precipitations occurred in this area in the same time-span, it has been possible to comprehend potential connection between precipitation and displacements. Hence, the 4 representative points have been compared with the 15-days cumulated rainfall, which have been chosen due to the higher compatibility with the evolution of the displacement. In particular the point P1, belonging to Class 1, shows a good agreement between rainfall and time series of the displacement (Fig 6.12 e). It is, therefore, possible to realize that the acceleration phase of the movement corresponds to intense and long rainfall events, unlike during periods with scarce rainfall, when a slowdown of the movement can be noticed. This remark is in agreement with the general behavior of slow and intermittent landslides, where there is a strong cause-and-effect relationship between rainfalls and velocity of the instability phenomena, especially for the superficial landslides. It is also worth to underline that, being the TerraSAR-X dataset antecedent to the landslide's reactivation, the SAR methodology has been able to recognize precursor stages of a future slope failure.

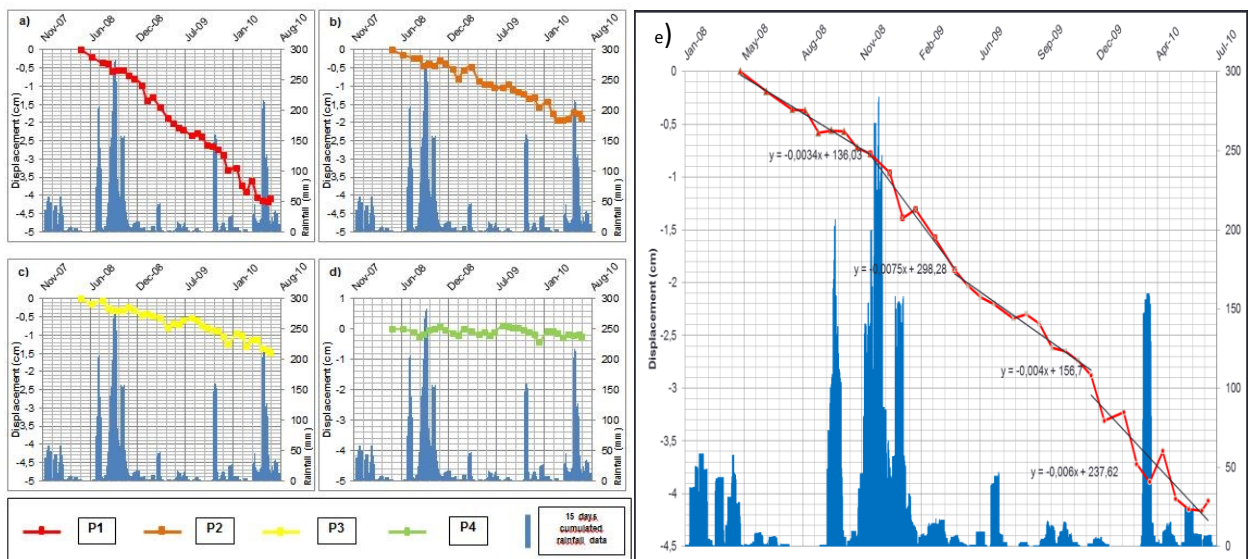


Figure 6.12 Comparison between significant points - rainfall data: a) P1 (more than 10mm/yr; b) P2 (between 5 and 7 mm/yr); c) P3 (between 3 and 5 mm/yr; d) P4 (stable point); e) Detail of the comparison between P1 and rainfall data.

6.1.2.2 PSInSAR

Thanks to an agreement between the University of Napoli Federico II, the Technische Universität München and the Deutsche Zentrum für Luft und Raumfahrt (German Aerospace Center), a collaboration started in October 2014, during which further analysis were performed. First of all, new TerraSAR-X images have been added to the original stack, through the participation to the TerraSAR-X data proposal Geo 2641. The original stack, originally composed of 35 and 34 images, respectively belonging to the descending and the ascending orbit, in the timespan 2008-2010, has been filled, so reaching the total amount of 66 images for both the orbits. If it was originally composed of images acquired every 22 days, now it is made of images with a revisiting period of 11 days. Firstly, the PSInSAR (Ferretti et al., 2001) has been implemented. Due to the high number of SAR images, a procedure has been adopted for the PS processing of the test area (Fig 6.13), in this case Cirò town, in order to improve the results, but also to speed up and lighten the processing. Hence, two criteria have been introduced: On one hand, a temporal baseline, splitting the stack in two parts (Period 1, between April 27, 2008 and August 2, 2009, and Period 2, between April 3, 2009 and June 28, 2010, hence with an overlap of about 100 days), and on the other hand, a spatial baseline of ± 100 m. All the interferograms characterized by a time-span higher than the temporal baseline introduced and a spatial baseline higher than the one set have been hence discarded. With the temporal baseline application, it has been possible to analyze points characterized by high coherence in a shorter time of analysis, while the spatial baseline criteria consists in a threshold useful to decrease the topography influence on the interferometric signal.

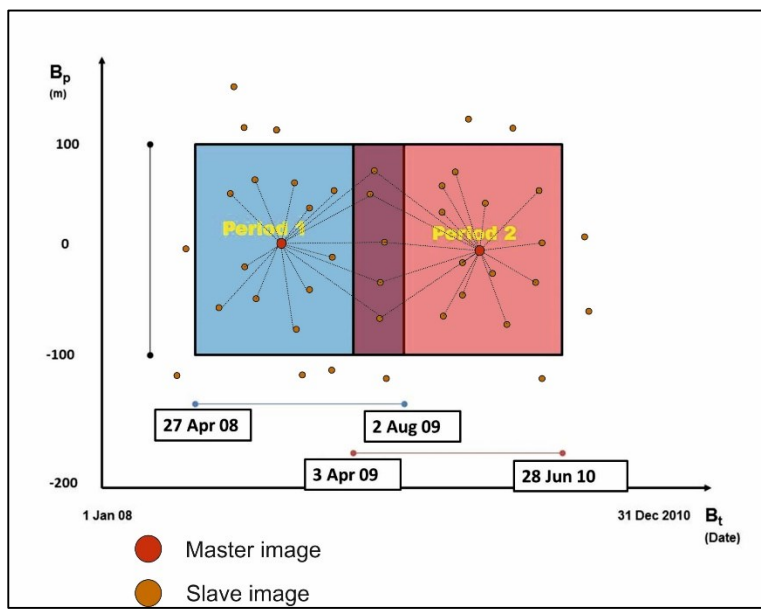


Figure 6.13 Scheme of the procedure adopted for the PSInSAR analysis.

The results obtained with the PSInSAR application confirm the trend and the localization of the displacements previously identified with the CPT technique.

Although also the PSInSAR application on the ascending stack (Fig 6.14, Fig. 6.15) has not provided valuable results, hence confirming the inappropriateness of such imaging geometry for any analyses on Cirò area (cf. section 6.1.2.4), it turned out to be valid on the descending dataset (Fig. 6.16, Fig. 6.17). In fact, both in the first (Fig. 6.16) and in the second period of analysis (Fig. 6.17), consisting of 28 and 31 images exploited, respectively, several PSs showing displacement rates up to -13 mm/yr have been identified along the main scarp of the Via de Gasperi landslide. In the first period 7 PSs have been detected in the landslide area, where 2 of them are characterized by velocities of the displacement higher than -10 mm/yr, while 3 PSs have been recorded in the analysis of the second period of investigation, where 2 of them display displacement rates higher than -10 mm/yr.

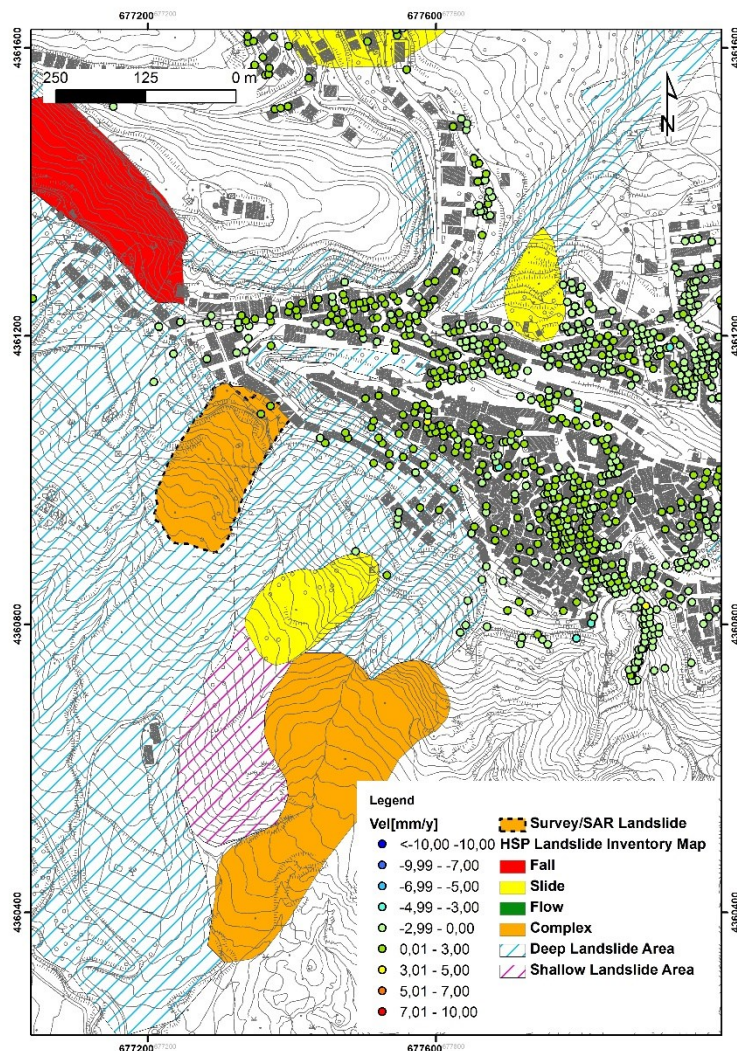


Figure 6.14 Displacement rate map obtained through PSInSAR application on the ascending dataset (1st period of analysis).

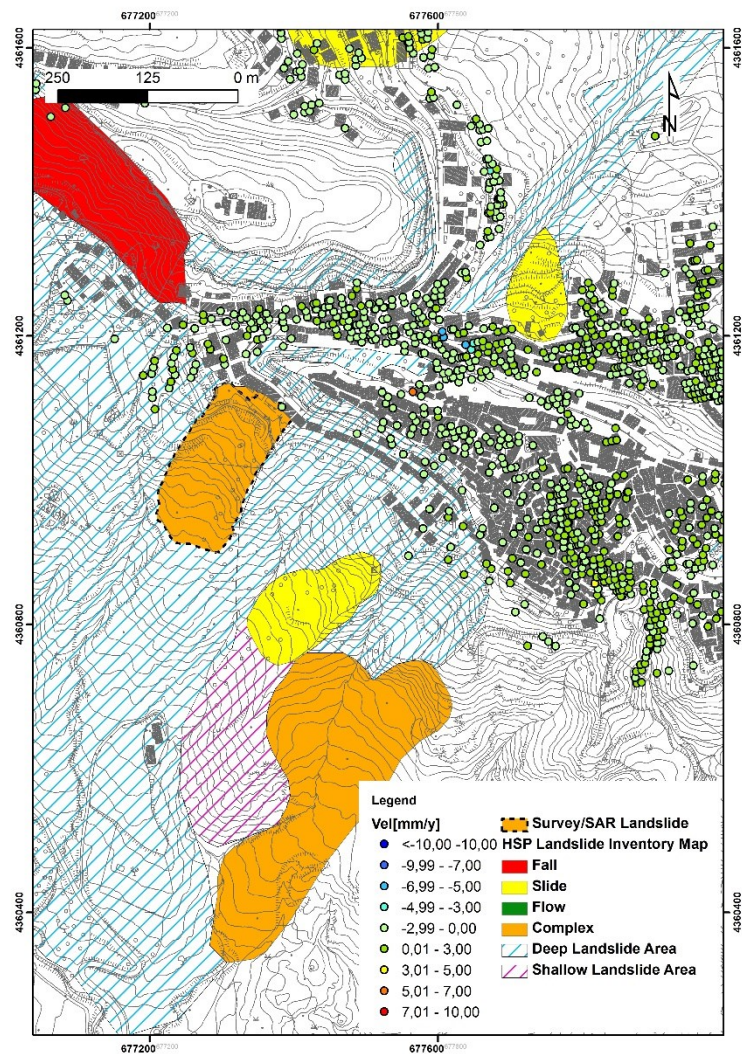


Figure 6.15 Displacement rate map obtained through PSInSAR application on the ascending dataset (2nd period of analysis).

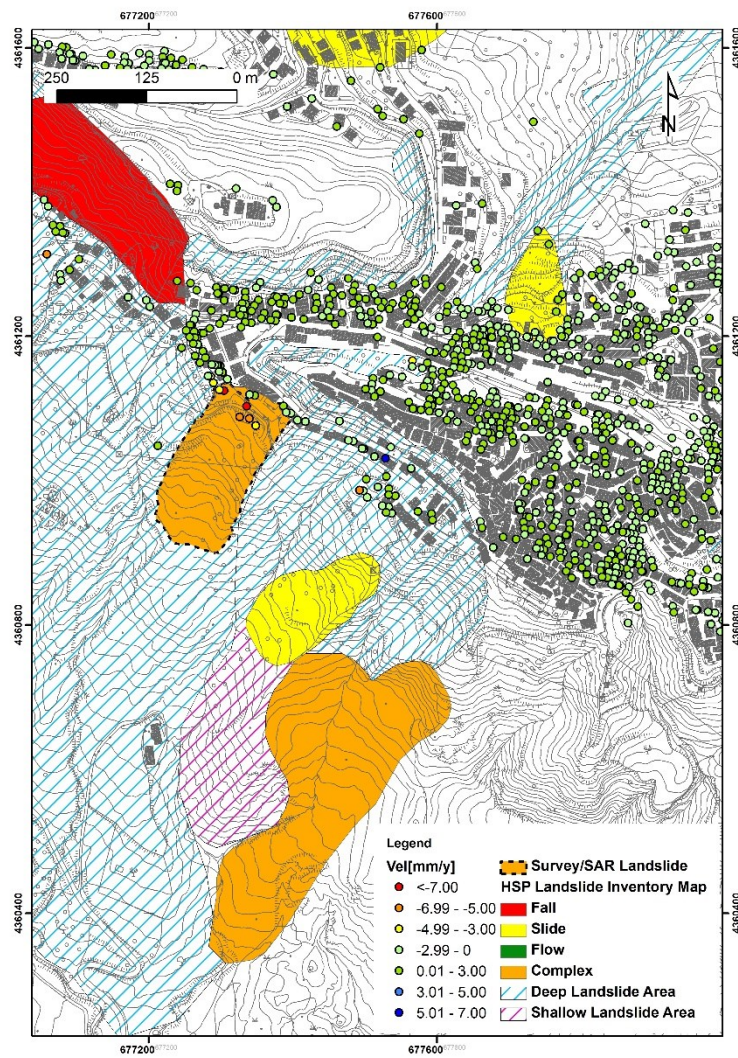


Figure 6.16 Displacement rate map obtained through PSInSAR application on the descending dataset (1st period of analysis).

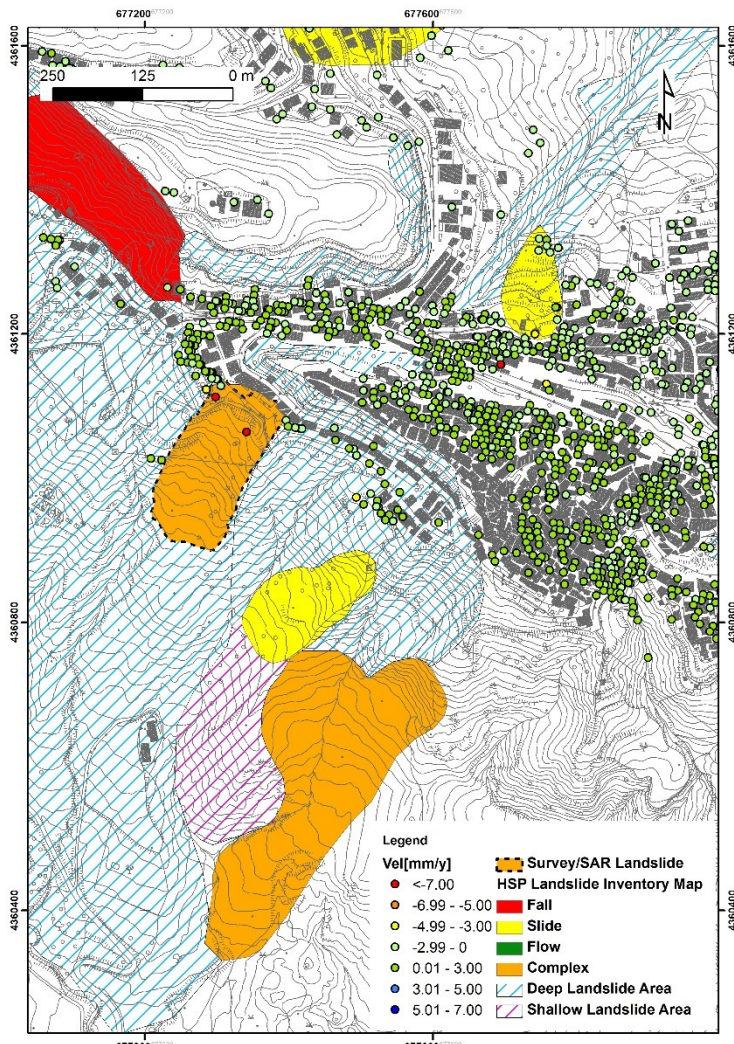


Figure 6.17 Displacement rate map obtained through PSInSAR application on the descending dataset (2nd period of analysis).

6.1.2.3 SBAS

The SBAS (Berardino et al., 2002) method has been applied on Cirò case using very tight baselines, thanks to the high stability of the TerraSAR-X satellite during the acquisition. The main parameters, applied both on the two whole stacks are summarized in Table 6.1:

Table 6.1 Main parameters for the SBAS application to the Cirò case study.

Temporal Baseline	100 days
Spatial Baseline	2.5% max. critical baseline (about 100 m)
Coherence Threshold	0.6
Multilooking Factor	5x4

As previously noted, the ascending dataset has not provided reliable results also with the SBAS application: No target has been detected in the area of interest, among the 5.762 individuated (Fig 6.18). Conversely, the implementation of the SBAS on the descending dataset shows very valuable outcomes (Fig 6.19), confirming the ones resulting from the other methods exploited. The localization of the displacement is clearly recognizable and in agreement with the field survey and the outcomes deriving from the previous experiences. The displacement rates identified with the SBAS technique on the 66 images belonging to the descending orbit are also very comparable with the velocities identified with the CPT (cf. section 6.1.2.1) and the PSInSAR (cf. section 6.1.2.2) application. In this case, among the 4789 points detected in the whole area of interest, 27 points can be attributed to the Via de Gasperi landslide, characterized by displacement rates up to -13 mm/yr, all located along the crest of the phenomena investigated.

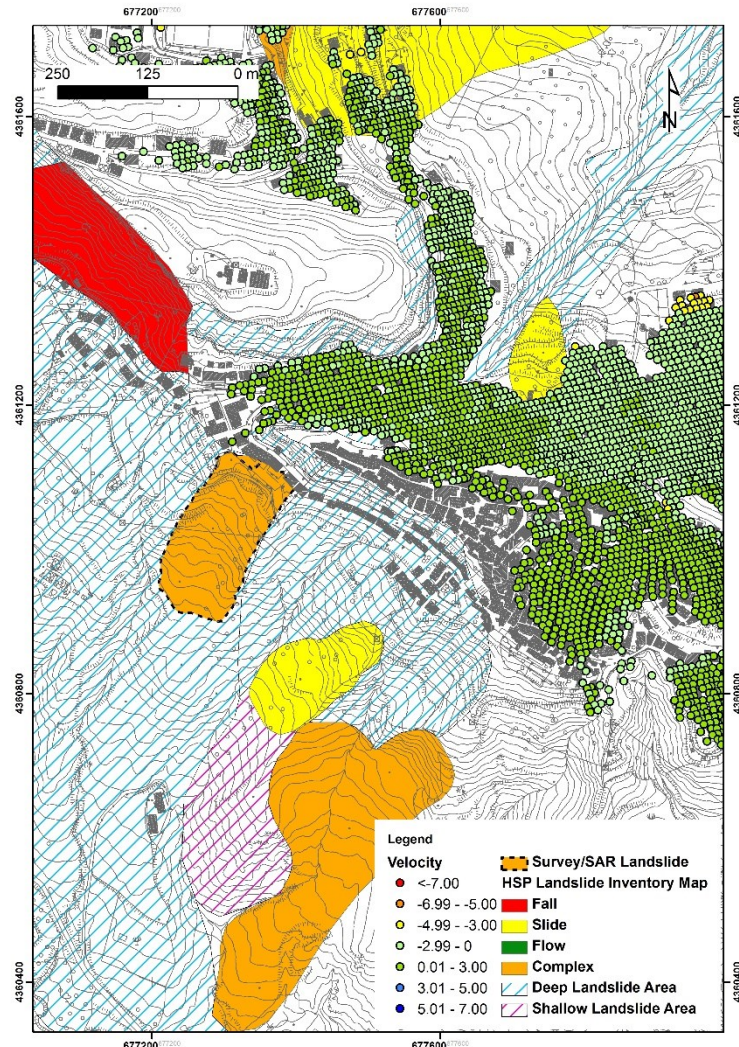


Figure 6.18 Displacement rate map obtained through SBAS application on the descending dataset.

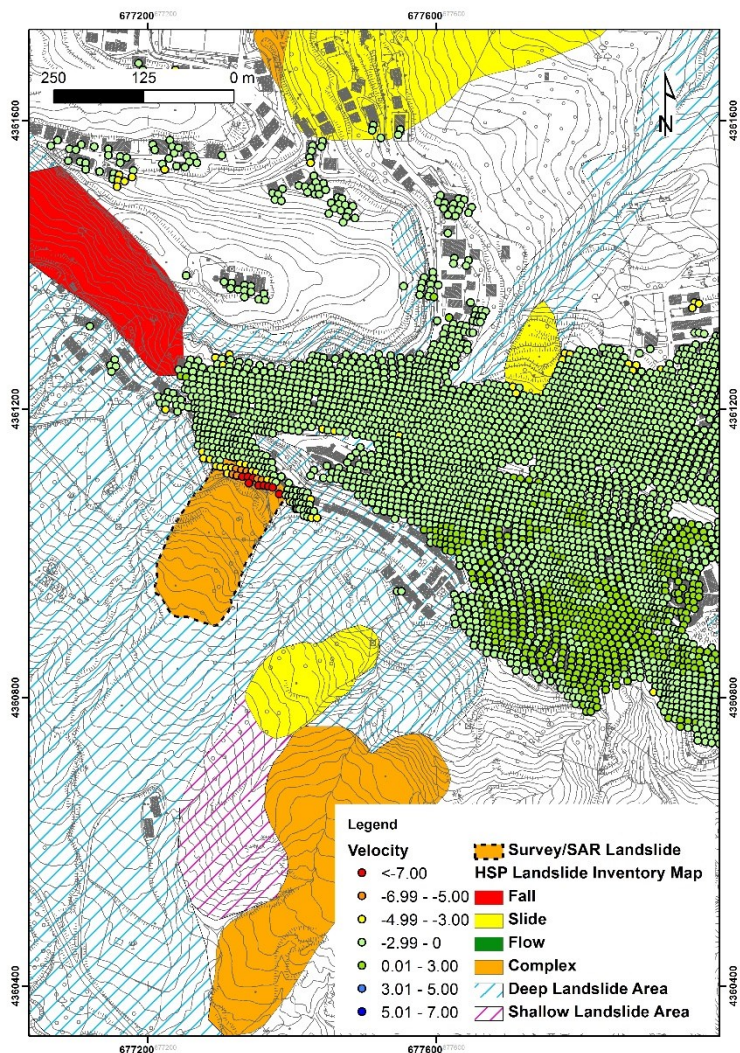


Figure 6.19 Displacement rate map obtained through SBAS application on the ascending dataset.

6.1.2.4 R-Index

As previously tested, the DInSAR analysis, with all the algorithms implemented, provided good results, in Cirò case study, only exploiting the descending dataset. The reason why the ascending stack has been not useful for the displacement investigation has to be related to the slope exposure and its relationship with the geometry of acquisition of the satellite sensor. An estimation of the points detectable by the satellite in a given area has been made by Notti et al. (2010), who developed the R-Index equation. The R-Index is defined as the ratio between the slant range and the ground range, taking also into account the geometry of acquisition of the radar and the geometry of the ground surface. These last products are ascribable to the slope and aspect models, respectively, which can be obtained from a DEM of the area of interest. The maximum value of the R-Index is 1, which corresponds to the best geometry detectable by the satellite, occurs when the slope is parallel to the LOS. On the other hand, the smaller is the R-Index, the harder to detect a PS: if this value tends to 0 it

means that the pixel is in foreshortening, while it will be in layover and in shadowing if the R-Index results negative. In all these three cases no PS is detectable. The R-Index computation on the SW facing slope of Cirò (Fig 6.15) confirms the preliminary analysis. In fact, the R-Index map of the ascending dataset shows a high density of pixels characterized by very bad quality, especially in the area of the 2011 landslide, with average value around zero. This means that the area is in foreshortening, hence, not useful for any DInSAR analysis. Conversely, the R-Index map on the descending dataset displays a very high quality of the pixels, affected by very low compression, then confirming the effectiveness of the DInSAR analysis on the descending stack.

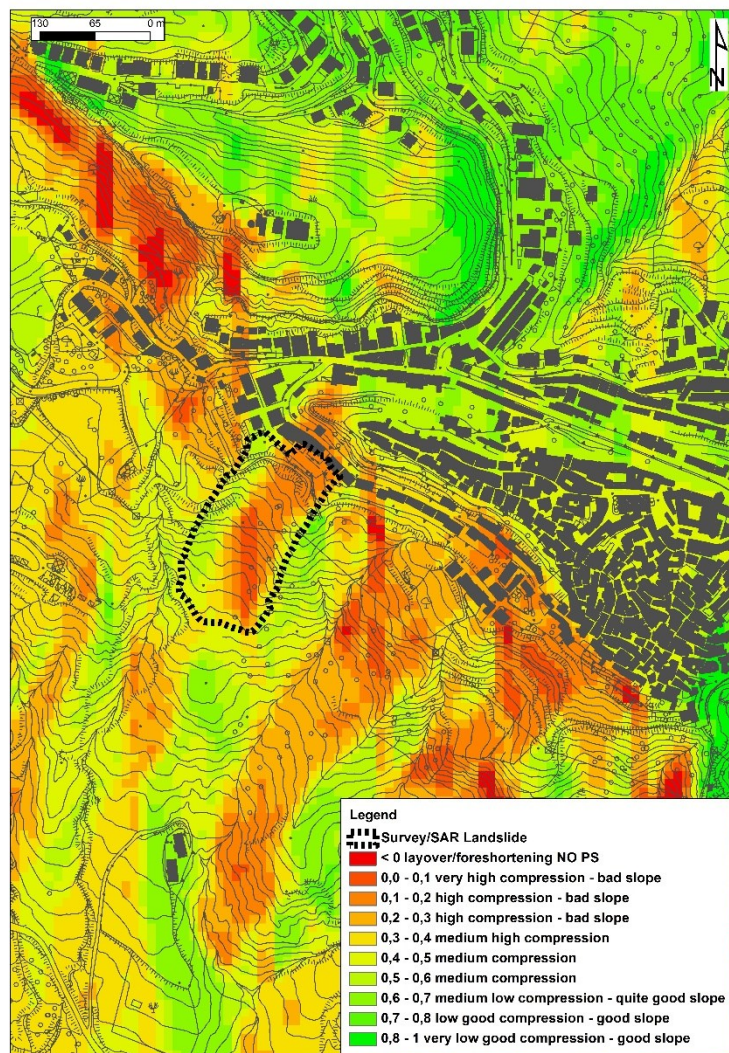


Figure 6.20 R-Index map for the ascending dataset.

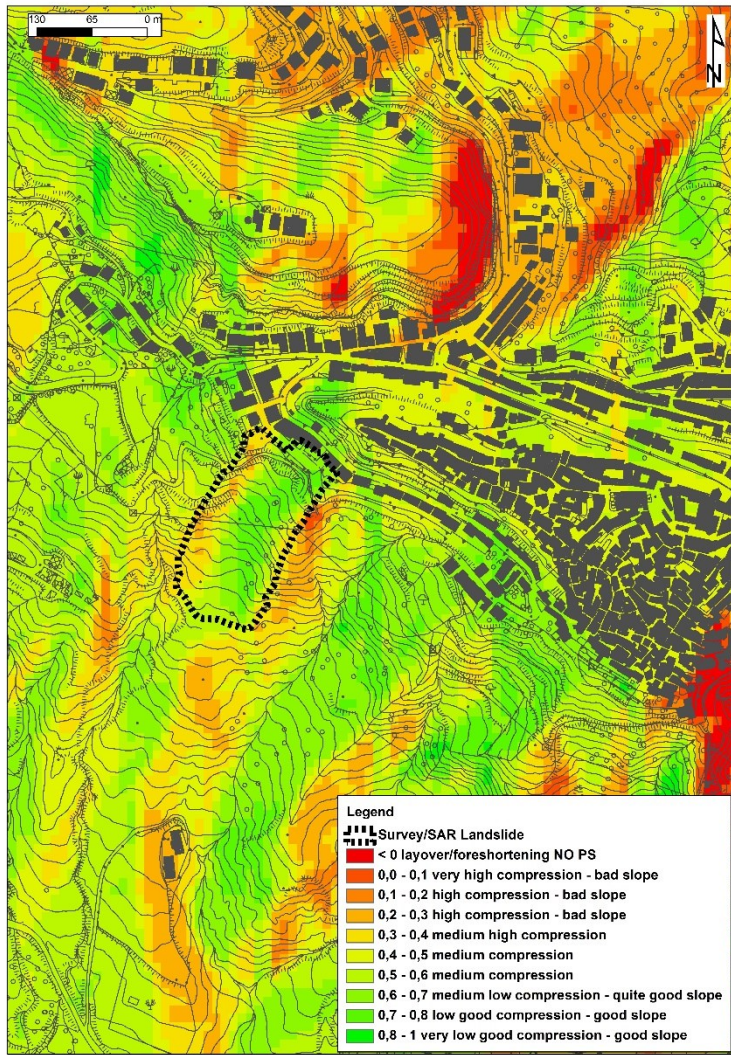


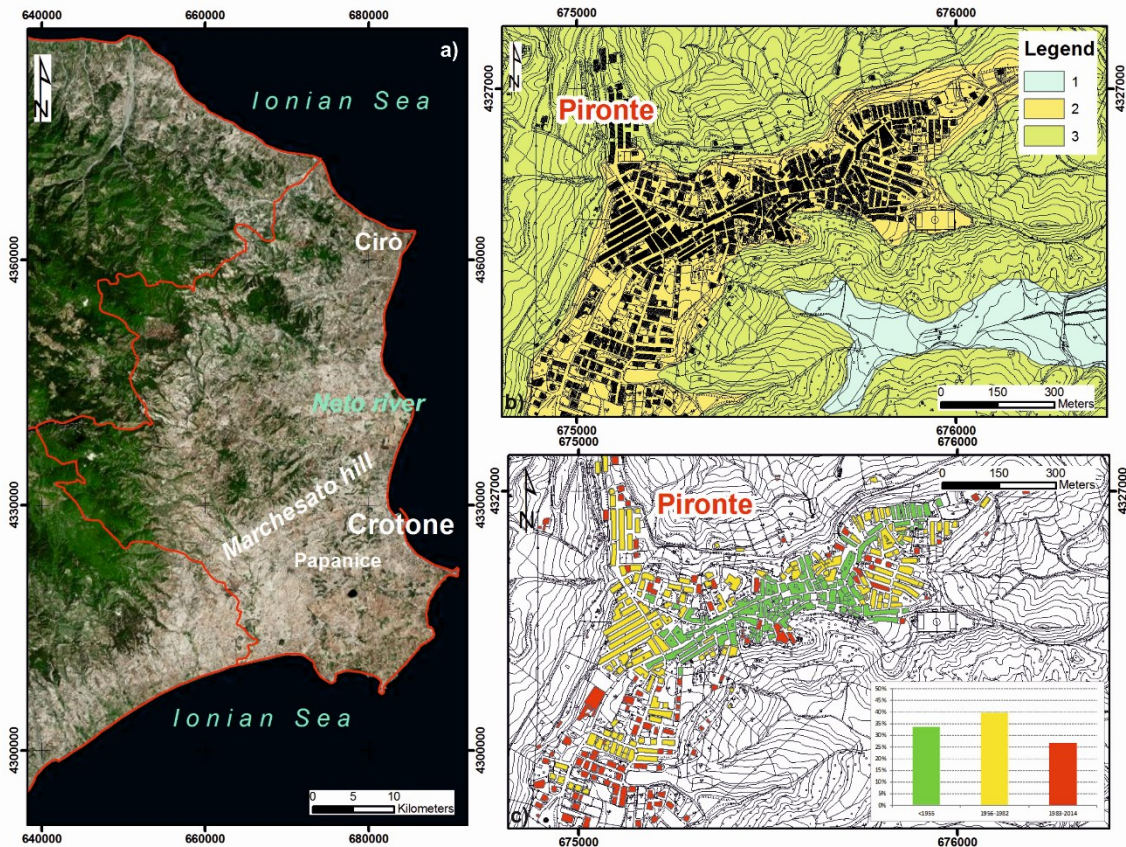
Figure 6.21 R-Index map for the descending dataset.

Through the results obtained in the Cirò test site, and attributable to tools such as the R-Index, the on-site analysis proved to be efficient for the purposes of this PhD project and it has been exported to another test site, the one of Papanice, in order to analyze the movements observed in the pre- and post-failure phase, moreover comparing the DInSAR analysis with conventional instruments.

6.2 Papanice case study

The second case study selected for the implementation of DInSAR methodologies, on which further analyses of the displacements have been done, is Papanice. It is a small settlement of ca. 3500 people, 11 km east of Crotone city center, on the top of the NW-SE trending Marchesato hill (Fig. 6.22 a). Geologically, the Papanice bedrock corresponds to the most recent part of the Crotone Basin, where the Cutro marly clay formation (Middle-Calabrian in age) crops out. Locally such formation can reach a thickness of few hundred meters and it is essentially made of marly and silty clay strata (Massari et al., 2002; Zecchin et al., 2012). A marine terrace formation, the so called S. Anna Synthem, overlies the Cutro marly clay formation and embodies the unit where the Papanice settlement is located. The synthem is composed of sands and conglomerates, at time intercalated with bioclastic limestones (Fig. 6.16 b). No evidence of tectonic and stress deformations have been recognized in the field; however, due to the weak resistance to the erosion and the low permeability of such materials, Papanice succession can be considered very prone to instability phenomena.

The area of investigation, the Pironte district, is, from a geomorphological point of view, a N-S oriented peninsula, and its top, whose upper surface is characterized by a flat area or locally with weak gradient, while the surrounding slopes present a higher inclination. This kind of setting is very prone to gravitational phenomena, especially during strong precipitation events, also responsible for the activation of seasonal streams. Such phenomena can also be retrogressive, thus involving buildings located on the edge of the flat area. As shown in the Landslide Inventory Map of the HSP, the whole settlement is surrounded by landslides (Figure 6.23): Most of them can be classified as areas affected by deep slow deformation, but slide and complex phenomena also occur. In the detail, the Pironte neighborhood is affected by two different landslides, on the slope facing east: A deep slow dormant deformation and a dormant rotational slide (Fig 6.23). The geomorphological setting of the area has been severely modified by the intense sprawl of Papanice, started in the early 60's: The Pironte neighborhood, area of the investigated landslides, was almost inhabited 50 years ago (Figure 6.22 c). About 30% of the whole urban area is dated before 1955, while the major development started in the 1956, and still in recent years (from 1983 onward), an evolution can be recorded, especially in the NW sector, where the Pironte neighborhood is located, and in the SW sector of the settlement. This urban growth also altered the risk scenario, exposing more areas to geohazards. Moreover, the use of landfill terrains, for flattening areas and making them suitable for the construction of buildings, as occurred in Pironte area, changed the local geotechnical setting.



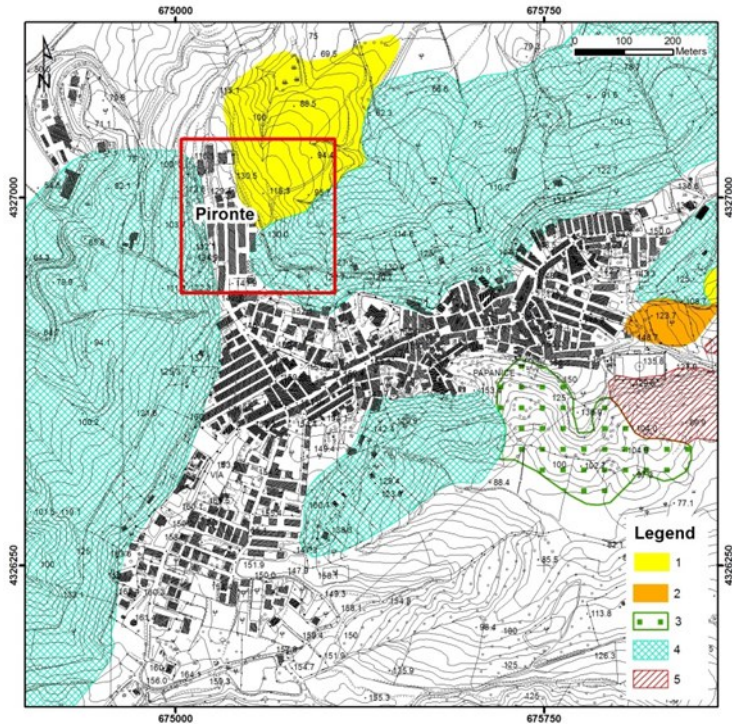


Figure 6.23 HSP Landslide inventory map of Papanice (2006). 1) Slide; 2) Complex landslide; 3) Area affected by shallow slow deformation/movement; 4) Area affected by deep slow deformation/movement; 5) Area affected by deep erosion. The red square marks the area of interest.

6.2.1 Setting of the landslide area

The geological campaign for the acquisition of information about Papanice landslide basically started from chronicle reports and the HSP Landslide Inventory Map redacted by the Calabria Regional Basin Authority. The landslides (totally about 10 hectares large) occurred in the Pironte area (Fig. 6.24 a) can be considered as reactivations of dormant landslides. These landslides' reactivation took place on February 23, 2012, and have been reshaped according to the fall 2013 and summer 2014 field activities, where the landslides present several evidences of displacement, characterized in particular by a retrogressive trend (Fig. 6.24 b). A general instability in the sector and in other slopes surrounding the settlement have been reported in the two years preceding the main event, according to the ARPACAL (Calabrian Regional Agency for the Environmental Protection) (2012). The movement strongly damaged man-made structures located in the urban area: Fractures and tilting of the prominent houses have been documented as well as fractures in the road surface, and the chronicle reported the evacuation of five houses. The landslide involved the most superficial part of the S. Anna Synthem, made of strongly weathered silty clays and also landfills due to human activities.

Within the SW landslide, the clearest evidence of the landslide reactivation is represented by a ca. 140 m long fracture along Via Piave, a road close to the slope (Figure 6.24 c). Longitudinally, also deep evidences are visible till a dirt road just below the last row of houses (Fig. 6.25), while superficial signs have been recognized on the whole slope. This sector of the slope presents more damage and more evidences, while in the northern part, the landslide appears to be less intense. Also damage to the gas and electric network have been observed as well as fences and road signs are inclined downslope (Fig. 6.25).

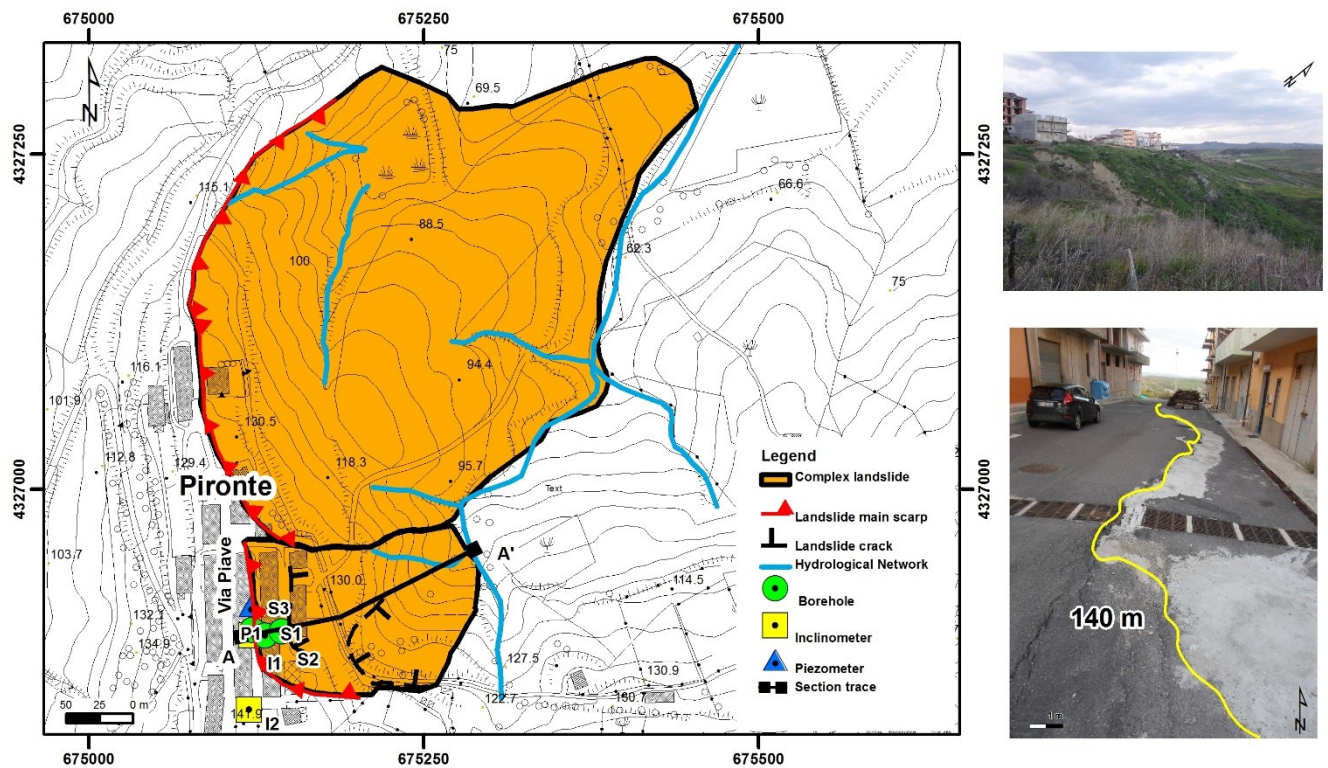


Figure 6.24 a) Field survey landslide inventory map (section A-A' is shown in Figure 6.30); b) Oblique view of the landslide involving Pironte neighborhood; c) Landslide main scarp.

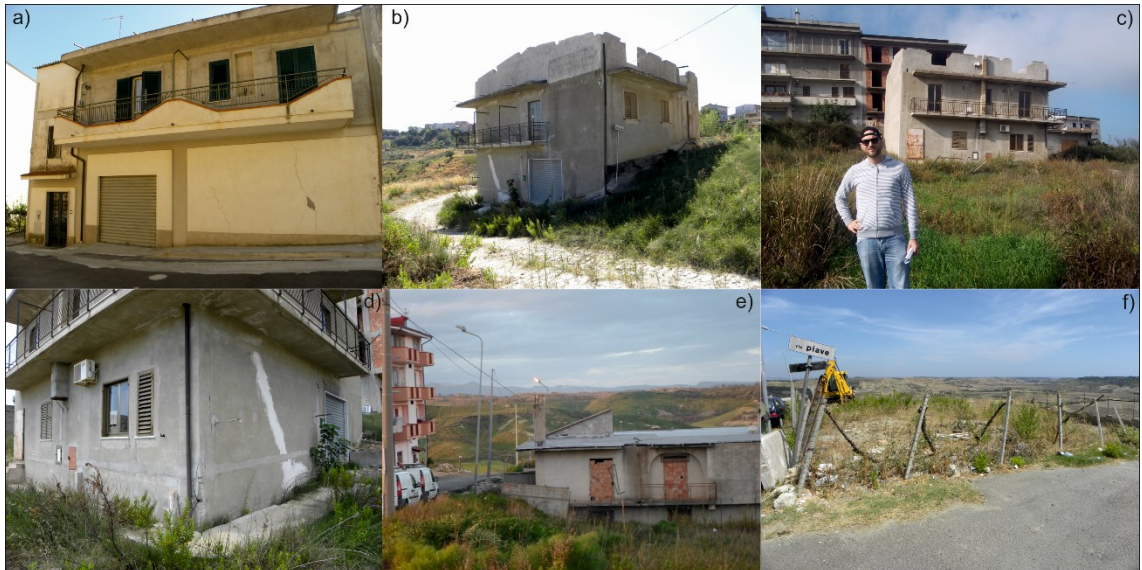


Figure 6.25 Damage reported along the landslide main scarp and within the landslide body. a) fracture on a house located along the main scarp; b), c) and d) damage reported on an abandoned house inside the Southern landslide; e) damage reported on an abandoned house inside the Northern landslide; f) fences and road signs clinched downwards.

6.2.2 Rainfall analysis

Also in this case, rainfall occurred in Papanice before the triggering phase represented a major issue for landslide generation. From February 21 to February 23 2012, an intense and prolonged rainfall event occurred in Calabria Region, with the most significant precipitations being registered on February 22.

Starting from February 21, an intense cloudiness has been observed (Figure 6.26 a), generating a high instability on the Ionian coastline of Calabria with frequent showers and thunderstorms. 126 mm have been registered in the rain gauge of Santa Cristina d'Aspromonte at the 00:00 of February 21. On February 22, rainfalls on the Ionian sector of Calabria intensified (Figure 6.26 b): They first hit the SE Ionian Coast and then the Crotone area. On February 23 the phenomenon became less concentrated (Figure 6.26 c), characterized by a reduction of the rainfalls on the Ionian area, with still diffuse but less intense rain.

The availability of a widespread network (252 rain gauges), set up by the Multi-hazard Functional Center of the ARPACAL (Figure 6.27), covering the whole regional territory, it has been possible to rebuild the spatial distribution of the precipitations. In many areas along the

Ionian coast and in the inner part of the region, the precipitations exceeded 200 mm.

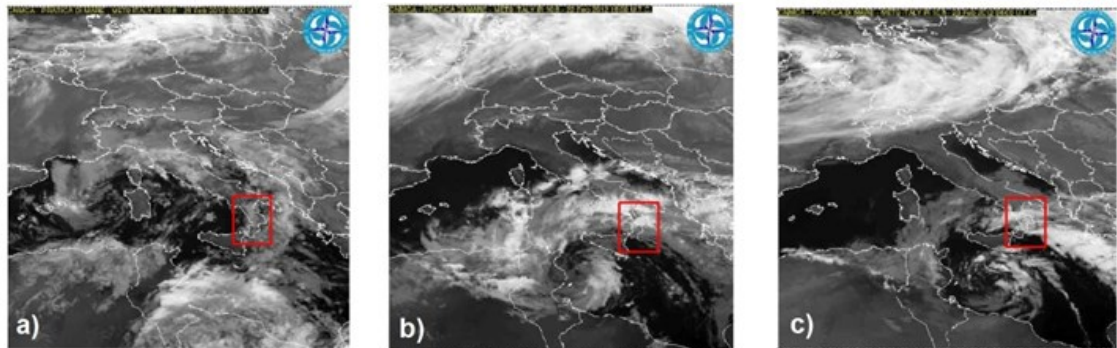


Figure 6.26 Second Generation InfraRed 10.8 Meteosat image (Italian Air Force Meteorological service): a) at the 21/02/2012, h. 18.00 ; b) 22/02/12 h. 18.00 ; c) 23/02/12 h. 06.00.

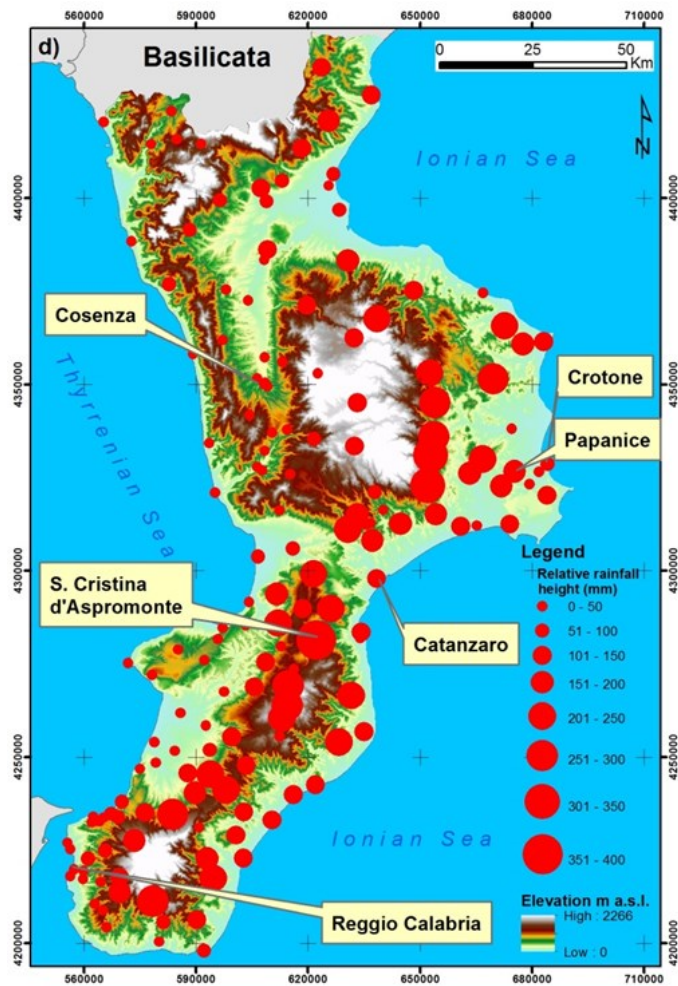


Figure 6.27 Localization of the measurement stations of the Multi-hazard Functional Center of the ARPACAL and relative rainfall heights for the period 21-23 February 2012.

In detail, regarding the Papanice area, rainfall data have been collected from the rain gauge Crotone - Papanice (Figure 6.28 a), located at a distance of 200 m from the landslide area. The cumulated rainfall of 2012 (640 mm), of February 2012 (281 mm) and the 19-25 February 2012 weekly rainfalls (185 mm) have been plotted (Figures 6.28 b, c and d). It is worth to point out that, from an analysis of the precipitation occurred in the last 10 years, an increase has been registered in the two years preceding the main landslide event (2009-2011), recording in this case an annual average of 1001.7 mm, while the average annual value of Papanice, recorded between 1997 and 2009 is of about 652 mm. To this regard, the February 2012 precipitations are equal to 45% (281 mm of 640 mm) of the annual rainfall occurred while the pre-event rainfall (21-23 of February 2012) corresponds to 28% of the 2012 annual amount (180 mm of 640 mm), surely representing the most important triggering factors for the reactivation of the landslide.

Taking into account the work of Vennari et al. (2014), which deals with the rainfall thresholds for shallow landslide occurrence in Calabria, the pre-event rainfall has been plotted on the duration versus the cumulated rainfall graph (Figure 6.29): The Papanice measurements perfectly match with the results obtained in the cited work.

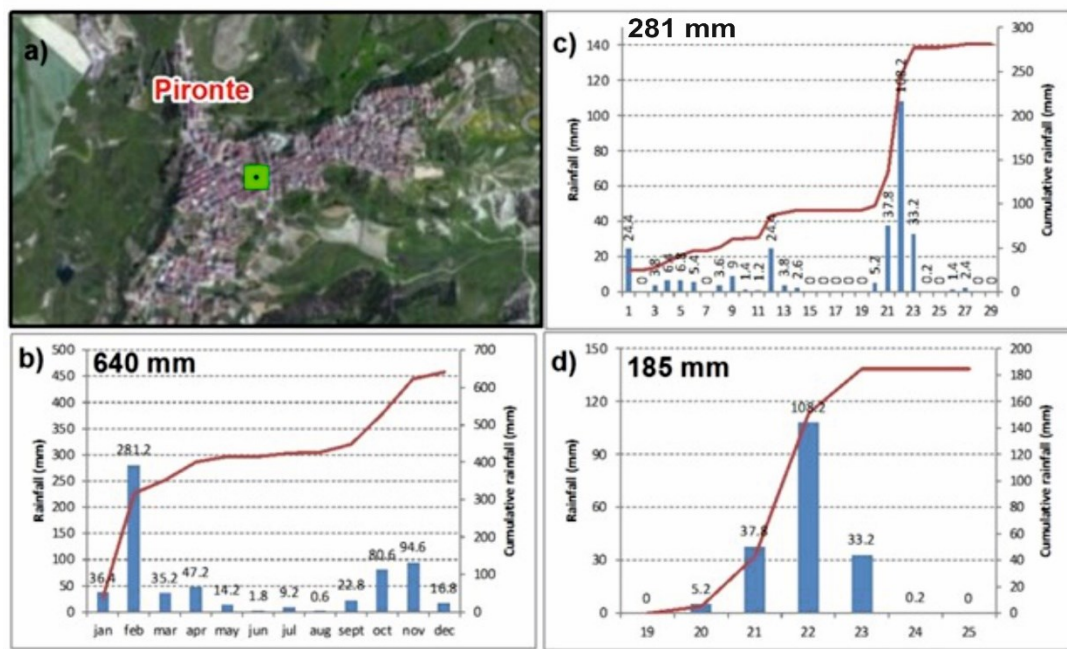


Figure 6.28 a) Localization of Papanice rain gauge. b) Rainfall diagram for the year 2012, in blue columns daily values, in red cumulative values; c) Rainfall diagram for February 2012; d) Rainfall diagram for the week 19-25 February 2012.

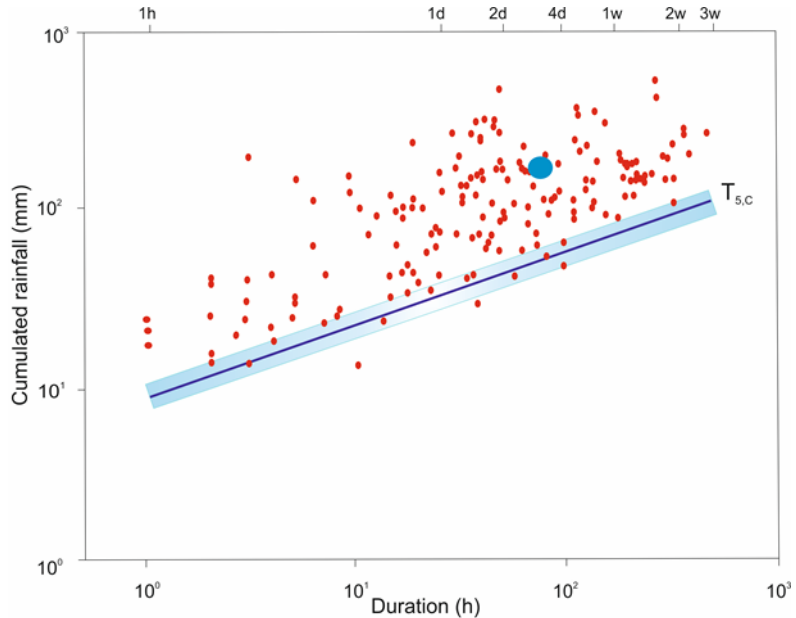


Figure 6.29 Rainfall duration vs. cumulated event rainfall, conditions which resulted in shallow landslides in Calabria (red dots), and related threshold at the 5% exceedance probability level. The blue line shows the threshold in linear coordinates. Shaded areas show uncertainties associated with the threshold. In blue dot the Papanice landslide. Modified from Vennari et al. (2014).

6.2.3 Instrumental campaign

In order to investigate the landslide's evolution and to protect the buildings located outside the landslide area, ARPACAL set up a monitoring campaign in the immediate aftermath of the triggering phase occurred on the 23 February 2012. It initially consisted in 6 boreholes (Fig. 6.24 a), all located along the crest of the landslide, useful to recreate a geological and geotechnical profile of the landslide. The stratigraphy of the slope has been reconstructed on the base of these investigations. Different lithological units have been defined, whose main parameters are here reported (Fig. 6.30):

- Lithotechnic unit 0: Chaotic material of the units 1 2 3;
- Lithotechnic unit 1: Mostly sandy and silty landfill; average geo-mechanical parameters: $\gamma=17-17.5 \text{ kN/m}^3$, $c=0.00 \text{ kPa}$, $\phi=27-30^\circ$;
- Lithotechnic unit 2: Alternation of silty-clay sands, clay-sandy silts and sandy-clay silts, avano-coloured (S. Anna synthem); average geo-mechanical parameters: $\gamma=19.8-20 \text{ kN/m}^3$, $c_u=0.00-83.36 \text{ Kg/cm}^2$, $c=3.92-13.72 \text{ kPa}$, $\phi=26-30^\circ$;

- Lithotechnic unit 3: Silty clay cover with locally grey bands (weathered soil of the Cutro marly clay formation); average geo-mechanical parameters: $\gamma=19.8\text{--}20 \text{ kN/m}^3$, $c_u=66.68\text{--}88.26 \text{ kPa}$, $c=12.75\text{--}18.63 \text{ kPa}$, $\varphi=22\text{--}25^\circ$;
- Lithotechnic unit 4: Marly silty clayey sedimentary substrate, grey-blue-coloured (Cutro marly clay formation); average geo-mechanical parameters: $\gamma=20\text{--}20.2 \text{ kN/m}^3$, $c_u=107.87\text{--}176.52 \text{ kPa}$, $c=17.65\text{--}27.46 \text{ kPa}$, $\varphi=26\text{--}27^\circ$;

Where, γ is the volume unit weight, c_u the undrained cohesion, c the cohesion and φ the friction angle.

The boreholes have been successively equipped with two inclinometer chains and one piezometer. Inclinometer data have been acquired every 14 days, during the time span 1 January 2013 - 14 April 2015. They show a maximum displacement at the shallowest level (-8 m for I1 and 11 m for I2) of about 2 mm in the above-mentioned timespan, thus demonstrating that the area behind the landslide is not yet affected by considerable deformation phenomena (Fig. 6.31 a).

Piezometer P1 (Fig. 6.31 b) is also located in proximity of the landslide and the data available are referred to daily measurements from 1 January 2013 to the 15 April 2015.

The comparison between piezometric readings and rainfall data, for the same time span, shows a good agreement. During dry and rainy periods, give decreases and increase, respectively. In particular, after the middle part of November 2013 a sudden uplift of the piezometric level has been registered, of about 1.2 m (from 1.4 to 0.2 m from the ground level) attesting at a very shallow depth, most likely due to leaking of urban pipes, as reported by a first survey of ARPACAL. After the resolution of such event, the groundwater table kept persistent at a very shallow level (between 0.2 and 0.4 m from the ground level), also considering the high precipitations registered (up to 115 mm in the 1st of December 2013), showing slight oscillations only according to the rains occurred, and it started to decrease as soon as the dry season started (e.g. cumulative rainfall of 51 mm during June and July 2014). In the final part of the time span analyzed, the piezometric levels show large fluctuations, between 0.4 and 1.1 m from the ground level, also here showing a correspondence with rains occurred.

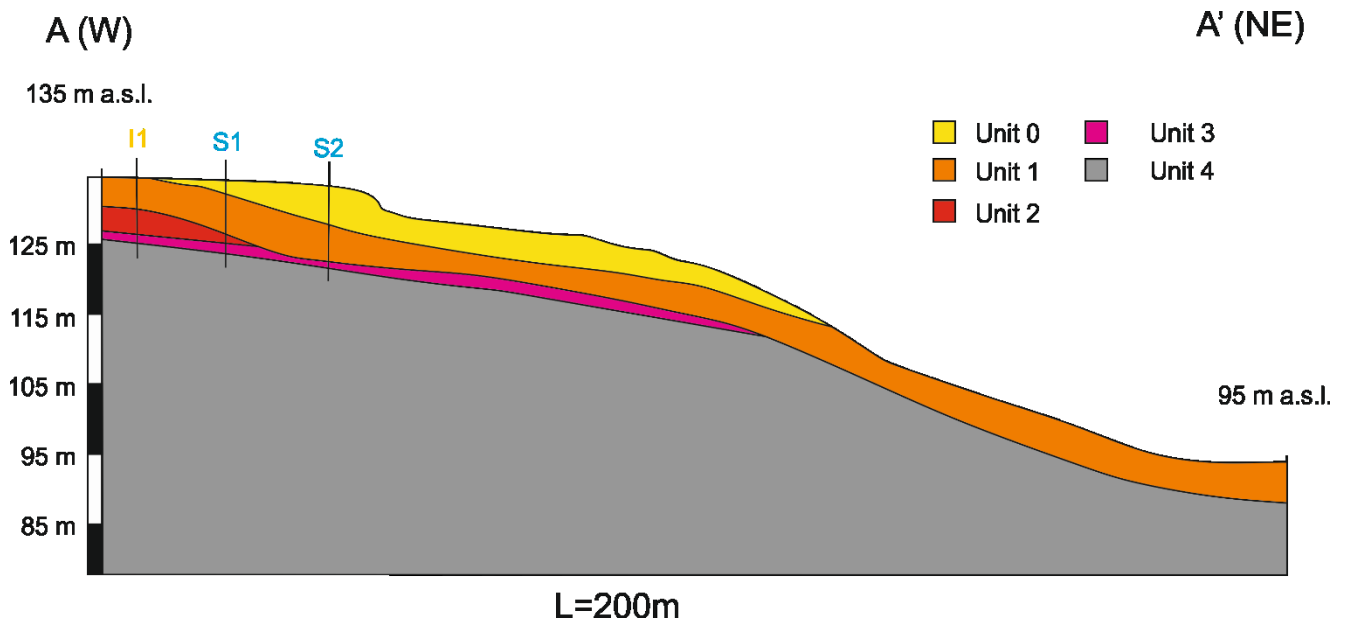


Figure 6.30 Geolithological section A-A'. The location of the section is shown in Figure 6.24. I1 is the inclinometer installed in the landslide area, S1 and S2 are the two boreholes.

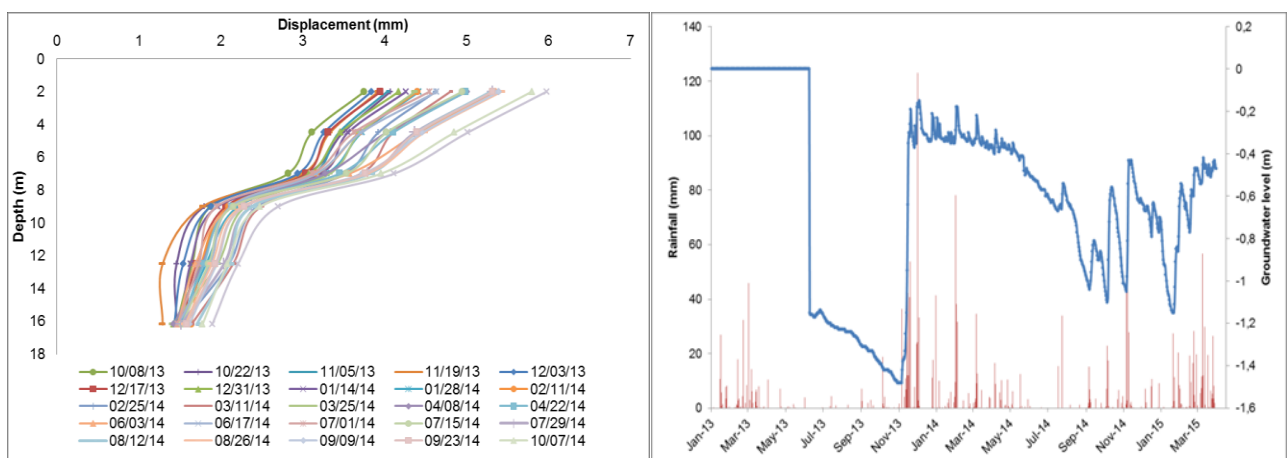


Figure 6.31 a) Inclinometric data of the inclinometer I1; b) Comparison between piezometric data from piezometer S1 (blue line) and daily rainfall from Papanice rain gauge (red).

6.2.4 2008-2010 DInSAR analysis

The analysis of the displacements occurred in Papanice area in the pre-failure phase has been carried out based on a stack of 66 and 67 TerraSAR-X StripMap Single Look Complex images, for the ascending and the descending stack, respectively, acquired in the time interval between April 2008 and June 2010. A DEM, obtained from the Regional Topographical Map (scale 1:5000) has been exploited for removing the topographic component of the interferometric phase, and finally, a crop of 2×1.5 km has been selected to define the area of interest.

For Papanice case study, the R-Index has been applied a-priori, in order to assess the quality of the pixels in the area of interest and to select the most effective stack to process. The R-Index computation for the descending dataset (Fig. 6.32) pointed out that the landslide area clearly corresponds to a non-detectable area for the DInSAR analysis, being in foreshortening, while for the ascending dataset (Fig. 6.32) shows a good quality of the pixels, making this stack good suited for the investigation. Based on these elaboration, both the SUBSOFT processor and the SARscape software have been successfully applied only on the ascending dataset.

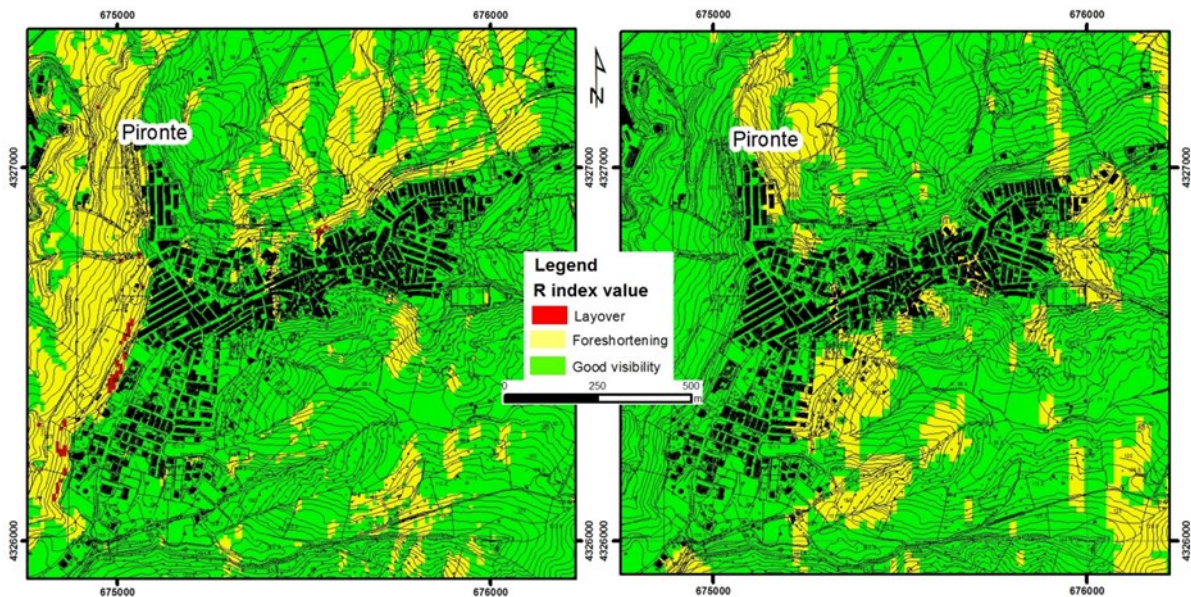


Figure 6.32 R-Index computation for ascending (left side) and descending (right side) orbits. Red colors show the layover areas (R-Index value < 0), Yellow areas show foreshortening (R-Index next to 0), Green areas mark a good visibility (R-Index > 0.4).

6.2.4.1 SUBSOFT processing

The SUBSOFT analysis has been carried out exploiting the TSC pixel selection method (cf. 4.2.8.3). A threshold of TSC equal to 0.7, which corresponds to a phase standard deviation of about 20° , has been set on 63 images selected (3 have been discarded to improve the accuracy of the results) (Fig. 6.33).

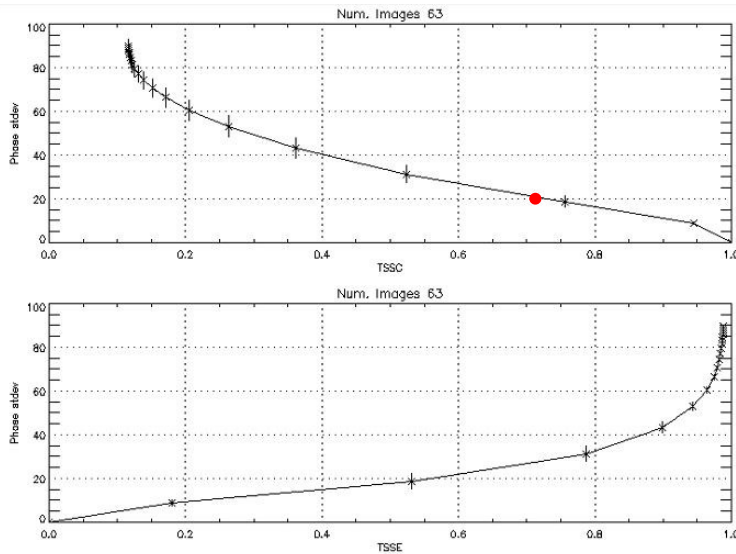


Figure 6.33 Phase standard deviation vs. TSC plot on the top; Phase standard deviation vs. TSE (Temporal subblock entropy) plot on the bottom. The red point indicates the TSC threshold selected.

The final pixel selection perfectly fits the Papanice urban area, and it consists of about 9000 points, whereas about one hundred are related to the displacement, located onto the top of the Via Piave landslide (Fig. 6.34). The average velocity of the displacement is -27.7 mm/yr, while the maximum rates of the displacement are located in the left sector of the Via Piave landslide (-36.0 and -35.6 mm/yr), other high rates can be found in correspondence of the main scarp of the landslide. Lower values of movement can be found in the right sector and down the valley of the slope of interest, with minimum rate of 14.8 mm/yr (Fig. 6.35) (Confuorto et al., 2015). All the values mentioned are calculated with respect to the Line of Sight (LOS).



Figure 6.34 Final pixel selection with the TSC method.

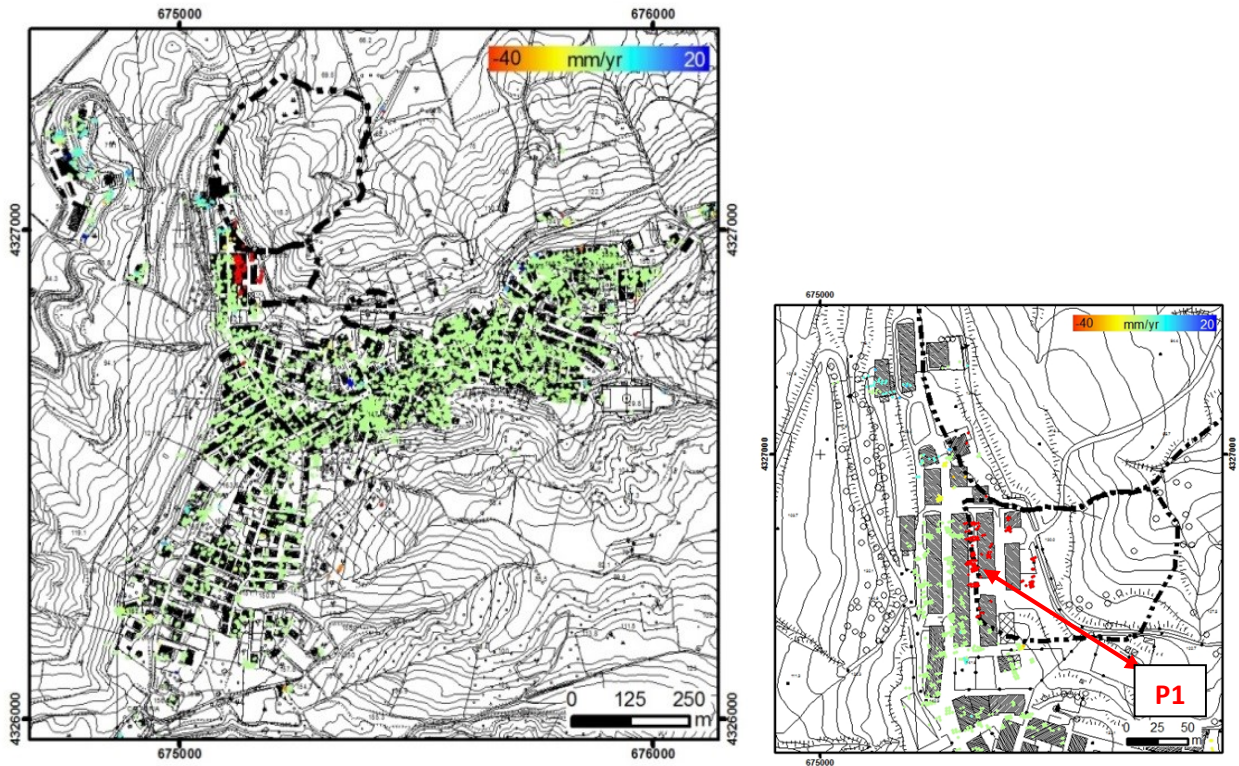


Figure 6.35 Displacement rate map obtained with the TSC application for the time interval 2008-2010. On the left, the whole Papanice settlement, on the right, zoom-in of the Via Piave landslide. The dashed-dotted lines represent the landslides after the geological and geomorphological survey.

6.2.4.2 SARscape processing

The two algorithms implemented on the SARscape software, PSInSAR and SBAS, have been either applied on Papanice case study.

PSInSAR has been carried out following the procedure previously implemented on Cirò case, so splitting the stack in two periods and introducing a spatial baseline of ± 100 m. For both of them, a product coherence threshold of 0.6 was selected, as the accuracy of PSI increases with increasing coherence. The first period of investigation has been evaluated on 29 images. In this case a total amount of 1393 points has been obtained, 7 of which show a displacement rate ascribable to the landslide. In particular the cluster of points, individuated by the PSI analysis, is located in the top left sector and in the middle part of the landslide; the average value of these points is of -25.4 mm/yr. The highest displacement rates are all positioned into the top left sector of the Via Piave landslide, with a maximum value of -32.1 mm/yr (Fig. 6.36). The second period is composed of 27 images. The sum of the PSs recognized is of 1543, but just one is ascribable to the main phenomenon. This point, located at the top left part of the main landslide, close to the main scarp, presents a displacement rate of -32.1 mm/yr (Fig. 6.37). Also in these cases, the displacement values are referred along the LOS.

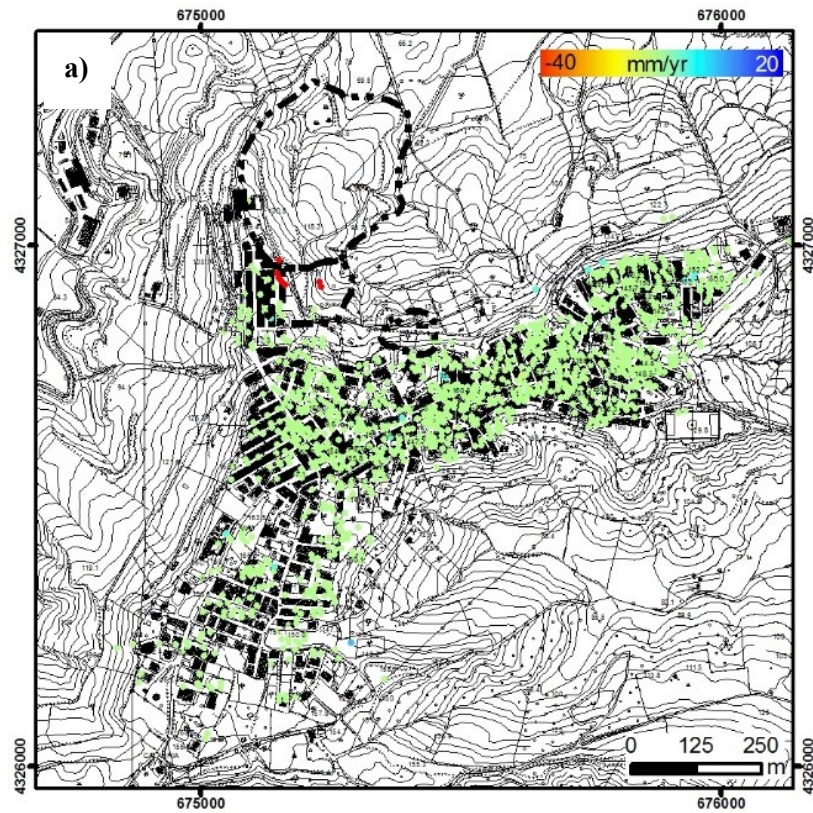


Figure 6.36 Displacement rate map obtained through the PSInSAR application to the 1st period of analysis.

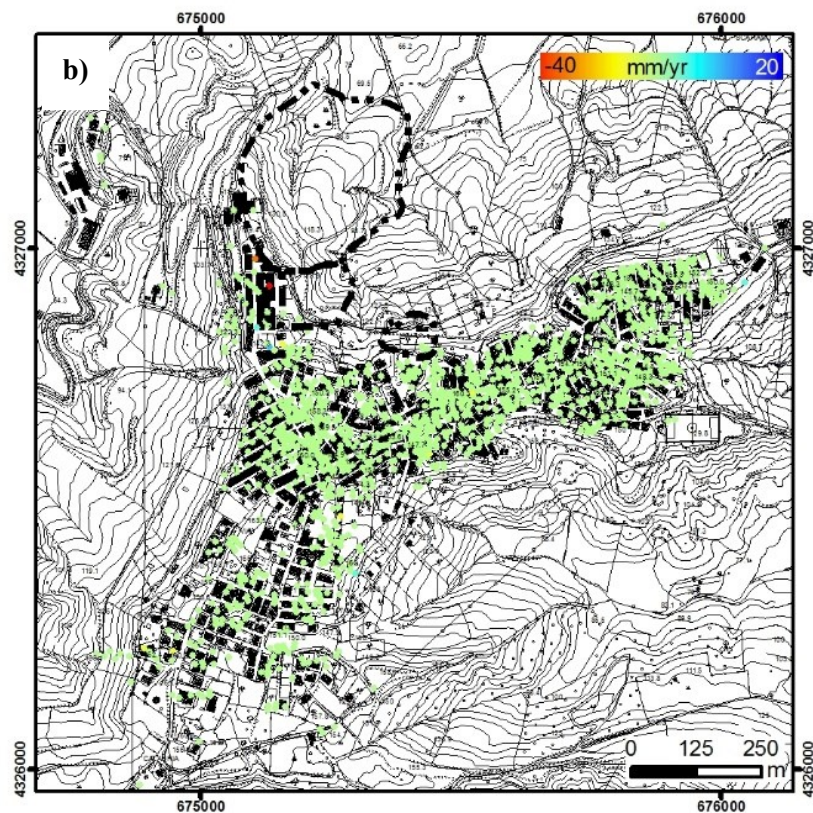


Figure 6.37 Displacement rate map obtained through the PSInSAR application to the 2nd period of analysis.

The SBAS processing has been carried out on the whole ascending stack, made of 66 images, and, as for Cirò case, the parameters shown in Table 6.2 have been chosen.

Table 6.2 Main parameters for the SBAS application on Papanice case study.

Temporal Baseline	100 days
Spatial Baseline	2.5% max. critical baseline (about 100 m)
Coherence Threshold	0.6
Multilooking Factor	5x4

The implementation of the SBAS allowed to detect 4545 CPs (Fig. 6.38), spread on the whole inhabited area (except for the northern tip of Pironte district). The 2012 landslide is clearly recognizable: 18 points, located along the scarp of the landslide individuated by the ground survey, shows displacement rates up to 20 mm/yr. The highest velocities are localized in the central part of the movement, lower velocities can be found in the SE sector. In this case SBAS indicates displacement rates lower than the ones detected by the other techniques.

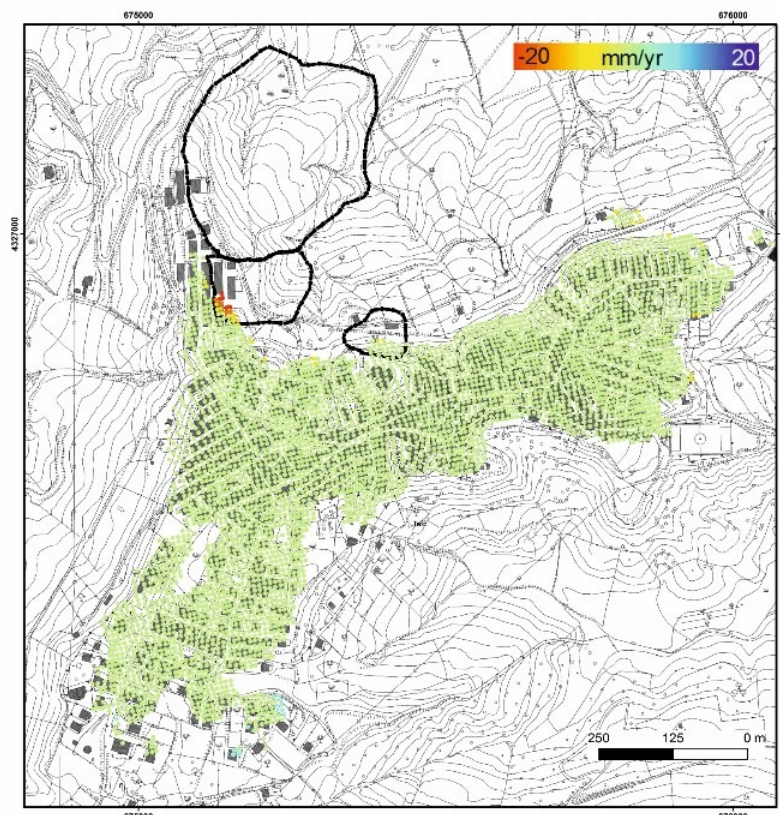


Figure 6.38 Displacement rate map obtained with the SBAS method for the time interval 2008-2010.

6.2.5 Summary of the 2008-2010 Papanice results

From the comparison between the various results obtained with the techniques adopted it is possible to affirm that, in every case, the landslide occurred on 23 February 2012 has been clearly recognized by MTI procedure, testified by the concentration of points located on the main scarp of the landslide. From an accurate analysis of the displacement rates derived from the three methods, a concentration of points characterized by the highest values of movement has been recognized in the top left sector of the landslide of Via Piave. This fact can be attributed to geomorphological factors: Usually the movements are faster in correspondence of the main scarp, and in this case, also the presence of a seasonal stream can have had a role. Moreover, following these results, it is also possible to update the landslide inventory map of Papanice, redacted in the 2006 HSP by the Calabria Basin Authority. First of all, the landslides were considered as dormant, while, from a joint application of field surveys and remote sensing, they are clearly updatable as active. Besides, also a retrogressive trend has been recognized, as proved by the actual landslide scarp, now located at Via Piave. As for Cirò, the time series of the displacement show a good connection with the rainfalls data, in fact accelerations of the movement are subsequent to abundant precipitations, as well as decelerations to dry periods. In Figure 6.39 the comparison between the time series of the point P1, selected with the CPT technique, and the 15-days cumulated rainfall, in the same time interval is shown. An acceleration of the movement can be noticed starting from January 2009, in occurrence of a cumulated rainfall increase, as well as the time series slows down when the precipitations are less abundant (April 2009) (Fig. 6.39) (Confuorto et al., 2015). The same behavior can be recognized also in the Fall 2009 - Spring 2010, confirming the strong relationship between rainfalls and slow and intermittent landslides.

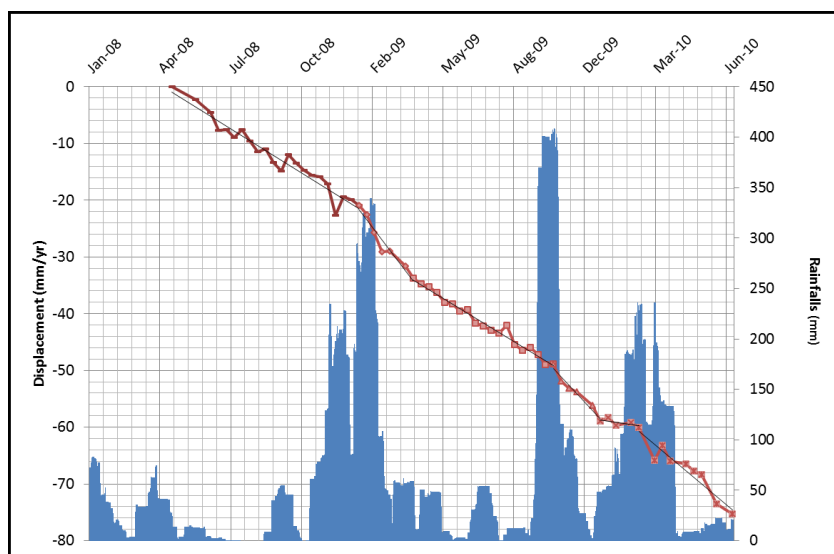


Figure 6.39 Comparison between time series of the displacement and the 15-days cumulated rainfall.

As regards the comparison between the software applied for this case study, many similarities, but also some differences, have been recognized, especially between PSInSAR and CPT: The range of the velocities (Fig. 6.40) and the location of the pixels showing displacement proved to be the same for both the two procedures adopted, while the SBAS tends to underestimate the velocities. However, the final results of the application of SUBSOFT showed a higher number of targets, with respect to the SARscape application (9000 to 1500 for PSInSAR and 4500 for SBAS) (Confuorto et al., 2015). Moreover, also a higher number of points located in the displacement area enables detailed analysis of surface movements. Furthermore, as regards the SARscape results, they showed a shift of the PSs of about 150 m westward, hence necessitating a correction through the individuation of ground control points, while the geocoding of the SUBSOFT software turned out to be correctly georeferenced, without any shift.

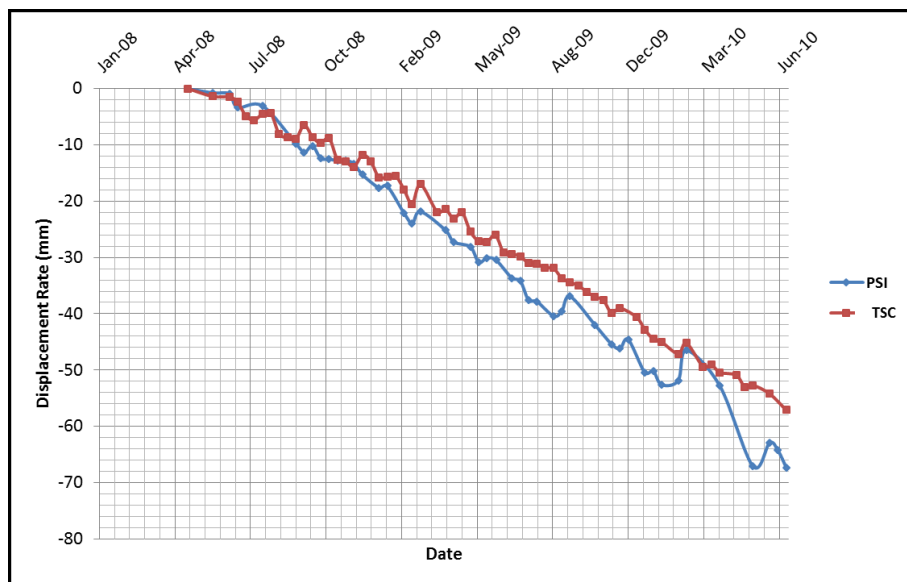


Figure 6.40 Comparison between time series of displacement obtained with PSI and CPT (TSC pixel selection method).

6.2.6 2013-2014 DInSAR results

DInSAR analysis of the Papanice landslide has been carried out also with the availability of TerraSAR-X covering the time span 2013-2014. These images cover the time interval between October 2013 and October 2014, with 34 and 39 SLC images, respectively along ascending and descending pass. As for the previous dataset (2008-2010), also in this case due to the R-Index elaboration, only the ascending stack has been processed on the two aforementioned software. The idea is, in this case, to analyze the displacement occurring in the post-failure phase, on a large scale, with the application of the SBAS algorithm, more suitable for analyses at a less detailed scale and on a regional context (Mora et al., 2003)

6.2.6.1 SARscape processing

The SARscape software has been here tested with the SBAS technique, for the assessment of the post-failure phase. Also in this case, according to the standard procedure, two values of temporal and spatial baseline have been selected, respectively 100 days and 2.5% of the critical spatial baseline (as shown in Table 6.3), which allowed to select 143 interferograms for the final estimation.

Table 6.3 Main parameters for the SBAS application on Papanice case study.

Temporal Baseline	100 days
Spatial Baseline	2.5% max. critical baseline (about 100 m)
Coherence Threshold	0.6
Multilooking Factor	5x4

More than 4000 points have been then recognized (Fig. 6.41), showing two different concentrations of points characterized by displacement: On the NW sector 12 points can be referred to the landslide, located within the border and in correspondence of the scarp of the main landslide documented during the field activities, with an average velocity of -4.5 mm/yr. Moreover, it is possible to identify another cluster located in the SE part, with an average displacement rate of -4.8 mm/yr and maximum value of -8.3 mm/yr. All values are considered respect to the LOS.

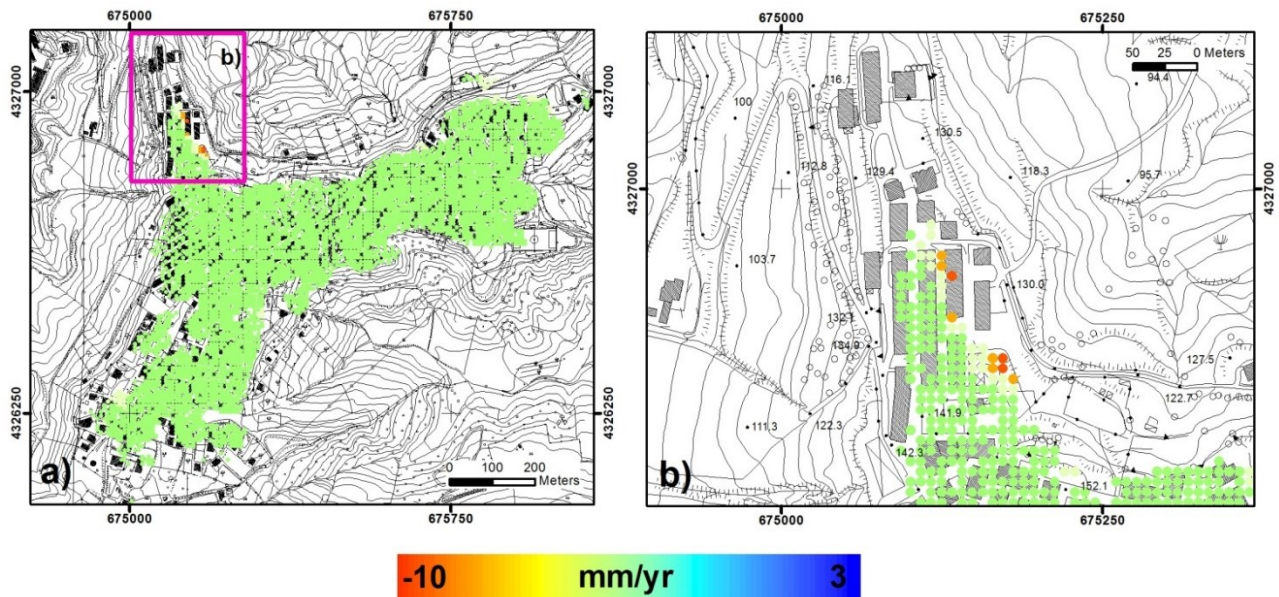


Figure 6.41 a) Displacement rate map obtained through the SBAS application for the time interval 2013-2014. In purple rectangle, a zoom in of the area of interest (b).

6.2.6.2 SUBSOFT processing

In order to verify the reliability of these results, thus to comprehend if the movement is effectively slowing down in the post-failure phase, or if SBAS tends to underestimate the velocities, as also occurred in the pre-failure investigation, also CPT, with the above-mentioned TSC criteria for the pixel selection, has been once again used, in this case, on a final selection of 34 images (Fig. 6.42). For the final pixel selection, a threshold of 0.7 has been set, as previously selected, resulting in more than 14000 targets. According to this elaboration, the landslide seems to confirm the pre-failure high velocities, showing cluster of points characterized by relatively high displacement rates, both in the NW sector, already classified as the fastest sector of the landslide in the previous period, and in the Southern one, where beforehand no displacement was identified. In this period the movement rates are higher, with an average displacement in the NW sector of -40 mm/yr, in the central sector the movements show rates of about -35 mm/yr as well, while in the SE sector mean values of -5.8 mm/yr are detectable.

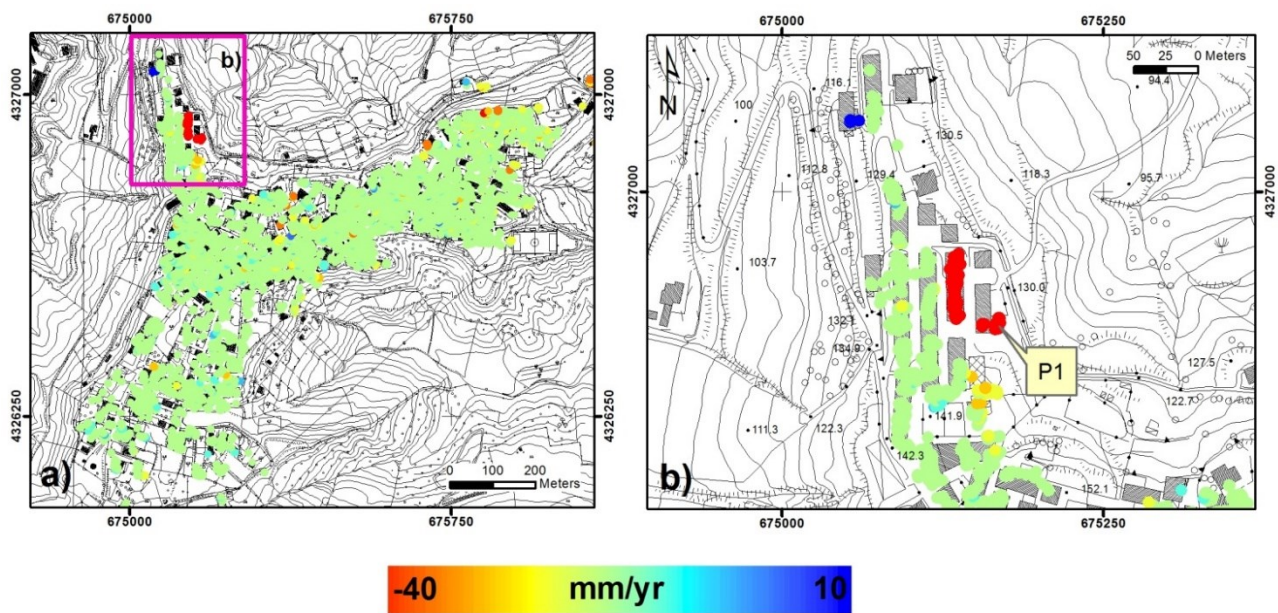


Figure 6.42 a) Displacement rate map obtained with the CPT-TSC method for the time interval 2013-2014. In purple rectangle, a zoom in of the area of interest (b).

6.2.7 Slope stability analysis

As mentioned in paragraph 6.2.1.3, the rise and the very shallow depth of the piezometric level during the time span considered can represent an important instability factor. In this case a depth of 0.2 m from the ground surface can represent the trigger of the movement occurred in December 2013, as testified by the time series considered. Starting from this assumption, a slope analysis on the

area involved by the gravitational phenomenon has been carried out, considering the water table level at a superficial depth, in order to find out which are the most significant parameters that brought this slope to instability. Such analysis has been carried out through Slope®, a software by GEOSTRU, which exploits the limit equilibrium method. The final aim is to obtain the Safety Factor (SF) of a slope, referring to a theoretical model based on the slope stratigraphy and evaluating the global stability through the relationship between maximum shear strength and the stresses acting on the slope surface:

$$SF = \frac{T_{max}}{T_{mob}} \quad (1)$$

with T_{max} representing the maximum shear strength available and T_{mob} being equal to the shear stress mobilized.

The limit equilibrium condition is achieved when $T_{max} = T_{mob}$, hence when $SF = 1$. Consequently, a slope can be considered stable when $SF > 1$ as well as unstable when $SF < 1$. Such analysis takes into account a representative section of the slope, as shown in Figure 6.24 a. In detail, two different periods have been considered: a) configuration of the slope before the trigger of the movement in 2012, obtained from the Regional Technical Cartography; b) configuration of the slope after the 2012 landslide, obtained by topographic survey done after the event by ARPACAL, in November 2012. Comparing the two profiles, it is possible to note how the morphology of the slope is substantially unchanged, even considering the landslide event (Fig. 6.43).

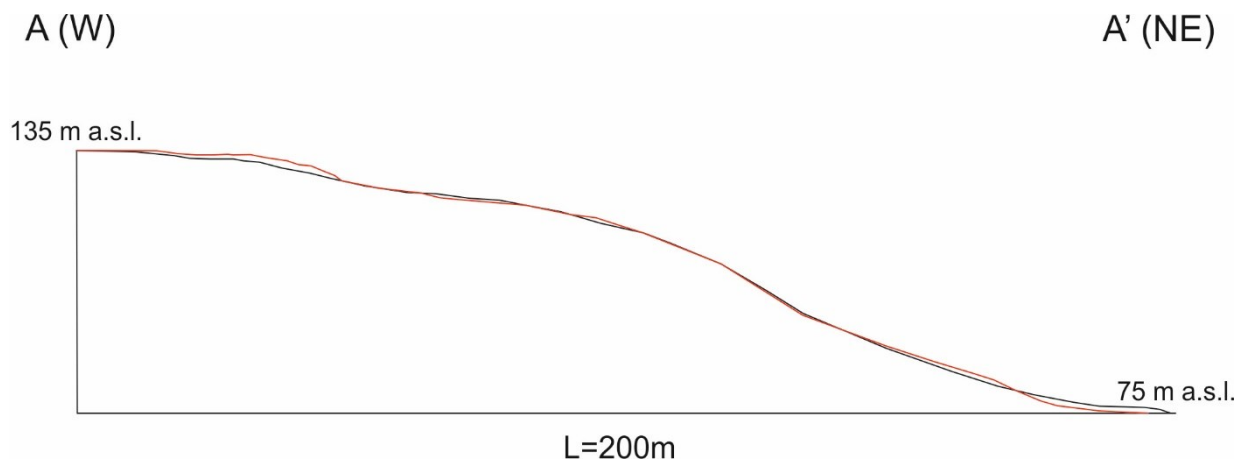


Figure 6.43 Profiles of the slope of analysis: a) pre-event configuration (red line), b) post-event configuration (black line). The location of the section is shown in Figure 6.24.

Water table in the pre-event condition has been considered at – 0.3 m from the ground level and continuous for all the profile. Such hypothesis has been considered according to the rainfall and piezometric data. A confirm to this last assumption is also represented by the comparison between time series derived from the DInSAR elaboration, and the piezometer P1 (Fig. 6.46), where it is

clearly noticeable the activation of the displacement in correspondence of the rise of the water table level, up to - 0.3 m from the ground level. Regarding the strength parameters, the chosen values are the residual ones and gained through a back-analysis procedure, varying, on the pre-event configuration the friction angle value, until reaching the value of strength mobilized. The stability analysis has been performed according to the Janbu method (Janbu, 1954). Thereby, the landslide body is divided into single elements, for each of which the equilibrium between forces and strength is calculated, obtaining, as a final result, the global SF. In order to characterize the soils, a simple constitutive model is adapted, based on Mohr-Coulomb theory (1954) entering the values of volume unit weight, cohesion and friction angle.

First, a back analysis based on the pre-event profile has been carried out, to determine the slope's condition at the 2012 activation. Three different slip surfaces have been hypothesized (Fig. 6.44), whose parameters of residual strength have been obtained. Since no information about the slip surface was available, a depth of about 8 m has been assumed, with the edge in proximity of Via Piave, according to cracks and fractures in the roadway, observed during the field survey and according to inclinometer data. Analyses were carried out changing the value of the residual friction angle of the units involved by the landslide, while all the other parameters were kept unchanged. Through an iterative procedure, the limit equilibrium, equal to $SF=1$, is reached when $\varphi'_0 = 17^\circ$, which represents the shear strength of the mobilized units along the specific slip surface.

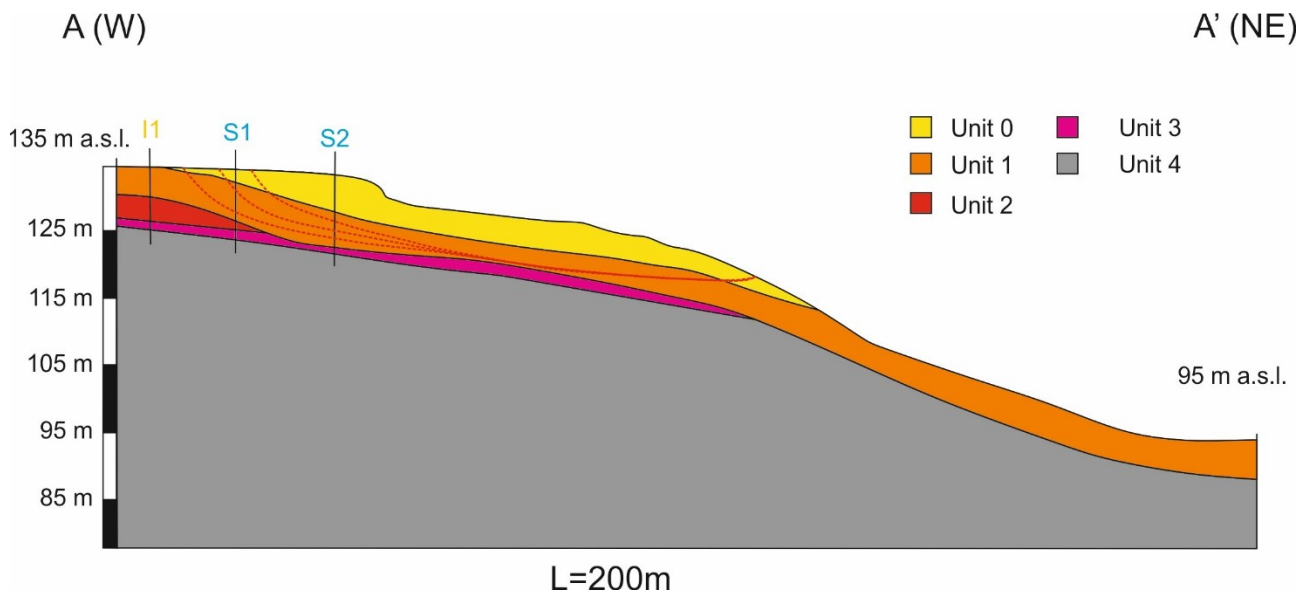


Figure 6.44 Simulation with the back-analysis, in red line the three hypothetical slip surfaces are represented.

Once got this value, the next step is to verify the condition in post-event configuration, starting from the same residual friction angle $\varphi'_0 = 17^\circ$. A similar stability analysis has been carried on the post-event configuration (Fig. 6.45).

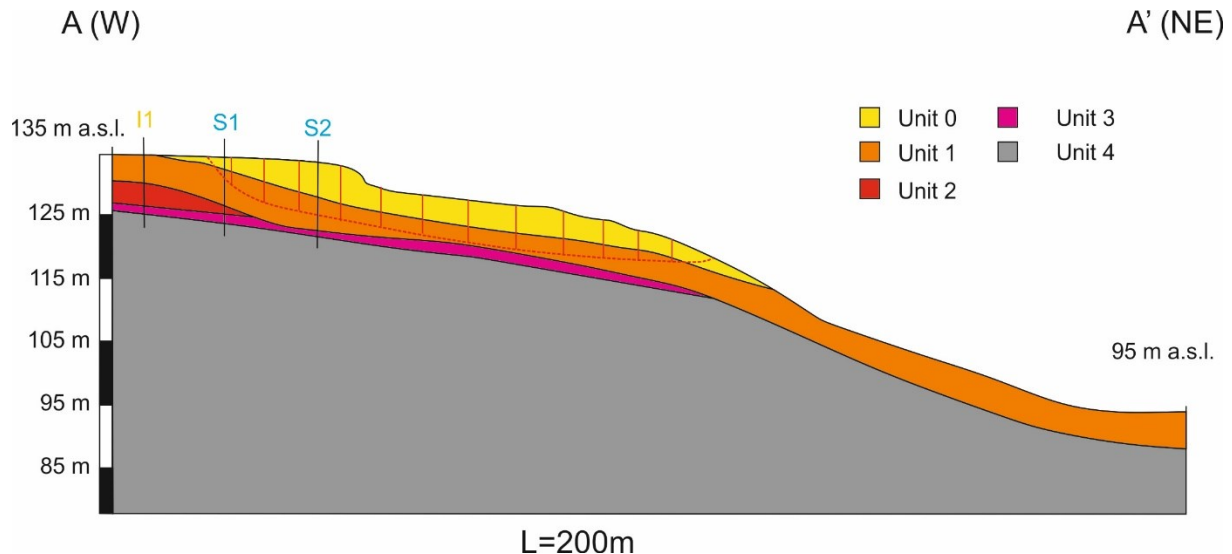


Figure 6.45 Stability analysis on the post-event profile.

The surface highlighted in Figure 6.45, obtained by this procedure, very similar to the one presumed for the pre-event phase, assumes a value of $SF = 0.97$ when the water table lies at -0.3 m from the ground level, thus posing a critical issue in the slope. Moreover, also according to MTI analyses, the area appears to be still moving, even after the triggering phase. As a consequence of these results, in order to increase the SF and to guarantee the maximum stability of the slope, a possible solution could be to operate on the water table level. A suggestion could be the implementation of drainage trenches along the whole landslide body, trying to decrease the groundwater level until at least about 0.8 m below the surface. In such condition, the SF results to be equal to 1.07, therefore obtaining the stability of the slope. Time series analysis confirms that the stability of the slope is obtained through the lowering of the water table level: A slowdown of the movement can be noticed when the groundwater level reaches -0.8 m from the ground level (Fig. 6.46), thus validating the connection between groundwater and triggering of slow-moving landslides.

6.2.8 Considerations on the results obtained

Through the interferometric analysis, it has been possible to detect and assess the 2012 Pananice landslide, both in the pre-failure and in the post-failure stage. The piezometric data have been considered very important in order to investigate the relationship between the slope movements and

the groundwater level. From the comparison with time series of displacement, derived from the interferometric analysis, and rainfall data, it is visibly noticeable the connection with acceleration, following abundant precipitations, as well as decelerations during dry periods, of the landslide (Fig. 6.39, Fig. 6.46). For instance, during a very rainy period occurred in November and December 2013 (275 mm between November 18 December 1), the time series derived from the CPT-TSC processing shows an acceleration of the displacement, starting from the December 3. In the same timespan the piezometric level was subjected to a sudden rise, an event which surely represents an important instability factor. A good correspondence is demonstrated also with the piezometric monitoring, as shown in Figure 6.46. In this case, the equivalence is between rises of the water table level and accelerations of the displacement. In detail, as mentioned before, a first important variation of the water level can be observed between November and December 2013, as a response to heavy rainfalls (275 mm in 14 days) and presumable leaking of the urban water pipes; the rise of such level is quantifiable in more than 1 m (from 1.4 to 0.2 m), thus reaching a very shallow depth. After that, the displacement seems to undergo a drastic acceleration, starting from the December 3 2013. In the subsequent phase the piezometric level keeps constant in a very shallow depth, between 0.2 and 0.4 m from the ground level, with small oscillations due to the different intensity of the daily precipitation. During this time span, the displacement also keeps persistent, with slight accelerations soon after intense rainfalls. Starting from the mid of May 2014, this superficial aquifer drops of at least of 0.2 m, throughout the dry season, and simultaneously it is noticeable a slowdown of the movement, as observable in the time series. In the last part of the investigation period the water level suffers by strong oscillations, due to very high daily rainfalls, where also the time series continues to show a rapid response of the surface to such events.

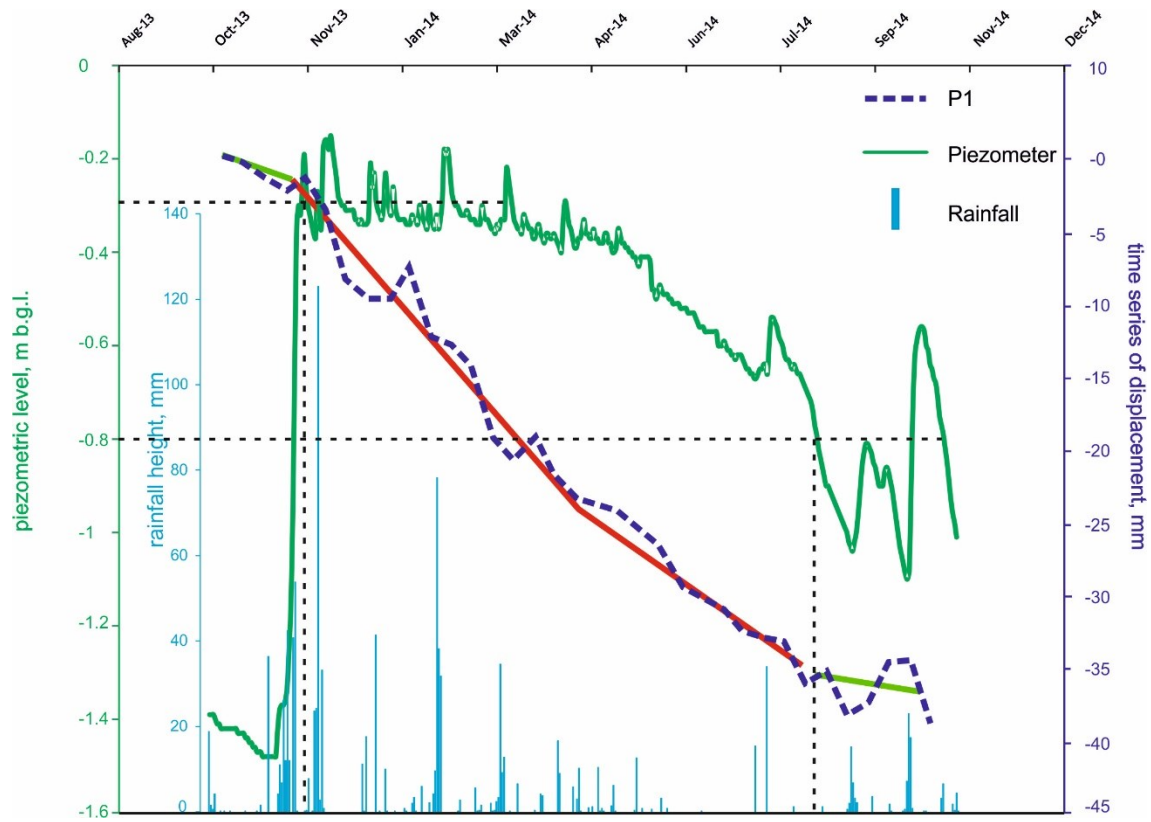


Figure 6.46 Comparison between piezometric and rainfall data with time series obtained with the CPT-TSC algorithm. In green line, slow phase of the movement, in red line, rapid phase of the movement.

After the results shown in the first part, in the time-span 2008-2010, one of the first objectives has been represented by a more complete analysis on the slope of interest, in order to investigate, through the application of remote sensing techniques, in co-operation with conventional methods, both the predisposing factors and the possible evolution of the movement in the next future. The first part showed how MTI methods are efficient to detect, even at a very local scale, displacements and precursor stages of slow-moving landslides. In the framework of the 2013-2014 analysis, the main objective has been to detect and to monitor the gravitational movements happened after the main event, occurred in the 2012. In this case, two different kinds of DInSAR algorithms were applied: CPT on the SUBSOFT processor and SBAS on SARscape. The idea was, in this second phase, to compare a PS-like method with an SBAS-like one, to evaluate the performance on such phenomena and settings and to highlight eventual differences or similarity in the elaboration. Moreover, the suitability of the SBAS on larger areas and on less detailed scale studies, allows making further analyses on different scale, extending the investigation on the entire Northern sector of Papanice settlement. The results obtained in the 2008-2010 time-span demonstrated the high accuracy of two PS-like techniques in such settings. A first result obtained in the post-failure period is that SBAS seems to underestimate velocities of the displacement in the landslide area, respect to the pre-failure stage, and also

compared to the field survey, during which the landslide shows still evidences of a movement with considerable displacements. Moreover, the SBAS analysis showed lower displacement rates even in the pre-failure analysis, confirming this assumption. Furthermore, through this algorithm, the time series result to be affected by noise, so characterized by less accurate measurements, proving to be not well suited for local deformations affecting, for example, small buildings (Mora et al., 2003). For this reason the comparison between SAR and piezometric data has been carried out exclusively with the CPT algorithm where the pixels have been selected through the TSC method. With such technique, more reliable velocities of the displacement have been obtained and a confirmation of such reliability is due to the comparison with rainfalls and piezometer, where the activation of the displacement begins in occurrence of the rapid rise-up of the groundwater level. However, both CPT and SBAS were once again able to detect the area affected by displacements, as seen by the high concentration of points located in the neighborhood next to the slope. This cluster is fully set in correspondence of the main scarp, and, as also displayed in the pre-failure phase, in the NW part of the landslide. Respect to the pre-failure movements, furthermore, in this time-span there is a clear evidence of an activation of movements in the opposite sector of the landslide. In the SE part of it, groups of at least 15 targets, showing average displacement rates of 5 mm/yr, have been equally identified with the two different techniques, and in both cases the maximum value is of 8.3 mm/yr, on a target located in the backyard of a woodshed next to the slope. Hence, the SAR analysis, even with different algorithms, is highlighting a new sector of the landslide previously stable, and, after the triggering phase, characterized by instability. This is a remarkable result which can also visibly point out the role of such methods for predictive purposes. In fact, as it has been possible to foresee the landslide in a previous timespan, the same can happen with this second time interval, so that this new area activation could be sign of an enlargement of the movement, thus involving new buildings and new areas. The integration of MTI methods with conventional devices and geotechnical analysis assumes, likewise, a paramount importance in the landslide analysis: The comparison between time series of displacement and piezometric monitoring showed the connection of such phenomena with rainfalls and with oscillations of the water table level, clearly pointing out and confirming the role of the groundwater for the triggering of the slow-moving landslide, as also proved during the slope stability test. The experience carried out on Papanice case pointed out the role of the interferometry, which, coupled with geological and geo-technical analyses, can represent a significant tool for the planning of remedial works, providing the right indication on how and where to operate in order to reduce the risk and to increase the stability of the area.

6.3 Update of the landslide inventory map

The other goal of this PhD project was to update the available landslide inventory map for the area of Crotone province, whose last update has been made in 2006. In the HSP, as mentioned in the paragraph 5.4, 478 landslides affecting the urban areas have been recognized, where 61% are dormant and the remaining 39% are active. However, it is worth to make clear that these figures refer to the whole Crotone province, while the TerraSAR-X stacks cover only part of it, excluding the municipalities located in the western border (such as Petilia Policastro, Roccabernarda, Verzino, etc.). Hence, analyses have been carried out on 11 municipalities: Crucoli, Carfizzi, Melissa, S. Nicola dell'Alto, Casabona, Strongoli, S. Severina, Rocca di Neto, S. Mauro Marchesato, Scandale and Cutro. Papanice and Cirò have been excluded because their landslide scenario has been analyzed in detail in the previous paragraphs. For the above-mentioned 11 municipalities, 194 landslides have been reported in the 2006 HSP, where 78 of them are classified as active (40 %), and 116 as dormant (60 %) (Fig. 6.47).

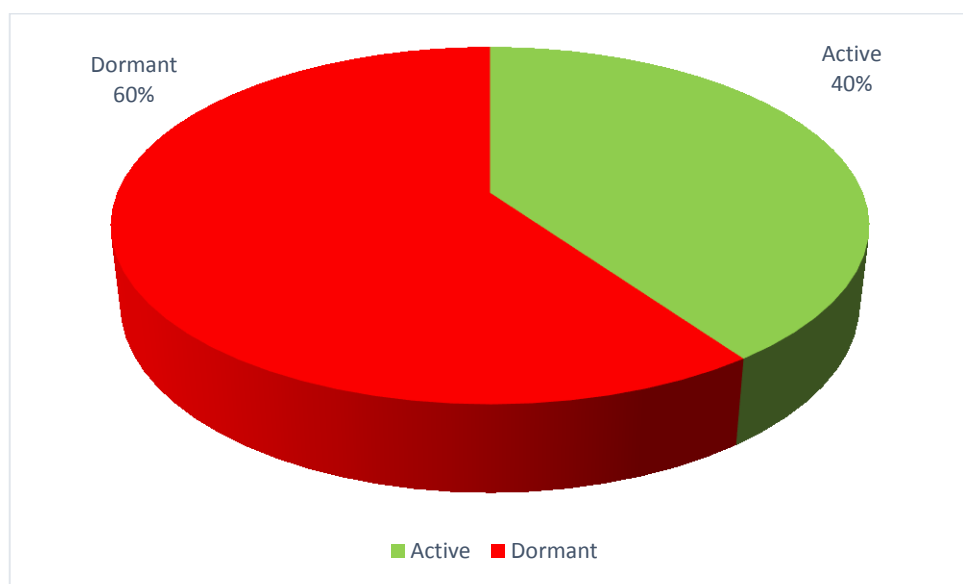


Figure 6.47 Pie-chart showing the state of activity of the landslides in the 11 municipalities selected, according to the HSP (2006).

In previous works, several procedures have been adopted to update the existing landside inventories (Meisina et al. 2008; Del Ventisette et al. 2014; Tofani et al. 2014; Di Martire et al. 2016). In this PhD project, a procedure developed in GIS environment, following the Liguria region criterion, developed in the framework of the analysis of PS data from ERS mission (1992-2000) for the elaboration of anomalous areas (University of Pavia, 2008), starting from interferometric data acquired has been applied. For anomalous areas are considered the clusters of PSs which, for physical and spatial

characteristics, can represent evidences of instability (Meisina et al., 2008). The parameters chosen for the extraction of the anomalous areas are:

1. Threshold of minimum velocity: Class of velocity considered stable, where velocities higher or lower than a given threshold can be considered as evidence of instability;
2. Maximum interpoint distance: Maximum distance between two close targets;
3. Number of targets: Number of targets within an area showing velocities higher or lower than the threshold set;
4. Homogeneity index: Ratio between the total number of targets within the area and the number of moving targets (with velocity higher or lower than the threshold set).

As regards the velocity threshold, a value of ± 3 mm/yr, along the LOS, has been selected following a statistical analysis. From the analysis of the frequency of the velocity it is possible to observe how they can assume approximately a Gaussian distribution (Fig. 6.48). The threshold value has been determined taking into account the sum between the average and the value of the standard deviation of the velocities multiplied for 3. In such way, 98% circa of the velocities fall into the interval among ± 3 mm/yr and has been considered as “normal value”, isolating and thus considering as “anomalous” all the velocities higher than this threshold set. Such value has been also fixed according to the expected velocities of deformation in such geomorphological contexts and according to the thresholds set in other works (Notti et al., 2014). A maximum interpoint distance of 20 m and more than one target within a pixel are the other two necessary conditions for the individuation of the anomalous area. The homogeneity index threshold value, which is the ratio between the total number of targets within the area and the number of moving targets, is 0.2; hence, all the pixels below this threshold have been discarded. Once individuated the anomalous areas, the following step has been to integrate and interpret this elaboration by means of field survey carried out with the help of photointerpretation.

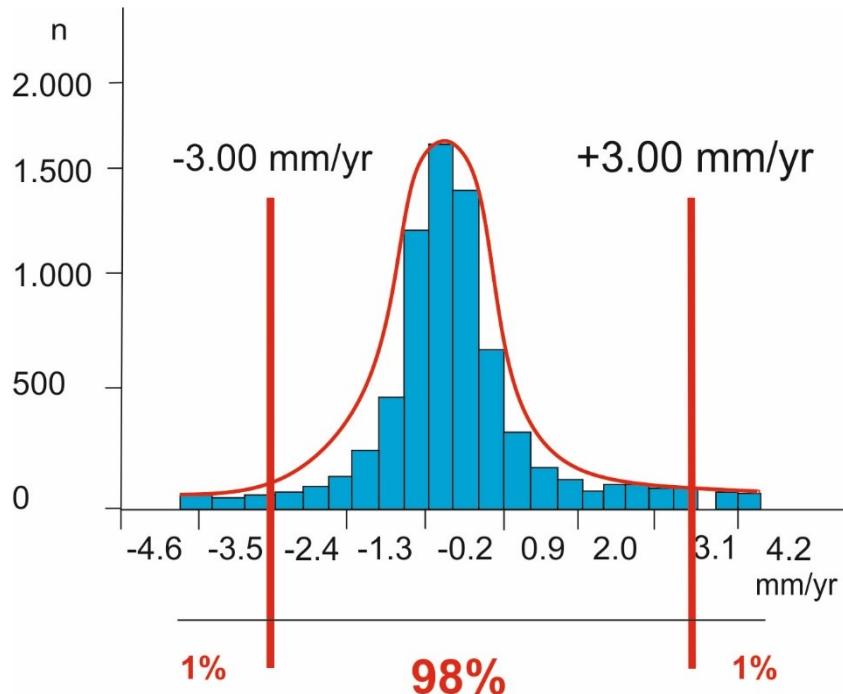


Figure 6.48 Frequency of the distribution of the velocities. 98% of the velocities falls within the interval “Average $+ 3 \times$ Stand. Dev”.

Field surveys have been performed between Fall 2013 and Summer 2015, while the photointerpretation has been carried out through the exploitation of ortophotos available on the Geoportal of the Italian Environmental Ministry (http://www.pcn.minambiente.it/viewer_old/) and on Google Earth®. Such interpretation allowed to identify the instability processes occurred in Crotone province between 2008 and 2015, hence updating the available landslide inventory map. In this case, an overlap between the anomalous areas identified and the landslides contained in the HSP database allowed to delineate the following classes, adapting those ideated in the framework of the LaDIS methodology (Di Martire et al., 2016):

- Areas affected by new landslide in the 2008-2015 period ;
- Areas affected by likely reactivations (dormant landslides according to the 2006 HSP, but corresponding to areas with significant target velocities in the 2008-2010 period);
- Areas characterized by a continuous landslide activity (active landslides according to the 2006 HSP, but corresponding to areas with significant target velocities in the 2008-2010 period);
- Areas characterized by a continuous landslide activity, but redefined according to the joint application of DInSAR and field survey.

In case through both DInSAR analysis and field survey no movement has been recognized in landslides considered as dormant in the HSP, the state of activity has been kept as dormant, the same has

been done in case the landslides were considered as active in the HSP, changing the state of activity in dormant.

In case there was no agreement between field and SAR, the following classes have been defined:

- Landslide detected through DInSAR application, not in the field survey;
- Landslide not detected through DInSAR application, but identified in the field survey.

Obviously, DInSAR analysis allows to detect very slow movements, according to Cruden & Varnes (1996), hence such methodologies has to be considered only for this kind of landslides (i.e. complex, slides, flows, deep and shallow movements interesting landslide deposits).

The detection of the anomalous areas has been carried out through a GIS model builder (Fig. 6.49). The first step is represented by the creation of a fishnet of 20×20 m square cells for each AOI (Area of Interest). Such fishnet is then intersected with the DInSAR final elaboration (PS or CP shape file). A selection of the PS velocities is successively done, through a SQL (Structured Query Language) expression, in which all the pixels with velocities higher than $|3|$ mm/yr are chosen. Simultaneously, the number of “moving” PSs is determined. Hereafter, joining the frequency of anomalous PSs velocities and the layer of the cells containing moving PSs identified it is possible to obtain a shape file characterized by cells with more than one moving PS and with velocity higher than $|3|$ mm/yr. The last step consists in the calculation of the Homogeneity Index (Hi), which is a very useful parameter for discretizing real moving areas from areas affected by potential noises by the DInSAR elaboration, and the consequent exclusion of the cells with Hi lower than 0.2.

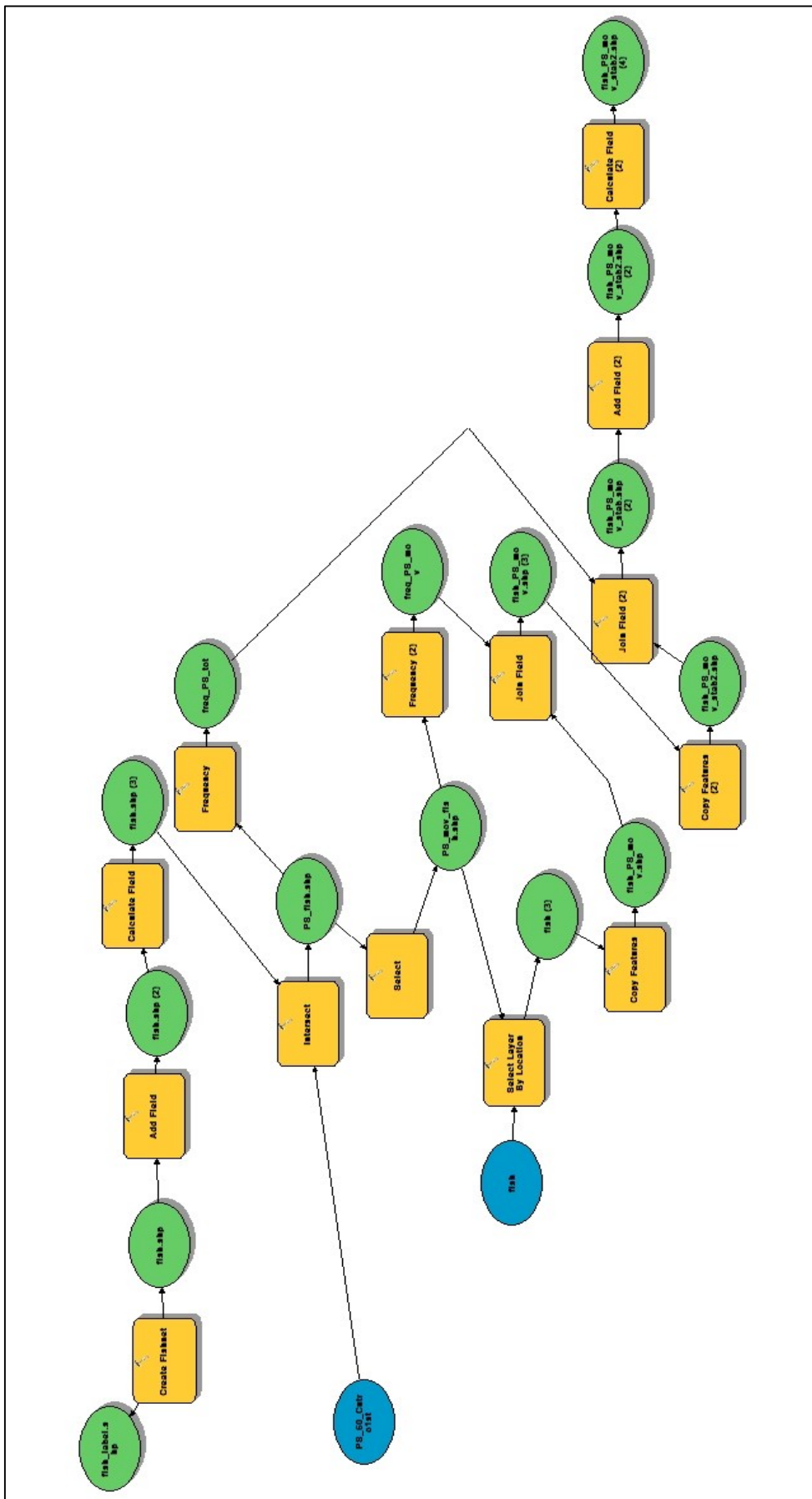


Figure 6.49 Scheme adopted for the identification of the anomalous areas.

For the achievement of the afore-mentioned objective, both the SBAS and the PSInSAR algorithms have been implemented on the available stack of TerraSAR-X images, acquired between 2008 and 2010. A preliminary analysis has been done in order to understand where the satellite's geometry of acquisitions do not allow to correctly detect the deformation (such as N-S slope direction, geometric distortions). Both the processings have been thus carried out following the indications given by the R-Index (Notti et al., 2010) computation. In fact, through the R-Index it has been possible to choose whether apply the DInSAR methods on the ascending or on the descending datasets for each area of interest, obtaining information about the quality of the pixel (Fig. 6.50 and 6.51). For instance, if a given area is in foreshortening, layovering or shadowing for the descending orbit, DInSAR processing is completed only on the ascending one.

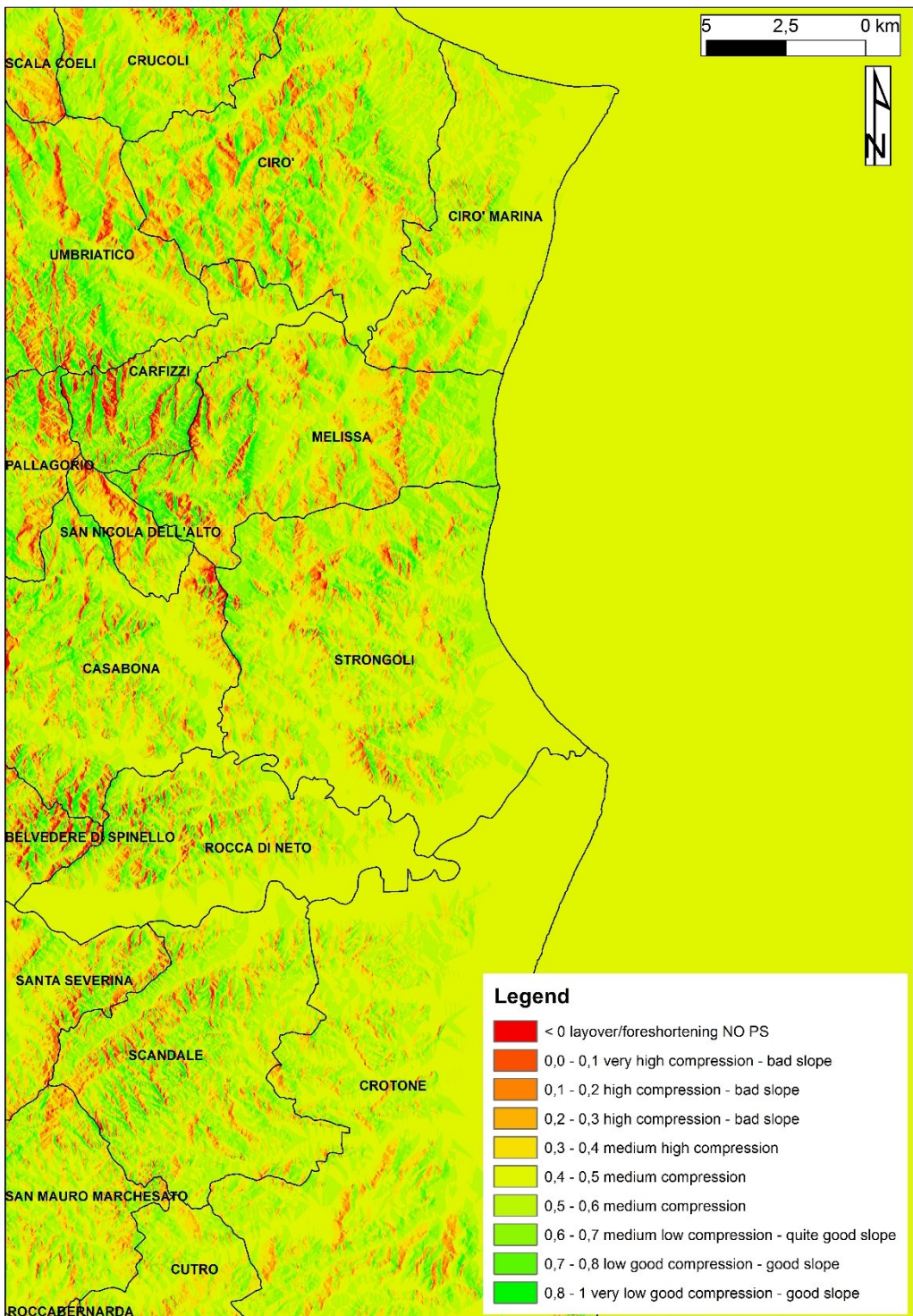


Figure 6.50 R-Index computation on the whole Crotone Province on the ascending dataset.

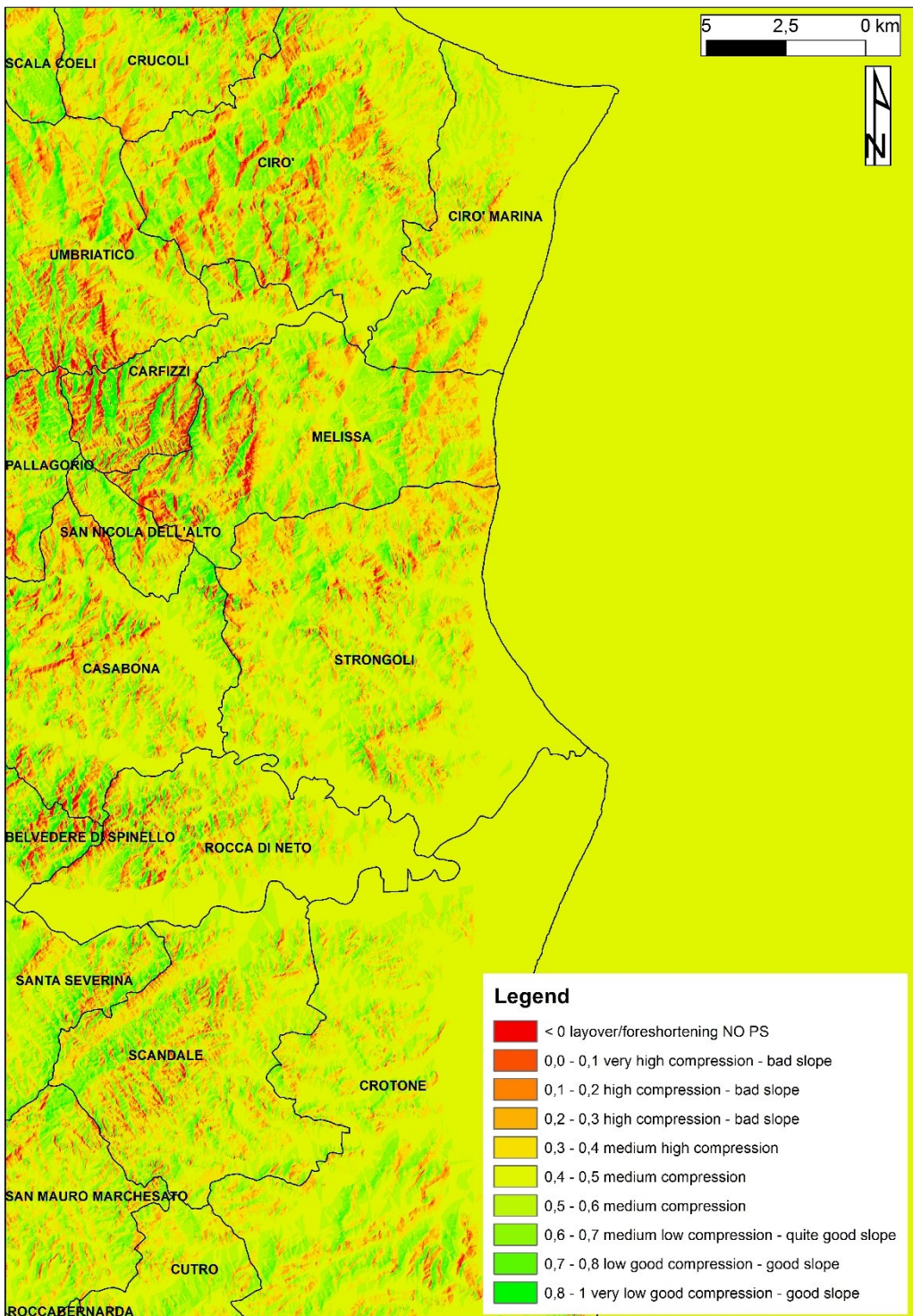


Figure 6.51 R-Index computation on the whole Crotone Province on the descending dataset.

Both the PSInSAR and the SBAS methods have been applied. However, the implementation of the anomalous area methodology on PSInSAR data presented many outliers, so resulting less trustworthy. Many anomalous areas have been in fact detected in most likely stable places (i.e. city center, flat

areas, etc.) (Fig. 6.52 and 6.53), hence not affected by any displacement. It has thus possible to confirm the very good capability of PSInSAR algorithm to recognize displacements at a very local scale, however, at the same time, PSInSAR demonstrated its less efficacy in wider settings, such as town or province scale. For this reason, the methodology has been applied only on SBAS data, obtained through the application of SARscape software. The whole procedure has been summarized in Figure 6.54.

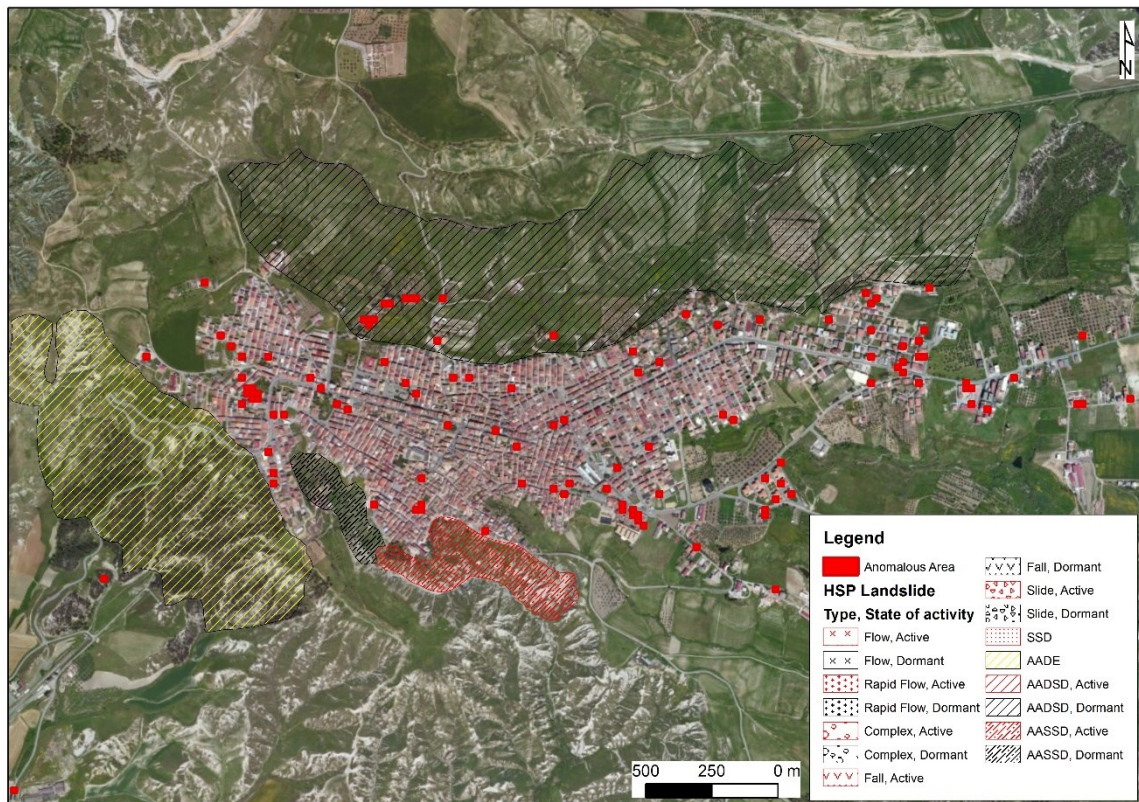


Figure 6.52 Map of the anomalous areas obtained with PSInSAR processed data: Cutro case.

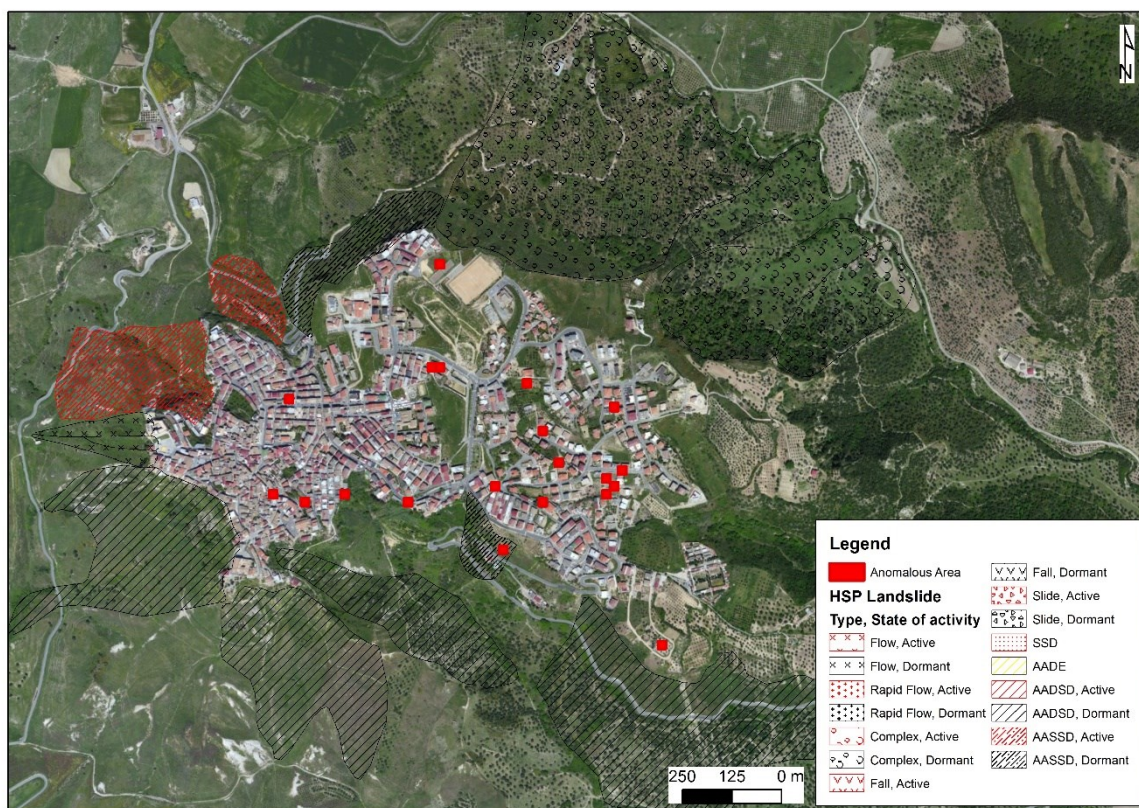


Figure 6.53 Map of the anomalous areas obtained with PSInSAR processed data: Strongoli case.

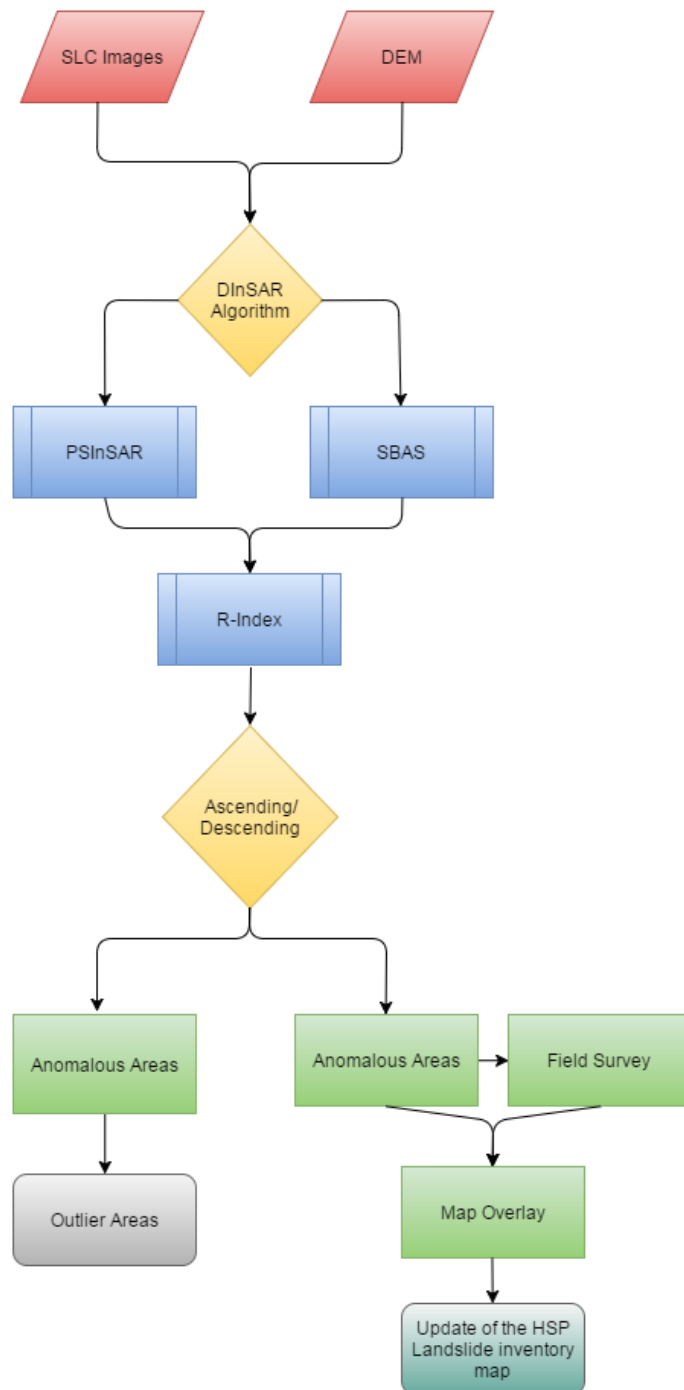


Figure 6.54 Flow Diagram of the procedure adopted for the update of the landslide inventory map.

6.3.1 Results

6.3.1.1 Crucoli

Crucoli is the northernmost municipality of Crotone Province, composed of ca. 3000 inhabitants. The historical center of the town is located along a NW-SE elongated-shaped hill, with also several houses placed on a E-W ridge. The geological setting of the area is characterized by the presence of the Sandstones of Mt. Caciocavallo at the bottom, and by the presence of the sandstones of Crucoli Formation at the top. Pliocene and Pleistocene deposits (clays, sands and conglomerates) crop out, sometimes as debris of marine terraces (Fig. 6.55). It is possible to find also recent deposits originated by the slope dynamic. The morphology of the historical center is related to the presence of these formations, characterized by high strength to erosion. The slopes where the arenaceous formations crop out are high and steep and they can generate falling and toppling phenomena; however, in the clayey slopes it is also possible to observe sliding and deep erosional phenomena. At the top of the slopes, the area on which the town has been founded presents a flat configuration.

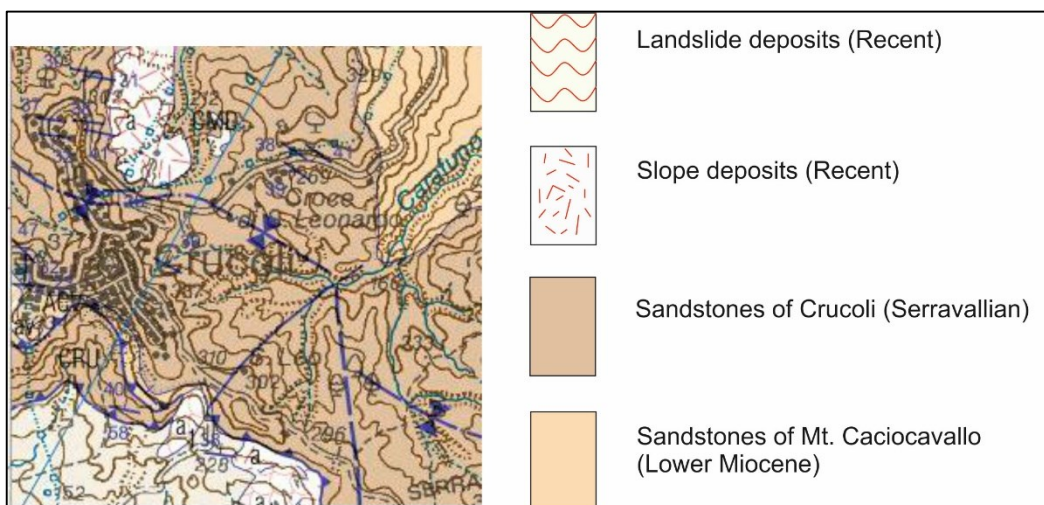


Figure 6.55 Geological map of Crucoli (modified from Geological map 1:50.000, ISPRA, 2006).

The HSP reports 20 landslides (Fig. 6.56), where ten are considered active and ten as dormant.

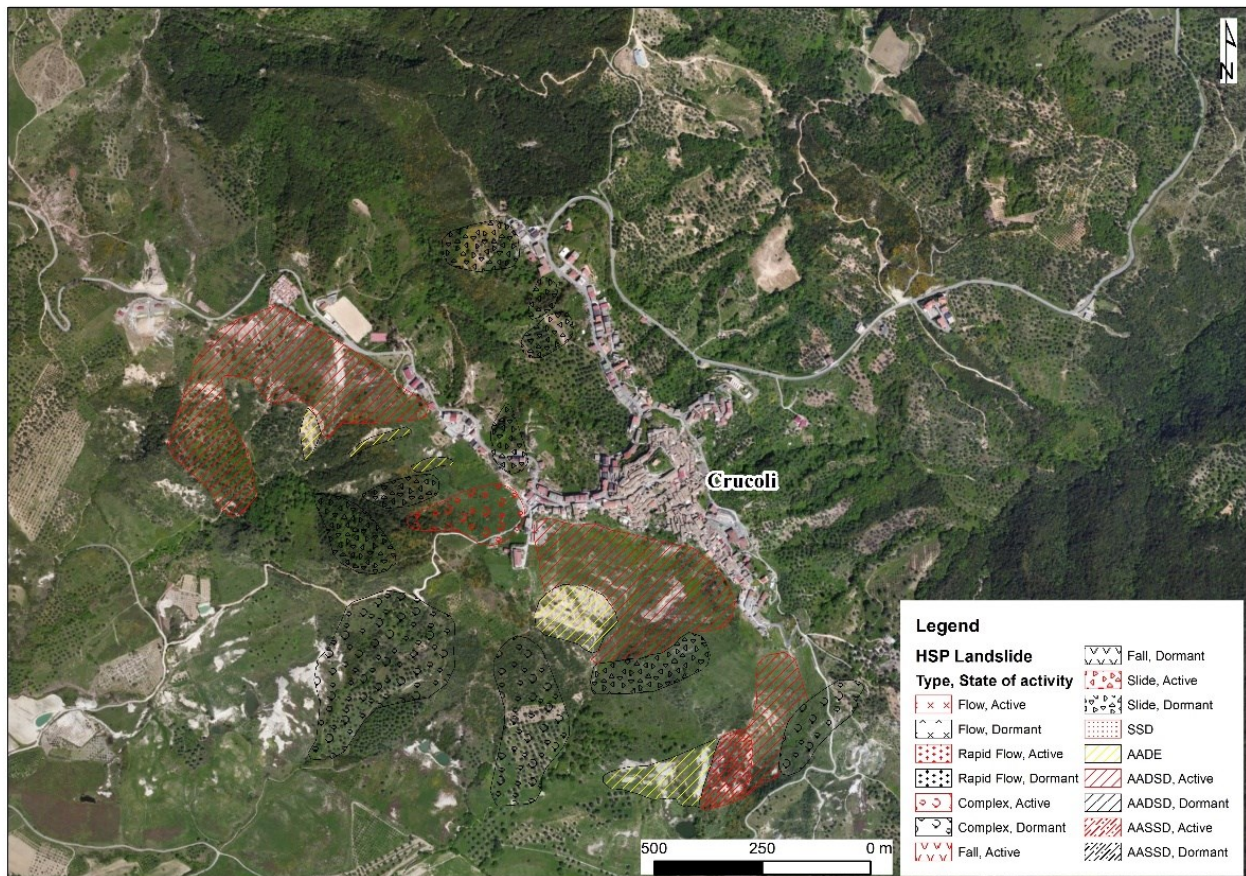


Figure 6.56 HSP map of Crucoli (Calabria Basin Authority, 2006).

DInSAR application allowed to identify almost 600 CPs, all located over the western part of Crucoli urban area (Fig. 6.57). Two anomalous areas have been identified (Fig. 6.58) through the above-mentioned procedure, one in the middle part of the urban area, on a slope facing NW, and the other one in the southern part. However, in the first case, no sign of displacement has been noticed during the field activities, hence suggesting to classify the landslide as detected through DInSAR application only, not in the field; in the second case, on the South facing slope, several evidences have been found (Fig. 6.59), as for instance damage to a house located along the main scarp and an remedial works to protect the slope. Landslide boundaries have been thus redefine, now showing a retrogressive trend. In addition, eight active landslides have been recognized during the field activity, but not through the SBAS application, and ten landslides have been classified as dormant, after the joint application of SBAS and field activity compared with the HSP inventory map.

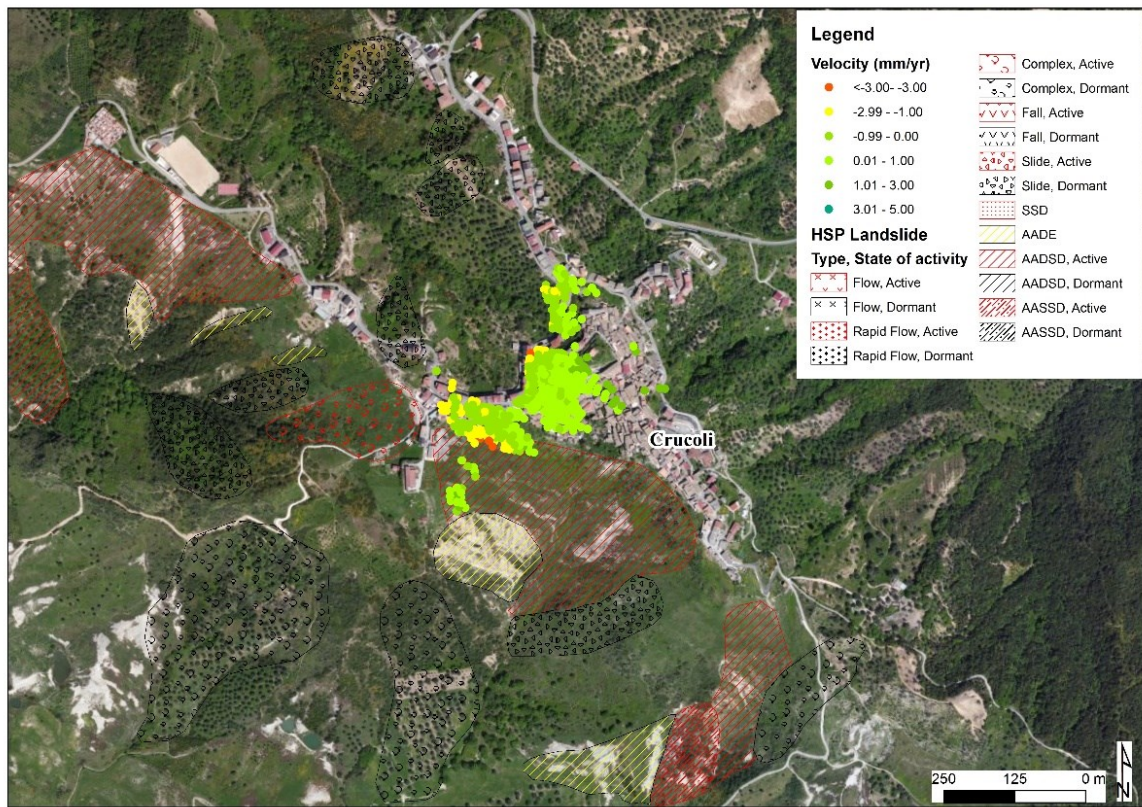


Figure 6.57 Displacement rates map obtained through the SBAS application to Crucoli.

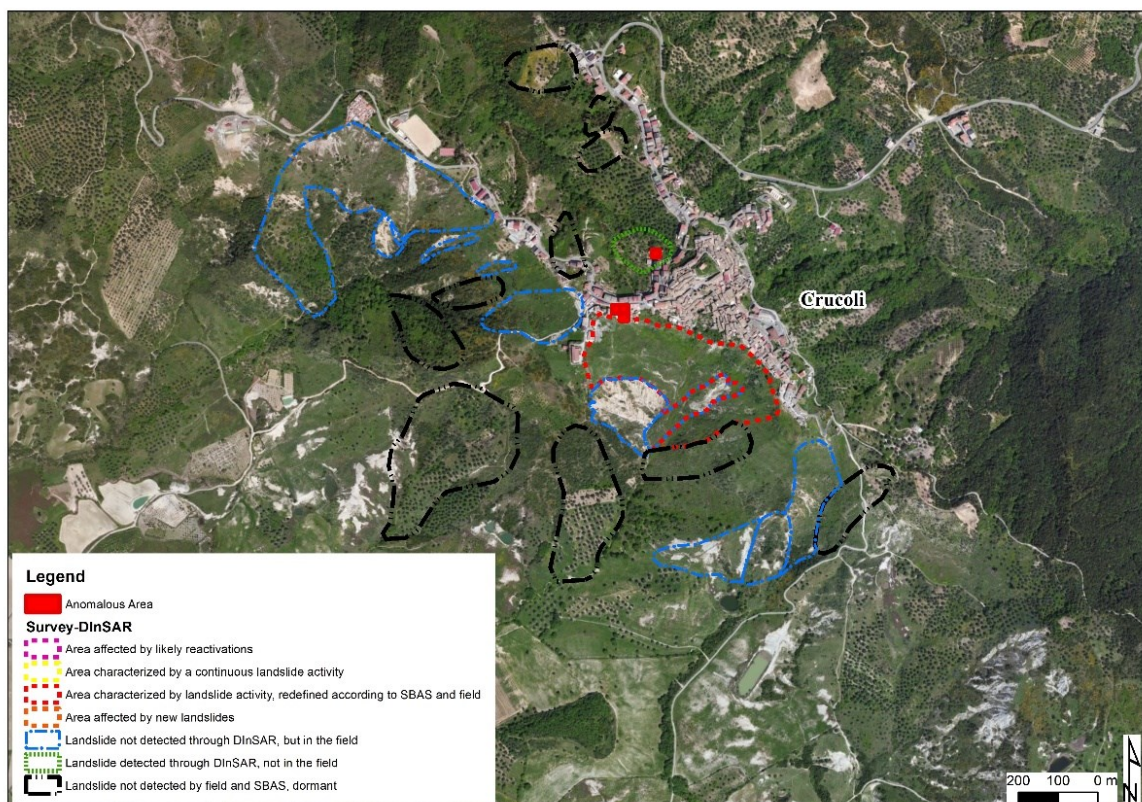


Figure 6.58 Landslide inventory map resulting from the joint application of DInSAR and field survey at Crucoli.



Figure 6.59 Evidences of the redefined landslide in the South-facing slope of Crucoli.a) and b) damage reported on an abandoned house and remedial works on the slope. c) and d) Flow-type landslide reported in the southern part of Crucoli.

6.3.1.2 Carfizzi

Carfizzi is a small village of 650 inhabitants, located in the NW of Crotone Province. It is founded on a W-E oriented hill, even though other buildings and local facilities are placed along the Provincial road that crosses the town. The main geological formation is the Umbriatico Formation, (Lower Miocene age), made of coarse-grained conglomerates, with upwards the Carfizzi sandstones, which is a 200 m-thick brown-colored quarzoarenite (Fig. 6.60). In the southern part, the morphology is characterized by V-shaped valleys and steep slopes, while in the western and northern part the slopes show a more gentle gradient. The HSP in Carfizzi area reports ten active landslides and two dormant landslides (Fig. 6.61).

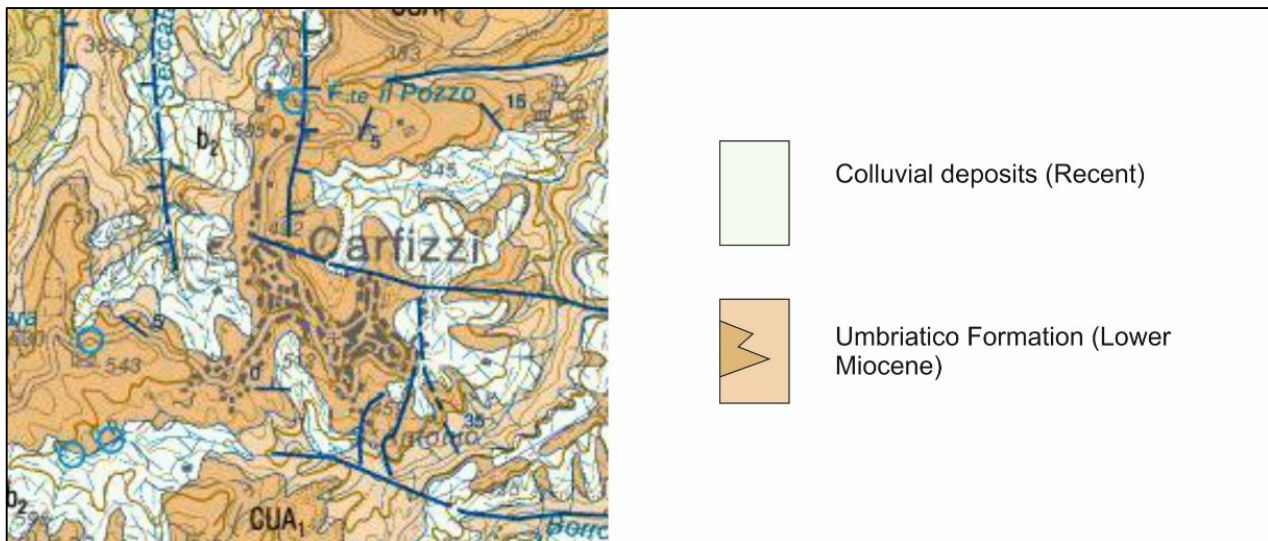


Figure 6.60 Geological map of Carfizzi (modified from Geological map 1:50.000, ISPRA, 2006).

Through the SBAS application it has been possible to identify more than 3.000 CPs all over the urban area of Carfizzi (Fig. 6.62). Three anomalous areas have been detected (Fig. 6.63): one in the northern sector, one in the southern area, and the last one in the western part, over a sport center. In the first two cases, no correspondence has been found during the field activity. In the last area identified, instead, evidences, such as fracture and cracks, and metallic gabions to protect the sport center (Fig. 6.64), have been noticed, allowing to identify a retrogressive trend and to redraw the landslide. In addition, four landslides have been recognized during the field survey, but not through the SBAS implementation, and six landslides have been considered as dormant, not recognizing any sign of displacement and not detecting any moving CP.

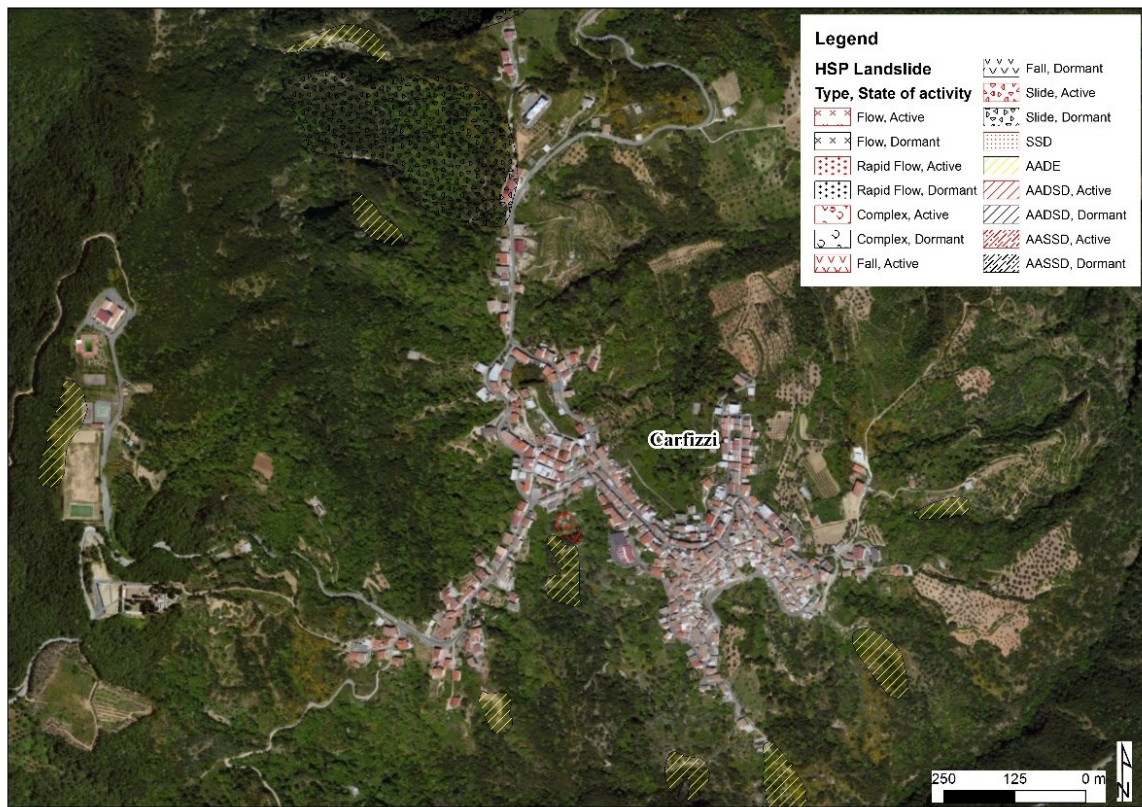


Figure 6.61 HSP map to Carfizzi (Calabria Basin Authority, 2006).

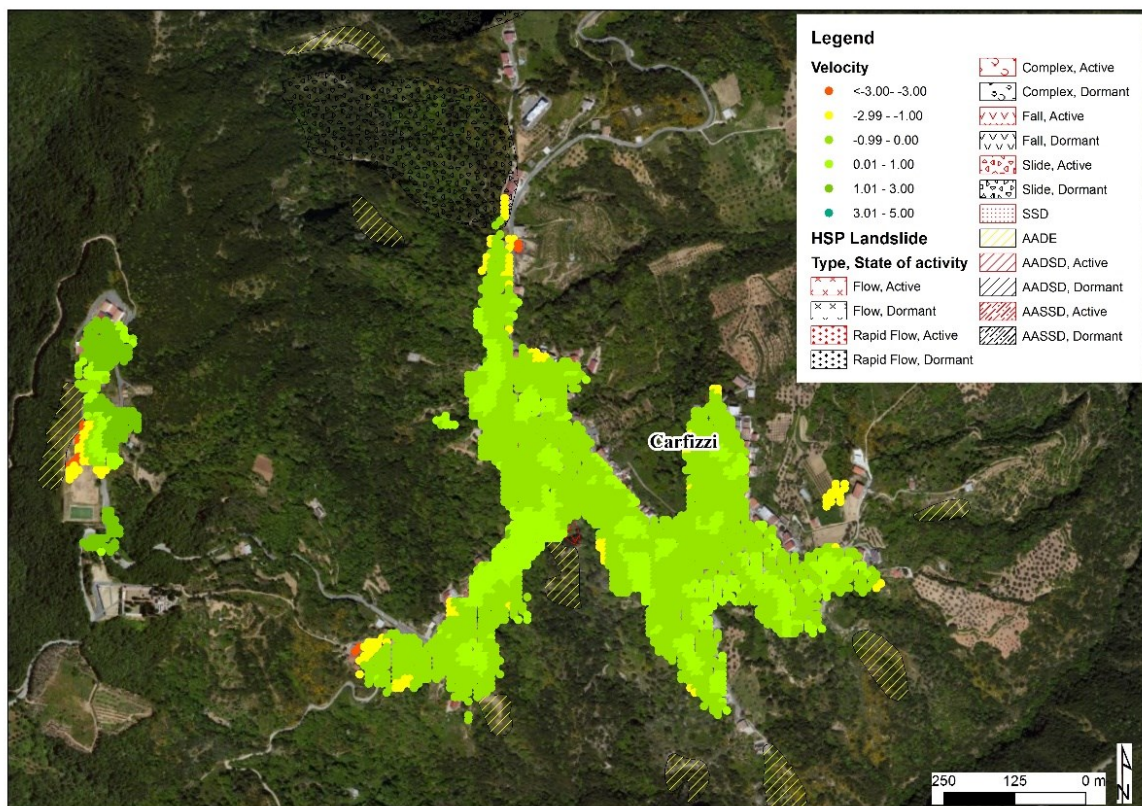


Figure 6.62 Displacement rates map obtained through the SBAS application at Carfizzi.

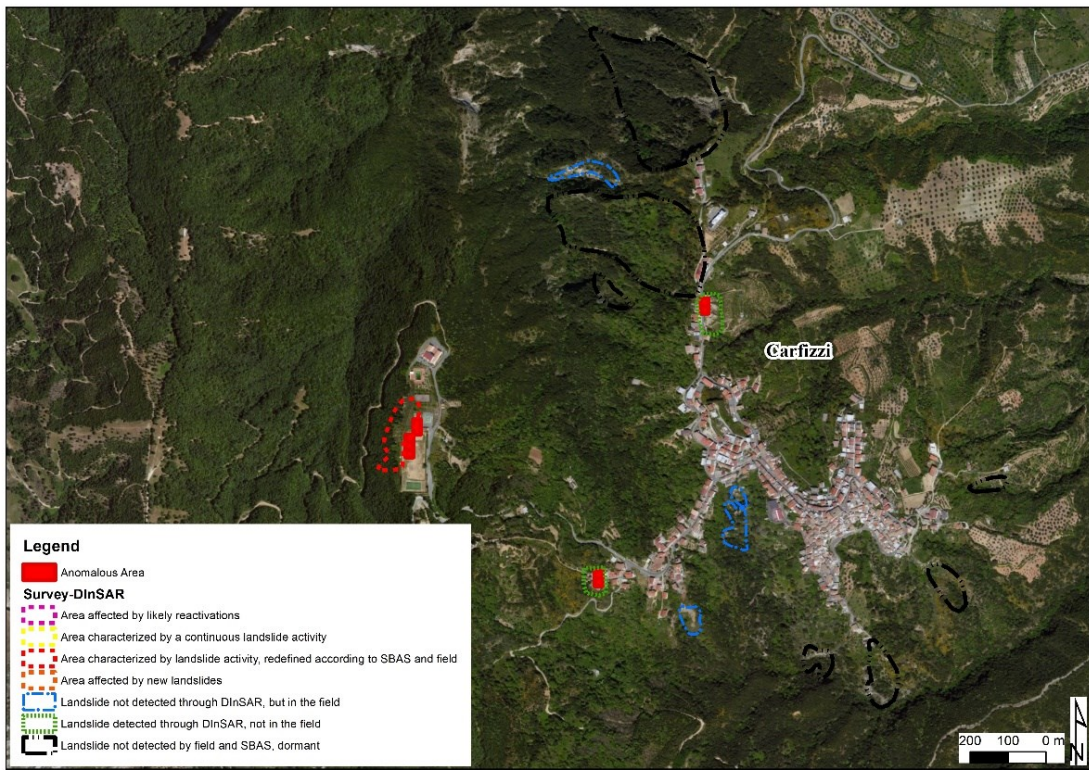


Figure 6.63 Landslide inventory map resulting from the joint application of DInSAR and field survey for Carfizzi.

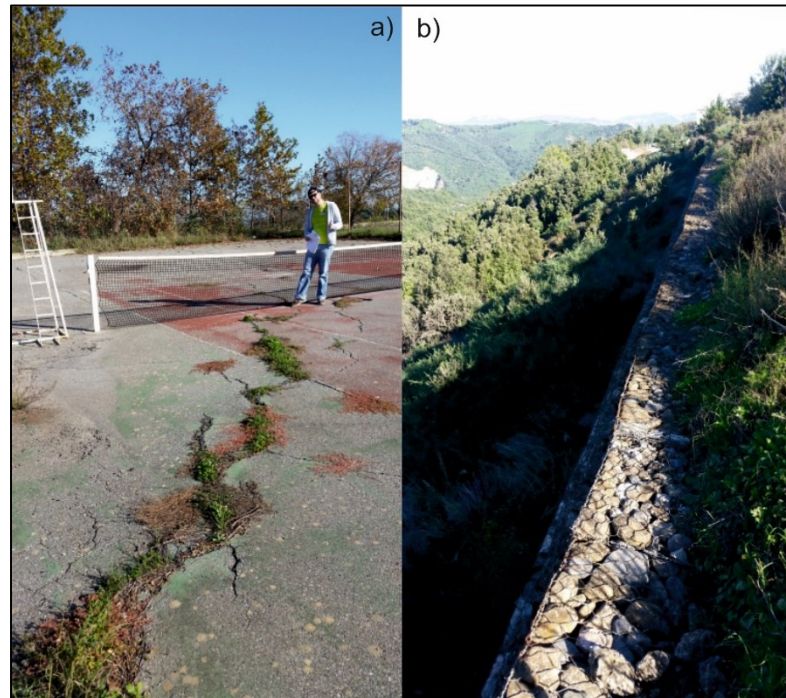


Figure 6.64 Evidences of the sport center landslide in Carfizzi. a) landslide cracks crossing the tennis pitch; b) gabions installed to protect the sport center.

6.3.1.3 Melissa

Melissa is a municipality located in the northern sector of Crotone Province. It consists of the historical settlement, located on to the top of a N-S elongated-shaped hill, and of a coastal settlement, Torre Melissa, with the urban area distributed along the coastline and along the State road no. 106. The geological setting of the Melissa settlement is dominated by the presence of the Umbriatico Formation (Serravallian), consisting of conglomerates in an arenaceous matrix, with arenaceous intercalations. It is possible to recognize clays and marly clays from the Ponda Formation (Miocene Age), cropping out in the eastern part of the settlement, as well as down the valleys alluvional deposits (Holocene Age) and colluvial deposits (Recent Age) (Fig. 6.65). The main outcropping formation in Torre Melissa area is the Varicolored Clay (Eocene Age), made of several successions of red, blue and green scaly clays, with intercalations of calcarenites and sanstones. In the northern area the Mt. Anastasia sandstones (Upper Tortonian Age) can be found, which is a sandstone with intercalations of grey-dark clays and silty clays (Fig. 6.65). On the slopes surrounding Torre Melissa also landslide deposits are reported. The presence of alluvial recent deposits marks the coastline setting.

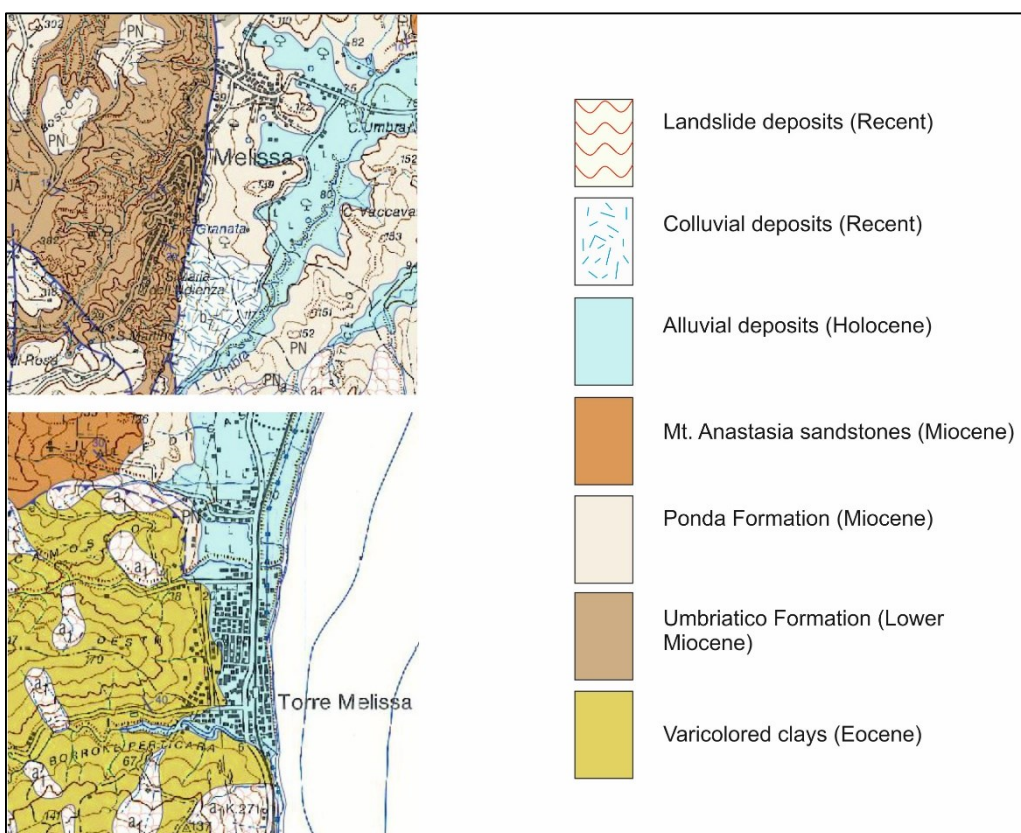


Figure 6.65 Geological map of Melissa (modified from Geological map 1:50.000, ISPRA, 2006).

From a geomorphological point of view, Melissa is located along a crest surrounded by sandy and clayey slopes, with both high and low gradient. The erosional action is very significant in some cases. At the back of Torre Melissa settlement low-gradient slopes can be recognized, due to the massive

presence of clay formations. These terrains are characterized by impermeability and by intense erosional processes, such as creep and slow flows. The coastline is mostly flat and sandy. The HSP reports nine landslides in Melissa area, four active and five dormant landslides (Fig. 6.66). In Torre Melissa, instead, thirteen landslides are reported, where five are active and eight are dormant (Fig. 6.66).

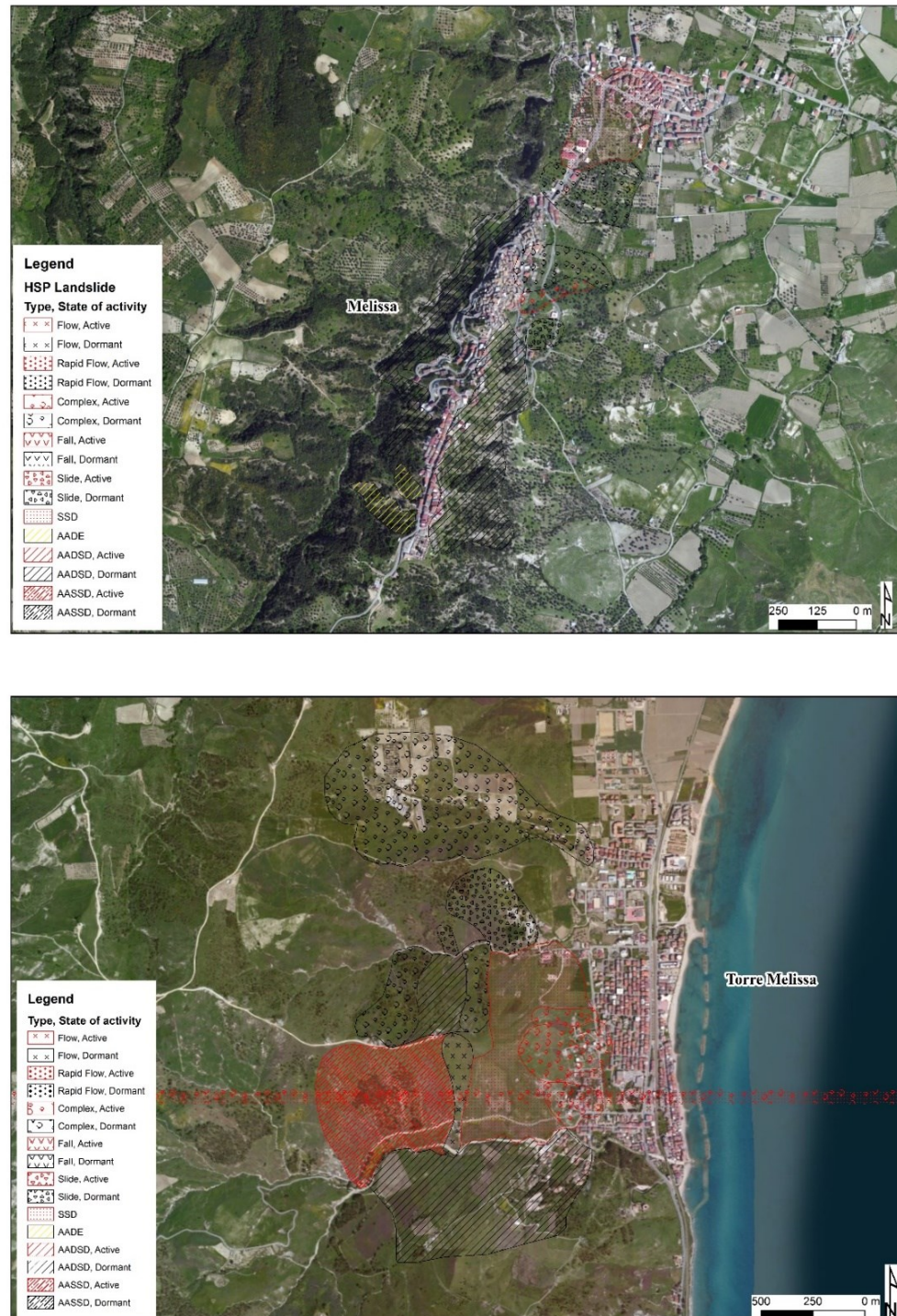


Figure 6.66 HSP map of Melissa, on the top, and Torre Melissa, on the bottom (Calabria Basin Authority, 2006).

In the area of Melissa, SBAS data allowed to recognize more than 3.000 targets, placed over the urban areas, while for Torre Melissa, more than 9.000 CPs have been found (Fig. 6.67). As concerns Melissa, three different anomalous areas have been detected (Fig. 6.68), attributable to two landslides. The first landslide, located in the northern sector of the town, which crosses the Provincial road no. 12, has been modified according to field survey and DInSAR application. Evidences of the movement are represented by several fractures found on a retaining wall and on a school located just below a steep slope (Fig. 6.69). The other area can be related to shallow displacements affecting loose materials. In this case it is an activation of a new landslide, previously not identified in the HSP. In addition, seven landslides have been considered dormant, following SBAS implementation and field survey.

At Torre Melissa, several anomalous areas which have been identified can be connected to four landslides previously identified in the HSP (Fig. 6.68). In this case, such landslides can be considered continuously active, due to a general concave-convexity of the terrain and to damage reported on some of the houses involved by the displacement (Fig. 6.69). Moreover, a landslide in the northern sector of Torre Melissa has been redefined according to the joint application of DInSAR elaboration and ground activity, six landslides have been considered dormant, and one landslide has been observed during the field activity, but not detected through SBAS. Several other anomalous areas can be documented. In this case, being the areas interested located on flat terrains and along the coast, most likely they might to be connected to water withdrawal and to coastal erosion.

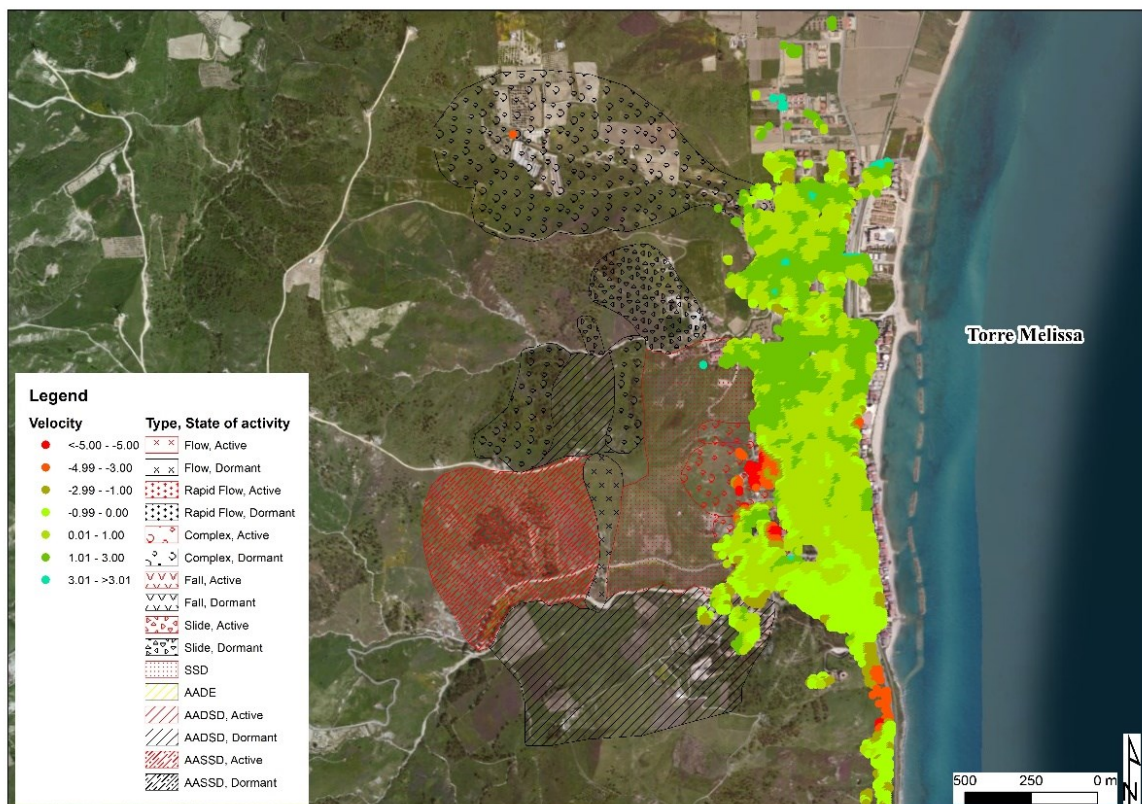
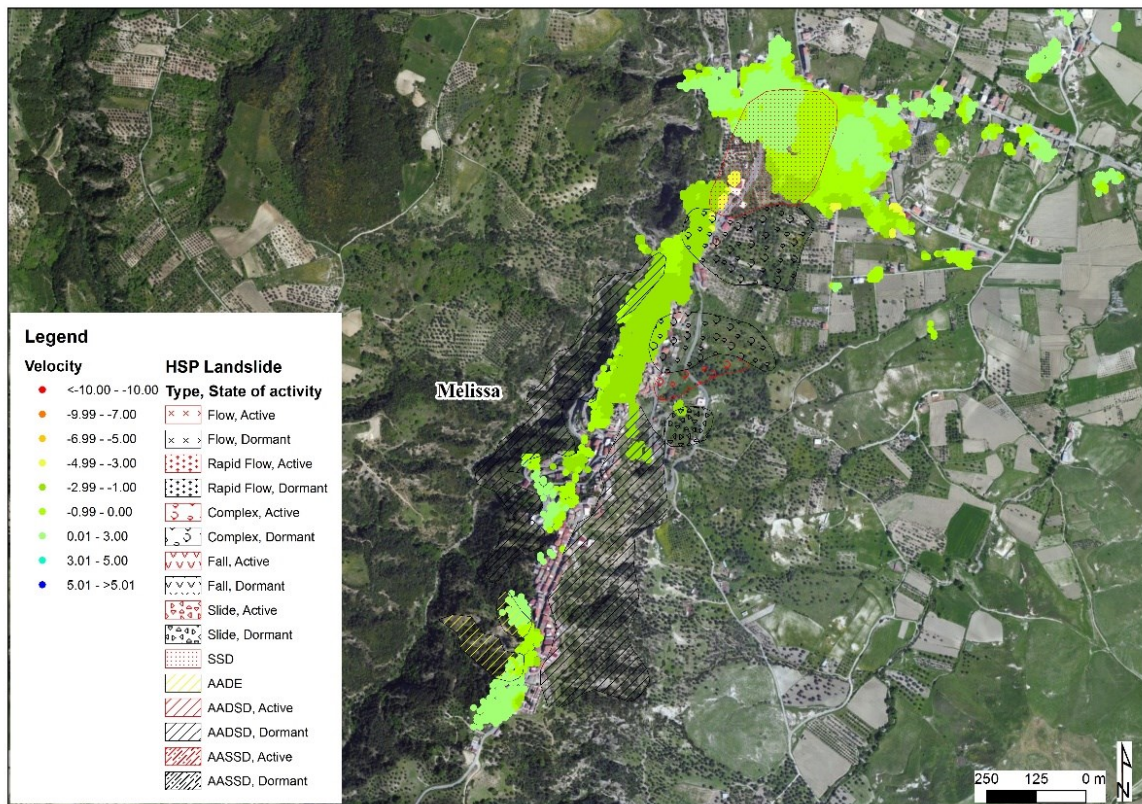


Figure 6.67 Displacement rates map obtained through the SBAS application on Melissa, on the top, and Torre Melissa, on the bottom.

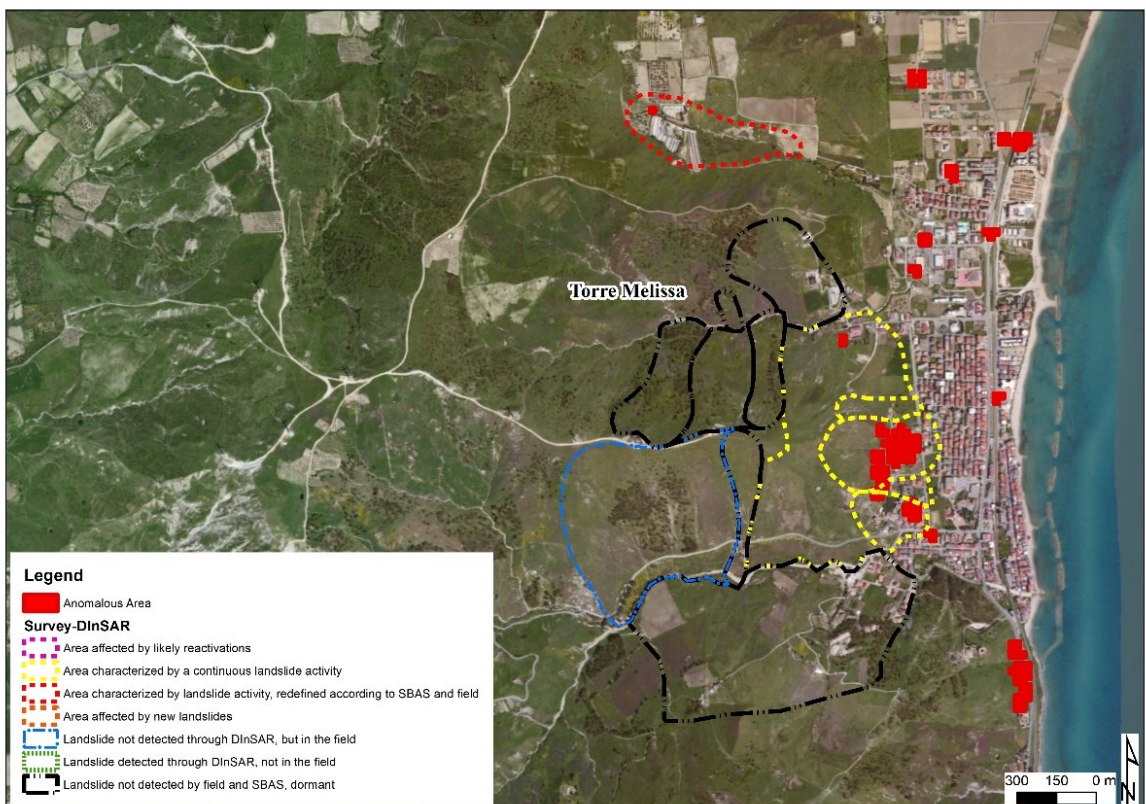
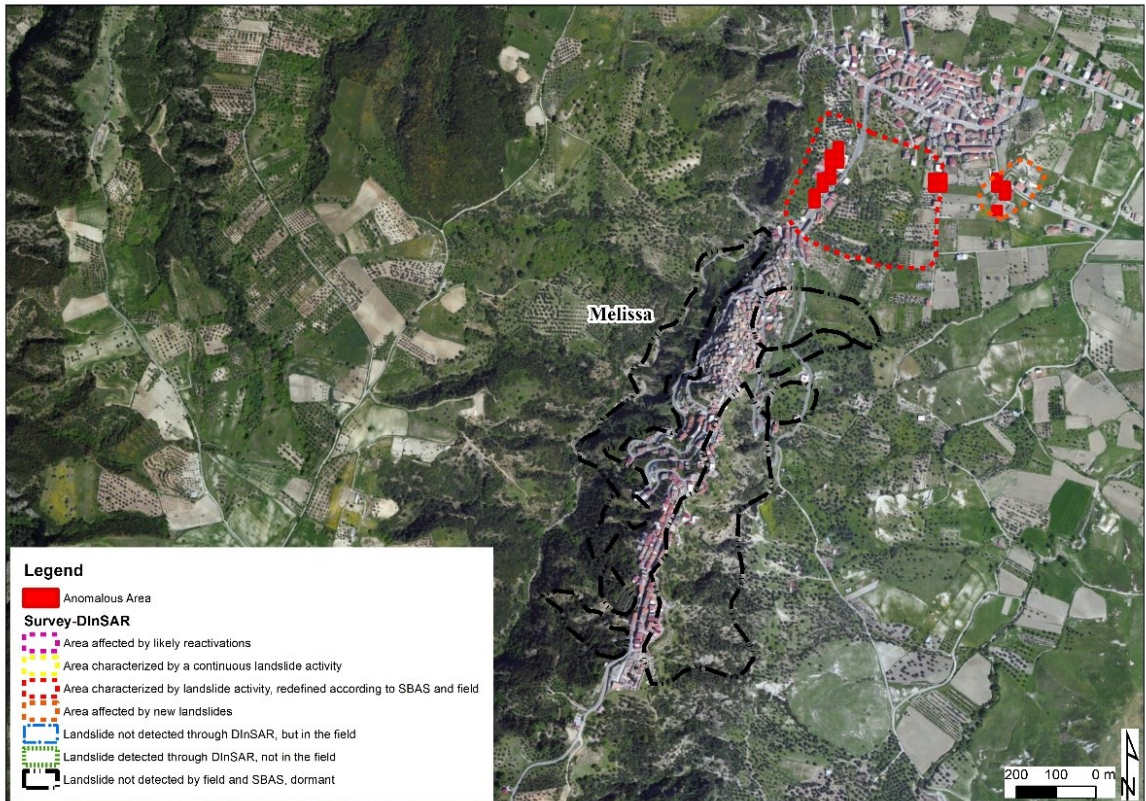


Figure 6.68 Landslide inventory map resulting from the joint application of DInSAR and field survey for Melissa, on the top, and Torre Melissa, on the bottom.



Figure 6.69 Evidences of the northern landslide in Melissa, on the top, and of the continuous landslide in Torre Melissa, on the bottom. a) and b) fracture in a retaining wall; c) fracture in the school, d) oblique view of the school and of the rocky slope in the background; e) concavity-convexity landscape in Torre Melissa; f) fractures reported in a house in Torre Melissa).

6.3.1.4 S. Nicola dell'Alto

S. Nicola dell'Alto is a small village located in the N-W sector of the Crotone Province, counting 850 inhabitants. The urban area is placed along a NW-SE ridge, at an elevation of about 500 m. The main geological formation cropping out in S. Nicola is the so-called S. Nicola dell'Alto breccias and conglomerates (Paleocene), made of terrigenous deposits and breccias in thick layers with mostly metamorphic elements. Evidences of the Umbriatico formation can be also found (Lower Miocene), as well as of the Lipuda Formation (Serravallian-Lower Tortonian), made of clays at the base, grading into torbiditic sandstones at the top (Fig. 6.70).

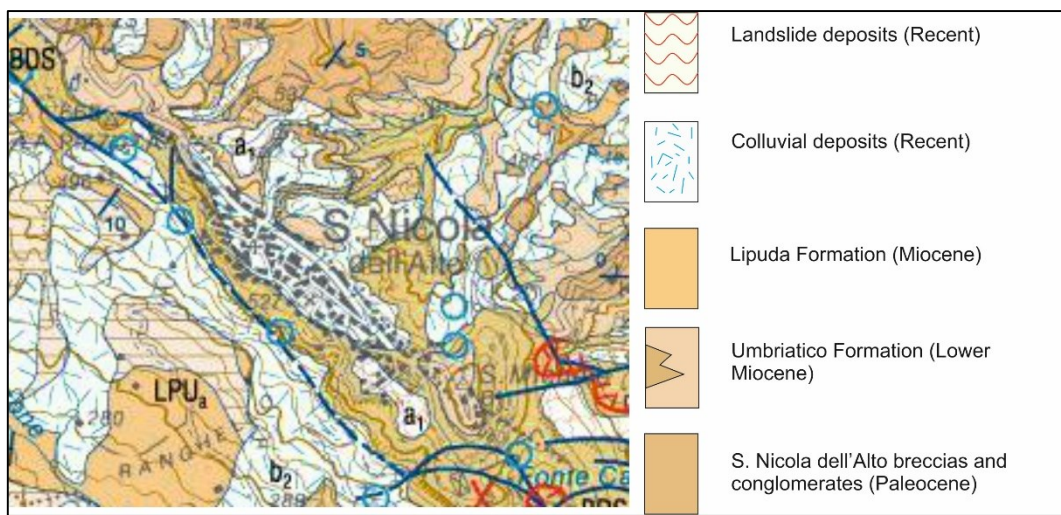


Figure 6.70 Geological map of S. Nicola dell'Alto (modified from Geological map 1:50.000, ISPRA, 2006).

From a geomorphological point of view, the slopes are very steep on both the sides of the town, in the NW part, erosional forms such as badlands can be also found. HSP reports five active landslides and seventeen dormant landslides (Fig. 6.71).

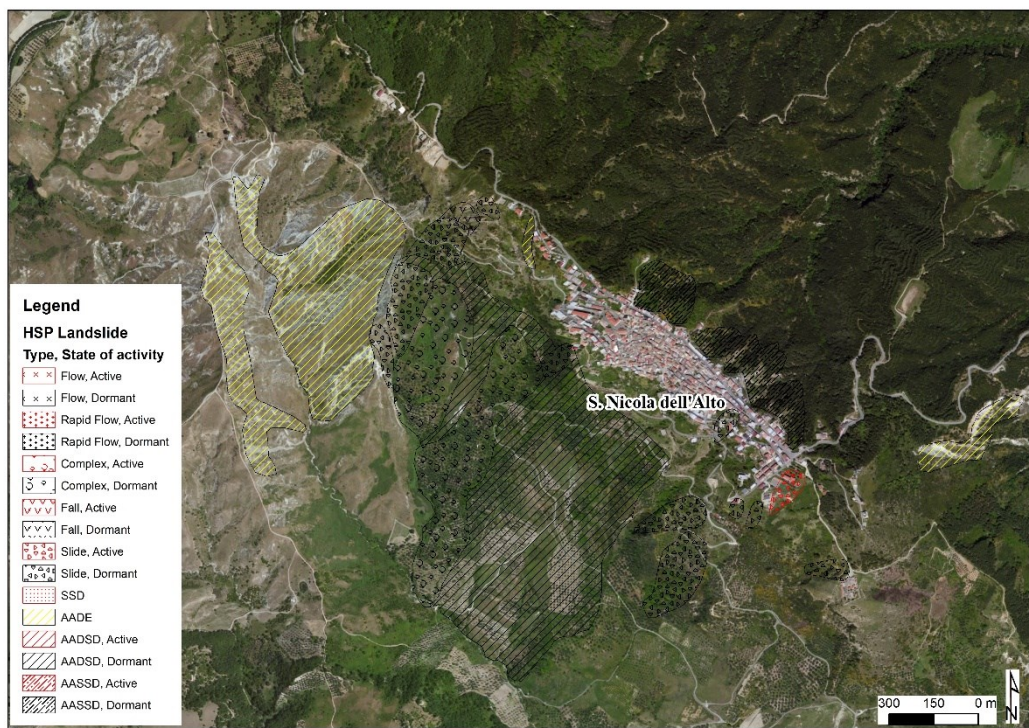


Figure 6.71 HSP map of S. Nicola dell'Alto (Calabria Basin Authority, 2006).

More than 3.500 targets have been detected through the SBAS application (Fig. 6.72), with the highest velocities of displacement located along the slope facing south. In this sector of the town, in fact, are located the anomalous areas identified through the procedure adopted, which allowed to redefine the landslide boundaries, noticing a retrogressive and enlargement trend (Fig. 6.73). Also in the SE sector of the town, in proximity of the Provincial road, another landslide has been redrawn according to the field evidences (damage to houses and roads, electric poles inclined downslope) (Fig. 6.74) and the anomalous area identification. Moreover, four landslide areas have been recognized only during the field activity, not by DInSAR elaborations, corresponding to areas affected by intense erosion, and thirteen landslides have been classified as dormant, following the joint application of SBAS and field observation.

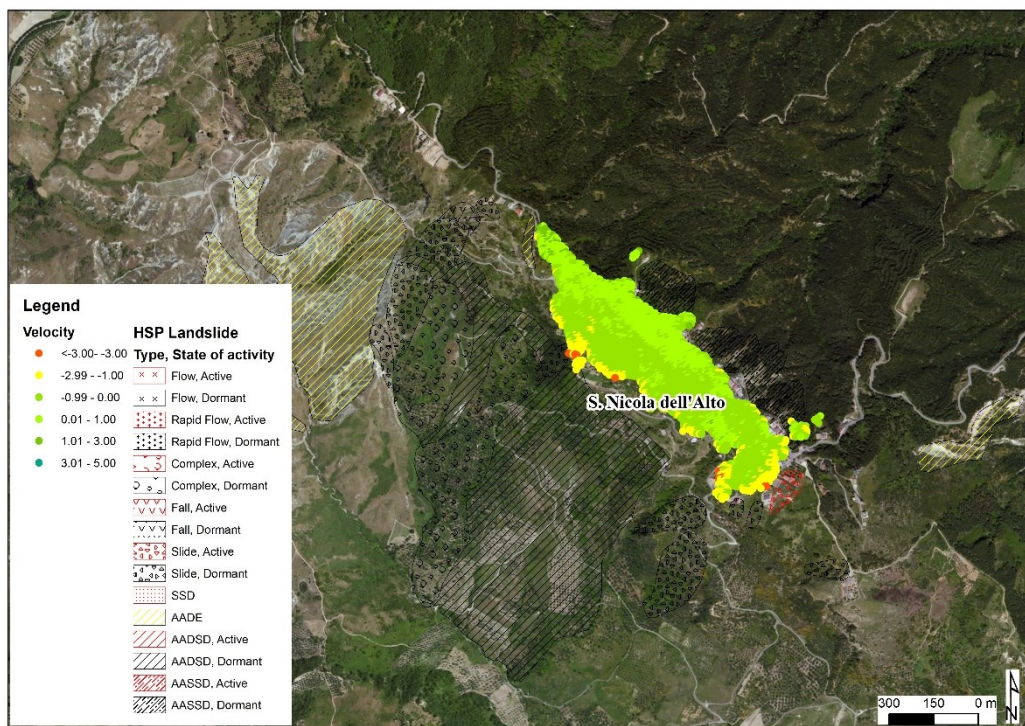


Figure 6.72 Displacement rates map obtained through the SBAS application on S. Nicola dell'Alto.

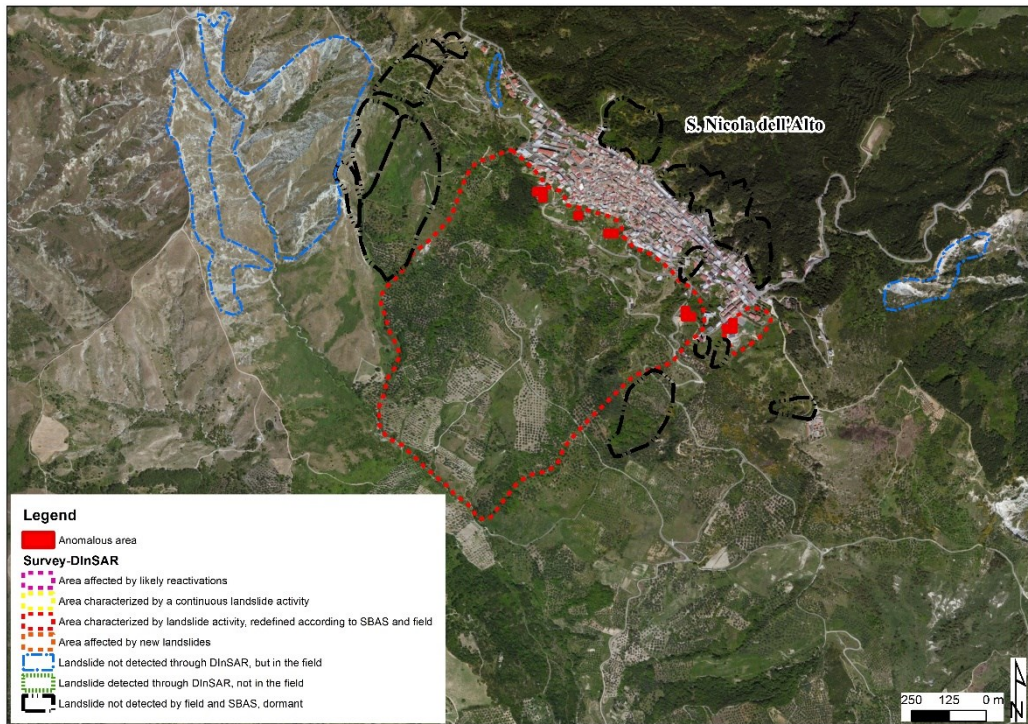


Figure 6.73 Landslide inventory map resulting from the joint application of DInSAR and field survey to S. Nicola dell'Alto.



Figure 6.74 Evidences of the SE landslide in S. Nicola dell'Alto. a) tilted electric lights and damage on the house; b) on the background, evidences of loose soils.

6.3.1.5 Casabona

Casabona is a municipality located in the central area of Crotone Province, counting 2.800 inhabitants (including the Zinga village). The urban area of Casabona is founded on the Casabona Formation (Upper Pliocene), composed of two lithofacies, one made of calcarenites and the other one of silty sandstones. In addition, the Castelsilano formation can be found, consisting in clastic deposits coming from the erosion of crystalline bedrock. Outcrops of the sandstone and clays of the Neto valley (Pliocene) can be also recognized, while the Zinga area is marked by the presence of the Timpa dei Cavalieri clay (Lower Pliocene), the Zinga (Middle Pliocene) and the Lipuda formations (Lower Miocene) (Fig. 6.76). The settlement of Casabona is located on a flat area, bounded by gentle slopes, while in Zinga the slopes are steeper; erosional forms (badlands), in fact, can be here recognized. HSP in Casabona and Zinga describes seven active and thirteen dormant landslides, for a total of twenty phenomena depicted (Fig. 6.76).

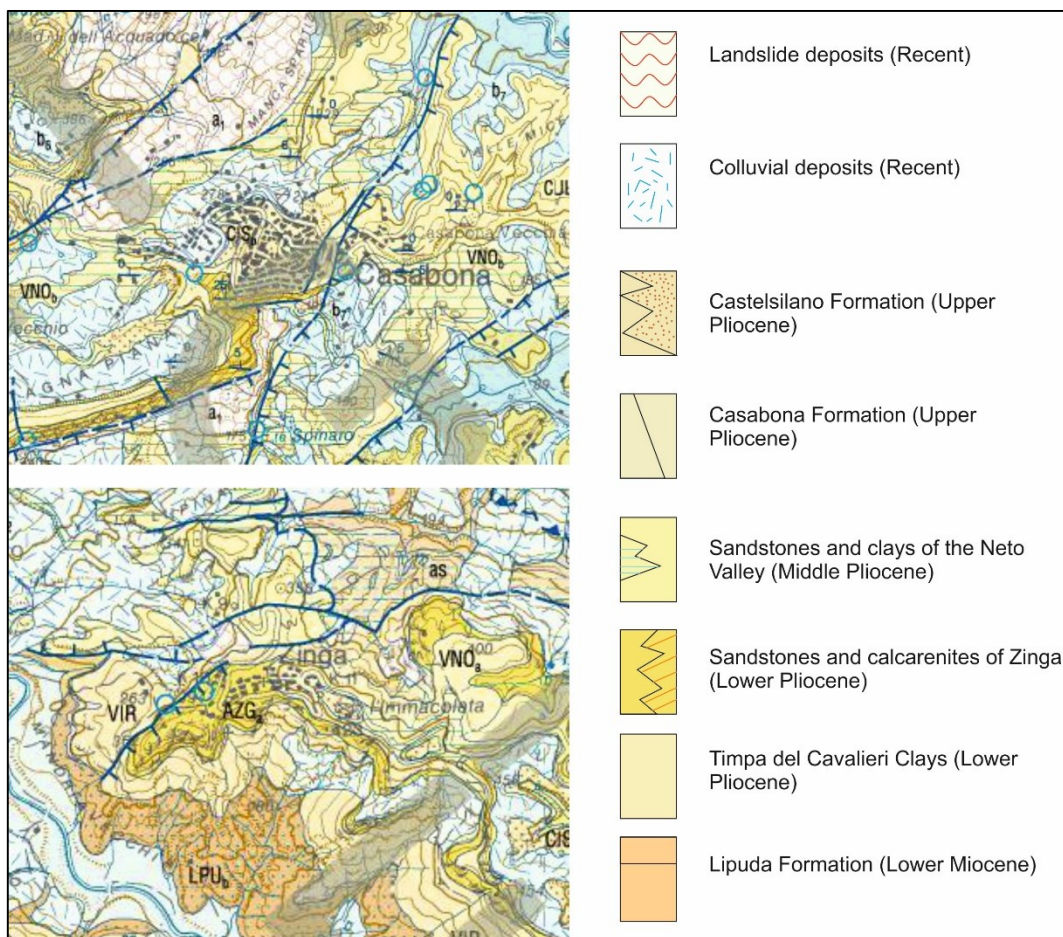


Figure 6.75 Geological map of Casabona, on the top, and Zinga, at the bottom (modified from Geological map 1:50.000, ISPRA, 2006).

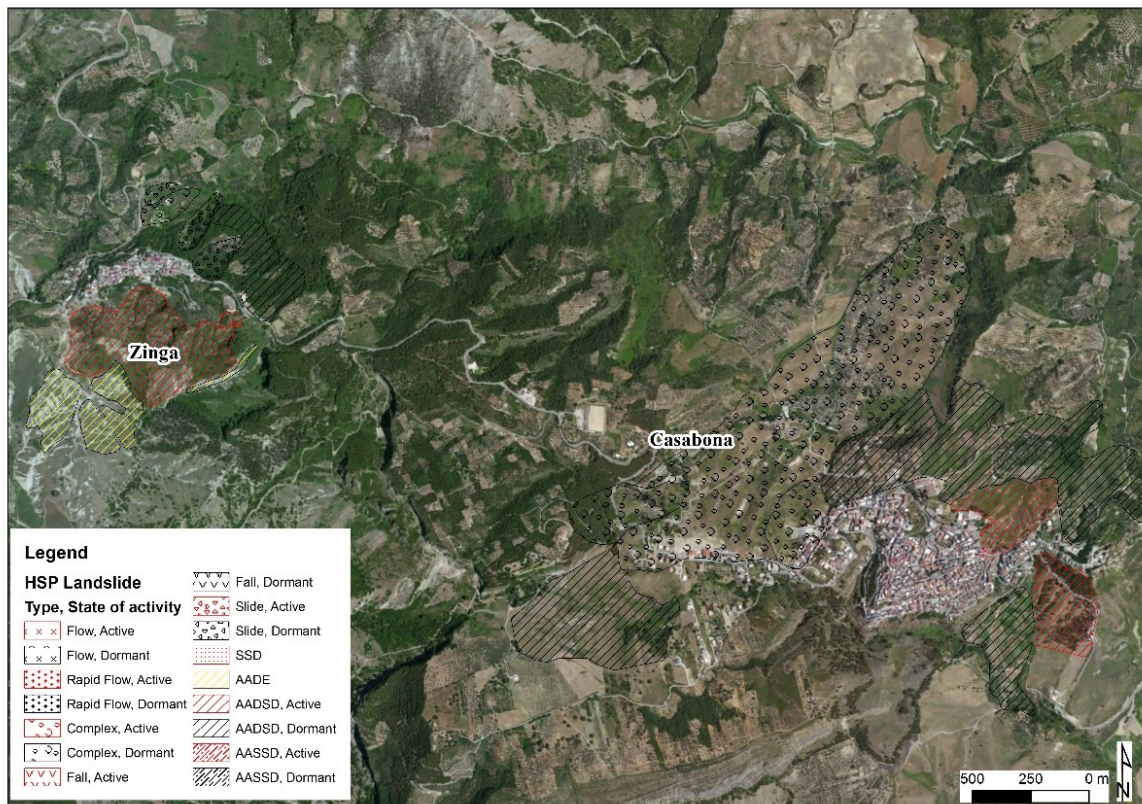


Figure 6.76 HSP map of Casabona (Calabria Basin Authority, 2006).

Almost 4.000 targets have been detected in the Casabona area, while in the Zinga neighborhood they are more than 1.000 (Fig. 6.77). The recognition of the anomalous areas in the western area of Casabona permitted to identify a sector affected by likely reactivation of a landslide formerly classified as dormant (Fig. 6.78). Moreover, other two clusters of anomalous concentrations have been generated; however, in this case no field evidences have been recognized. At last, seven landslides have been considered as dormant in the field and through the SBAS. In Zinga area, one anomalous area has been detected in correspondence of the local cemetery, and, as a consequence, following also field evidences (nude soil, concave-convexity of the ground), a landslide has been redefined. Moreover, other four landslides have been recognized only in the field, and five landslides have been considered as dormant (Fig. 6.79).

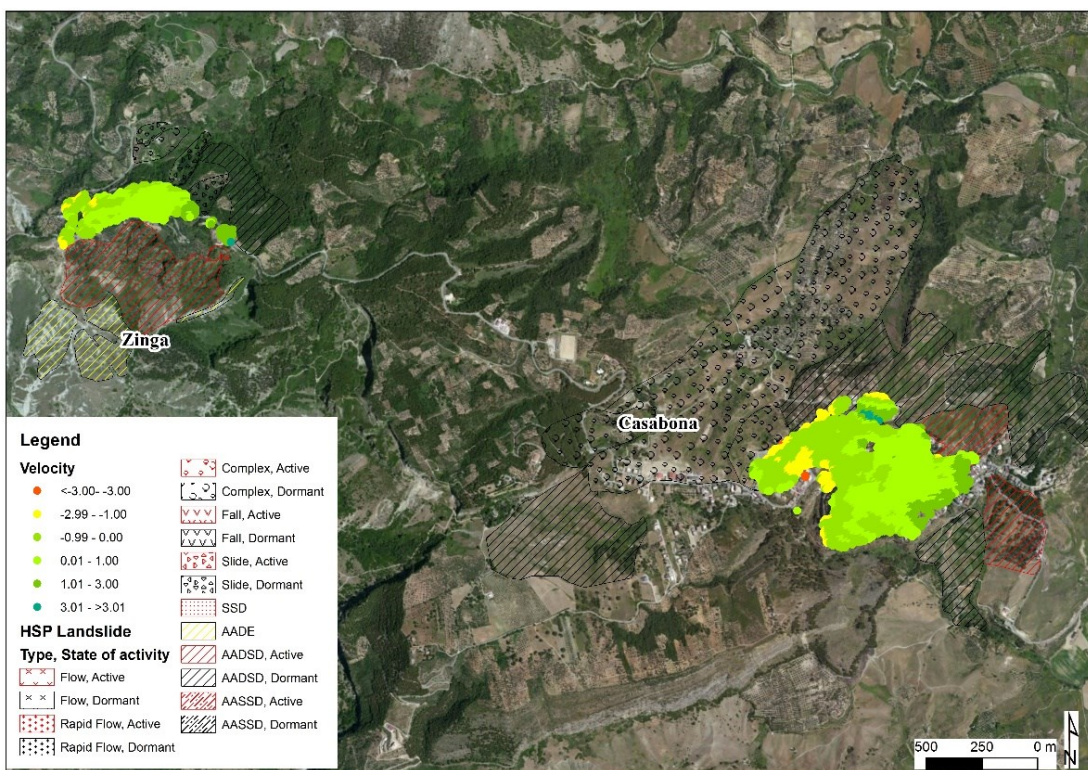


Figure 6.77 Displacement rates map obtained through the SBAS application to Casabona.

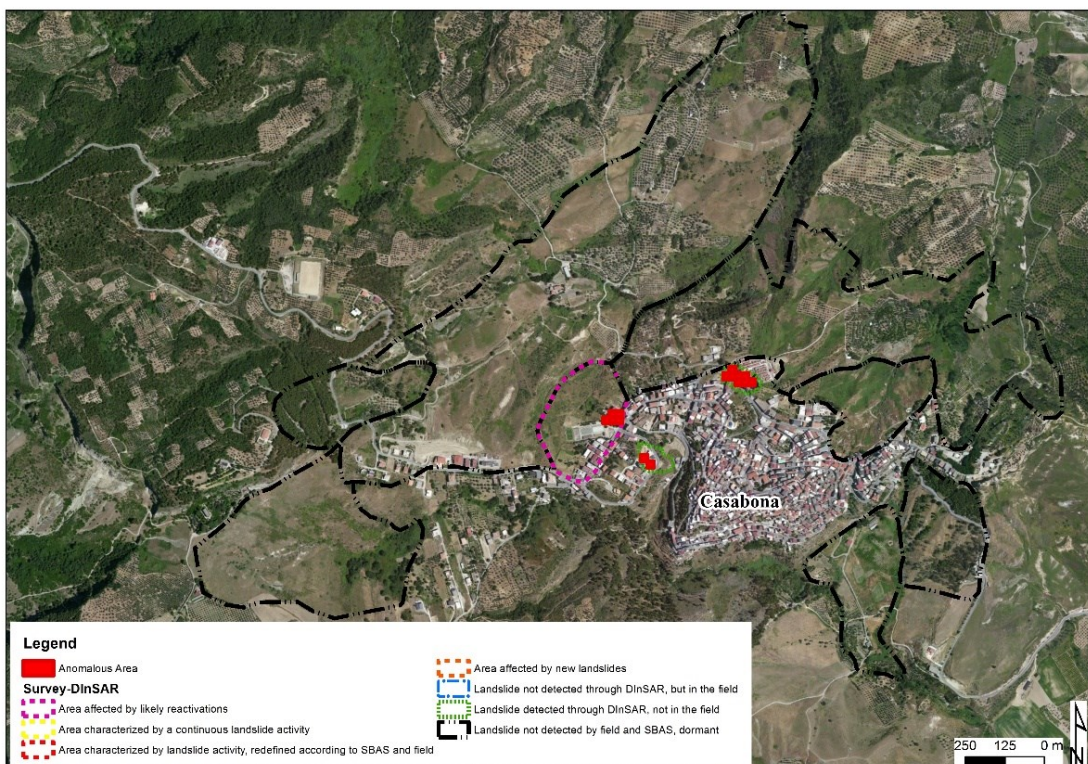


Figure 6.78 Landslide inventory map resulting from the joint application of DInSAR and field survey to Casabona.

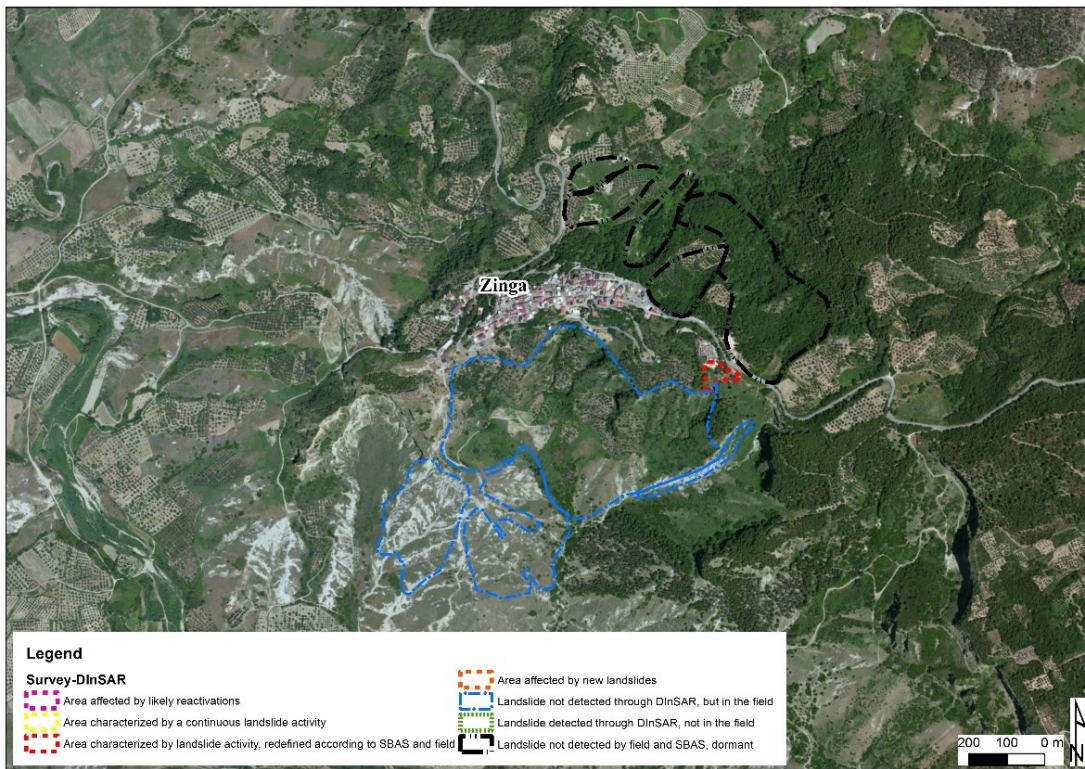


Figure 6.79 Landslide inventory map resulting from the joint application of DInSAR and field survey to Zinga area.

6.3.1.6 Strongoli

The territory of Strongoli is located in the central part of Crotone Province. The main geological formation is the Cutro marly clay (Piacenzian-Calabrian age), which is made of clays, marly and silty clays. The Strongoli member can be here distinguished, made of yellow from fine-grained to coarse-grained sandstones (Fig. 6.80).

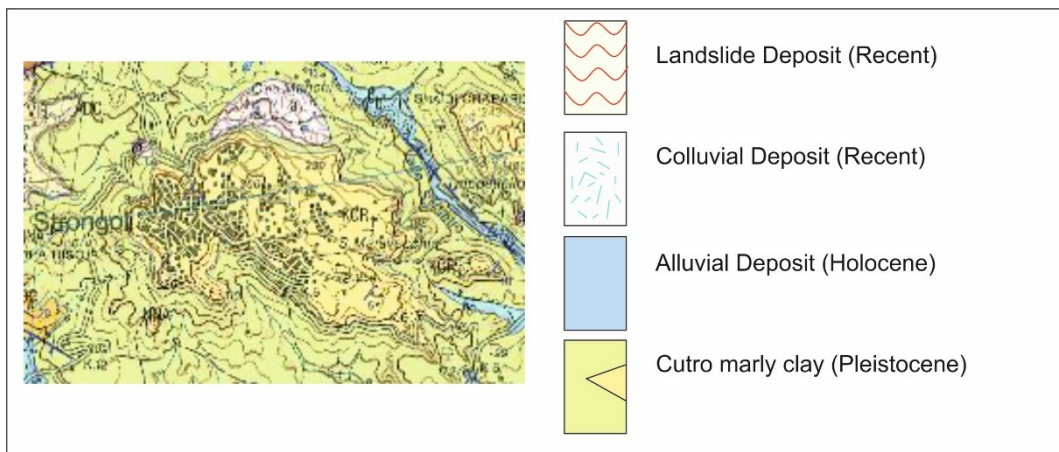


Figure 6.80 Geological map of Strongoli (modified from Geological map 1:50.000, ISPRA, 2006).

The inhabited area is placed on a flat area, the surrounding slopes show both steep gradients and gentle inclinations. The erosional action is very significant at Strongoli. The HSP reports in Strongoli two active landslides and thirteen dormant landslides, for a total of fifteen phenomena depicted (Fig. 6.81).

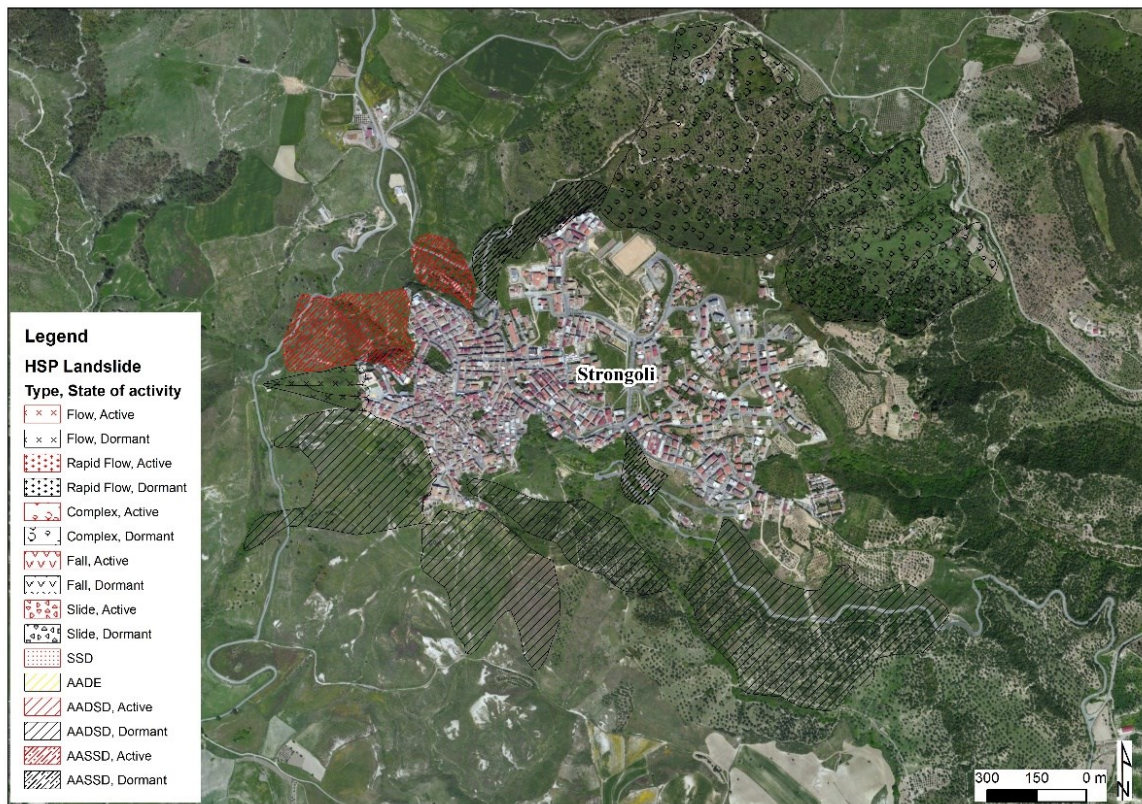


Figure 6.81 HSP map of Strongoli (Calabria Basin Authority, 2006).

On the whole territory of Strongoli, more than 8.000 CPs have been identified through the SBAS application (Fig. 6.82). Hereafter, three anomalous areas have been spotted (Fig. 6.83). The first one, on the NW sector of the town, allowed to redefine the landslide area, identifying a retrogressive trend, affecting the houses located along the border of the flat area and the slope, which shows evidences of detachments of rocky materials (Fig. 6.84). The second anomalous area supported the recognition of a new landslide, located below a house of recent construction, whose weight most likely reduced the stability of the slope located below (Fig. 6.84). Finally, in correspondence of the third anomalous area, no field evidences have been identified. At last, fourteen landslides have been classified as dormant, by the combined action of SBAS and field survey.

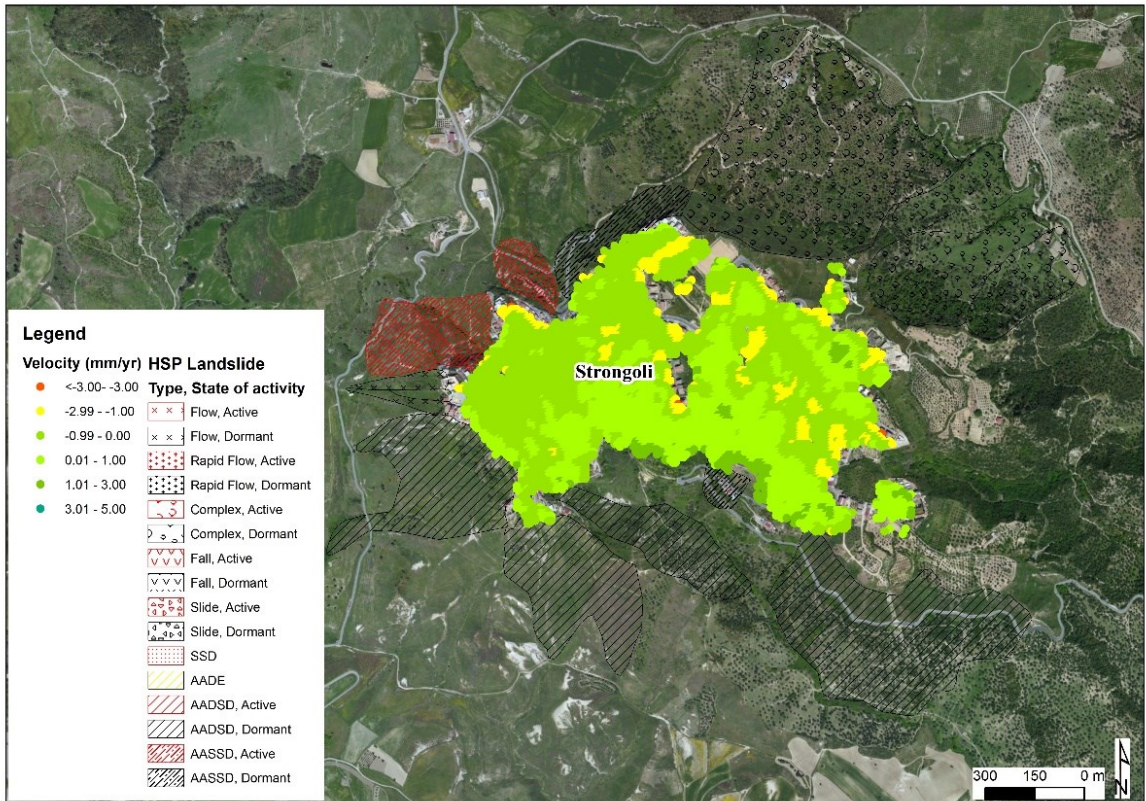


Figure 6.82 Displacement rates map obtained through the SBAS application to Strongoli.

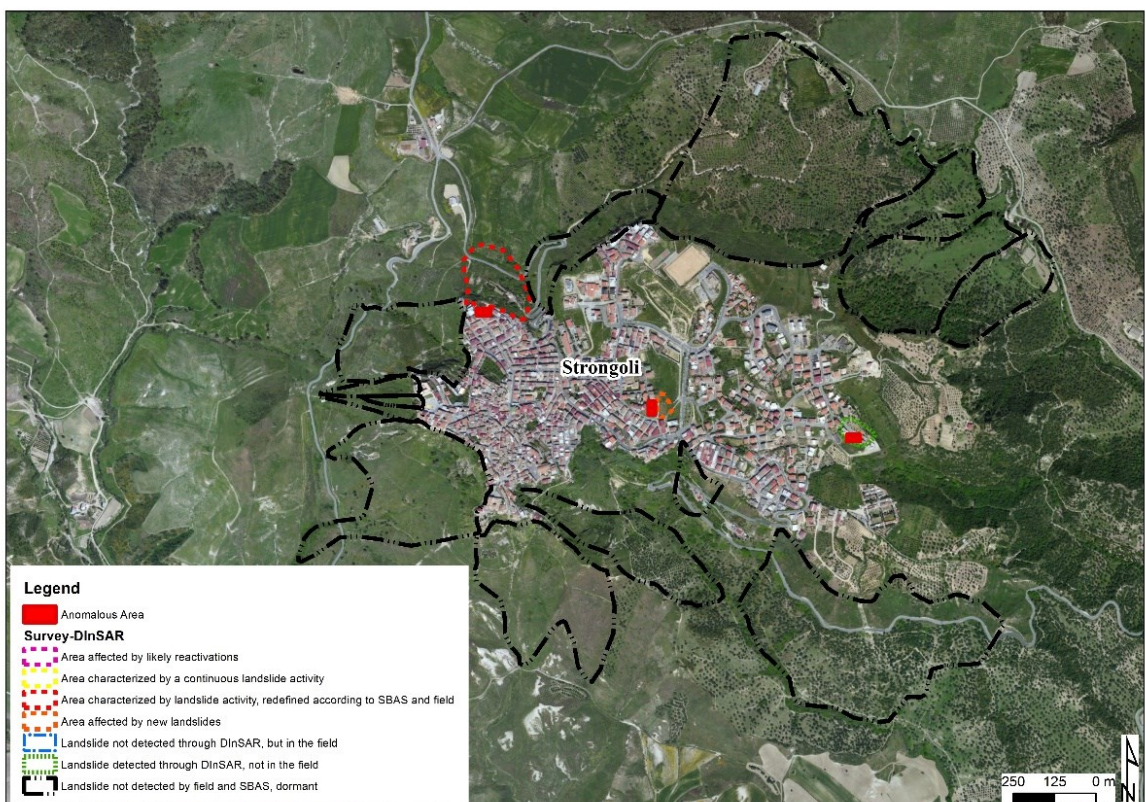


Figure 6.83 Landslide inventory map resulting from the joint application of DInSAR and field survey to Strongoli.



Figure 6.84 Evidences of the landslides in Strongoli: on the top, landslide redefined in the northern sector, on the bottom, new landslide in the central sector.

6.3.1.7 Rocca di Neto

Rocca di Neto is a municipality placed in the central band of Crotone Province, whose name derives from the Neto River, which crosses the municipal area. The main geological formation is the Cutro marly clay, but outcrops of the Scandale sandstone can be found, in the western part of the town. Down the valley different generation of alluvial sediments can be recognized (Fig. 6.85). The urban area is located upon a flat area, and the surrounding slopes present a high gradient, in particular in the northern sector. The southern part is characterized by more gentle inclinations. In the HSP twelve landslides are reported, six of them are active and six are dormant (Fig. 6.86).

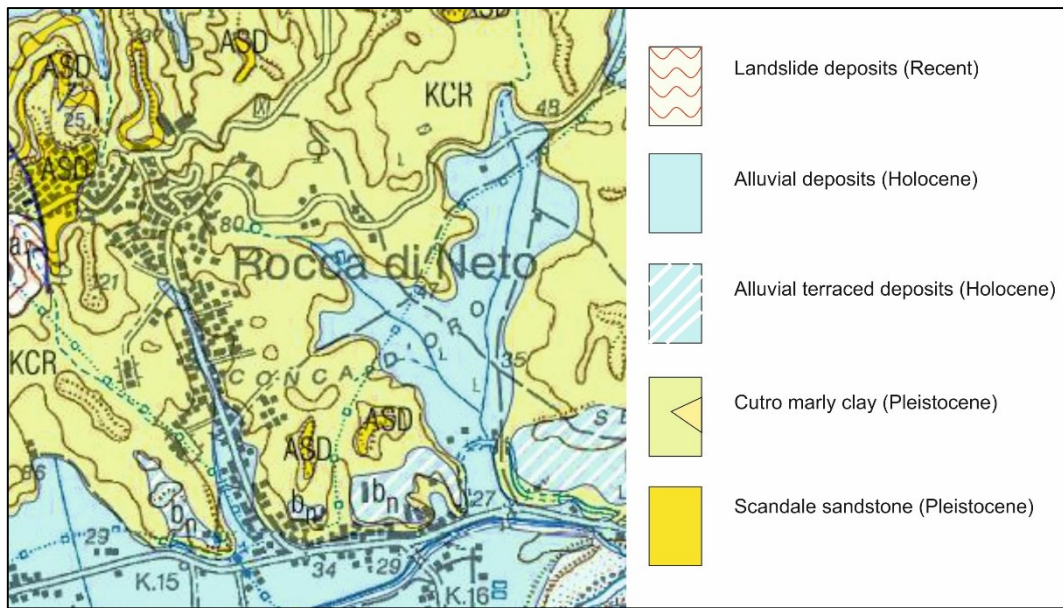


Figure 6.85 Geological map of Rocca di Neto(modified from Geological map 1:50.000, ISPRA, 2006).

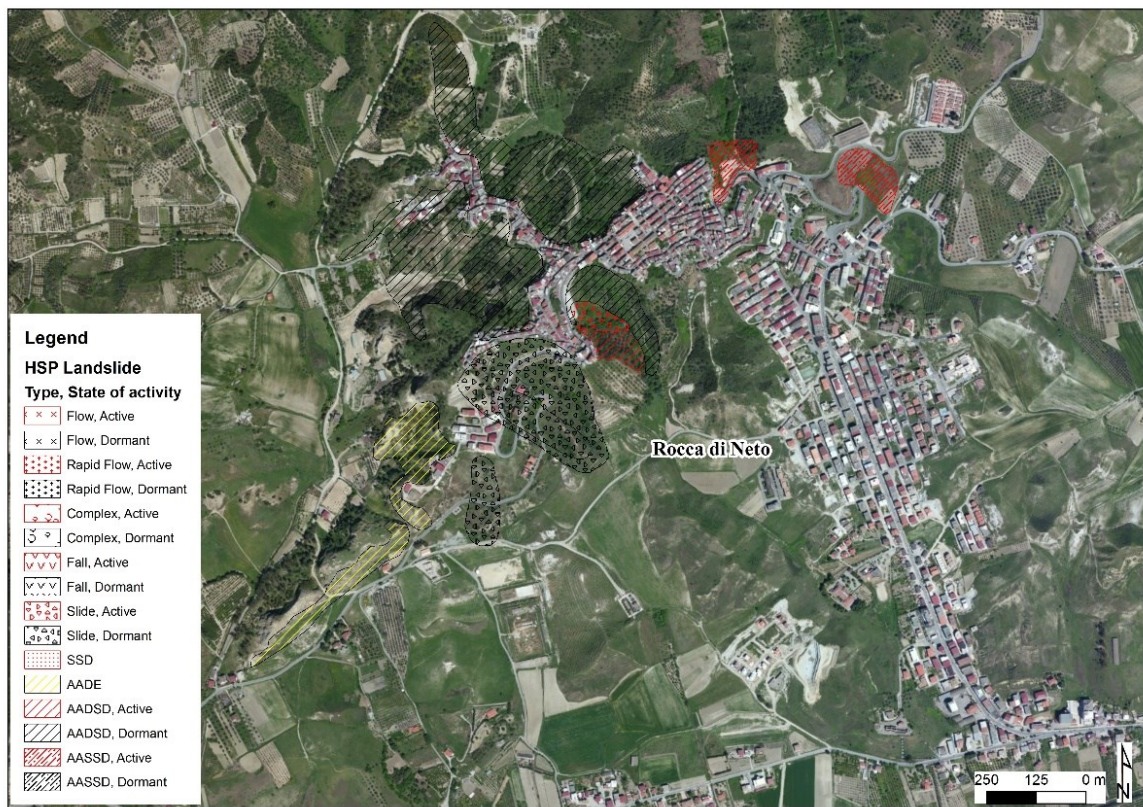


Figure 6.86 HSP map of Rocca di Neto (Calabria Basin Authority, 2006).

Through the SBAS implementation, it has been possible to detect 6.500 targets, covering almost the whole urban area of Rocca di Neto town (Fig. 6.87). Six anomalous areas, derived from the SBAS results, have been identified (Fig. 6.88). In two cases, in the western and in the northern sector, it has

been possible to redefine the landslide boundaries. In the first case, an active landslide has been recognized in a sector previously interested by instability; however, the active movement affects a part of the area previously interested. Evidences are fractures and nude soil outcrops on the slope, and at the base, rows of metallic gabions have been placed to protect the road crossing the area (Fig. 6.90). The second case is a landslide area, affecting several houses located along the main scarp and a road, crossing longitudinally the landslide. During the field activity, a swampy area, filled also with waste materials and garbage, just beneath the road level, has been noticed (Fig. 6.89). In addition, evidences of diffuse erosion on the flank of the landslides have been reported, testifying the high presence of superficial and underground water circulation (Fig. 6.89). According to local citizens, remedial works for protecting houses and roads located upstream, such as piles and retaining walls, have been installed, however, the displacement is still in act. In the SE sector of Rocca di Neto, four new landslides have been detected. In this case, the displacements occur in loose shallow terrains, very close to houses located in the area (Fig. 6.90). In the western area, moreover, two landslides have been recognized only during the field activity, while eight landslides have been classified as dormant.

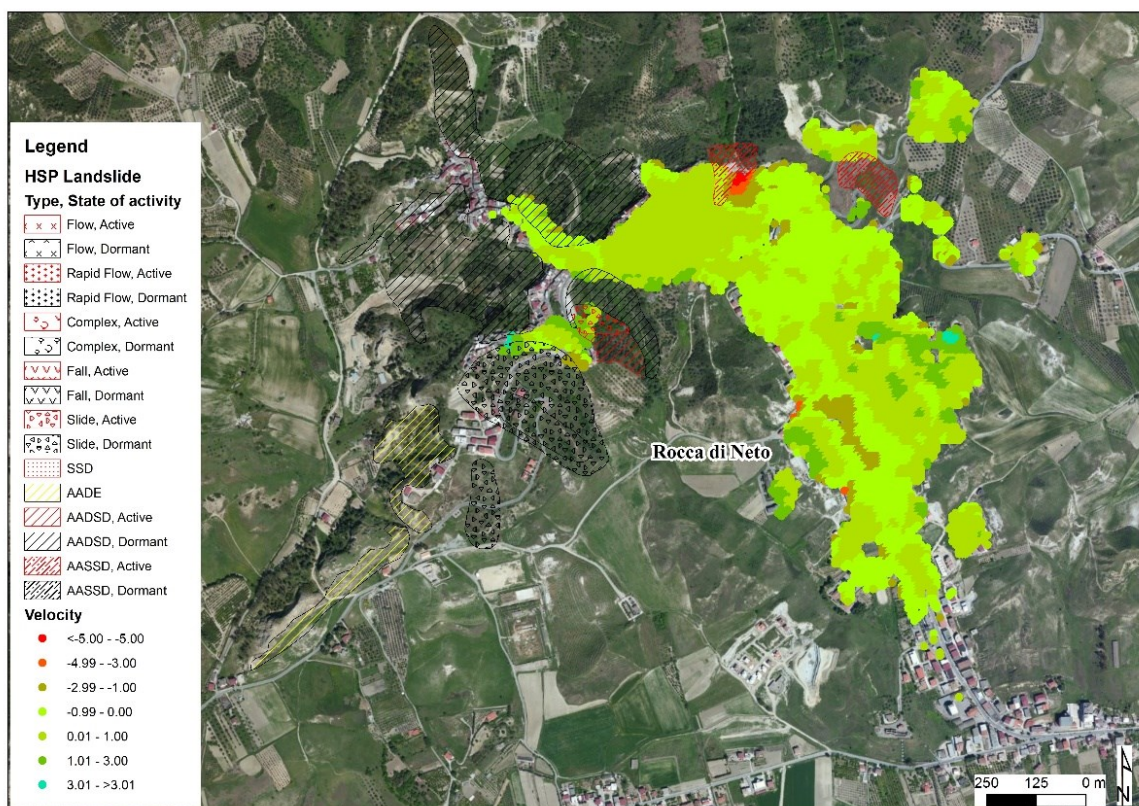


Figure 6.87 Displacement rates map obtained through the SBAS application on Rocca di Neto.

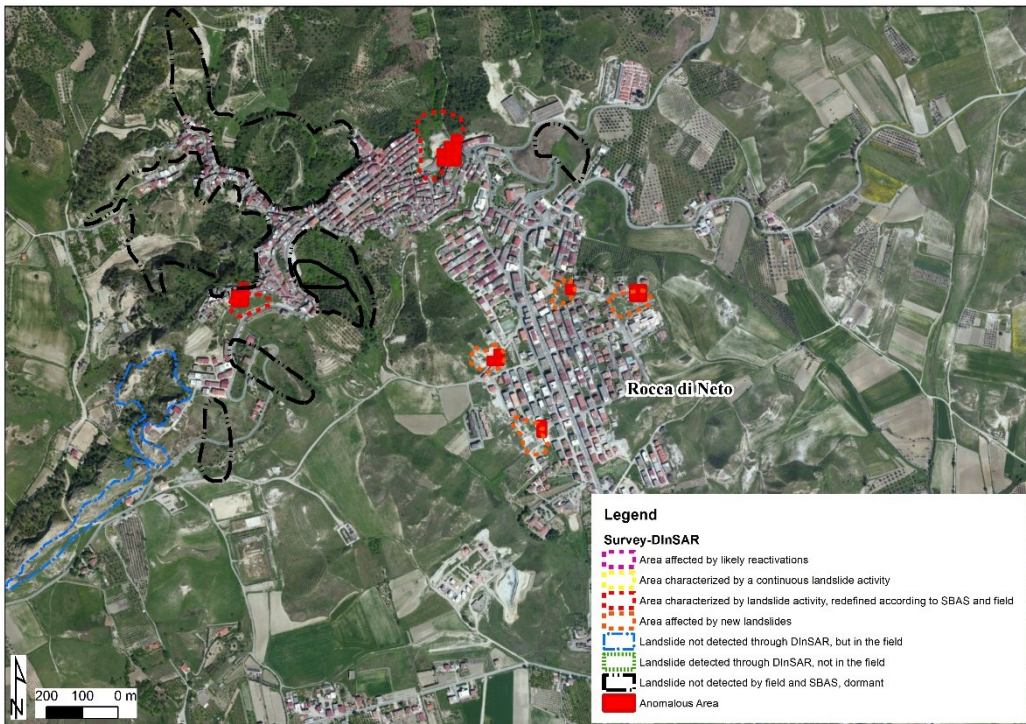


Figure 6.88 Landslide inventory map resulting from the joint application of DInSAR and field survey to Rocca di Neto.



Figure 6.89 Evidences of the northern landslide in Rocca di Neto, redefined after the field survey and the SBAS elaboration. a) damage and cracks reported on a sidewalk; b) swampy area reported in the landslide body; c) and d) evidence of gully erosion and superficial water circulation; e) broken wall; f) garbage in the landslide body

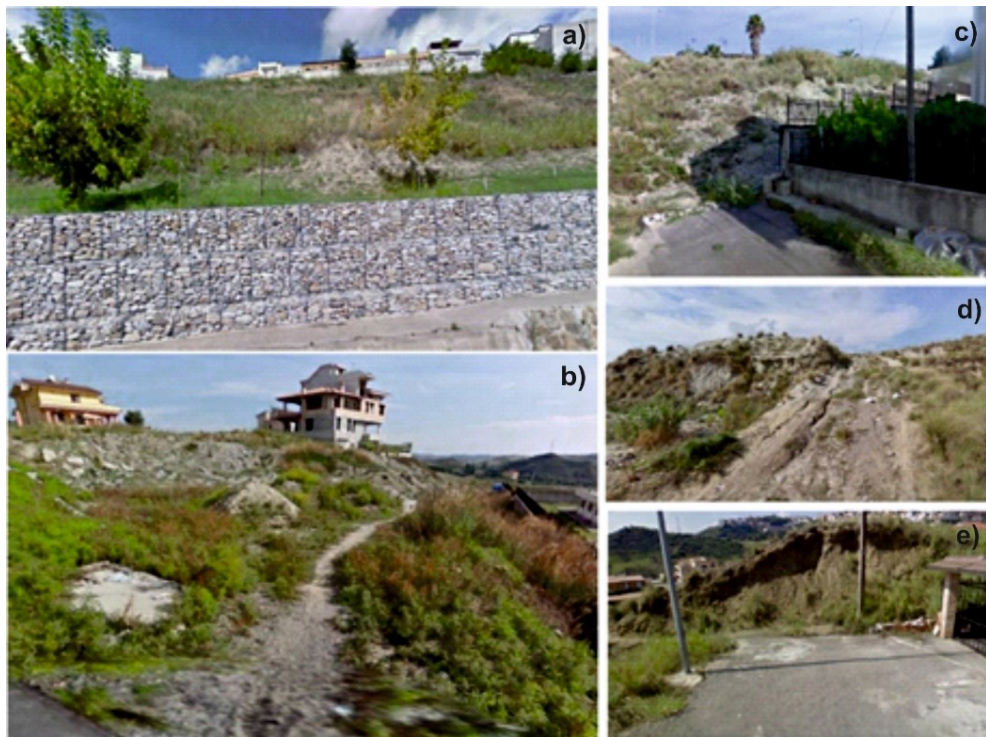


Figure 6.90 Evidences of the landslides in Rocca di Neto: a) redefined landslide in the western sector; b) c) d) and e) new landslides in the SE sector.

6.3.1.8 Santa Severina

Santa Severina is a municipality located in the central part of Crotone province, beneath the Neto River valley. The historical settlement is located on a 70 m-thick arenaceous rock of Pliocene age, belonging to the Molassa di Zinga Formation (Pliocene). Such formation lies on a clayey bedrock (Fig. 6.91).

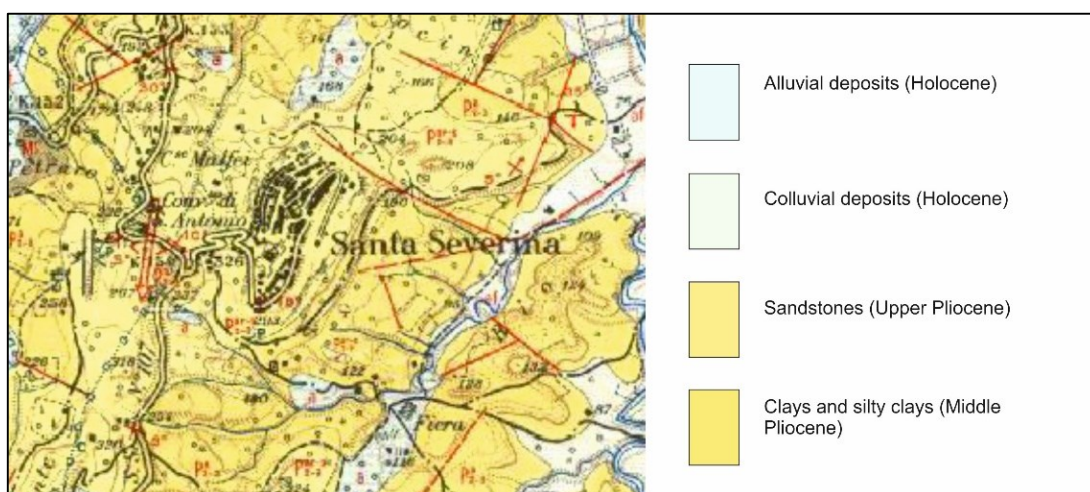


Figure 6.91 Geological map of S. Severina (modified from Geological map 1:25.000, CASMEZ, 1959).

The arenaceous rock presents vertical cliffs, subject to several erosional actions, generating also debris accumulations at the base of the slope. The rest of the town shows more gentle slopes, subject to slow and shallow movements. HSP reports thirty-one landslides, among which nineteen are considered as active, and twelve as dormant (Fig. 6.92).

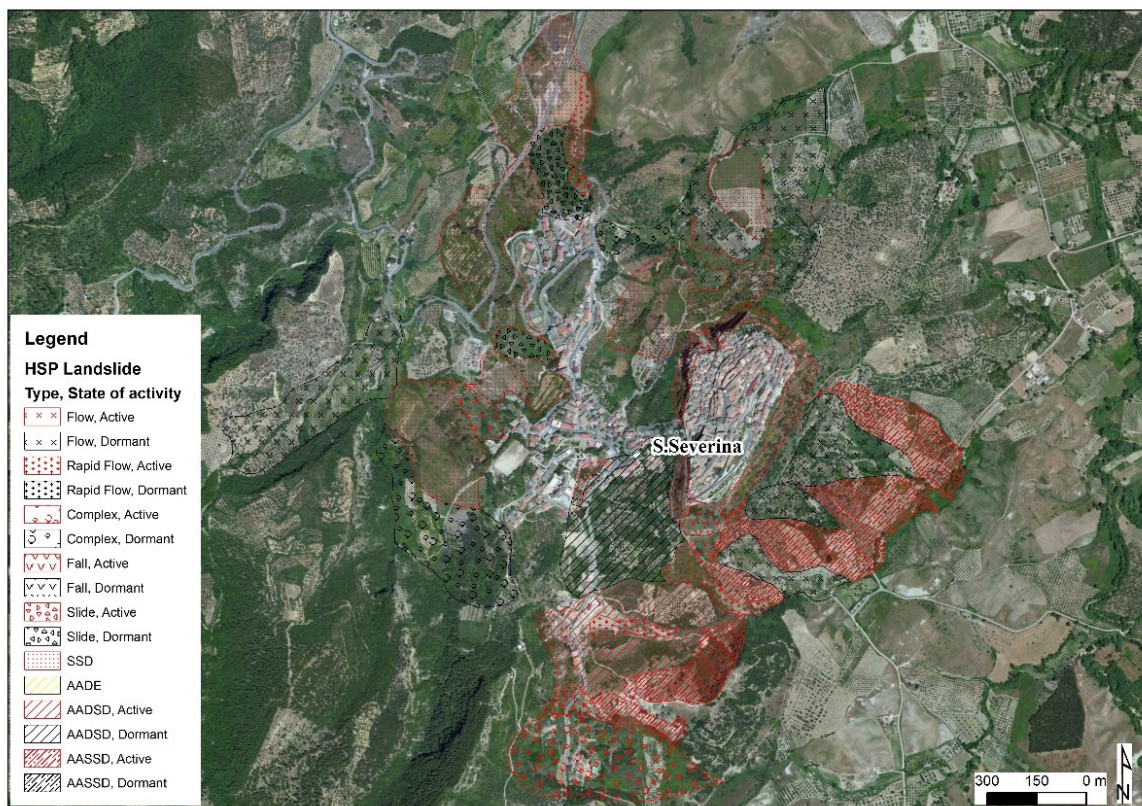


Figure 6.92 HSP map of Santa Severina (Calabria Basin Authority, 2006).

More than 1.000 points have been found through the SBAS technique (Fig. 6.93), which enabled the generation of two anomalous areas, both located in the western part of the town (Fig. 6.94). In both cases, such features allowed to modify the landslide boundaries, identifying a retrogressive trend. In the northern part, damage to few houses have been reported during the field activity (Fig. 6.95); in the southern sector, protective gabions, as well as the vegetation, are slightly inclined downslope (Fig. 6.95), thus testifying a slow deep movement in both cases. Moreover, ten landslides, located on both sides of the town, have been identified exclusively during the field activity, while eighteen landslides have been considered as dormant.

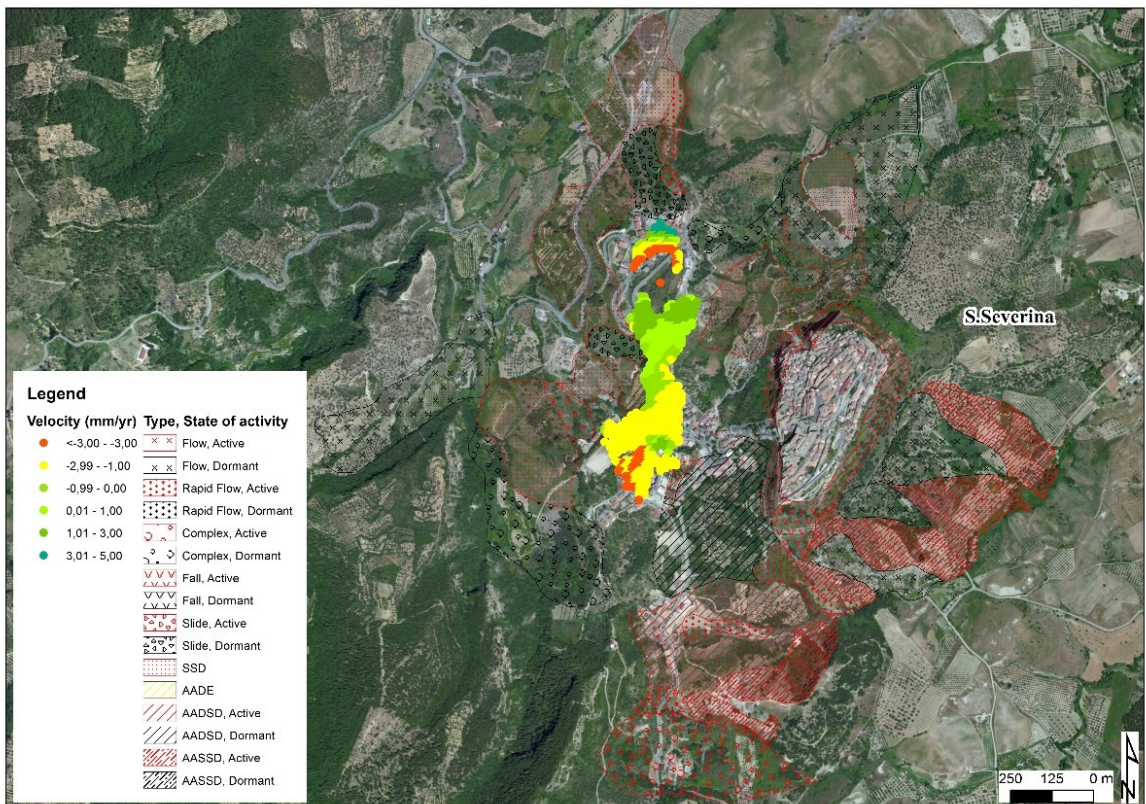


Figure 6.93 Displacement rates map obtained through the SBAS application to S. Severina.

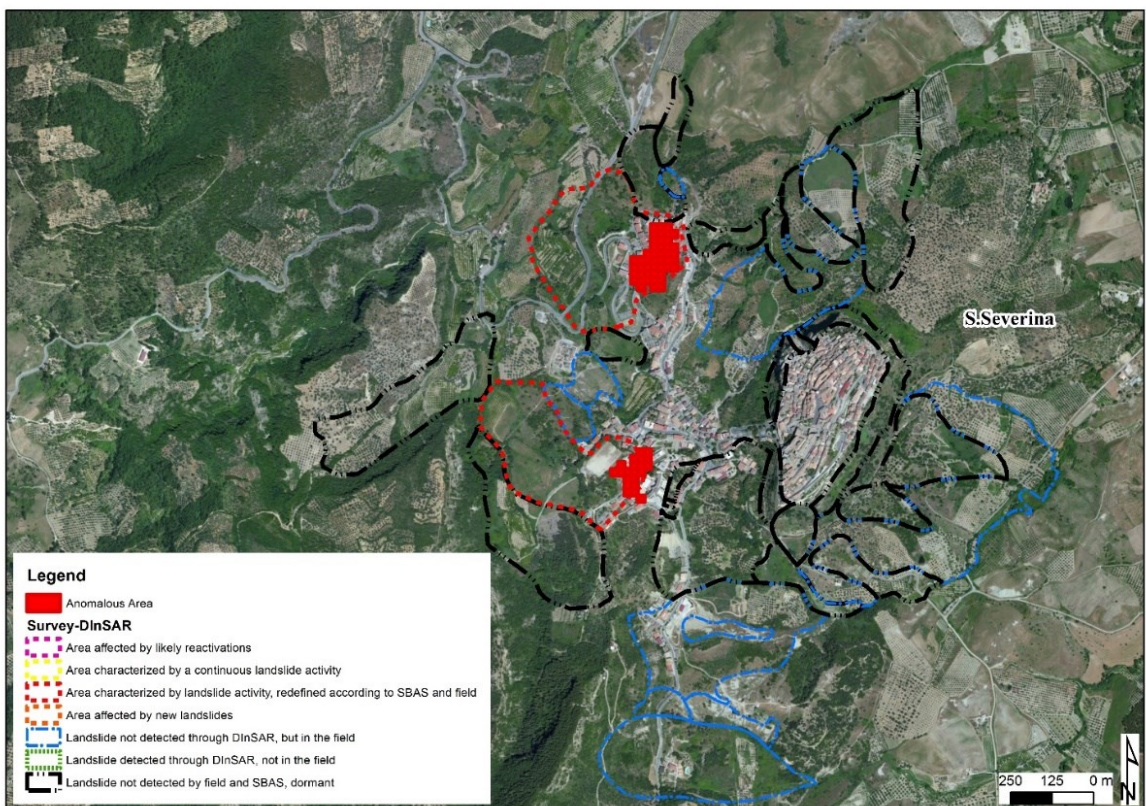


Figure 6.94 Landslide inventory map resulting from the joint application of DInSAR and field survey to S. Severina.



Figure 6.95 Evidences of the landslides in Santa Severina: on the left, crack reported in a house within the redefined landslide in the NW sector; on the right, damaged retaining wall reported in the SW sector redefined landslides.

6.3.1.9 San Mauro Marchesato

San Mauro Marchesato is a municipality of 2.100 inhabitants, located in the central part of the Crotone province. The geological setting is dominated by the overlap between clays and sandstones, Pliocene in age (Fig. 6.96). The inhabited area is located on a ridge with direction NE-SW, and the surrounding slopes present low gradient and several erosional forms. In the HSP nineteen landslides have been recognized, five of which are considered active and fourteen dormant (Fig. 6.96).

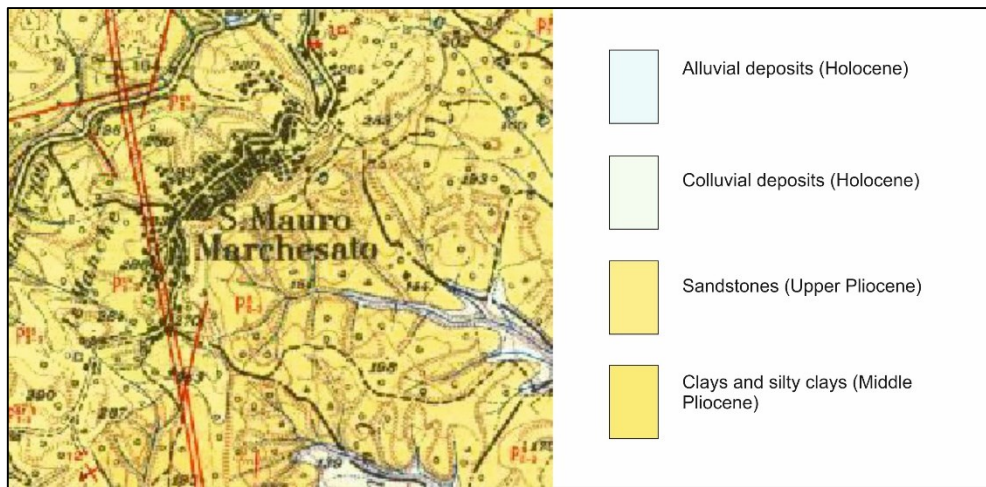


Figure 6.96 Geological map of S. Mauro Marchesato (modified from Geological map 1:25.000, CASMEZ, 1959).

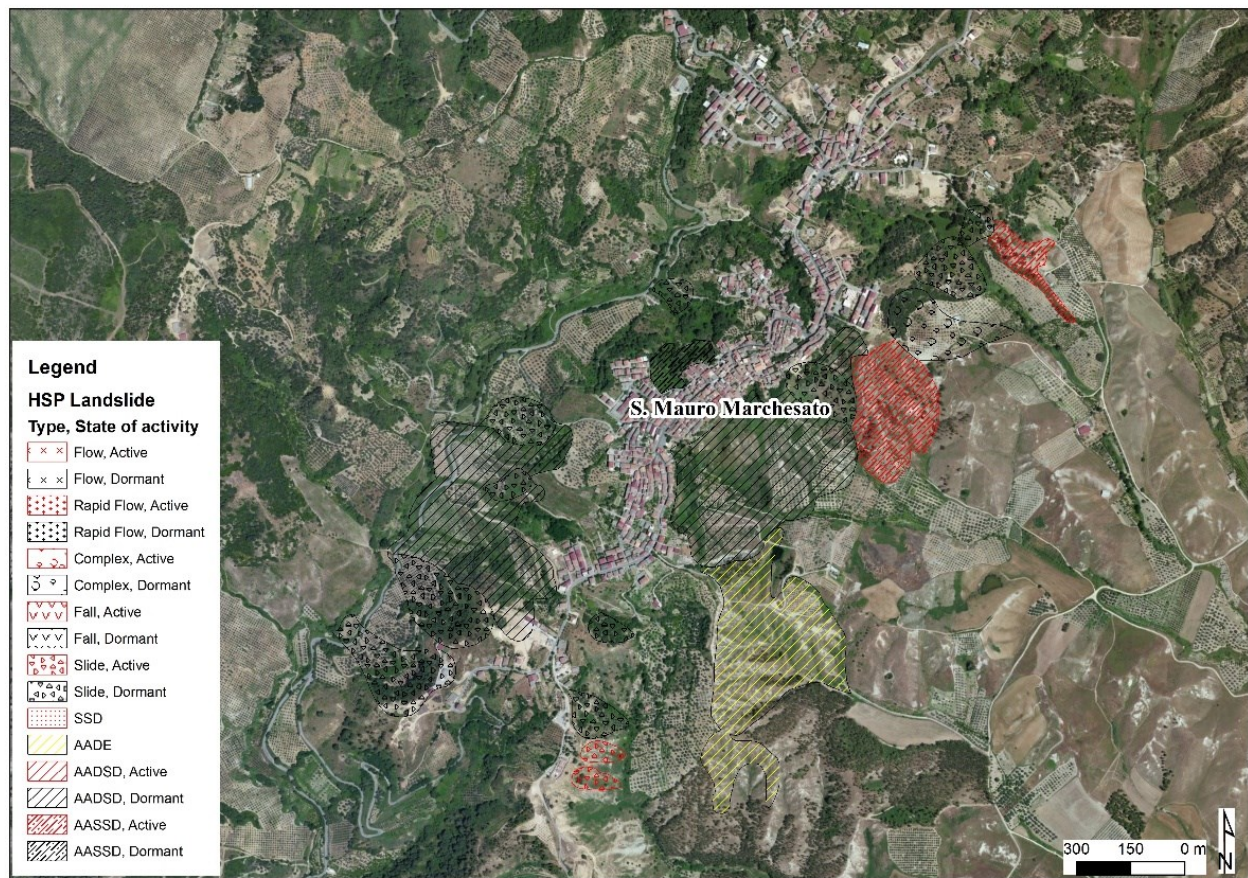


Figure 6.97 HSP map of San Mauro Marchesato (Calabria Basin Authority, 2006).

More than 4.000 targets have been identified on the territory of San Mauro Marchesato (Fig. 6.98). One anomalous area has been derived from the SBAS data, in the northern sector, however, not finding any correspondence in the field (Fig. 6.99). Moreover, seven landslides have been recognized

exclusively through the field activity, all located along the eastern and northern sector of the town, and finally, fifteen landslides have been considered as dormant, after the DInSAR elaboration and the field survey.

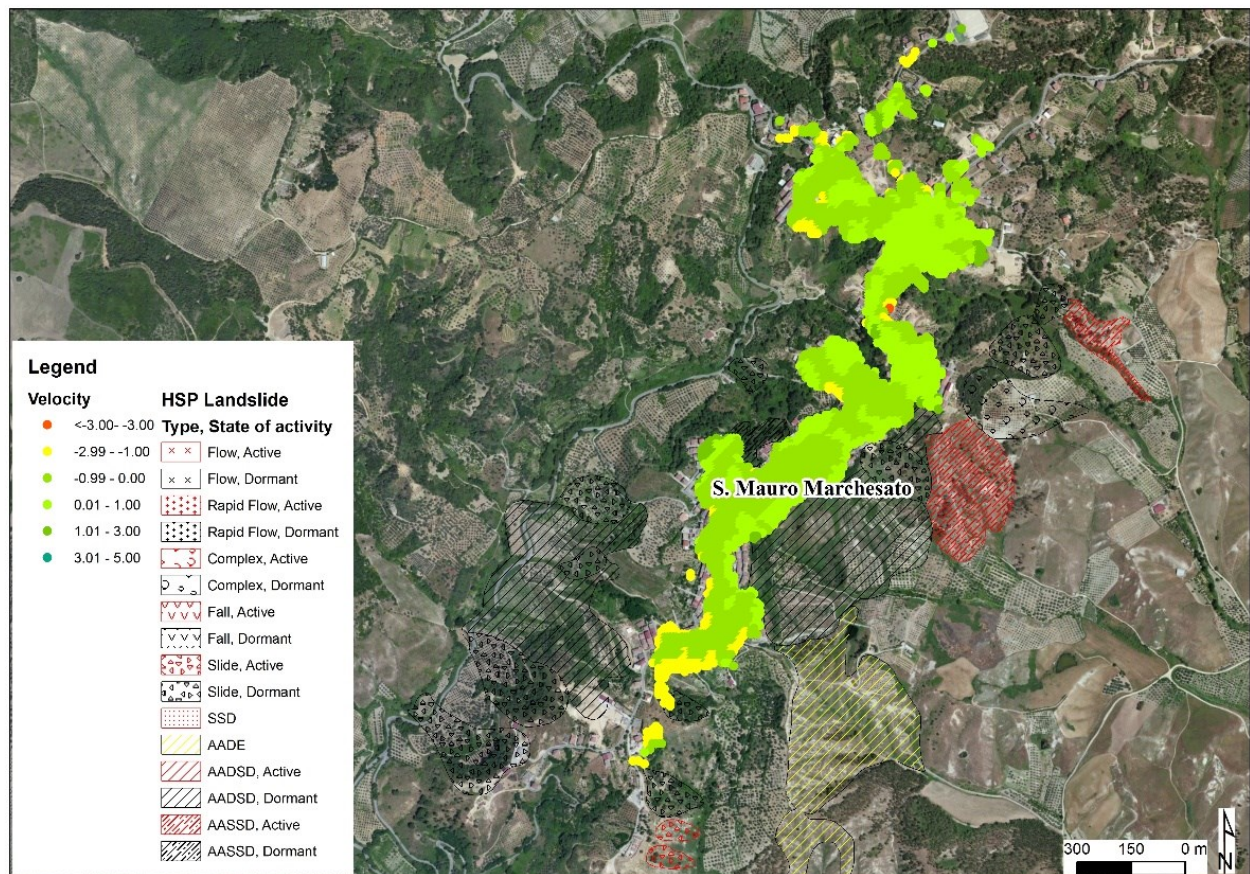


Figure 6.98 Displacement rates map obtained through the SBAS application to S. Mauro Marchesato.

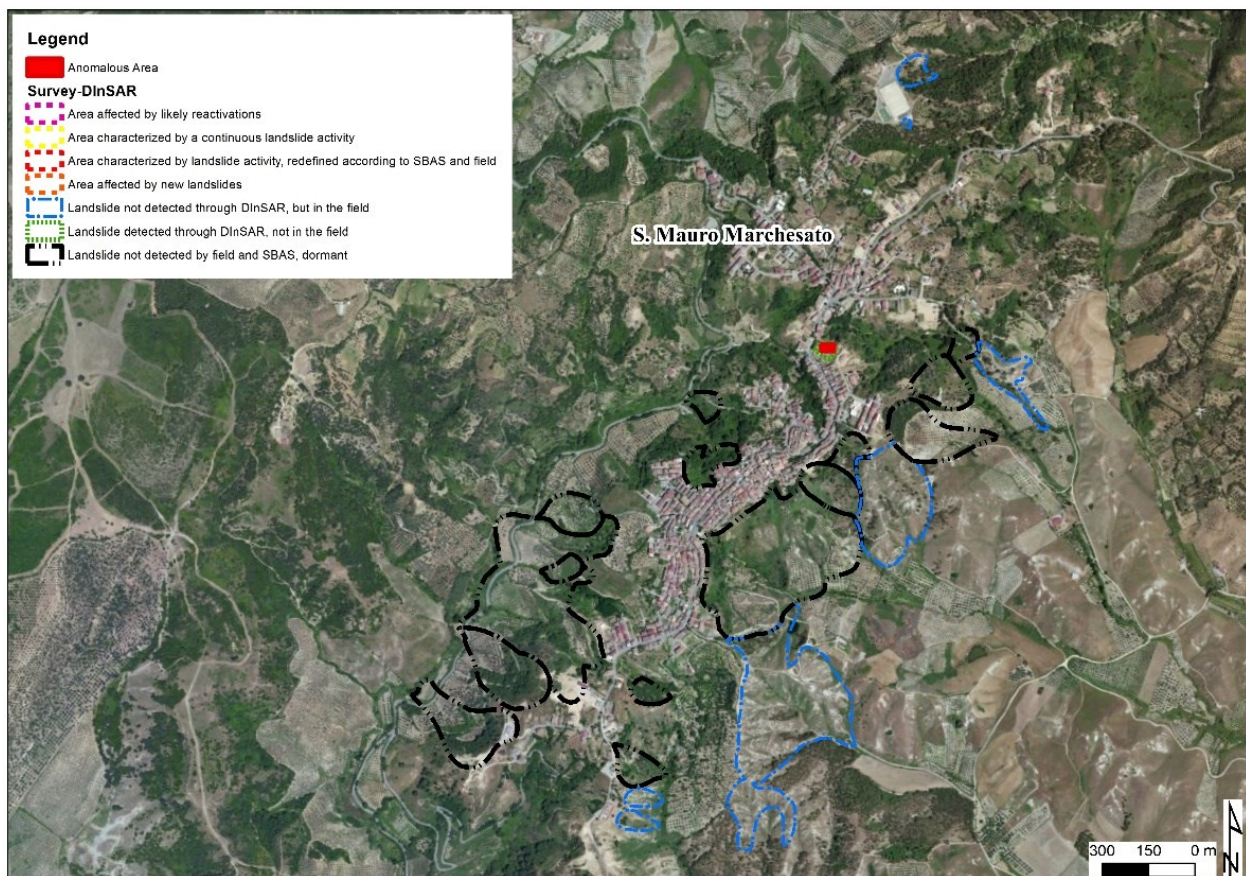


Figure 6.99 Landslide inventory map resulting from the joint application of DInSAR and field survey to S. Mauro Marchesato.

6.3.1.10 Scandale

Scandale is a municipality of about 3.000 inhabitants, located in the central part of Crotone Province. The geological setting of the area is characterized by the presence of Pliocene terrains, mostly composed of the sandstones and dark sands of Middle Pliocene age, with few outcrops, especially in the northern sector, of silty clays of Calabrian age (Fig. 6.100).

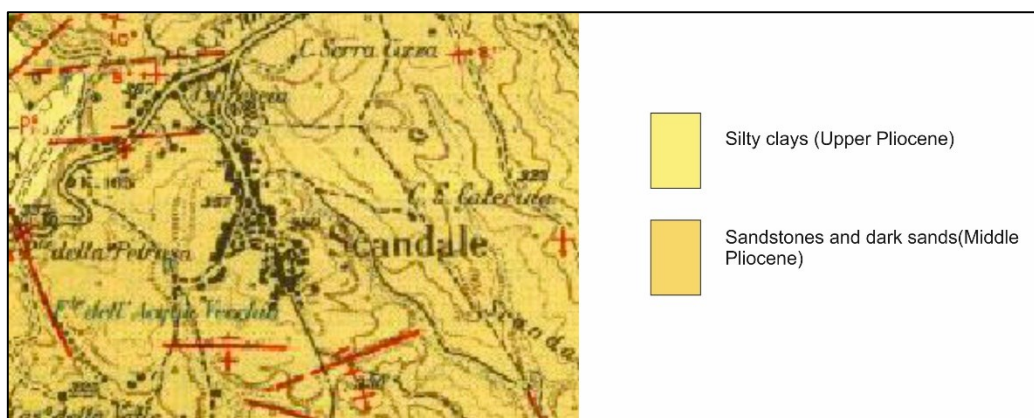


Figure 6.100 Geological map of Scandale (modified from Geological map 1:25.000, CASMEZ, 1959).

The urban area is sited along a SW-NE elongated-shaped hill, with a segment southwards. The surrounding slopes present a higher inclination onto the top, grading toward the bottom into gentler inclinations, sometimes with erosional forms, especially in the NW sector. HSP identified three active landslides and fourteen dormant landslides, for a total of seventeen phenomena depicted (Fig. 6.101).



Figure 6.101 HSP map of Scandale (Calabria Basin Authority, 2006).

Ca. 6.700 targets have been generated through the SBAS application to Scandale town (Fig. 6.102), allowing to obtain three different anomalous areas (Fig. 6.103). In the area located in the NW facing slope no correspondence has been found in the field, hence classifying the area as landslide detected in the field, not through DInSAR, while in the southern sector of the town, the two anomalous areas identified allowed to detect two new landslides, previously not included in the HSP database. The first one, located westward, affects a slope located upon a road and below a group of houses (Fig. 6.104); the second landslide, located eastward, is sited in correspondence of a river channel, whose banks undergo to diffuse erosion, most likely in occurrence of intense rainfall events (Fig. 6.104). In addition, sixteen landslides have been classified as dormant, after the joint application of DInSAR and field activity.

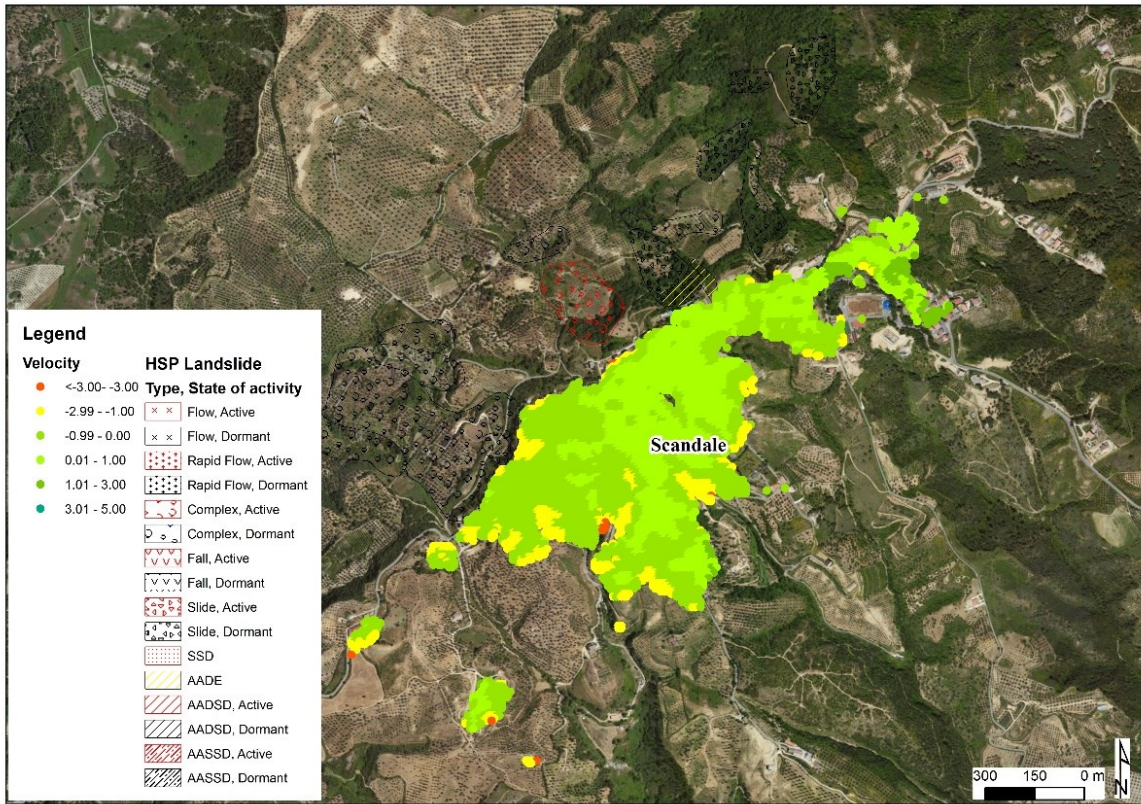


Figure 6.102 Displacement rates map obtained through the SBAS application to Scandale.

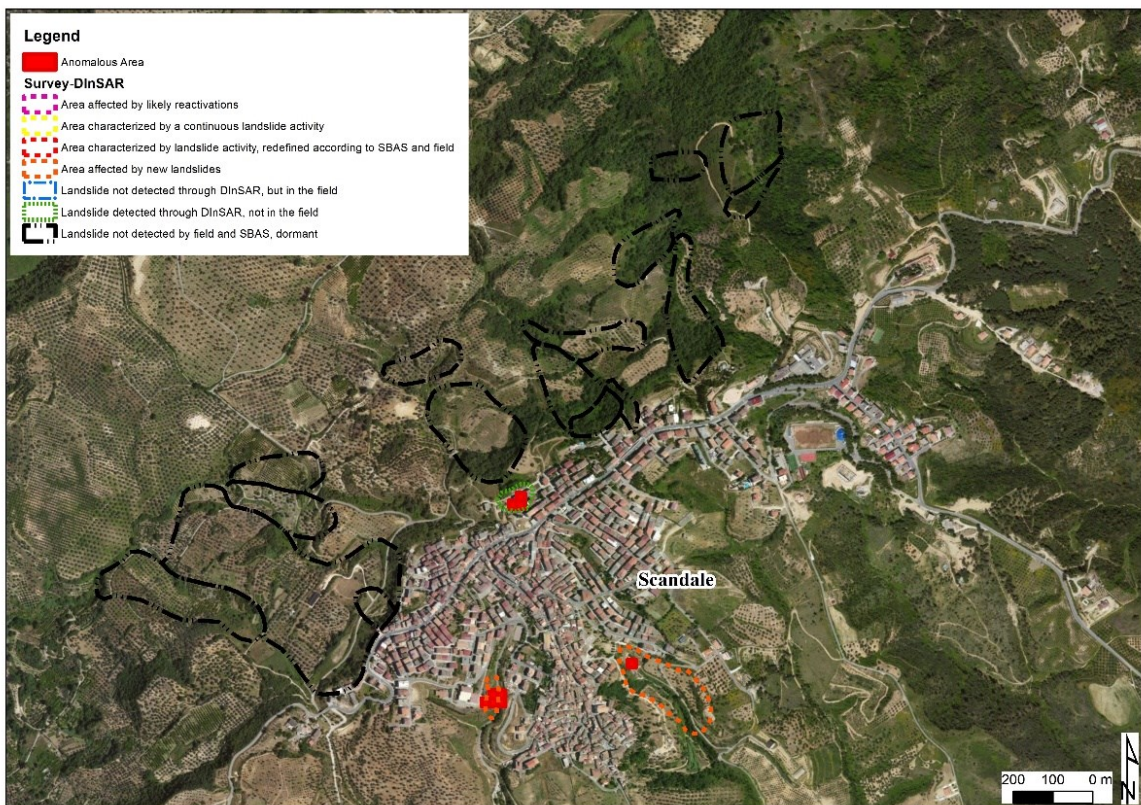


Figure 6.103 Landslide inventory map resulting from the joint application of DInSAR and field survey to Scandale.



Figure 6.104 Evidences of the landslides in Scandale: on the left, evidences of the new landslide in the SW sector; on the right, fracture in the new landslide in the SE sector.

6.3.1.11 Cutro

Cutro is a municipality of more than 10.000 inhabitants located in the southern sector of the Crotone Province. The local geological setting is marked by the overlap between the Pleistocene dark sands and conglomerates at the top and the grey, blue-grey silty clays of Pliocene age, belonging to the Cutro Marly Clay Formation, at the bottom (Fig. 6.105).

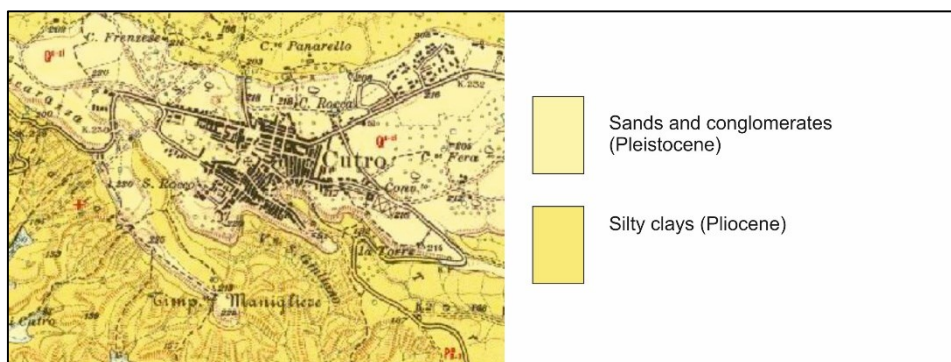


Figure 6.105 Geological map of Cutro (modified from Geological map 1:25.000, CASMEZ, 1959).

The town can be divided into two different sectors, from a geomorphological point of view: a first part, characterized by a hilly morphology and sometimes, especially in the southern sector, by a significant erosional activity, testified by the presence of badlands involving the clay lithology, and a flat morphology, where the town has been founded, slightly graded toward the coast, made of marine terraces deposits. The latter can be found in different generations, due to the several eustatic cycles occurred in the Crotone area. HSP counts only four landslides, but very large in extension, and two have been classified as active and two as dormant (Fig. 6.106).

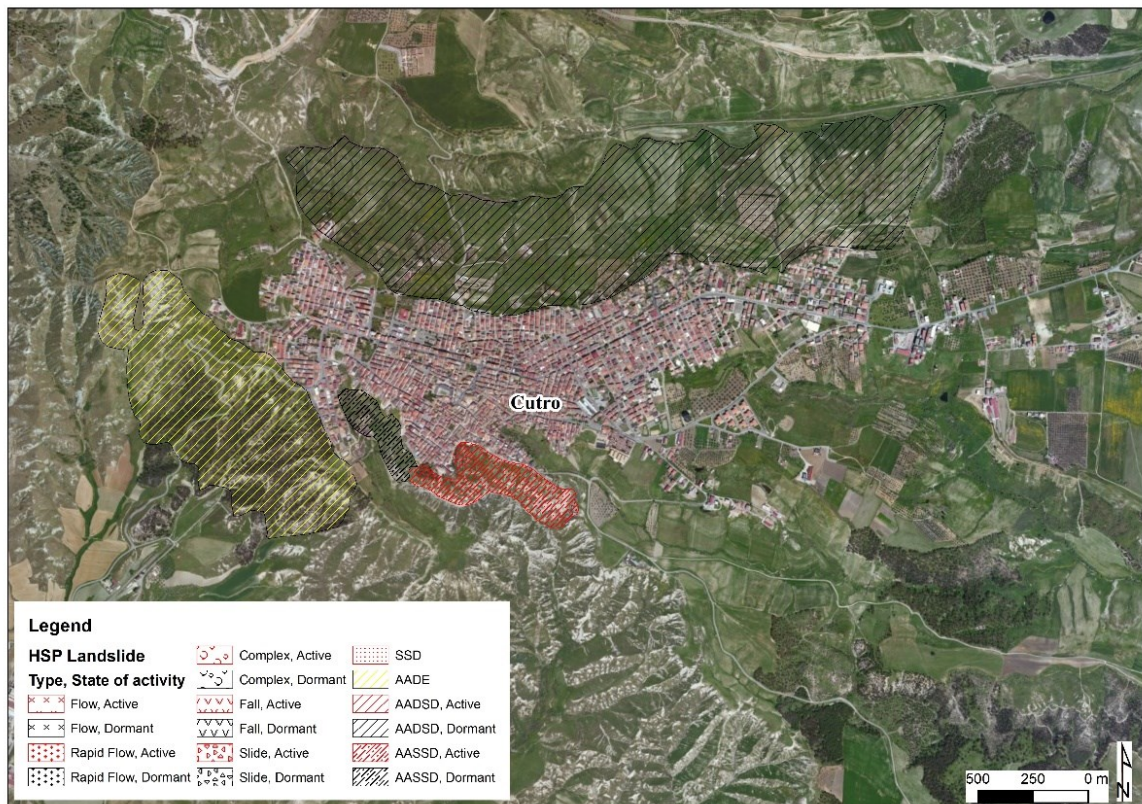


Figure 6.106 HSP map of Cutro (Calabria Basin Authority, 2006).

22.000 targets have been recognized through the SBAS application to Cutro area (Fig. 6.107), which enabled to recognize several aggregates of anomalous areas (Fig. 6.108). A first significant concentration of anomalous areas has been recognized in the north-facing slope, allowing to redefine the state of activity and the boundary of a deep slope deformation area, now considerable as active and interesting mostly the eastern part of the slope, according to SBAS data and field survey (Fig. 6.109 a and b). In the southern sector, a first concentration of anomalous area allowed to define the continuous activity of an area affected by diffuse erosion of clayey material; eastward, a cluster of anomalous area identified the pre-failure activity of a landslide which, according to news reports, on February 23, 2012, caused damage to several houses, to a concrete platform and to remedial works for water regulation (Fig. 6.109 c, d, e and f). Damage have been reported also during the field activities, and the landslide has been redefined, affecting a part of the slope previously identified as affected by deformation. In the SE sector of the town, three anomalous areas have been recognized exclusively through the SBAS application, while in the eastern part of the town other anomalous areas are located on flat areas, hence they cannot be interpreted as landslides, but could be attributed to vertical motions related to water extraction for agricultural use, being located in farmlands. At last, one landslide has been classified both during field activities and through SBAS implementation as dormant.

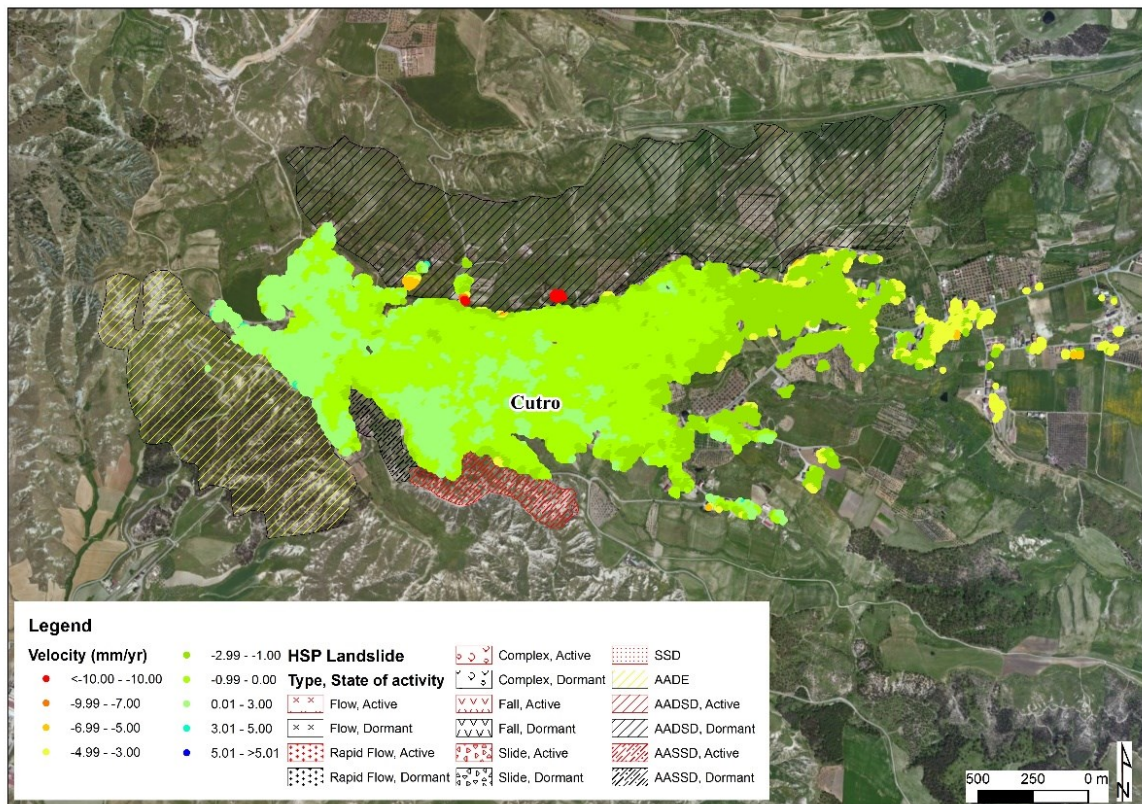


Figure 6.107 Displacement rates map obtained through the SBAS application to Cutro.

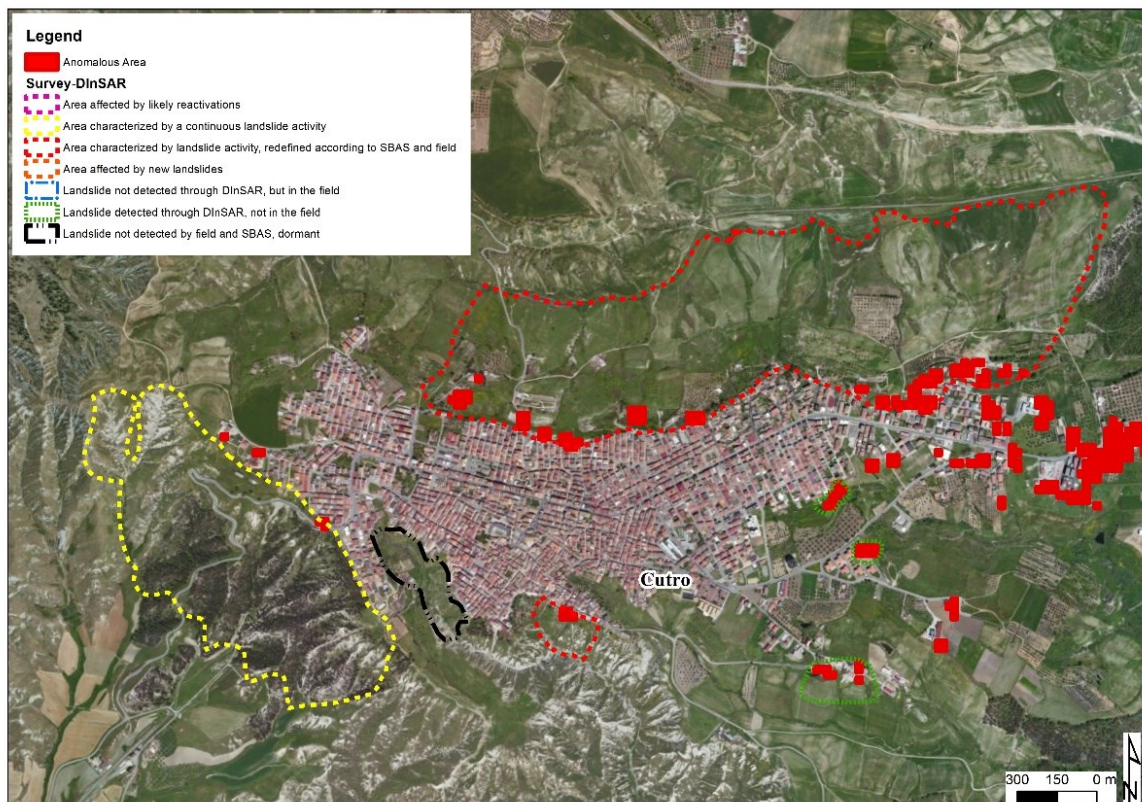


Figure 6.108 Landslide inventory map resulting from the joint application of DInSAR and field survey to Cutro



Figure 6.109 Evidences of the landslides in Cutro: a), concavity and convexity of the redefined landslide in the Northern sector b) crack in a wall within the redefined landslide in the Northern sector; c), d), e), f) damage to house, to roads and to remedial works within the redefined landslide in the Southern sector.

6.3.2 Summary of the results

The application of the anomalous areas methodology, carried out on 11 municipalities of Crotone Province, has led to interesting results. As also done within the framework of the LaDIS methodology (Di Martire et al., 2016), it has been possible to critically analyze the results, trying to comprehend the potentialities and the constraints of the landside inventory map obtained. A total of 208 landslides has been reported after the joint application of the SBAS algorithm on TerraSAR-X imagery acquired in the time-span 2008-2010, and the field survey (with the help of photointerpretation) between 2013 and 2015. With respect to the HSP landslide inventory map of 2006, an increase of 14 landslides has been thus stated, equal to the 7 %. The 208 landslides detected during such activities are divided as follows: 81 have been classified as active and 127 as dormant (Fig. 6.110). The 81 active landslides can be further distinguished in 28 landslides detected by both the DInSAR application and the field activities, while 42 have been detected only during field survey and 11 only through the SBAS application (Fig. 6.111). The landslides undetected by the satellite were mostly events occurred into much vegetated areas (24 cases), or landslides characterized by high velocities (5 phenomena), or deformations occurring on N-S oriented slopes (13 landslides) (Fig. 6.112). In all these scenarios, DInSAR methods confirmed to be incompatible. Conversely, landslides detected only by the satellite might be

most likely attributed to very slow deformation, which turned out to be undetectable by means of conventional techniques and by human eye. Moreover, the 28 landslides identified by both the approaches have been also divided into different classes: 5 are landslides showing a continuous active state, both in HSP and more recently, 8 are new landslides identified within this approach, previously not identified in HSP, one is a reactivation of a landslide marked as dormant in the HSP and 14 landslides have been redefined according to SBAS data and field survey (Fig. 6.113). At last, 127 landslides have been considered as dormant, due to the lack of anomalous areas and confirmed during the field activities. It is worth to point out, summarizing the above-mentioned numbers, that 155 landslides, equal to the 75%, have been defined thanks to the combined application; however, 53 landslides, equal to 25 % have not found any coincidence (Fig. 6.114). Therefore, the results obtained on the 11 test sites of Crotone Province confirmed the suitability of DInSAR methodologies, especially of the SBAS, for the monitoring of landslides over large areas. However, 25% of the landslides where no coincidence between field observation and DInSAR data has been found, underline the need of further improvements: On one hand, regarding the poor coverage of such techniques, especially due to the lack of natural reflectors, and, on the other hand, towards a higher suitability of the satellite to monitor fast movements and/or with a main N-S oriented component. This brings to the need to integrate the satellite information with field activity. In the cases where only SAR data allowed to recognize movement, a further field check could be useful. For instance, ground-based monitoring systems's installation could support the investigation. As shown in previous works (i.e. Tofani et al., 2014), in fact, the integration of in situ and SAR interferometry data can effectively allow a landslide characterization (Di Martire et al., 2016). Despite the abovementioned limitations, the application of SAR interferometry demonstrated to be a useful tool for the individuation and mapping of landslide for the update of inventory maps. In particular, the great amount of detectable targets, obtainable through the recent high-resolution satellite constellations (e.g. COSMO-SkyMed, TerraSAR-X), and advanced processing techniques can allow to obtain more detailed results.

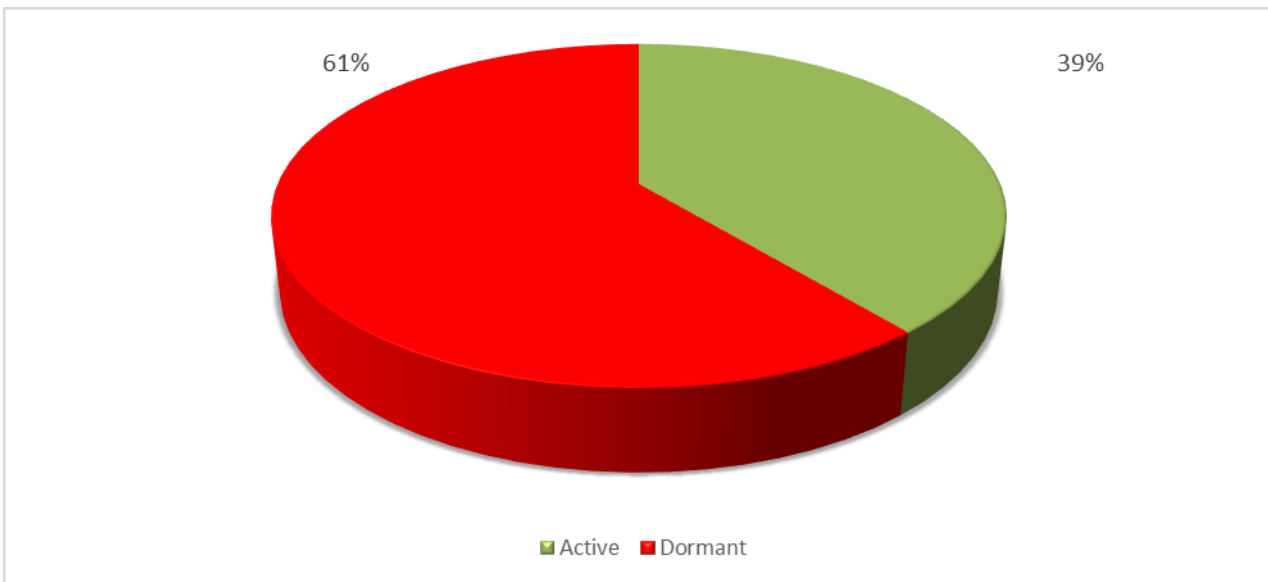


Figure 6.110 State of activity of landslides in the 11 test sites, according to SBAS elaboration and field activity.

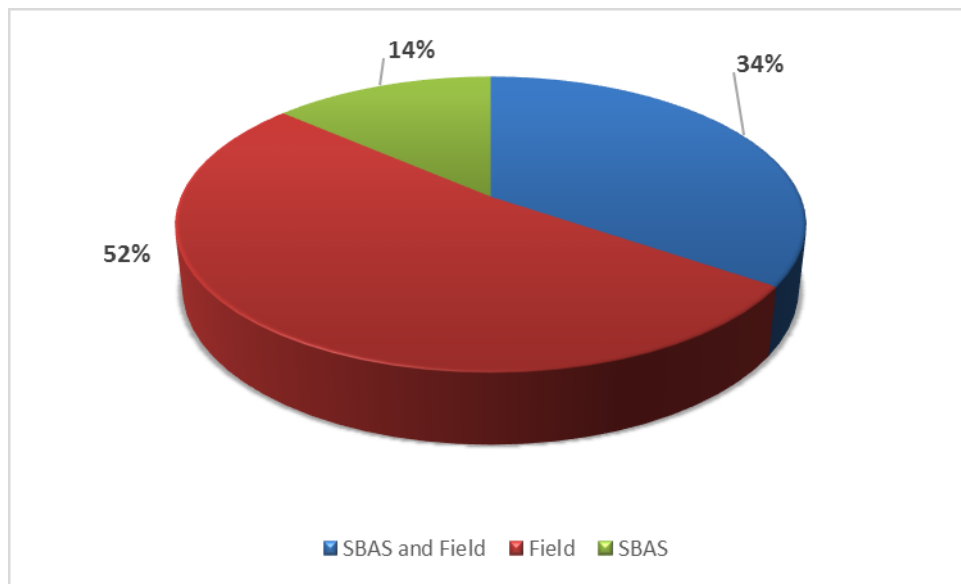


Figure 6.111 Active landslides detected by the overlap between SBAS and field, only in the field, and only through SBAS.

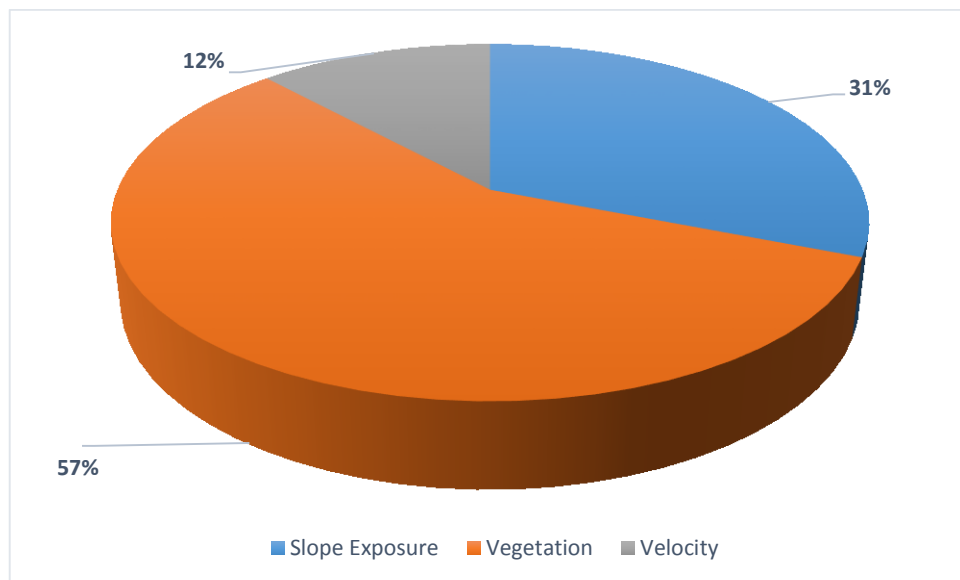


Figure 6.112 Landslides undetected by the satellite.

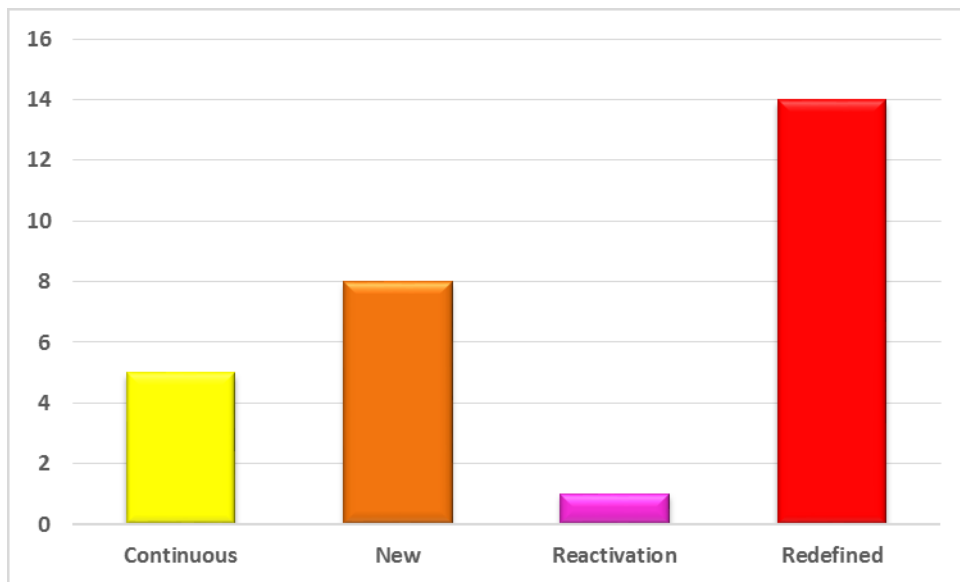


Figure 6.113 Active landslides detected by both SBAS and field activities.

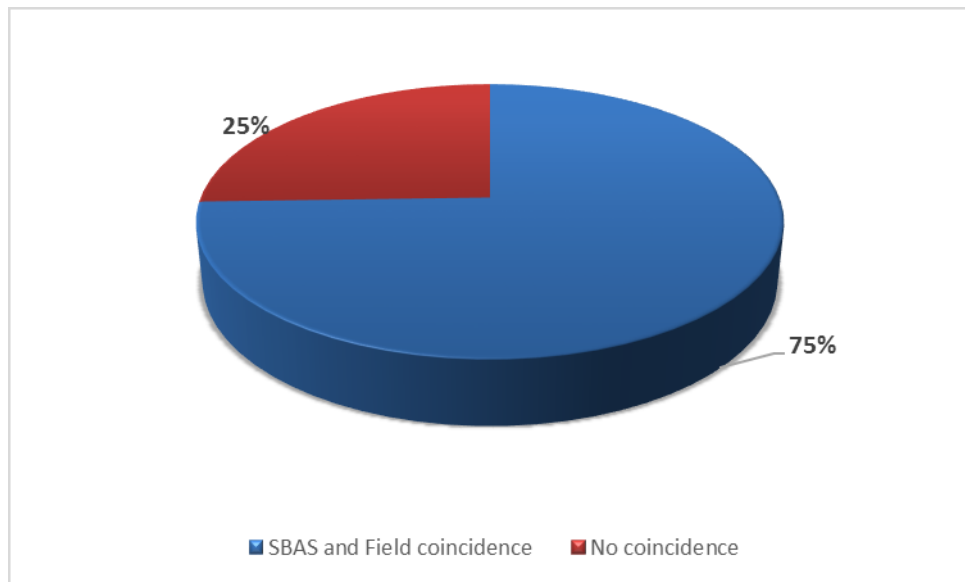


Figure 6.114 Landslides detected with and without coincidence between SBAS and field survey.

CHAPTER 7: SUBSIDENCE CASE STUDIES

Crotone province is not only affected by landslide phenomena, but also several cases of subsidence are reported. Several cycles of subsidence and uplift are described in literature (Zecchin et al., 2012), such as the tectonic subsidence phases during Zanclean, Piacenzian, Gelasian-Calabrian and Ionian age, and phases dominated by uplift (mid-Pliocene, early Gelasian, mid-Pleistocene, late Ionian to recent). The recent uplift of the Crotone area was characterized by an extensional tectonic regime, highlighted by the activation of ENE- and NNE-trending normal faults dissecting the marine terraces and older units (Cosentino et al., 1989; Zecchin et al., 2004b). Although a general uplifting trend in Crotone basin, several cases of subsidence have been recognized, where the role of human actions was very significant for the generation and the acceleration of such phenomena. Two case studies have been selected for the application of interferometric techniques, located at Belvedere di Spinello and Capo Colonna, respectively.

7.1 Belvedere di Spinello case study

On April 25, 1984, three different phenomena occurred on the western border of the salt mining area of Belvedere di Spinello, as described by Roda et al., (2006): The formation of a collapsing pipe, the slide of the hill located on the western side of the mining area and the spillage from the collapsing pipe of salty water which inundated the underlying plain. The beginning of the extraction activities started in the 1969, by Montedipe, which exploited a rocky salt layer, whose roof is located at variable depth, between 250 to 450 m from ground surface.

7.1.1 Belvedere di Spinello setting

The rocky salt deposit of Belvedere di Spinello, lying in the subsoil of the hilly area, located eastward respect to the urban area, is part of the eastern border of the Crotone basin (Fig. 7.1). The outcropping sedimentary rocks are all dated to the Neogene, and the salty deposit is part of the Messinian evaporitic succession (Fig. 7.2). The sedimentary succession starts with the sandstones and the conglomerates of the San Nicola Formation, passing upwards to the Argille marnose del Ponda (marly clay), of Tortonian age. According to Roda (1964), three different evaporitic formations can be distinguished: Lower Evaporitic Formation, Salty detrital Formation, and Upper Evaporitic Formation. The conglomeratic formation of the Carvane Conglomerates overlie the evaporitic layers. Above the Clayey Marl Cavalieri can be found: It is a 300 m thick formation of Zanclean age made of, grading upward, sands, sandy clays and silty clays and finally clayey marls. At the top of the Belvedere di

Spinello succession, the Zinga Molasse, made of sandstone, is placed. The three lower Pliocene formations (Carvane, Cavalieri and Zinga) are not crossed by the mining area wells, because the most recent Pliocene formations lies directly on the evaporitic deposits. In the mining area, in fact, the Spartizzo formation, made of lagoon deposits, the Scandale sandstones and the Cutro marly clays, respectively, complete the sedimentary succession.

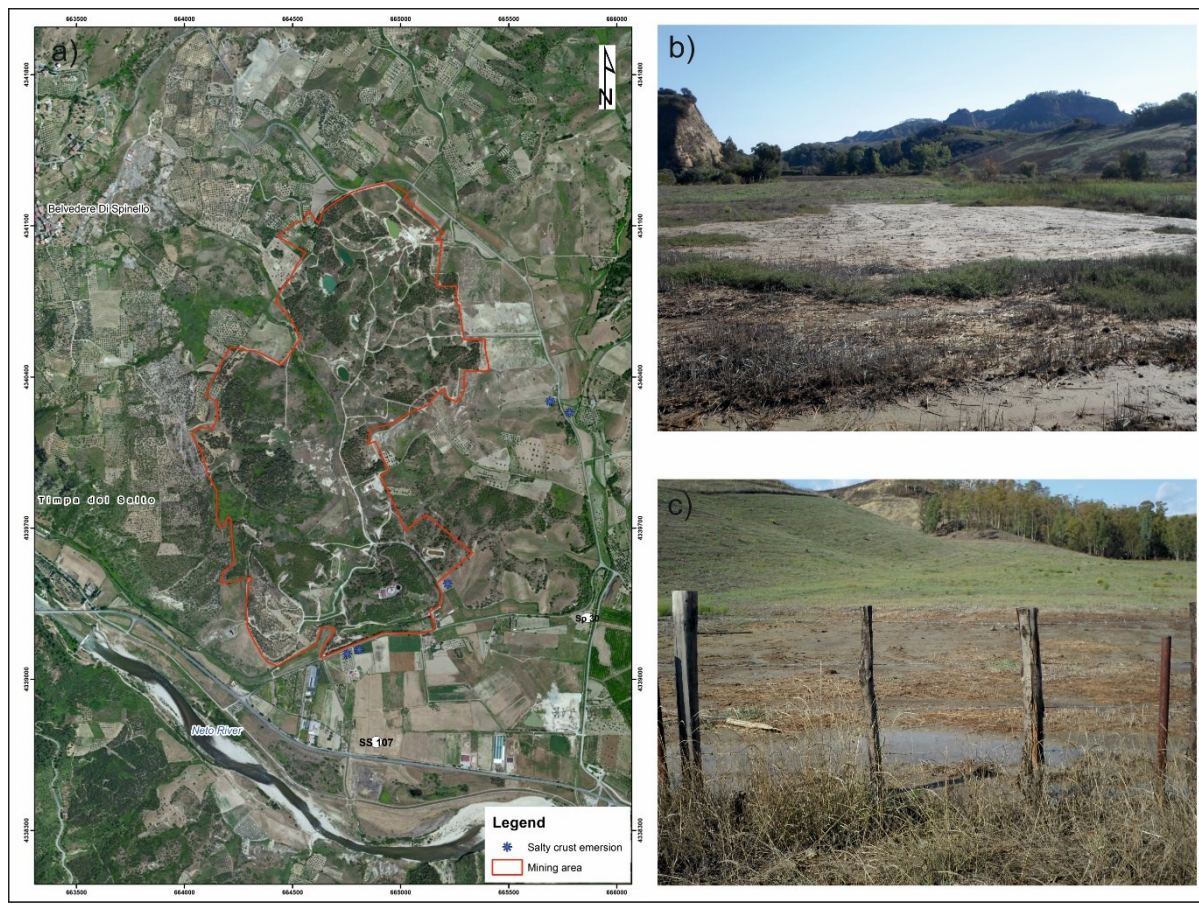


Figure 7.18 a) Mining area of Belvedere di Spinello; b) and c) salty crust emersions.

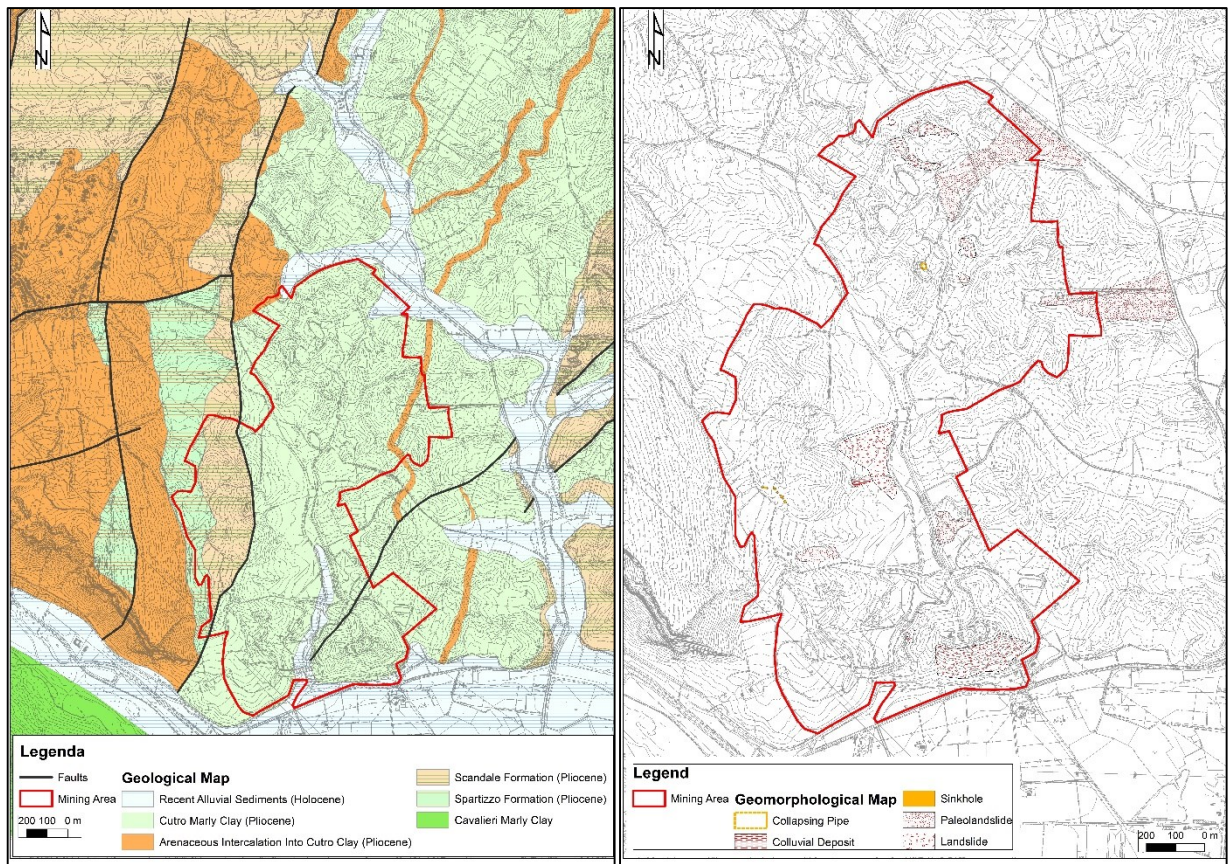


Figure 7.19 On the left, geological map of the mining area of Belvedere di Spinello (modified from Roda, 1965); on the right, Geomorphological map of the mining area of Belvedere di Spinello, modified from Ietto F. & Federico (2007).

7.1.2 Description of the mining activities

The mining operations started in 1969. The productive area is delimited on the surface to West by the Timpa del Salto fault, to North and to East by the Provincial road connecting the urban settlement to the highway, and to South by such highway. The methodologies for the salt extractions were based on the dissolution of the rocky salt and the retrieve of the saturated salty brine. Firstly a technique exploiting a couple of wells has been adopted, one well for the injection of fresh water, the other one for the drawing of salty fluid. This kind of activity has been carried out until 1986, but, in the meantime, a remarkable number of cavities, sometimes interconnected, formed. A first collapsing pipe developed in the 1983, without consequences, due to the poor quantity of fluid leaked. The most important event happened on April 25, 1984, outside of the wells area: it was characterized by a very high quantity of fluid spilled, and by the simultaneous generation of a shallow landslide. Afterwards, in the southern part of the mining area, the extractions by means of single wells started, equipped with two tubes, one for fresh water injection, and the other one for the salty brine extraction,

while the operations in the northern sector were interrupted. This methodology implies the formation of confined pipes, being so less impactful, also allowing to avoid the formation of collapsing pipes.

7.1.3 Hazards related to the mining activities

Since the beginning of the salt extractions, a generalized subsidence in correspondence of the mining area has been reported. Such phenomenon has always been under control by the company; however, no data has been ever released. Ietto A. (1988) reported the measurements carried out in three months, between February and May 1984, by a Ministerial committee. In this time-span, values of subsidence variable between 13.06 and 7.22 cm have been retrieved. A hypothesis of several meters of subsidence has been done, even considering that such a high value of deformation rate is linked to a specific event (Ietto, 1988).

Between April 19 and 20 1984, several cracks on the Timpa del Salto hill have been noticed by local farmers. In the morning of April 25, the whole slope collapsed, its estimated volume of mobilized material was of 300.000 m³ (Ietto, 1988). According to Roda & Martelli (2006), first a collapsing pipe, 50 × 120 m, formed, then the mudflow occurred, towards NE, toward the opening of the pipe, finally the salty brine leaked down the valley. A direct consequence was the flooding of the terrains of the Neto river alluvial plain, occupying a surface of 120 ha, before flowing into the river and then to the sea. The flood caused the desertification of 120 ha of vegetation and the death of the fluvial fauna along 20 km of watercourse.

Moreover, Cecchi & Martina (1976) have described several episodes of salty brines spilled, even at a considerable distance from the well, since 1976. These episodes are reported also after 1976, where evidences of salty crusts have been found even at 700-800 m from the border of the mining area. Recently, in fact, the Provincial road located on the eastern side of the mining area has been closed in 2011, due to the emersion of salty crusts to the surface (Fig. 7.1), hence being afraid of new landslides. This road has been reopened only in June 2015.

7.1.4 DInSAR results

The DInSAR analysis on Belvedere di Spinello mining area, for the monitoring of subsidence phenomena related to the salt extractions, has been carried out exclusively on the descending TerraSAR-X dataset, due to the lack of coverage on the western part of Crotone province territory by the ascending one. The time span analyzed was between April 2008 and June 2010, and the SARscape software has been applied, exploiting the PSInSAR and SBAS techniques.

7.1.4.1 PSInSAR

For the PSInSAR analysis, the procedure shown in the paragraph 6.1.2.2 has been here proposed, so splitting the stack into 2 periods of analysis and applying a spatial baseline of ± 100 m. An area of interest of 7 km^2 has been selected, and a DEM 5×5 , obtained from the Regional Topographic Map, has been used for the removal of the topographic component.

The first period of analysis (April 2008 - August 2009) shows 520 points, located mostly in correspondence of man-made structures and rocky outcrops (Fig. 7.3). The majority of the points are in correspondence of the state road, of the provincial road bringing to Belvedere di Spinello town, and in correspondence of structures and access road related to the mining area. A remarkable result obtained by the PSInSAR analysis is the concentration of about 40 points showing displacement rates higher than 10 mm/yr located just outside the southern border of the mining area, in correspondence of the main access road to the salt mine and several buildings used for farming and breeding. In some cases, the displacement velocities reported overcome 20 mm/yr. Others PSs showing displacement rates higher than 10 mm/yr can be found in the SE part of the mining area, nearby the mining well Ba5. No PS has been detected within the border of the mining area, except for few points in the NW sector, not showing considerable displacement rates, due to the massive presence of forest trees, which do not allow SAR interferometry to work correctly (due to temporal de-correlation of the signal).

In the second period of analysis (April 2009 - June 2010) more than 600 PSs have been detected (Fig. 7.4). Also in this case PSs are located in correspondence of roads and buildings. A cluster of more than 10 points can be recognized under the southern border of the mining area, with velocities of the displacement up to 7 mm/yr, while a more remarkable cluster of PSs characterized by displacement rates up to 10 mm/yr is located within the mining area, on several buildings used by the mining company. Other two points have been detected nearby the wells no. 28 and 29.

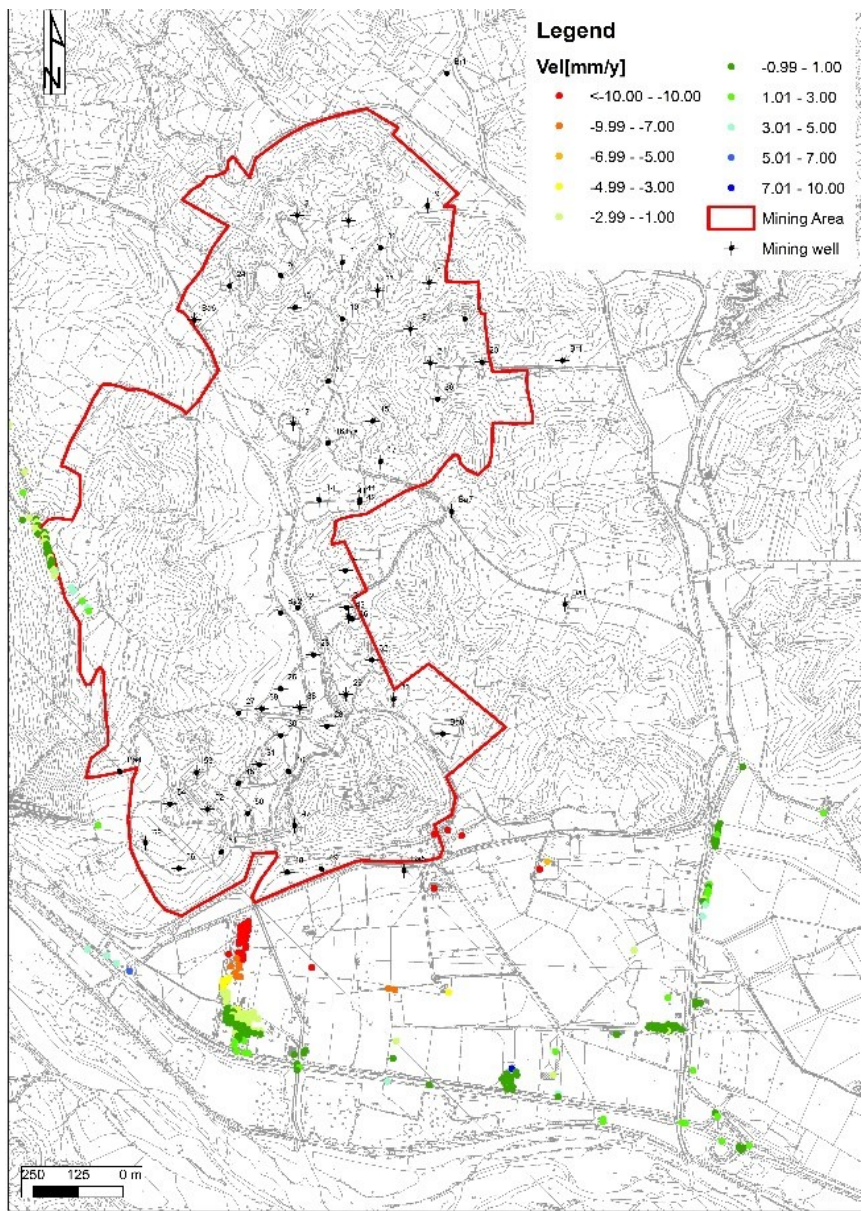


Figure 7.20 Displacement rate maps obtained through the PSInSAR processing of the 1st period of analysis.

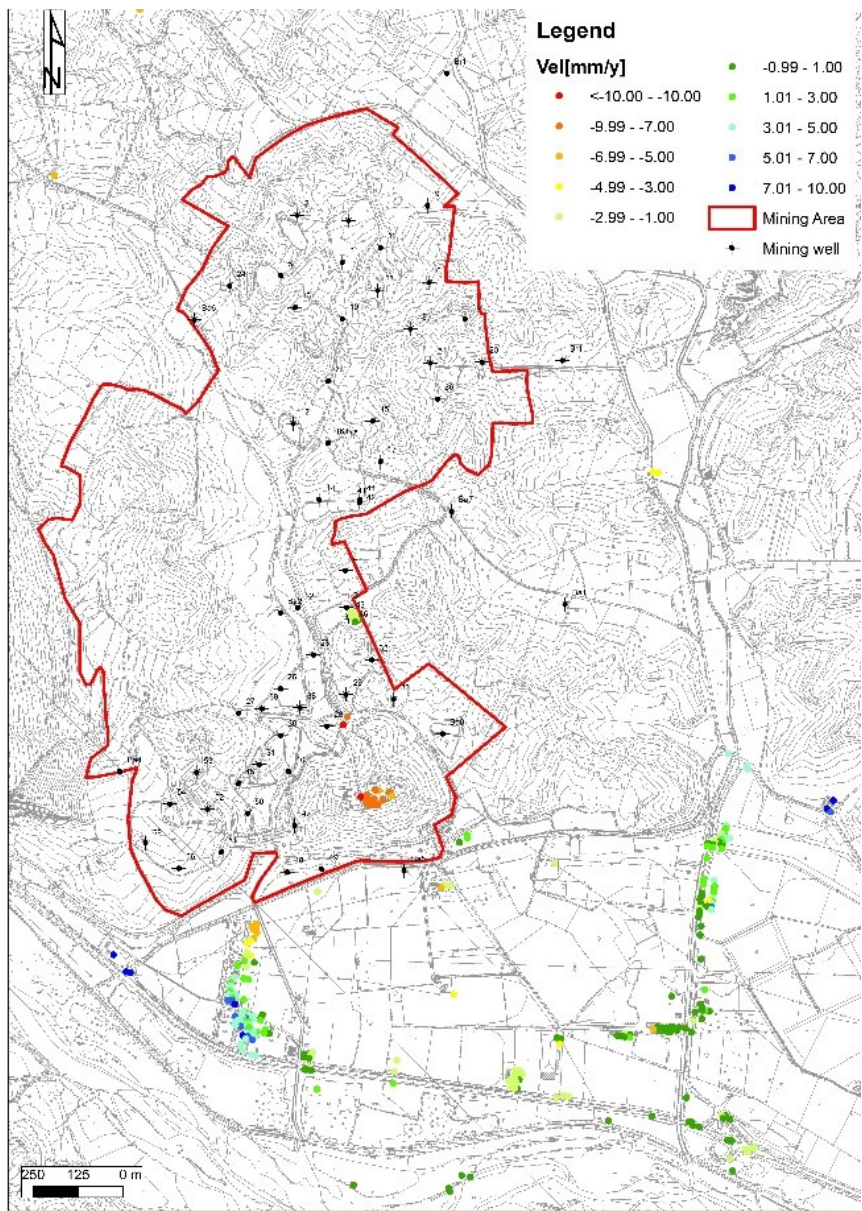


Figure 7.4 Displacement rate maps obtained through the PSInSAR processing of the 2nd period of analysis.

7.1.4.2 SBAS

The SBAS method has been here applied on the whole available stack. The main parameters are reported in Table 7.1.

Table 7.1 Main parameters for the SBAS application on Belvedere di Spinello case study.

Temporal Baseline	100 days
Spatial Baseline	2.5% max. critical baseline (about 100 m)
Coherence Treshold	0.6
Multilooking Factor	5x4

More than 3000 CPs have been detected, so resulting to be more effective than PSInSAR on Belvedere test site (Fig. 7.5). Also in this case the areas crossed by the highway and the provincial road seem to be stable. However, the closer to the mining area, the more unstable. In fact, in occurrence of buildings located southward to the mining area, several CPs characterized by velocities of displacement up to 17 mm/yr have been recognized. Moreover, clusters of points showing deformation rates higher than 20 mm/yr are located within the southern part of the mining area, in correspondence of buildings and of the wells Ba8 and 28. Through the SBAS application it has been also possible to detect points showing displacements in the central sector of the mining area, eastward, nearby the well 43 and 46, also here characterized by velocities up to 20 mm/yr.

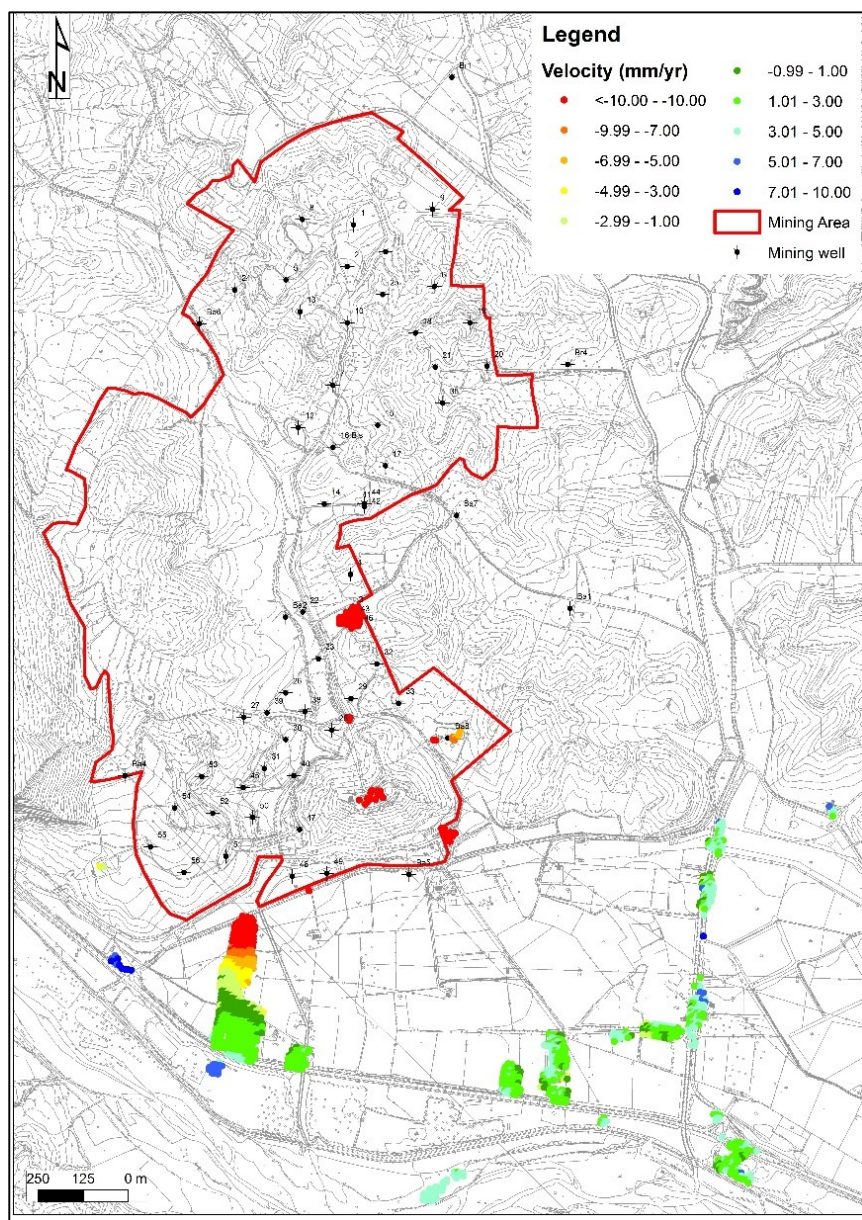


Figure 7.5 Displacement rate maps obtained through the SBAS processing.

7.1.4.3 Considerations on the results obtained

The DInSAR analysis is a valuable tool for the monitoring of anthropogenic subsidence. Here in Belvedere di Spinello it has been possible to confirm the validity of such techniques. However, the massive presence of high vegetation makes almost impossible to correctly detect measurement points, especially exploiting X-Band images. In the case of Belvedere di Spinello, both PSInSAR and SBAS detected a subsidence pattern related to the mining activity for the salt extraction, however, a validation through “ground truth” data of such elaboration would strengthen the results obtained. A future perspective for Belvedere di Spinello area would be to collect in situ data, also related to the extraction volumes, and to improve the visibility of the area, through, for instance, the installation of corner reflectors or clearing the vegetation, which could allow detecting more targets within the mining boundaries.

7.2 Capo Colonna case study

The monitoring of cultural heritage and archaeological sites affected by ground deformation is significant for their preservation and protection. In fact, archaeology is one of the sciences which greatly benefits from remote sensing application. UNESCO, for World Heritage sites preservation and management, has also recommended the role of interferometry as, for instance, in the case of the subsidence monitoring of Mexico City (UNESCO, 2010).

DInSAR has been here applied to investigate the displacements occurring in Capo Colonna area (Fig. 7.6), located in the Crotone municipality. It is an archaeological site, whose name derives from the only remaining column of the old Hera Lacinia temple, belonging to the Magna Graecia city of Kroton, and dated to the 6th century BC (Fig. 7.7 a). Witnesses of other ruins of Roman origin are also present, along the coastline, as well as a XVI century's Nao tower and the sanctuary dedicated to the Madonna Nera of Capo Colonna (Fig. 7.7 a). Of the original temple, unfortunately, just one column is nowadays visible, due to centuries of robbery of construction materials. The processing and the interpretation of the SAR data has been carried out exclusively on the TerraSAR-X 2008-2010 stacks, on which the SBAS algorithm has been applied.



Figure 7.6 Capo Colonna promontory. The ruins of the Hera Lacinia temple and the lighthouse fall into the red rectangle. The blue line represents the perimeter of the Archaeological area. Green dots represent the ENI wells for gas extraction, blue dots are for the main buildings located in the promontory.



Figure 7.7 a) Roman ruins in Capo Colonna archaeological site. Nao Tower and the Sanctuary on the background; b) prism of rock isolated by systems of fractures; c) and d) ruins located along the coastline.

7.2.1 Capo Colonna setting

Capo Colonna area is located in the southern and eastern part of the Crotone basin. The promontory, in particular, is characterized by Pleistocene and Pliocene sedimentary formations, arranged in layers and dislocated in different levels, made of marine terrace deposits (Fig. 7.7). The Pliocene deposits are made of grey and grey-blue silty clays (Roda, 1964; Mellere et al., 2005) and are separated by an unconformity from the Pleistocene deposits, represented by sands, sandstones and calcaranites (Mellere et al., 2005).

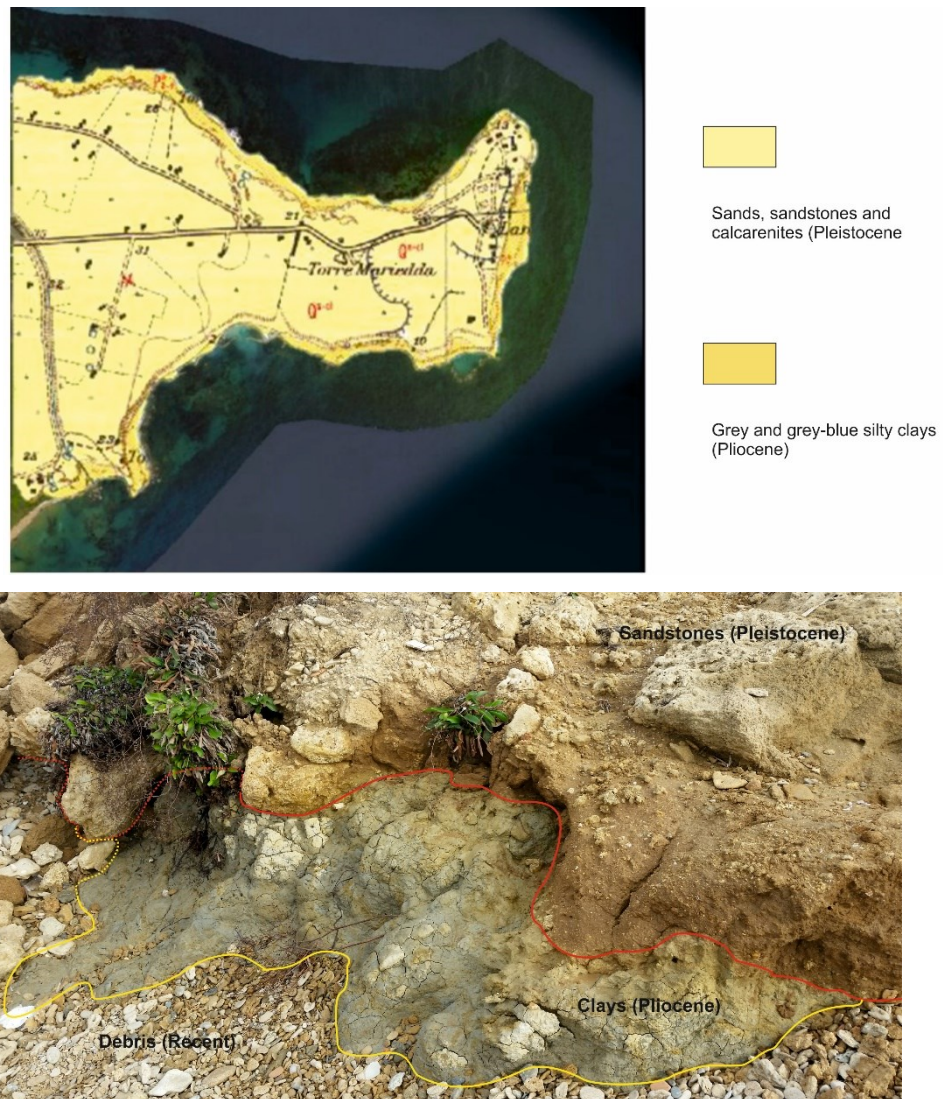


Figure 7.8 On the top, geological map of Capo Colonna (modified from Geological Map 1:25.000, (1967). On the bottom, typical stratigraphic sequence of Capo Colonna.

This specific geological setting is significantly prone to landsliding: The clays at the base of the cliffs influence their stability, due to the weak strength to wave and wind erosion, consequently triggering the falling and toppling of the overlying lithoid portion (Ietto et al., 2008). In addition, a widespread gully erosion, due to the runoff action of rainwater, also affects the Pliocene clays. The SE part of the peninsula is the sector most hit by the erosional activity, where winds are more powerful: The main fetch, in fact, comes from Egypt (SE), hence increasing the energy of the waves (Procopio et al., 1998). Although the majority of the ruins are located on the edge of the coastal cliffs vulnerable to wave erosion and coast retreat, subsidence is the main geohazard affecting the safety and the preservation of the archaeological remains. The main causes for the generation of vertical motions in the Capo Colonna promontory can be attributed to combination of natural processes, such as the settlement of the sedimentary succession, the presence of a continue seismic activity and the

sea-level changes due to eustatic cycles, and anthropogenic causes. Since the late 1970's, and especially in the last years, the vulnerability of the area has increased because of the gas extraction performed by ENI (*Ente Nazionale Idrocarburi*) and water withdrawal for agricultural use (Lena & Bonomi, 2004). Subsidence phenomena interact also with the stability of the rocky cliffs, accelerating the retreat of the coast. Damage to buildings located within the promontory nearby the lighthouse and the column have been reported, such as fractures and cracks. In some cases, several houses have been shored up (Fig. 7.9). The causes should be addressed to the subsidence phenomena.



Figure 7.9 Damage reported during a field survey in November 2015: a) crack in a perimeter wall; b) abandoned buildings; c) reinforced house; d) fracture in an abandoned house.

7.2.2 DInSAR results

The SBAS analysis has been performed on the whole Lacinio promontory, which covers an area of about 6 km² (Fig. 7.6). In Table 7.2 the main parameters used are shown.

Table 7.2 Main parameters for the SBAS application to Capo Colonna case study.

Temporal Baseline	100 days
Spatial Baseline	2.5% max. critical baseline (about 100 m)
Coherence Threshold	0.6
Multilooking Factor	5x4

For the descending orbit, the deformation pattern is clearly visible and homogeneous for the whole promontory, characterized by displacement velocities up to -16 mm/yr away from the satellite LOS in the time span analyzed (Fig. 7.10). The average rate of displacement is equal to -9.2 mm/yr, calculated over 950 CPs detected in the entire area. By the evaluation of the outcomes of the SBAS

application on the descending stack, it has been possible to identify different patterns of deformation, which have been analyzed in more detail. The highest velocities of displacement are located nearby the “ENI well 1” (Fig. 7.6) with rates up to -12 mm/yr away from the sensors (in LOS). Clusters of targets showing higher deformations can be also found in two farms over rural and cultivated areas, located westwards respect to the archaeological site, where higher velocities up to -15 mm/yr are most likely attributable to the additional contribution of water pumping for agricultural use. Moreover, targets showing significant displacements are located along the sandstone cliffs, both in the northern and in the southern sector of the promontory, where the patterns identified through the SAR analysis can be ascribable to the combined action of land subsidence and wave erosion effects. Among the ruins and on the tip of the promontory no targets have been detected, due to a loss of coherence in the signal during the time interval of acquisition.

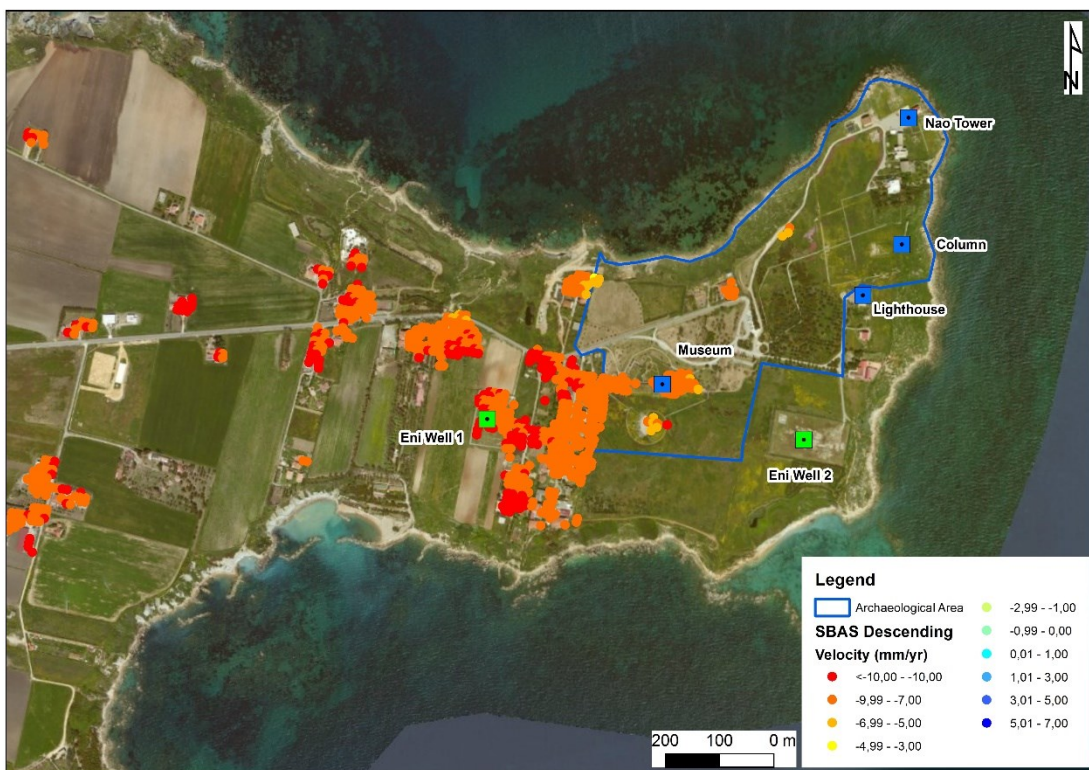


Figure 7.10 Displacement rate map through SBAS on the descending dataset.

The subsiding trend has been clearly recognized also exploiting the ascending dataset (Fig. 7.11): More than 500 CPs, through the application of the SBAS technique, have been detected. The mean displacement rate is of -9 mm/yr away from the sensors (in LOS). As similarly observed in the descending results, also for this dataset higher deformation velocities have been recognized in the area around the “ENI well 1”, where it is possible to identify velocities up to 12 mm/yr along the

LOS. However, also a pattern showing rates up to 13 mm/yr has been spotted in correspondence of the second gas well situated next to the historical site (Fig. 7.6), on the SE tip of the Capo Colonna peninsula. The SE sector of the Lacinio promontory, in correspondence of the museum, some private houses close to the museum, of the second well and nearby the lighthouse is also characterized by displacement rates higher than 10 mm/yr. Finally, few points are located next to the rocky cliff, especially in the northern sector, and, as previously stated, they can be attributed to the combination of falling and toppling of the sea cliffs and to vertical motion. However, even in this second case, DInSAR analysis turned out to be not enough suitable for the area surrounding the column and the ruins; therefore, no targets have been recognized. Notwithstanding this, a comparison between the results here shown and the ones obtained by Tapete & Cigna (2012a; 2012b) has been done, showing a good agreement between the displacement rates identified, even though they refer to a different time span (1992-2010, ERS and ENVISAT imagery) (Fig. 7.12).

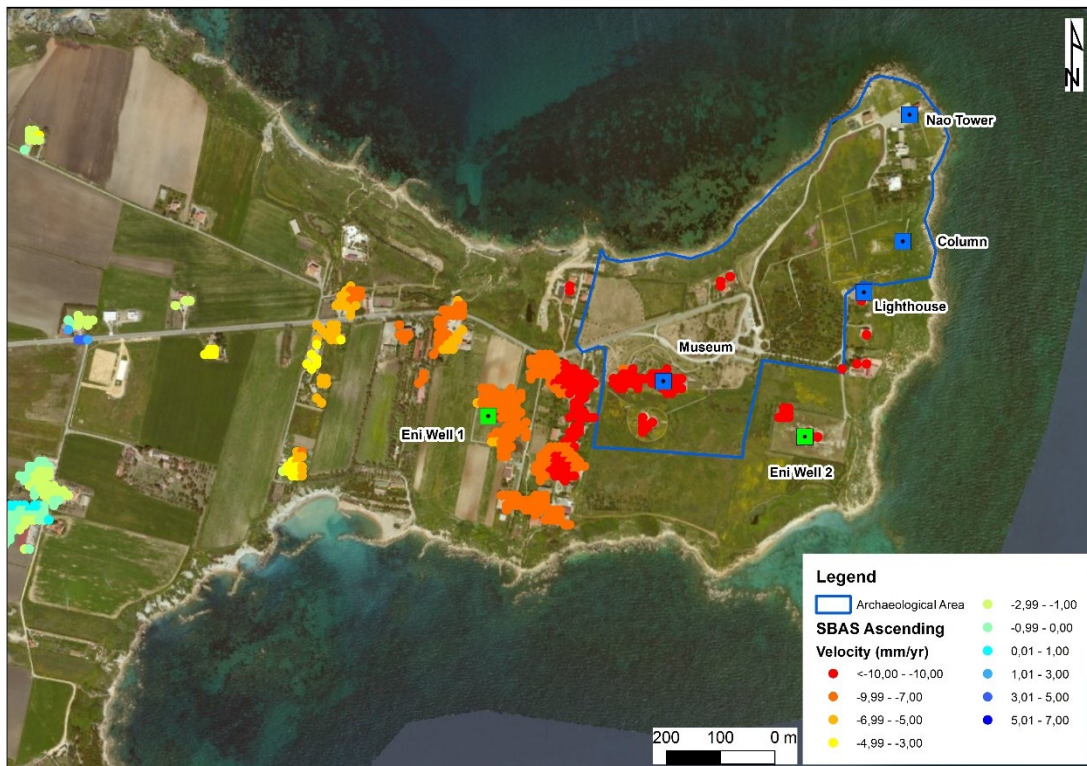


Figure 7.11 Displacement rate map with SBAS on the descending dataset.

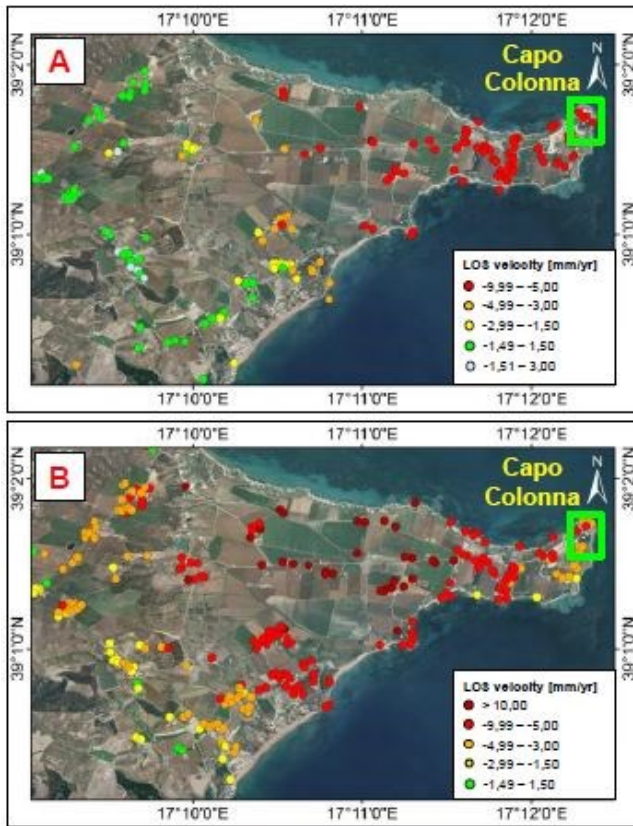


Figure 7.12 Displacement rates map: a) ERS descending data; b) ENVISAT ascending data (Tapete & Cigna, 2012). In green rectangle the archaeological site.

The availability of both ascending and descending datasets allowed to eliminate many SAR spatial distortions, and therefore, combining the two datasets, to decompose the velocity vector. Considering a x,y,z Cartesian coordinate system, in which the three directions coincide with the horizontal E-W, the horizontal N-S and the vertical components, respectively, the velocity vector V can be calculated as:

$$\bar{V} = V_x * \bar{s}_x + V_y * \bar{s}_y + V_z * \bar{s}_z \quad (1)$$

where V_x , V_y and V_z are the vector velocity components along the horizontal (E-W and N-S) and the vertical directions, and s_x , s_y and s_z are the unit vectors of the three coordinate axes.

Therefore, using the velocity values V_{asc} and V_{desc} , obtained from the two interferometric analysis, the following system can be calculated:

$$V_{asc} = V_x * s_{xasc} + V_y * s_{yasc} + V_z * s_{zasc} \quad (2)$$

$$V_{desc} = V_x * s_{xdesc} + V_y * s_{ydesc} + V_z * s_{zdesc} \quad (3)$$

where V_{asc} and V_{desc} are the velocity values in ascending and descending orbit, respectively, and s_{xasc} , s_{yasc} , s_{zasc} , s_{xdesc} , s_{ydesc} , and s_{zdesc} represent the direction cosines of the two velocity vectors. In this reference system the number of unknown variables (V_x , V_y and V_z) is greater than the number of the equations and, thus, not solvable. However, considering the geometry of acquisition, the component on N-S direction can be consider negligible, so that the velocity in this direction is approximated to zero, the equation can be solved and it is possible to estimate the vertical component, which turns to be very useful for subsiding areas:

$$V_z = \frac{V_{desc}*s_{xasc}-V_{asc}*s_{xdesc}}{s_{xasc}*s_{zdesc}-s_{xdesc}*s_{zasc}} \quad (4)$$

The result, as shown in Fig. 7.13, is a map with the total amount of displacement calculated in the time span (April 2008 - June 2010) and along the vertical direction. This value has been interpolated in a cell of 60 m of radius for each point and averaging the values up to 12 points within this radius. As observable, the maximum vertical movement reaches values up to about 35 mm (Fig. 7.13): The cloud with the highest value is located along the coastline, in the northern sector, whereas the influence of cliff erosion overlaps the subsiding trend. Within the area surrounding the ENI well 1 values of vertical displacement of 28 mm can be recognized. Towards the inland, the displacement trend decreases, reaching minimum values of 12 mm in the two years of monitoring (2008-2010).

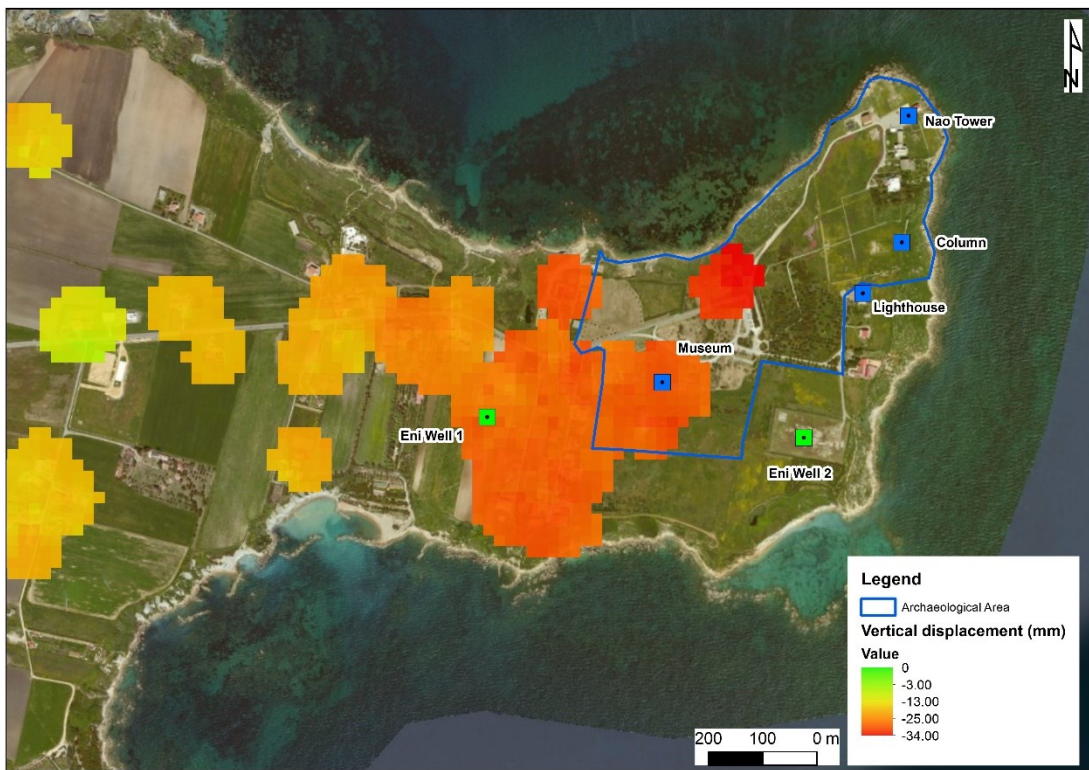


Figure 7.13 Map of the total vertical displacements occurring in Capo Colonna area between April 2008 and June 2010.

The results previously shown demonstrated the reliability of DInSAR method and proved to be promising for the analysis of vertical deformation, however, still present are limitations of the visibility, especially along the coastline. In order to improve the visibility in the area, particularly along the cliff, at the eastern extremity of the promontory and around the column and the ruins, 80 corner reflectors were placed in October 2014 (Fig. 7.14), thanks to an agreement with the *Sovrintendenza dei Beni Archeologici della Calabria*. COSMO-SkyMed StripMap products have also been acquired (October 2014 - June 2015) soon after their installation, allowing to identify the installed corner reflectors as shown in the High Resolution image (Fig. 7.15). From the comparison of TerraSAR-X and COSMO-SkyMed amplitude maps, it has been possible to obtain, in the latter, an increase of the amplitude value between 10 and 15 dB in average. For instance, in three points correspondent to three corners installed along the Lacinio promontory (Figure 7.16), an increase from an average of 40 dB, obtained with the exploitation of TerraSAR-X imagery, to an average of 52 dB (COSMO-SkyMED) has been registered (Table 7.3). Hence, thanks to such peculiar tools, a clear improvement in the visibility of the surrounding areas can be guaranteed.



Figure 7.14 Location of the corner reflectors installed. All around, photos of some of the corners.

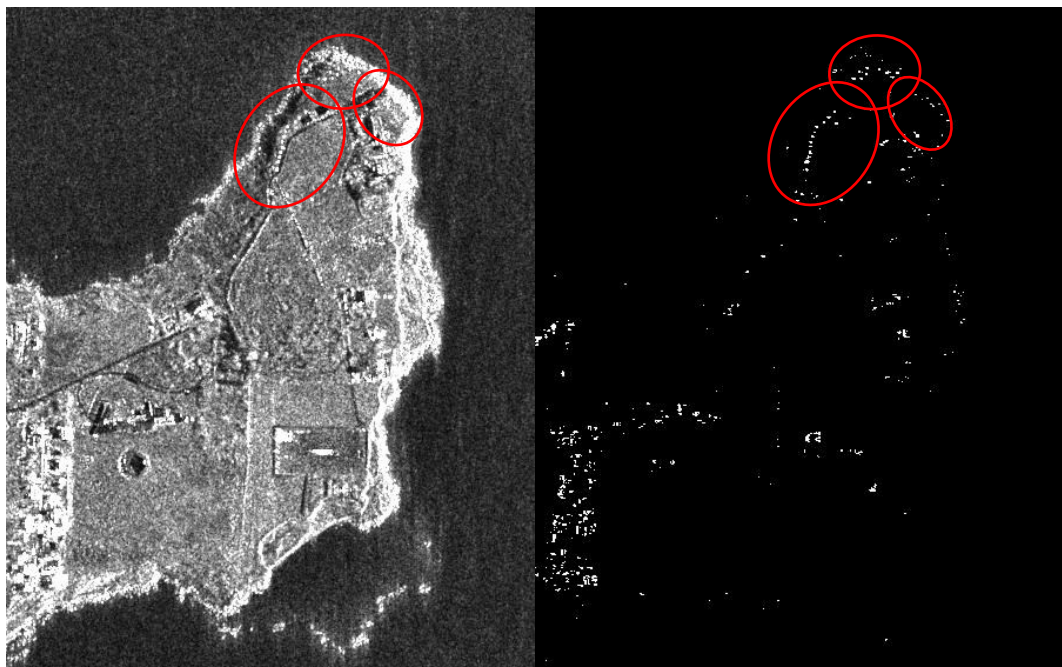


Figure 7.15 On the left, COSMO-SkyMed HR image; on the right, Pixel selection with COSMO-SkyMed products. The red circles encompass the corner reflectors.



Figure 7.16 CosmoSKY-MED HR image. In orange circle, point 1, in yellow circle point 2, in red circle, point 3.

Table 7.3 Amplitude value of each point with the available imagery

	Point 1	Point 2	Point 3
TSX 08-10 Asc	44,17 dB	41,98 dB	40,86 dB
TSX 08-10 Desc	37,81 dB	41,89 dB	42,55 dB
Csk 14/15	52,46 dB	51,29 dB	52,09 dB

7.2.3 Future outlooks

DInSAR methods proved to be efficient for the monitoring of the combined action of subsidence and coastal erosion in Capo Colonna archaeological site. Thanks to the acquisition of COSMO-SkyMed products, it will be possible to analyze at a greater detail the various displacement events affecting the area of Capo Colonna. Further studies, in fact, need to be done for a more detailed analysis regarding the relationship between the gas extractions performed in the promontory area by

ENI, since the late 1970's, with 4 inland wells and 3 other off-shore platforms, and the subsidence, which, as testified by this work, is still active. From the analysis of the time series of displacement and through an accurate modeling of the geological and geotechnical setting, it could be possible to estimate and quantify the role of the fluid extraction on the vertical motion. Moreover, the corner reflectors, placed along the edge of the coastline, will enable for development in the visibility of the area and consequently, for improved analyses concerning the coastal erosion due to the wave action.

CHAPTER 8: CONCLUSIONS

Prevention and mitigation of deformational phenomena require effective technologies to reduce the hazard affecting human life. In fact, ground failures and ground instability hazards are globally widespread phenomena caused by natural geological and climatic processes (e.g. landslides and slope movements, soil volumetric changes in relation to dry and wet periods, soil/rock dissolution, oscillations of ground water levels, seismic and volcanic activity, neo-tectonic uplift or subsidence) or induced by anthropogenic sources (e.g. ground water pumping, gas and oil withdrawal, mining activity, subsurface and surface engineering works). They determine a significant number of human losses of life and injuries as well as extensive economic damage to private and public properties. Therefore, monitoring plays a key-role in natural hazard management and it assumes a paramount task for providing cost-effective solutions in order to mitigate or minimize disaster losses. In the last decades, remote sensing devices provided an important support in disaster monitoring at relatively low costs. Among the remote sensing techniques, Multi Temporal Interferometry is a valuable tool which achieved relevant improvements, especially through the availability of imagery characterized by very high resolution and short revisit time. As testified by the case studies included in this present research project and previously depicted (Chapter 6 and 7), interferometric techniques proved to be a valuable tool for the monitoring and the analysis of the deformational phenomena occurring on the Earth surface. Moreover, it has been demonstrated the various range of applications and, consequently, its versatility in different contexts. With the present contribution, Differential Interferometry Synthetic Aperture Radar (DInSAR) techniques allowed to, on one hand, comprehend slope failures mechanisms on a very local scale (i.e. Cirò and Papanice), contributing to the definition of type, triggering factors and its temporal evolution; on the other hand they provided for a reliable support to landslide mapping and to the update of the inventory, recognizing unstable areas in urban settlements. In addition, vertical motions, generated by different sources, have been also studied by means of interferometric techniques, which showed their efficacy also in areas characterized by predominant vertical deformations, as in the case of areas affected by subsidence.

The first part of this work dealt with the acquaintance of the basic concepts of DInSAR principles, in order to better comprehend and therefore use SAR data correctly. In a second phase, the selection of the case studies for the implementation of Multi Temporal Interferometry (MTI) has been done through newspaper and on-line news consultation, field survey, and following the requirement of SAR imagery (W-E oriented slope, slow rates of displacements, areas poorly vegetated).

In the paragraph 6.1 the case history of Cirò town has been depicted. TerraSAR-X data have been processed through two different software, on which various algorithms are implemented. The

first one, the SUBSOFT processor, is based on the Coherent Pixel Technique (CPT) algorithm, while the latter, SARscape, exploits Small Baseline Subset (SBAS) and Persistent Interferometry SAR (PSInSAR) methods. DInSAR analysis on the ascending dataset turned out to be inadequate, not detecting any target showing displacement in the area of the 2011 landslide with all the algorithms employed. However, the results obtained through the processing of the descending dataset allowed to identify several targets, with displacement rates up to 20 mm/yr in correspondence of the main scarp of the landslide, and therefore, to redefine, jointly with field survey, the landslide boundaries, detecting a retrogressive and widening trend and describing an area twice as before. Moreover, in order to analyze the main factors which caused the slope failure in Cirò, a comparison between time series of displacement obtained with DInSAR methods and rainfall data has been carried out, pointing out the crucial role of intense precipitations for landslides characterized by slow and intermittent kinematics. At last, it has been observed why DInSAR analysis resulted to be inefficient on the ascending dataset: The application of R-Index permitted to detect geometrical distortions, such as foreshortening, layover and shadowing, in the processing of the aforementioned stack and hence to confirm the effectiveness of DInSAR analysis on the descending stack.

The investigation of a landslide occurred in Papanice settlement has represented the main focus of the paragraph 6.2. In this case, R-Index has been applied a-priori, showing the better suitability of the ascending dataset. The first part of the work in Papanice dealt with the acquisition of rainfall data and with the acquaintance of the geomorphology of the area affected by ground deformation. Successively, DInSAR methods have been applied to analyze the pre-failure stage, exploiting TerraSAR-X imagery between 2008 and 2010, hence identifying the antecedent deformations, which brought the slope to failure in 2012. On a further stage of the work, the monitoring of the displacements occurred in the post-failure phase highlighted the evolution of the landslide, confirming the velocities of the displacement identified in the first part, and clearly displaying the activation of the deformation in a sector previously not affected by any movement. In both cases, the strong connection between intense precipitations and slope failure has been demonstrated. Furthermore, the good agreement between piezometric monitoring, rainfall data and time series of displacement in the post-failure phase pointed out the role of water table height for the generation of landslides, where the activation of the movement occurred in correspondence of the rise of the water table to the ground level. The role of interferometry can support also geotechnical analyses: As observed for Papanice, a slope stability test, considering the water table at a superficial depth, thus following the indications given by the DInSAR analysis, has been headed. The results obtained showed how the stability of the slope can be obtained only through the drop of the water table level up to 1 m below the ground surface.

The experience carried out at Papanice hence pointed out the role of the interferometry, whose application, jointly with geological and geotechnical analyses can represent a significant tool for the planning of remedial works.

The application of MTI techniques at a larger scale of analysis has been the other goal related to landslide monitoring faced in this thesis. Starting from the Hydro-geomorphological Setting Plan (HSP) of Calabria Basin's Authority (2006), the processing on 11 municipalities of Crotone Province has been carried out in order to monitor their stability and to update the existing landslide inventory map. To this aim, a procedure based on the detection of "anomalous areas" has been adopted. The application of the aforementioned procedure, jointly with field survey, allowed to update the landslide inventory map to 2015. A 7% increase of landslides has been documented (from 194 to 208), while the percentage of active landslides remained unchanged, recognizing about 40% of landslides as active. Hence, in this case a low time-consuming and low-cost procedure has been proposed, following indications provided by interferometric data and the procedure adopted, accounting for field surveys in order to validate such elaborations. Therefore, the application of SAR interferometry demonstrated to be a useful tool also for the individuation and mapping of landslide and for the update of inventory maps.

It is worth to mention that DInSAR techniques have been successfully applied also in areas affected by subsidence. Two case studies in Crotone province have been selected.

The first site studied is the Belvedere di Spinello salt mine. Here, sinkholes and subsidence have been reported since the beginning of the extraction activities, in 1969; however, the site is best known for the 1984 slope collapse and the leakage of the salty fluids, which inundated the alluvial plain. Subsidence and salty crusts emersions have been still reported nowadays. DInSAR methodologies detected, in the time-span 2008-2010, a subsiding trend up to 20 mm/yr in the southern part of the mining area. However, the presence of high vegetation made impossible to detect measuring points in the other sectors of the area, and, in addition, the lack of ground-truth data did not allow to validate the results obtained.

The second case history of subsidence in Crotone refers to the archaeological site of Capo Colonna. Subsidence is here due to a mix of natural and anthropogenic causes. Moreover, a significant coastal erosion endangers the ruins located along the promontory facing the Ionian Sea. In this case, the elaboration of DInSAR methods has been headed with SBAS algorithm, allowing to detect displacements up to 20 mm/yr. Moreover, the availability of both the ascending and the descending stack enabled the estimation of the vertical component of the movement. The maximum vertical displace-

ments, being located along the coastline and nearby the *Ente Nazionale Idrocarburi* (ENI) gas extraction wells, confirm the effects of coastal erosion and introduce a debate in the scientific community about the role of gas withdrawal for the subsidence in the promontory.

In this thesis, three different algorithms have been exploited: CPT, available on the SUBSOFT processor, PSInSAR and SBAS implemented on the SARscape software. From an examination of the results obtained in the various applications, it has been possible to evaluate the benefits and the constraints of each technique:

- a) CPT, especially with the Temporal Sublook Coherence (TSC) pixel selection criterion, demonstrated its reliability in every context where it has been implemented, showing in fact, a wide spatial coverage and a good trustworthiness of the results obtained.
- b) PSInSAR proved to be efficient especially for very detailed analyses, as noticed in the two case studies of Cirò and Papanice. In fact, in both cases reliable velocities of displacement have been identified through the PSInSAR application, and the very good agreement of the related time series of displacement with CPT time series and with rainfall data underline its accuracy. However, its application in wider contexts, as for instance observed for the update of the landslide inventory map, presented many outliers, not confirming its reliability in such settings.
- c) SBAS turned out to be particularly useful for analyses at a less-detailed scale. As noticed in its application for the update of the landslide inventory map, no outlier value has been detected in areas most likely not affected by displacement; moreover, the very good spatial coverage allowed to completely analyze landslides in every municipality covered by TerraSAR-X imagery. However, for very local scale studies, differences have been highlighted, especially regarding the displacement rates, where SBAS in many cases seemed to underestimate the velocities.

The application of DInSAR to the different case studies and to the various areas allowed to critically analyze the results obtained, recognizing not only benefits, but also some constraints deriving from its application. One of the most common limitations, noticed also in this thesis, is surely represented by the geometrical distortions. For instance, as observed in both the cases of Cirò and Papanice, only one of the two stacks available provided for reliable results. Geometrical distortions are mostly due to the slope exposure: The best scenario for the ideal SAR monitoring is in slopes facing west or east, because the SAR instrument is pointed to the direction of the presumed movement, while in slopes facing south or north (parallel to azimuth direction) DInSAR cannot detect movements. The other source of geometrical distortions is the slope gradient. In fact, steep slopes limit the elimination of the residual topographic phase, especially when DEM is not very accurate. In

this work, geometrical distortions have been mostly caused by slope orientation. However, the availability of both ascending and descending stacks, and the use of tools such as R-Index allowed to estimate the pixel quality and therefore to recognize an area affected by geometrical distortions. R-Index proved to be a valuable tool especially for the analysis at a larger scale, for the update of landslide inventory maps. The a-priori estimation of the quality of the pixel allowed to discard the bad cases and therefore to fasten the process. Other instruments available in the scientific community for the assessment of the pixel quality have been developed, such as in Plank et al. (2013) or in Notti et al. (2014), which, can provide for a valuable supporting tool for DInSAR analysis. The other common limitation of DInSAR methodologies is represented by the image coherence. The coherence in SAR interferometry is strictly related to the lack of good reflectors (natural or artificial) and to the presence of vegetation. In the landslide cases analyzed, points detected were mostly attributable to urban areas, the same has been noticed also in the subsidence cases. The investigation at Belvedere di Spinello consented to identify vertical motions only in the southern part of the mining area, while, the remaining, completely vegetated, has not provided for any information. One of the possibility to overcome such limit is the installation of corner reflectors. As testified by the case of Capo Colonna, the installation of corner reflectors allowed to obtain an increase of the amplitude signal; therefore, in the future much more targets will be detected by SAR sensors, obtaining more information about the displacements occurring in the area.

Despite the limitations of SAR application, generally this work demonstrated the potentiality of such techniques, especially when integrated with conventional geological and geomorphological methods.

The slope-scale analysis demonstrated how conventional monitoring, especially through the availability of ground truth data, came in support of DInSAR techniques; however, they cannot substitute completely remote sensing, because the latter in many cases demonstrated their reliability, and the relatively low costs and the rapidity of elaboration are very significant parameters to take into account. The innovative character included in this thesis is embodied by the use of interferometry as an instrument capable to provide a help for the planning and the application of remedial works in landslide cases. As also mentioned in the previous chapters, the integration between remote sensing and conventional geological methods can represent a very useful supporting tool for urban planning or landslide hazard assessment, on behalf of public administration.

The update of the inventory map, produced by the combined application of DInSAR and conventional methods, can represent a contribution for the local and regional authorities, for landslide mitigation purposes, or to dispose a quasi-real-time monitoring system. The need for continuous and

real time landslide monitoring has been always stated by the scientific community. Different authors proposed monitoring systems based on the exploitation of ground-based SAR interferometry (e.g. Tarchi et al., 2003; Casagli et al., 2010), others used Global Positioning Systems (GPSs) for continuous monitoring (e.g. Gili et al., 2000; Malet et al., 2002); however, the use of such technologies is strictly related to a detail-scale, while the use of spaceborne interferometry allows to monitor landslides at a larger scale, as demonstrated by this thesis. The elaboration of inventory maps updated by means of interferometry demonstrated the efficacy of SAR data in land management, hence confirming the role of SAR imagery and processing as an ordinary tool for local public institutions. Anyway, the use of radar interferometry for prevision and mitigation of landslides has been promulgated by numerous national and international research projects. It is worth to remember, among the multitude: LEWIS project (Landslide Early Warning Integrated System, 2002), SLAM (Service for LAndslide Monitoring, 2003), TELLUS (2006), MORFEO (*MOnitoraggio e Rischio da Frane con dati EO*, Monitoring and landslide risk with EO data, 2008), DORIS (2010) and EC-FP7 PanGeo (2011). The continuous availability of SAR imagery, especially after the launch of the Sentinel-1 mission in 2014, assumes therefore a key-role for ground monitoring, providing for endless data to SAR-users and to the stakeholders.

8.1 Future perspectives

Many case studies have been introduced and developed during this thesis. The results so far obtained can be considered satisfactory, even though the need of further developments and progresses cannot be neglected. In this sense, the accessibility to free-of-charge Sentinel-1 data, whose mission started in 2014, and to TerraSAR-X and COSMO-SkyMed products, whose missions are still operative, will allow to further investigate on all these cases. With the availability of such imagery, it would be possible to follow landslides' evolution and to develop a quasi-real time monitoring of unstable areas, for preventing and eventually mitigating the related risk. For instance, as observed in Papanice, the monitoring of landslides characterized by slow and intermittent kinematic cannot be underrated even after the triggering phase, being always moving phenomena. Therefore, the need for a constant monitoring in critical areas, such as Papanice, Cirò and the other cases resulted from the large areas monitoring is a paramount objective to achieve, in order to protect buildings located nearby landslide areas. The increase of SAR acquisitions could also simply mean more opportunities to obtain radar data with suitable angles of view, which would allow to improve the analyses for specific morphologies and therefore overcome the geometrical distortion effects encountered in all the case studies. In the area affected by subsidence, improvements can be obtained, as shown at Capo Colonna, by the installation of corner reflector. These instruments will allow to acquire more information, analyzing

at a greater detail the various displacement events affecting the promontory. Thus, further investigations need to be done at Capo Colonna, for a more detailed analysis regarding the relationship between gas extraction and subsidence, and also to better monitor the rates of coastal retreat, which endangers the ruins located along the coastline.

References

- Adam, N., Kampes, B., Eineder, M., Worawattanamateekul, J., Kircher, M. (2003). The development of a scientific permanent scatterer system. In ISPRS Workshop High Resolution Mapping from Space, Hannover, Germany.
- Adam, N., Kampes B., Eineder M. (2005). Development of a scientific permanent scatterer system: Modifications for mixed ERS/ENVISAT time series. Envisat & ERS Symposium. V. 572.
- Ahrens, C. D. (2007). Meteorology Today: An Introduction to Weather, Climate, and the Environment, 8th edition. Thomson Brooks/Cole, Belmont, CA.
- Almagià, R. (1910). Studi geografici sulle frane in Italia. Memorie della Società Geografica Italiana, XIV, Roma. (In Italian).
- Amodio Morelli, L., Bonardi, G., Colonna, V., Dietrich, D., Giunta, G., Ippolito, F., Liguori, V., Lorenzoni, S., Paglionico, A., Perrone, V., Picarretta, G., Russo, M., Scandone, P., Zanettin-Lorenzoni, E., Zuppetta, A. (1976). L'Arco Calabro-Peloritano nell'orogene Appenninico-Maghrebide. Memorie della Società Geologica Italiana 17, 1-60. (In Italian).
- Angeli, M. G., Pasuto, A., Silvano, S. (2000). A critical review of landslide monitoring experiences. Engineering Geology, 55(3), 133-147.
- Antonini, G., Cardinali, M., Guzzetti, F., Reichenbach, P., Sorrentino, A. (1993). Carta Inventario dei Fenomeni Franosi della Regione Marche ed aree limitrofe. CNR, Gruppo Nazionale per la Difesa dalle Catastrofi Idrogeologiche, Publication n. 580, 2 sheets, scale 1:100.000. (In Italian).
- Antonini, G., Ardizzone, F., Cardinali, M., Galli, M., Guzzetti, F., Reichenbach, P. (2002a). Surface deposits and landslide inventory map of the area affected by the 1997 Umbria-Marche earthquakes. Bollettino della Società Geologica Italiana 121 (2), 843-853.
- Antonini, G., Ardizzone, F., Cacciano, M., Cardinali, M., Castellani, M., Galli, M., Guzzetti, F., Reichenbach, P., Salvati, P. (2002a). Rapporto conclusivo protocollo d'intesa fra la Regione dell'Umbria, Direzione Politiche Territoriali Ambiente e Infrastrutture, ed il CNR IRPI di Perugia per l'acquisizione di nuove informazioni sui fenomeni franosi nella regione dell'Umbria, la realizzazione di una nuova carta inventario dei movimenti franosi e dei siti colpiti da dissesto, l'individuazione e la perimetrazione delle aree a rischio da frana di particolare rilevanza, e l'aggiornamento delle stime sull'incidenza dei fenomeni di dissesto sul tessuto insediativo, infrastrutturale e produttivo regionale. Unpublished report, 140 pp. (In Italian).
- Aronica, G. T., Brigandì, G., Morey, N. (2012). Flash floods and debris flow in the city area of Messina, north-east part of Sicily, Italy in October 2009: the case of the Giampilieri catchment. Natural Hazards Earth Systems Science, 12, 1295-1309.
- ARPACAL (Regional agency for the environmental protection of Calabria Region) (2011). Geological study for the monitoring of Via De Gasperi landslide, Cirò. (In Italian). Unpublished report.
- ARPACAL (Regional agency for the environmental protection of Calabria Region) (2013). Installation of a real time monitoring system of the Pironte and of the Via Oceania Primary School landslides, in Papanice, Crotone, (In Italian). Unpublished report.

Autin, W.J. (2002). Landscape evolution of the Five Islands of south Louisiana: scientific policy and salt dome utilization and management. *Geomorphology* 47(2-4), 227-244.

Bamler, R., & Hartl, P. (1998). Synthetic aperture radar interferometry. *Inverse problems*, 14(4), R1.

Barbieri, M., & Lichtenegger, J. (2005). Introduction to SAR for geology. Spaceborne radar applications in Geology.

Bardi, F., Frodella, W., Ciampalini, A., Bianchini, S., Del Ventisette, C., Gigli, G., Fanti, R., Moretti, S., Basile, G., Casagli, N. (2014). Integration between ground based and satellite SAR data in landslide mapping: The San Fratello case study. *Geomorphology*, 223, 45-60.

Barone, M., Dominici, R., Lugli, S. (2007). Interpreting gypsarenites in the Rossano basin (Calabria, Italy): A contribution to the characterization of the Messinian salinity crisis in the Mediterranean. In: Arribas, J., Critelli, S., Johnsson, M.J. (Eds.), *Sedimentary Provenance and Petrogenesis: Perspectives from Petrography and Geochemistry*: Geological Society of America Special Publication, 420, 135-148.

Barone, M., Dominici, R., Muto, F., Critelli, S. (2008). Detrital modes in a late Miocene wedge-top basin, northeastern Calabria, Italy: compositional record of wedge-top partitioning. *Journal of Sedimentary Research*, 78, 693-711.

Barrett, E.C. & Curtis L. F. (1976). *Introduction to Environmental Remote Sensing*. Chapman and Hall Ltd.,

Bartov, Y., Agnon, A., Enzel, Y., Stein, M. (2006). Late Quaternary faulting and subsidence in the central Dead Sea basin. *Israeli Journal of Earth Science*, 55(1), 17-31.

Bell, F. G., Stacey, T. R., Genske, D. D. (2000). Mining subsidence and its effect on the environment: some differing examples. *Environmental Geology*, 40(1-2), 135-152.

Berardino, P., Fornaro, G., Lanari, R., Sansosti, E. (2002). A new Algorithm for Surface Deformation Monitoring based on Small Baseline Differential SAR Interferograms. *IEEE Transactions on Geoscience and Remote Sensing*, 40(11), 2375-2383.

Berti, D., Guarneri, E.M., Silvestri, S. (2003). L'evento alluvionale del 23-27 Gennaio 2003 nella regione Molise. Analisi degli effetti nei riguardi del rischio geomorfologico e idraulico. Relazione tecnica, APAT. (In Italian).

Bianchini, S., Tapete, D., Ciampalini, A., Di Traglia, F., Del Ventisette, C., Moretti, S., Casagli, N. (2014). Multi-temporal evaluation of landslide-induced movements and damage assessment in San Fratello (Italy) by means of C-and X-band PSI data. *Mathematics of Planet Earth*, 257-261. Springer Berlin Heidelberg.

Blanco-Sánchez, P., Mallorquí, J. J., Duque, S., Monells, D. (2008). The Coherent Pixels Technique (CPT): An advanced DInSAR technique for nonlinear deformation monitoring. *Pure and Applied Geophysics*, 165, 1167-1194.

Bonardi, G., Cavazza, W., Perrone, V., Rossi, S. (2001). Calabria-Peloritani terrane and northern Ionian Sea. In: Vai, G.B., Martini, I.P. (Eds.), *Anatomy of an Orogen: The Apennines and Adjacent Mediterranean Basins*. Kluwer Academic Publishers, Bodmin, 287-306.

- Booth, A. M., Roering, J. J., Perron, J. T. (2009). Automated landslide mapping using spectral analysis and high-resolution topographic data: Puget Sound lowlands, Washington, and Portland Hills, Oregon. *Geomorphology*, 109(3), 132-147.
- Bovenga, F., Nutricato, R., Refice, A., Wasowski, J. (2006). Application of multi-temporal differential interferometry to slope instability detection in urban/peri-urban areas. *Engineering Geology*, 88(3), 218-239.
- Brabb, E.E. (1991). The world landslide problem. *Episodes* 14 (1), 52-61.
- Brardinoni, F., Slaymaker, O., Hassan, M.A. (2003). Landslide inventory in a rugged forested watershed: a comparison between air-photo and field survey data. *Geomorphology* 54 (3-4), 179-196.
- Brunsdon, D., & Prior, D. B. (1984). Slope instability.
- Bucknam, R.C., Coe, J.A., Chavarria, M.M., Godt, J.W., Tarr, A.C., Bradley, L.-A., Rafferty, S., Hancock, D., Dart, R.L., Johnson, M.L. (2001). Landslides Triggered by Hurricane Mitch in Guatemala — Inventory and Discussion. U.S. Geological Survey Open File Report 01-443.
- Caine, N. (1980). The rainfall intensity: duration control of shallow landslides and debris flows. *Geografiska Annaler. Series A. Physical Geography*, 23-27.
- Calcaterra, D., Parise, M., Palma, B., Pelella, L. (2000a). Multiple debris flows in volcaniclastic materials mantling carbonate slopes, Proc. 2nd Int. Conf. On Debris flow Hazards Mitigation, Taipei, 99-107.
- Calcaterra, D., Di Martire, D., Ramondini, M., Calò, F., Parise, M. (2008). Geotechnical analysis of a complex slope movement in sedimentary successions of the southern Apennines (Molise, Italy). *Landslides and Engineered Slopes*, Taylor & Francis Group, London, 299-305.
- Calcaterra, D., Ramondini, M., Calò, F., Longobardi, V., Parise, M., Galzerano, C.M. (2008). DInSAR techniques for monitoring slow-moving landslides. *Landslides and Engineered Slopes*, Taylor & Francis Group, London, 1095-1101.
- Calò, F., Parise, M., Ramondini, M., Singhroy, V. (2009). Application of DInSAR techniques to the monitoring of intermittent slope movements in the Southern Appennines of Italy. *Fringe 2009 Workshop*, Frascati, Italy.
- Calò, F., Calcaterra, D., Iodice, A., Parise, M., Ramondini, M. (2012) Assessing the activity of a large landslide in southern Italy by ground-monitoring and SAR interferometric techniques. *International Journal of Remote Sensing*, 33(11), 3512-3530.
- Campbell, J. B., & Wynne, R. H. (2011). *Introduction to remote sensing*. Guilford Press.
- Cardinali, M., Ardizzone, F., Galli, M., Guzzetti, F., Reichenbach, P. (2000). Landslides triggered by rapid snow melting: the December 1996-January 1997 event in Central Italy. In: Claps, P., Siccardi, F. (Eds.), *Proceedings 1st Plinius Conference*, Maratea. Bios Publisher, Cosenza, 439-448.
- Cardinali, M., Antonini, G., Reichenbach, P., Guzzetti, F. (2001). Photo geological and landslide inventory map for the Upper Tiber River basin. CNR, Gruppo Nazionale per la Difesa dalle Catastrofi Idrogeologiche, Publication n. 2116, scale 1:100,000.
- Carminati, E., Martinelli, G. (2002). Subsidence rates in the Po Plain, northern Italy: the relative impact of natural and anthropogenic causation. *Engineering Geology*, 66, 241-255.

- Casagli, N., Catani, F., Del Ventisette, C., Luzi, G. (2010). Monitoring, prediction, and early warning using ground-based radar interferometry. *Landslides*, 7(3), 291-301.
- Cascini, L., Fornaro, G., Peduto, D. (2010). Advanced low- and full-resolution DInSAR map generation for slow-moving landslide analysis at different scales. *Engineering Geology*, 112, 29-42.
- CASMEZ, (1959). Carta geologica della Calabria, foglio 237 - II NE, S. Severina. (In Italian).
- CASMEZ, (1959). Carta geologica della Calabria, foglio 238 - III NO, Scandale. (In Italian).
- CASMEZ, (1959). Carta geologica della Calabria, foglio 238 - III SO, Cutro. (In Italian).
- Casu, F., Manconi, A., Pepe, A., Lanari, R. (2011). Deformation time-series generation in areas characterized by large displacement dynamics: the SAR amplitude pixel-offset SBAS technique. *Geoscience and Remote Sensing, IEEE Transactions on*, 49(7), 2752-2763.
- Cecchi, G., Martina, G. (1976). Timpa del Salto mine (Crotone Province). *Bollettino Associazione Mineraria Subalpina*, 13, 114-142. (In Italian).
- Cevasco, A., Pepe, G., Brandolini, P. (2013). Geotechnical and stratigraphic aspects of shallow landslides at Cinque Terre (Liguria, Italy). *Rendiconti Online Società Geologica Italiana*, 24, 52-54.
- Chandler, R. J., Pellegrini, M., Tosatti, G. (1995). Le cause del disastro. Stava perché. Curcu & Genovese, Trento, 221-230. (In Italian)
- Chung, C. J. F., & Fabbri, A. G. (1999). Probabilistic prediction models for landslide hazard mapping. *Photogrammetric engineering and Remote Sensing*, 65(12), 1389-1399.
- Chung, C. J. F., & Fabbri, A. G. (2003). Validation of spatial prediction models for landslide hazard mapping. *Natural Hazards*, 30(3), 451-472.
- Chung, C. F., & Fabbri, A. G. (2005). Systematic procedures of landslide hazard mapping for risk assessment using spatial prediction models. *Landslide hazard and risk*. Wiley, New York, 139-177.
- Ciampalini, A., Bardi F., Bianchini, S., Frodella, W., Del Ventisette, C., Moretti, S., Casagli, N. (2014). Analysis of building deformation in landslide area using multisensor PSInSART™ technique. *International Journal of Applied Earth Observation and Geoinformatic*, 33, 166-180.
- Cigna, F., Bateson, L., Jordan, C., Dashwood, C. (2013). Nationwide monitoring of geohazards in Great Britain with InSAR: feasibility mapping based on ers-1/2 and Envisat imagery. *IEEE International Geoscience Remote Sensing Symposium (IGARSS)*, 672-675.
- Colesanti, C., Ferretti, A., Prati, C., Rocca F. (2003). Monitoring landslides and tectonic motion with the Permanent Scatterers technique. *Engineering Geology*, 68(1-2), 3-14.
- Colesanti, C., Wasowski, J. (2006). Investigating landslides with space-borne Synthetic Aperture Radar (SAR) interferometry. *Engineering Geology*, 88, 173-199.
- Coltorti, M., Dramis, F., Gentili, B., Pambianchi, G., Crescenti, U., Sorriso Valvo, M. (1985). The December 1982 Ancona landslide. A case of deep-seated gravitational slope deformation evolving at unsteady rate. *Zeitschrift fur geomorphologie*, 29(3), 335-345.
- Colwell, R. N. (1968). Determining the prevalence of certain cereal disease by means of aerial photography. *Hilgardia* 26, 223-286.

Conforti, M., Aucelli, P. P., Robustelli, G., Scarciglia, F. (2011). Geomorphology and GIS analysis for mapping gully erosion susceptibility in the Turbolo stream catchment (Northern Calabria, Italy). *Natural hazards*, 56(3), 881-898

Confuorto, P., Plank, S., Di Martire, D., Ramondini, M., Thuro, K., Calcaterra, D. (2015). Slow-moving Landslide Monitoring with Multi-temporal TerraSAR-X data by means of DInSAR Techniques in Crotone Province (Southern Italy). Proceedings of FRINGE'15: Advances in the Science and Applications of SAR Interferometry and Sentinel-1 InSAR Workshop, Frascati, Italy, 23-27 March 2015, Ouwehand L., Ed., ESA Publication SP-731.

Cosentino, D., Gliozzi, E., Salvini, F. (1989). Brittle deformations in the Upper Pleistocene deposits of the Crotone Peninsula, Calabria, southern Italy. *Tectonophysics*, 163, 205-217.

Costantini, M. (1998). A novel phase unwrapping method based on network programming. *Geoscience and Remote Sensing, IEEE Transactions on*, 36(3), 813-821.

Costantini, M., Iodice, A., Magnapane, L., Pietranera, L. (2000). Monitoring terrain movements by means of sparse SAR differential interferometric measurements. In *Geoscience and Remote Sensing Symposium, 2000. Proceedings. IGARSS 2000. IEEE 2000 International*, 7, 3225-3227.

Cotecchia, V. (1978). Systematic reconnaissance mapping and registration of slope movements. *Bulletin of the International Association of Engineering Geology-Bulletin de l'Association Internationale de Géologie de l'Ingénieur*, 17(1), 5-37.

Cotecchia, V. (2006). The second Hans Cloos lecture. Experience drawn from the great Ancona landslide of 1982. *Bulletin of Engineering Geology and the Environment*, 65(1), 1-41.

Critelli, S., & Le Pera, E. (1998). Post-Oligocene sediment-dispersal systems and unroofing history of the Calabrian microplate, Italy. *International Geology Review*, 40(7), 609-637.

Critelli, S. (1999). The interplay of lithospheric flexure and thrust accommodation in forming stratigraphic sequences in the southern Apennines foreland basin system, Italy. *Memorie dell'Accademia Nazionale dei Lincei*, 10, 257-326.

Critelli, S., Muto, F., Tripodi, V., Perri, F. (2011). Relationships between lithospheric flexure, thrust tectonics and stratigraphic sequences in foreland setting: the southern Apennines foreland basin system, Italy. In: Schattner, U. (Ed.), *New Frontiers in Tectonic Research-At the Midst of Plate Convergence*. InTech Open Access Publisher, 121-170.

Crosetto, M., Tscherning, C. C., Crippa, B., Castillo, M. (2002). Subsidence monitoring using SAR interferometry: Reduction of the atmospheric effects using stochastic filtering. *Geophysical Research Letters*, 29(9).

Crosetto, M., Biescas, E., Duro, J., Closa, J., Arnaud, A. (2008). Generation of Advanced ERS and Envisat Interferometric SAR Products Using the Stable Point Network Technique. *Photogrammetric Engineering and Remote Sensing*, 74(4), 443-451.

Cruden, D.M. & Varnes, D.J. (1996). Landslide types and process. In: Turner, A.K., Schuster, R.J. (Eds.), *Landslides: Investigation and Mitigation*, Special Report 247. Transportation Research Board, National Research Council, National Academy Press, Washington, DC, 36-75.

Culshaw, M. G., & Waltham, A. C. (1987). Natural and artificial cavities as ground engineering hazards. *Quarterly Journal of Engineering Geology and Hydrogeology*, 20(2), 139-150.

De Luca D.L., (2014). Analysis and modelling of rainfall fields at different resolutions in southern Italy. *Hydrological Sciences Journal*, 56(8), 1536-1558.

DeGraff, J. V. (1985). Using isopleth maps of landslide deposits as a tool in timber sale planning. *Bulletin of the Association of Engineering Geologists*, 22(4), 445-453.

DeGraff, J. V., & Canuti, P. (1988). Using isopleth mapping to evaluate landslide activity in relation to agricultural practices. *Bulletin of the International Association of Engineering Geology-Bulletin de l'Association Internationale de Géologie de l'Ingénieur*, 38(1), 61-71.

Del Prete, M., Guadagno, F. M., Hawkins, A. B. (1998). Preliminary report on the landslides of 5 May 1998, Campania, southern Italy. *Bulletin of Engineering Geology and the Environment*, 57(2), 113-129.

Del Ventisette, C., Righini, G., Moretti, S., Casagli, N. (2014). Multitemporal landslides inventory map updating using spaceborne SAR analysis. *International Journal of Applied Earth Observation and Geoinformation*, 30, 238-246.

Dewey, J. F., Helman, M. L., Knott, S. D., Turco, E., Hutton, D. H. W. (1989). Kinematics of the western Mediterranean. Geological Society, London, Special Publications, 45(1), 265-283.

De Zan, F., & Guarneri, A. M. (2006). TOPSAR: Terrain observation by progressive scans. *Geoscience and Remote Sensing, IEEE Transactions on*, 44(9), 2352-2360.

Di Martire, D., Iodice, A., Ramondini, M., Ruello, G., Calcaterra, D. (2011). Combined observations of surface displacements using Differential Interferometry SAR (DInSAR), GPS and traditional monitoring techniques. *Geophysical research abstracts*, 13, 6772-6772.

Di Martire, D., Iglesias, R., Monells, D., Centolanza, G., Sica, S., Pagano, L., Mallorquì, J.J., Calcaterra, D. (2014). Comparison between Differential SAR interferometry and ground measurements data in the displacement monitoring of the earth-dam of Conza della Campania (Italy). *Remote Sensing of Environment*, 148, 58-69.

Di Martire, D., Tessitore, S., Brancato, D., Ciminelli, M. G., Costabile, S., Costantini, M., Graziano, G. V., Minati, F., Ramondini, M., Calcaterra, D. (2016). Landslide detection integrated system (LaDIS) based on in-situ and satellite SAR interferometry measurements. *Catena*, 137, 406-421.

Dikau, R., Brundsen, D., Schrott, L., Ibsen, M.L. (1996). *Landslide Recognition: Identification, Movement and Causes*. Wiley, Chichester.

DORIS (2010). *Ground Deformations Risk Scenarios: an Advanced Assessment Service. Global Monitoring for Environment and Security program*. <http://www.doris-project.eu/> [accessed on 13 November, 2015]

Dramis, F., & Sorriso-Valvo, M. (1994). Deep-seated gravitational slope deformations, related landslides and tectonics. *Engineering Geology*, 38(3), 231-243.

EC-FP7 PanGeo (2014). <http://www.pangeoproject.eu/> [accessed on 10 February, 2016]

Eineder, M., & Holzner, J. (2000). Interferometric DEMs in alpine terrain-limits and options for ERS and SRTM. In *Geoscience and Remote Sensing Symposium, 2000. Proceedings. IGARSS 2000. IEEE 2000 International* 7, 3210-3212.

EPOCH (1993). *The temporal occurrence and forecasting of landslides in the European community* (Ed: Flageollet, J. C.). Contract No. 90 0025, 3 Volumes.

- Faccenna, C., Becker, T.W., Luente, F.P., Jolivet, L., Rossetti, F. (2001). History of subduction and back-arc extension in the Central Mediterranean. *Geophysical Journal International*, 145, 809-820.
- Faccenna, C., Piromallo, C., Crespo-Blanc, A., Jolivet, L., Rossetti, F. (2004). Lateral slab deformation and the origin of the western Mediterranean arcs. *Tectonics*, 23, TC1012
- Fatland, D. R., & Lingle, C. S. (1998). Analysis of the 1993-95 Bering Glacier (Alaska) surge using differential SAR interferometry. *Journal of Glaciology*, 44(148), 532-546.
- Galloway, D. L., Hudnut, K. W., Ingebritsen, S. E., Phillips, S. P., Peltzer, G., Rogez, F., Rosen, P. A. (1998). Detection of aquifer system compaction and land subsidence using interferometric synthetic aperture radar, Antelope Valley, Mojave Desert, California. *Water Resources Research*, 34(10), 2573-2585.
- Fell R., Corominas J., Bonnard C., Cascini L., Leroi E., Savage W. (2008). Guidelines for landslide susceptibility, hazard and risk zoning for land use planning. *Engineering Geology*, 102, 85-98.
- Ferretti, A., Prati, C., Rocca, F. (2000). Nonlinear subsidence rate estimation using permanent scatterers in differential SAR interferometry. *IEEE Transactions on Geoscience and Remote Sensing*, 38 (5), 2202-2212.
- Ferretti, A., Prati, C., Rocca, F. (2001). Permanent scatterers in SAR interferometry. *IEEE Transactions on Geoscience and Remote Sensing* 39(1), 8-20.
- Ferretti, A., Savio, G., Barzaghi, R., Borghi, A., Musazzi, S., Novali, F., Prati, C., Rocca, F. (2007) Sub-millimeter Accuracy of InSAR Time Series: Experimental Validation. *IEEE Transactions On Geoscience And Remote Sensing*, 45, 5.
- Ferretti, A., Fumagalli, A., Novali, F., Prati, C., Rocca, F., Rucci, A. (2011). A new algorithm for processing interferometric data-stacks: SqueeSAR. *IEEE Transactions on Geoscience and Remote Sensing*, 49(9), 3460-3470.
- Fiaschi, S., Di Martire, D., Tessitore, S., Achilli, V., Ahmed, A., Borgstrom, S., Calcaterra, D., Fabris, M., Ramondini, M., Serpelloni, E., Siniscalchi, V., Floris, M. (2015). Monitoring of land subsidence in Ravenna Municipality using two different DInSAR techniques: comparison and discussion of the results. *Ecology*, 23(1), 38-50.
- Fielding, E. J., Blom, R. G., Goldstein, R. M. (1998). Rapid subsidence over oil fields measured by SAR interferometry. *Geophysical Research Letters*, 25(17), 3215-3218.
- Finetti, I.R., Lentini, F., Carbone, S., Del Ben, A., Di Stefano, A., Forlin, E., Guarneri, P., Pipan, M., Prizzon, A. (2005a). Geological outline of Sicily and lithospheric tectono-dynamics of its Tyrrhenian margin from new CROP seismic data. In: Finetti, I.R. (Ed.), *CROP Deep Seismic Exploration of the Mediterranean Region*. Elsevier, Amsterdam, 319-375.
- Fiorucci, F., Cardinali, M., Carlà, R., Rossi, M., Mondini, A.C., Santurri, L., Ardizzone, F., Guzzetti, F. (2011). Seasonal landslides mapping and estimation of landslide mobilization rates using aerial and satellite images. *Geomorphology*, 129 (1-2), 59-70.
- Fornaro, G., Pauciullo, A., Serafino, F. (2007). Multipass SAR Processing for urbanized areas imaging and deformation monitoring at small and large scales. *Urban Remote Sensing Joint Event URS 2007*, Paris, 11-13 April.

Fortuna, R., 2006. Il contributo della mineralogia applicata all'interpretazione del comportamento fisico-meccanico dei terreni argillosi coinvolti in una frana in località Agnone (IS). Tesi di laurea. (In Italian).

Franceschetti, G. & Lanari, R. (1999). Synthetic Aperture Radar Processing, CRC Press, Boca Raton (FL), ISBN 8493-7899.

Fried, D. L. (1977). Least-square fitting a wave-front distortion estimate to an array of phase-difference measurements. *JOSA*, 67(3), 370-375.

Frost, V. S., Stiles, J. A., Shanmugan, K. S., Holtzman, J. C. (1982). A model for radar images and its application to adaptive digital filtering of multiplicative noise. *Pattern Analysis and Machine Intelligence, IEEE Transactions on*, (2), 157-166.

Fruneau, B., Achache, J., Delacourt, C. (1996). Observation and modelling of the Saint- Etienne de Tinee landslide using SAR interferometry. *Tectonophys*, 265 (3-4), 181- 190.

Gabriel, A. K. & Goldstein, R. M. (1988) Crossed orbit interferometry: theory and experimental results from SIR-B. *International Journal Remote Sensing*, 9 857-72.

Gabriel, A. K., Goldstein, R. M., Zebker, H. A. (1989). Mapping small elevation changes over large areas: Differential interferometry, *Journal Geophysical Research*, 94, 9183-9191.

Gagnon, H. (1975). Remote sensing of landslide hazards on quick clays of eastern Canada. Proceeding 10th International Symposium Remote Sensing of Environment. Environmental Research Institute of Michigan, Ann Arbor, Michigan II, 803-810.

Galli, M., Ardizzone, F., Cardinali, M., Guzzetti, F., Reichenbach, P. (2008). Comparing landslide inventory maps. *Geomorphology* 94, 268-289.

Galloway, D.L., Hudnut, K.W., Ingebritsen, S.E., Phillips, S.P., Peltzer, G., Rogez, F., Rosen, P.A. (1998). Detection of aquifer synthetic aperture radar, Antelope Valley, Mojave Desert, California. *Water Resources Research*, 34 (10), 2573-2585.

Galloway, D. L., & Burbey, T. J. (2011). Review: regional land subsidence accompanying groundwater extraction. *Hydrogeology Journal*, 19(8), 1459-1486.

Gambolati, G., Ricceri, G., Bertoni, W., Brighenti, G., Vuillermin, E. (1991). Mathematical simulation of the subsidence of Ravenna. *Water Resource Research*, 27(11), 2899-2918.

Gattinoni, P., Scesi, L., Arieni, L., Canavesi, M. (2012). The February 2010 large landslide at Maierato, Vibo Valentia, Southern Italy. *Landslides*, 9(2), 255-261.

Gili, J. A., Corominas, J., Rius, J. (2000). Using Global Positioning System techniques in landslide monitoring. *Engineering geology*, 55(3), 167-192.

Giordan, D., Allasia, P., Manconi, A., Baldo, M., Santangelo, M., Cardinali, M., Corazza, A., Albanese, V., Lollino, G., Guzzetti, F. (2013). Morphological and kinematic evolution of a large earthflow: The Montaguto landslide, southern Italy. *Geomorphology*, 187, 61-79.

Glenn, N.F., Streuker, D.R., Chadwick, D.J., Thackray, G.D., Dorsch, S.J. (2006). Analysis of Lidar derived topographic information for characterizing and differentiating landslide morphology and activity. *Geomorphology*, 73, 131-148.

Gliozi, E. (1987). I terrazzi del Pleistocene superiore della Penisola di Crotone (Calabria). *Geologica Romana*, 26, 17-79. (In Italian).

Goldstein, R. M., Zebker, H. A., Barnett, T. P. (1989). Remote sensing of ocean currents. *Science*, 246 (4935), 1282-1285.

Goldstein, R. M., Engelhardt, H., Kamb, B., Frolich, R. M. (1993). Satellite radar interferometry for monitoring ice sheet motion: application to an Antarctic ice stream. *Science*, 262 (5139), 1525-1530.

Goldstein, R. M., & Werner, C. L. (1998). Radar interferogram filtering for geophysical applications. *Geophysical Research Letters*, 25(21), 4035-4038.

Graham, L. C. (1974). Synthetic interferometer radar for topographic mapping. *Proceedings of the IEEE*, 62(6), 763-768.

Guerriero, L., Revellino, P., Coe J., Focareta, M., Grelle, G., Albanese, V., Corazza, A. Guadagno F.M. (2013). Multi-temporal Maps of the Montaguto Earth Flow in Southern Italy from 1954 to 2010. *Journal of Maps*, 9(1), 135-145.

Guha-Sapir, D, Hoyois, Ph., Below, R. (2014). Annual Disaster Statistical Review 2013: The Numbers and Trends. Brussels: CRED.

Gupta, R. P. (2013). *Remote sensing geology*. Springer Science & Business Media.

Guthrie, R.H., Evans, S.G. (2004a). Magnitude and frequency of landslides triggered by a storm event, Loughborough Inlet, British Columbia. *Natural Hazards and Earth System Sciences*, 4, 475-483.

Guthrie, R.H., Evans, S.G. (2004b). Analysis of landslide frequencies and characteristics in a natural system, coastal British Columbia. *Earth Surface Processes and Landforms*, 29 (11), 1321-1339.

Gutiérrez F., Galve J.P., Lucha P., Castañeda C., Bonachea J., Guerrero J. (2011). Integrating geomorphological mapping, trenching, InSAR and GPR for the identification and characterization of sinkholes: A review and application in the mantled evaporite karst of the Ebro Valley (NE Spain). *Geomorphology*, 134, 2011, 144-156.

Guzzetti, F., Carrara, A., Cardinali, M., Reichenbach, P. (1999). Landslide hazard evaluation: a review of current techniques and their application in a multi-scale study, Central Italy. *Geomorphology*, 31, 181-216.

Guzzetti, F., Cardinali, M., Reichenbach, P., Carrara, A. (2000). Comparing landslide maps: a case study in the upper Tiber River Basin, Central Italy. *Environmental Management*, 25 (3), 247-363.

Guzzetti, F., Reichenbach, P., Cardinali, M., Galli, M., Ardizzone, F. (2005). Probabilistic landslide hazard assessment at the basin scale. *Geomorphology*, 72, 272-299.

Guzzetti, F., Mondini, A. C., Cardinali, M., Fiorucci, F., Santangelo, M., Chang, K. T. (2012). Landslide inventory maps: New tools for an old problem. *Earth-Science Reviews*, 112(1), 42-66.

- Hansen, A. (1984a). Engineering geomorphology: the application of an evolutionary model of Hong Kong. *Zeitschrift für Geomorphologie*, 51, 39-50.
- Hansen, A. (1984b). Strategies for classification of landslides. In: Brunsden, D., Prior, D.B. (Eds.), *Slope Instability*. Wiley, New York, 523-602.
- Hanssen, R. (2001). Radar interferometry. Kluwer Academic Publishers, Dordrecht (The Netherlands).
- Harp, E.L., Jibson, R.L. (1995). Inventory of landslides triggered by the 1994 Northridge, California earthquake. U.S. Geological Survey Open File Report, 95-213.
- Harp, E.L., Jibson, R.L. (1996). Landslides triggered by the 1994 Northridge, California earthquake. *Seismological Society of America Bulletin*, 86, 319-332.
- Haugerud, R., Harding, D.J., Johnson, S.Y., Harless, J.L., Weaver, C.S., Sherrod, B.L. (2003). High-resolution topography of the Puget Lowland, Washington - a bonanza for earth science. *GSA Today*, 13, 4-10.
- Herrera, G., Tomás, R., López-Sánchez, J. M., Delgado, J., Mallorqui, J. J., Duque, S., Mulas, J. (2007). Advanced DInSAR analysis on mining areas: La Union case study (Murcia, SE Spain). *Engineering Geology*, 90(3), 148-159.
- Herrera, G., Notti, D., García-Davalillo, J.C., Mora, O., Cooksley, G., Sánchez, M., Arnaud, A., Crosetto, M. (2011). Analysis with C- and X-band satellite SAR data of the Portalet landslide area. *Landslides*, 8, 195-206.
- Herrera, G., Gutiérrez, F., García-Davalillo, J. C., Guerrero, J., Notti, D., Galve, J. P., Fernandez-Merodo, J. A., Cooksley, G. (2013). Multi-sensor advanced DInSAR monitoring of very slow landslides: The Tena Valley case study (Central Spanish Pyrenees). *Remote Sensing of Environment*, 128, 31-43.
- Hix, G. L. (1995). Land subsidence and ground water withdrawal. *Water Well Journal*, 49(11), 37-39.
- Hoffmann, J, Galloway, DL, Zebker, H.A. (2003). Inverse modelling of interbed storage parameters using land subsidence observations, Antelope Valley, California. *Water Resour Res* 39(2), 1031.
- Hooper, A., Zebker H., Segall, P., Kampes, B., 2004. A new method for measuring deformation on volcanoes and other natural terrains using InSAR persistent scatterers, *Geophysical Research Letter*, 31, 23611.
- Hooper, A. (2006). Persistent scatter radar interferometry for crustal deformation studies and modeling of volcanic deformation. *Dissertation Abstracts International*, 67-05, 2435.
- Hooper, A., (2008). A multi-temporal InSAR method incorporating both persistent scatterer and small baseline approaches, *Geophys. Res. Lett.*, 35, 16302.
- Hovius, N., Stark, C.P., Allen, P.A. (1997). Sediment flux from a mountain belt derived by landslide mapping. *Geology*, 25, 231-234.
- Hovius, N., Stark, C.P., Hao-Tsu, C., Jinn-Chuan, L. (2000). Supply and removal of sediment in a landslide-dominated mountain belt: Central Range, Taiwan. *Journal of Geology*, 108, 73-89.

Hu, R.L., Yue, Z.Q., Wang, L.C., Wang, S.J. (2004). Review on current status and challenging issues of land subsidence in China. *Engineering Geology*, 76, 65-77.

Huang, S., Chen, B. (1991). Integration of Landsat and terrain information for landslide study. Proceedings of 8th Thematic Conference on Geological Remote Sensing. ERIM, Denver, Colorado (USA), 743-754.

Hungr, O., Evans, S. G., Bovis, M. J., Hutchinson, J. N. (2001). A review of the classification of landslides of the flow type. *Environmental & Engineering Geoscience*, 7(3), 221-238.

Hutchinson, J.N. (1988). General report: morphological and geotechnical parameters of landslides in relation to geology and hydrology. 5th International Symposium on Landslides, Lausanne, 1, 3-35.

Ietto, A. (1988). Analisi di una catastrofe prevedibile: la miniera di salgemma di Belvedere di Spinello (Calabria). Atti XXIV Cong. Geol. It. Ed. Patron, 485-503. (In Italian).

Ietto, F., Federico, M., (2007). The salt mine and resources of the Neto valley (Calabria, Italy). *L'Acqua*, 5, 55-64.

Iglesias, R., Mallorqui, J.J., Monells, D., López-Martíne, C., Fabregas, X., Aguasca, A., Gili, J.A., Corominas, J. (2015). PSI Deformation Map Retrieval by Means of Temporal Sublook Coherence on Reduced Sets of SAR Images. *Remote Sensing*, 7, 530-563.

Imakiire, T., and Mamoru K. (2012). Wide-area land subsidence caused by “the 2011 off the Pacific Coast of Tohoku Earthquake. *Soils and Foundations*, 52.5, 842-855.

Iovine, G. G. R., Lollino, P., Gariano, S. L., Terranova, O. G. (2010). Coupling limit equilibrium analyses and real-time monitoring to refine a landslide surveillance system in Calabria(southern Italy). *Natural Hazards and Earth System Sciences*, 10(11), 2341-2354.

IRPI (Research Institute for Geo-Hydrological Protection), (2015). Periodic report on landslides and floods hazard for the Italian population. (In Italian).

ISPRA (Istituto Superiore per la Protezione e la Ricerca Ambientale), (2014). Rapporto di sintesi sul dissesto idrogeologico in Italia. (In Italian).

ISPRA (Istituto Superiore per la Protezione e la Ricerca Ambientale), (2006). Carta geologica d'Italia, Foglio 554, Crucoli.

ISPRA (Istituto Superiore per la Protezione e la Ricerca Ambientale), (2006). Carta geologica d'Italia, Foglio 562, Cirò.

ISPRA (Istituto Superiore per la Protezione e la Ricerca Ambientale), (2006). Carta geologica d'Italia, Foglio 571, Crotone.

Itoh, Y., Takemura, K., Ishiyama, T., Tanaka, Y., Iwaki, H. (2000). Basin formation at a contractional bend of a large transcurrent fault: Plio-Pleistocene subsidence of the Kobe and northern Osaka Basins, Japan. *Tectonophysics*, 321(3), 327-341.

Iverson, R. M., Reid, M. E., LaHusen, R. G. (1997). Debris-flow mobilization from landslides 1. *Annual Review of Earth and Planetary Sciences*, 25(1), 85-138.

Iverson, R. M. (2000). Landslide triggering by rain infiltration. *Water resources research*, 36(7), 1897-1910.

Jahn, A. (1964). Slopes morphological features resulting from gravitation. *Z. Geomorph*, 5, 59-72.

Janbu, N. (1954). Application of composite slip surfaces for stability analysis. In Proc. European Conf. on Stability of Earth Slopes, Stockholm, 3, 43-49).

Julio-Miranda, P., Ortíz-Rodríguez, A. J., Palacio-Aponte, A. G., López-Doncel, R., Barboza-Gudiño, R. (2012). Damage assessment associated with land subsidence in the San Luis Potosí-Soledad de Graciano Sanchez metropolitan area, Mexico, elements for risk management. Natural hazards, 64(1), 751-765.

Kampes, B. M. (2006). Radar interferometry. Springer.

Kappel, W.M., Yager, R.M., Todd, M.S. (1999). The Retsof Salt Mine Collapse. In: Galloway DL, Jones DR, Ingebritsen SE (eds) Land Subsidence in the United States, 1182, US Geological Survey CircularUS Geological Survey, Reston, 111-120.

Kirkby, M. J. (1967). Measurement and theory of soil creep. The Journal of Geology, 359-378.

Klinger, Y., Michel, R., Avouac, J. P. (2000). Co-seismic deformation during the Mw7. 3 Aqaba Earthquake (1995) from ERS-SAR interferometry. Geophysical research letters, 27(22), 3651-3654.

Knott, S. D., & Turco, E. (1991). Late Cenozoic kinematics of the Calabrian arc, southern Italy. Tectonics, 10(6), 1164-1172.

Kwok, R., Fahnestock, M.A. (1996). Ice sheet motion and topography from radar interferometry. IEEE Transactions on Geoscience and Remote Sensing, 34 (1), 189- 200.

Lanari, R., Lundgren, P., Sansosti, E. (1998). Dynamic deformation of Etna volcano observed by satellite radar interferometry. Geophysical Research Letters, 25(10), 1541-1544.

Lee, K. L. (1979). Subsidence earthquake at a California oil field. In Evaluation and Prediction of Subsidence, 549-564.

Lee, J. S., Jurkevich, L., Dewaele, P., Wambacq, P., Oosterlinck, A. (1994). Speckle filtering of synthetic aperture radar images: A review. Remote Sensing Reviews, 8(4), 313-340.

Lena, G. & Bonomi, S. (2004). Coastal erosion and archaeological monuments in Calabria. Geologia dell'ambiente, 8-14. (In Italian)

Lentini, F., Carbone, S., Catalano, S., Di Stefano, A., Gargano, C., Romeo, M., Strazzulla, S., Vinci, G. (1995). Sedimentary evolution of basins in mobile orogenic belts: examples from the Tertiary sequences of the Peloritani Mts. (NE Sicily). Terra Nova, 7, 161-170.

LEWIS (2002). http://cordis.europa.eu/result/rcn/83810_en.html

Li, F., & Goldstein, R. (1987). Studies of multi-baseline spaceborne interferometric synthetic aperture radars. In IGARSS'87-International Geoscience and Remote Sensing Symposium, 1, 1545-1550.

Lopes, A., Nezry, E., Touzi, R., Laur, H. (1993). Structure detection and statistical adaptive speckle filtering in SAR images. International Journal of Remote Sensing, 14(9), 1735-1758.

Lu, Z., Mann, D., Freymueller, J.T., Meyer, D.J. (2000). Synthetic aperture radar interferometry of Okmok volcano, Alaska: Radar observations. Journal of Geophysical Research, 105, 10791-10806.

Luca, F., Robustelli, G., Conforti, M., Fabbricatore, D. (2011). Geomorphological map of the Crotone Province (Calabria, South Italy). Journal of Maps, 7(1), 375-390.

Lugli, S., Dominici, R., Barone, M., Costa, E., Cavozzi, C. (2007). Messinian halite and residual facies in the Crotone basin (Calabria, Italy). In: Schreiber, B.C., Lugli, S., Babel, M. (Eds.), *Evaporites through Space and Time*: Geological Society Special Publication, 285, 169-178.

Lundgren, P., Berardino, P., Coltell, M., Fornaro, G., Lanari, R., Puglisi, G., Sansosti, E., Tesauro, M. (2003). Coupled magma chamber inflation and sector collapse slip observed with synthetic aperture radar interferometry on Mt. Etna volcano. *Journal of Geophysical Research: Solid Earth*, 108(B5).

Malamud, B.D., Turcotte, D.L., Guzzetti, F., Reichenbach, P. (2004a). Landslides, earthquakes and erosion. *Earth and Planetary Science Letters*, 229, 45-59.

Malamud, B.D., Turcotte, D.L., Guzzetti, F., Reichenbach, P. (2004b). Landslide inventories and their statistical properties. *Earth Surface Processes and Landforms*, 29 (6), 687-711.

Malet, J. P., Maquaire, O., Calais, E. (2002). The use of Global Positioning System techniques for the continuous monitoring of landslides: application to the Super-Sauze earthflow (Alpes-de-Haute-Provence, France). *Geomorphology*, 43(1), 33-54.

Malinverno, A., Ryan, W.B.F. (1986). Extension in the Tyrrhenian Sea and shortening in the Apennines as a result of arc migration driven by sinking of the lithosphere. *Tectonics*, 5, 227-245.

Mancini, F., Stecchi, F., Zanni, M., Gabbianelli, G. (2009). Monitoring ground subsidence induced by salt mining in the city of Tuzla (Bosnia and Herzegovina). *Environmental Geology*, 58(2), 381-389.

Manconi, A., Casu, F., Ardizzone, F., Bonano, M., Cardinali, M., De Luca, C., Gueguen, E., Marchesini, I., Parise, M., Vennari, C., Lanari, R., Guzzetti, F. (2014). Brief Communication: Rapid mapping of landslide events: the 3 December 2013 Montescaglioso landslide, Italy. *Natural Hazards and Earth System Sciences*, 14(7), 1835-1841.

Massari, F., Prosser, G., Capraro, L., Fornaciari, E., Consolato, C. (2010). A revision of the stratigraphy and geology of the south-western part of the Crotone Basin (South Italy). *Italian Journal of Geosciences*, 129, 353-384.

Massonnet, D., Thatcher, W., Vadon, H. (1996). Detection of postseismic fault zone collapse following the Landers earthquake. *Nature*, 382, 489-497.

Massonnet, D., Feigl, K.L. (1998). Radar interferometry and its application to changes in the Earth's surface. *Reviews of Geophysics*, 36(4), 441-500.

Allen, D. R., & Mayuga, M. N. (1970). Subsidence in the Wilmington Oil Field, Long Beach, California, USA. In Int Ass Sci Hydrol & UNESCO Land Subsidence Symp Proc VI, 66-87.

McCalpin, J. (1984). Preliminary age classification of landslides for inventory mapping. Proceedings 21st annual Engineering Geology and Soils Engineering Symposium. University Press, Moscow, Idaho, 99-111.

McDonald, H.C., Grubbs, R.C. (1975). Landsat imagery analysis: an aid for predicting landslide prone areas for highway construction. Proceeding NASA Earth Resource Symposium, 1b, 769-778. NASA, National Aeronautics and Space Administration, Washington, D.C.

Meisina, C., Zucca, F., Notti, D., Colombo, A., Cucchi, A., Savio, G., Giannico, C., Bianchi, M. (2008). Geological interpretation of PSInSAR data at regional scale. *Sensors*, 8, 7469-7492.

- Mellere, D., Zecchin, M., Perale, C. (2005). Stratigraphy and sedimentology of faultcontrolled backstepping shorefaces, middle Pliocene of Crotone Basin, Southern Italy. *Sedimentary Geology* 176, 281-303.
- Meulenkamp, J.E., Hilgen, F., Voogt, E. (1986). Late Cenozoic sedimentary tectonic history of the Calabrian Arc. *Giornale di Geologia*, 48 (1-2), 345-359.
- Mohr, O. (1914). Treatises on mechanic-engineering (2nd ed). Ernst, Berlin. (In German).
- Mora, O., Mallorquí, J.J., Broquetas, A. (2003). Linear and nonlinear terrain deformation maps from a reduced set of interferometric SAR images. *IEEE Transactions on Geoscience and Remote Sensing*, 41, 2243-2253.
- Mora, O., Mallorqui, J. J., Duro, J., Broquetas, A. (2001). Long-term subsidence monitoring of urban areas using differential interferometric SAR techniques. In *Geoscience and Remote Sensing Symposium, 2001. IGARSS'01. IEEE 2001 International*, 3, 1104-1106.
- MORFEO (2008). http://www.morfeoproject.it/index.php?option=com_frontpage&Itemid=1 [accessed on 25 November, 2015]
- Nalin, R., Massari, F., Zecchin, M. (2007). Superimposed cycles of composite marine terraces: the example of Cutro terrace (Calabria, Southern Italy). *Journal of Sedimentary Research*, 77, 340-354.
- Notti, D., Garcia-Davalillo, J.C., Herrera, G. Mora, O. (2010). Assessment of the performance of X-band satellite radar data for landslide mapping and monitoring: Upper Tena valley case study. *Natural Hazards and Earth System Sciences*, 10, 1865-1875.
- Notti, D., Herrera, G., Bianchini, S., Meisina, C., García-Davalillo, J.C., Zucca, F. (2014). A methodology for improving landslide PSI data analysis. *International Journal of Remote Sensing*, 35, (6), 2186-2214.
- Notti, D., Calò, F., Cigna, F., Manunta, M., Herrera, G., Berti, M., Meisina, C., Tapete, D., Zucca, F. (2015). A User-Oriented Methodology for DInSAR Time Series Analysis and Interpretation: Landslides and Subsidence Case Studies. *Pure and Applied Geophysics*, 172(11), 3081-3105.
- Novellino, A., De Agostini, A., Di Martire, D., Ramondini, M., Floris, M., Calcaterra, D. (2015). Using Data from Multiple SAR Sensors in Landslide Characterization: Case Studies from Different Geomorphological Contexts in Italy. In *Engineering Geology for Society and Territory*, 2, 395-398. Springer International Publishing.
- Ogniben, L. (1955). Le argille scagliose del Crotone. *Memorie e Note Istituto di Geologia Applicata di Napoli*, 6, 1-72.
- Ogniben, L. (1969). Schema introduttivo alla geologia del confine calabro-lucano. *Memorie della Società Geologica Italiana*, 8, 453-763.
- Onions, C. T. (1933). The Oxford English dictionary.
- Osmanoglu, B., Dixon, T. H., Cabral-Cano, E., Wdowinski, S. (2008). Mexico City Subsidence. AGU Fall Meeting Abstracts, 1, 0653.
- Palmentola, G., Carobene, L., Mastronuzzi, G., Sansò, P. (1990). I terrazzi marini Pleistocenici della Penisola di Crotone (Calabria). *Geografia Fisica e Dinamica Quaternaria*, 13(1), 75-80. (In Italian).

Parise, M. (2001). Landslide mapping techniques and their use in the assessment of the landslide hazard. *Physics and Chemistry of the Earth, Part C: Solar, Terrestrial & Planetary Science*, 26(9), 697-703.

Parise, M. & Trocino, A. (2005). Gypsum karst in the Crotone province (Calabria, southern Italy). Slovenska akademija znanosti in umetnosti.

Pašek, J. (1975). Landslides inventory. *Bulletin of the International Association of Engineering Geology-Bulletin de l'Association Internationale de Géologie de l'Ingénieur*, 12(1), 73-74.

Peltzer, G., Rosen, P.A. (1995). Surface displacement of the 17 Eureka valley, California, earthquake observed by SAR interferometry. *Science*, 268, 1333-1336,

Peltzer, G., Rosen, P., Rogez, F., Hudnut, K. (1996). Post seismic rebound in fault stepovers caused by pore fluid flow. *Science*, 273, 1202-1204.

Peltzer, G., Crampé, F., Hensley, S., Rosen, R. (2001). Transient strain accumulation and fault interaction in the eastern California shear zone, *Geology*, 29, 975-978.

Perissin, D., Prati, C., Rocca, F. (2009). PSInSAR Analysis over the Three Gorges Dam and urban areas in China. *Urban Remote Sensing Joint Event*, 1-5.

Petley, D. (2012). Global patterns of loss of life from landslides. *Geology*, 40(10), 927-930.

Phien-Wej, N., Giao, P. H., Nutalaya, P. (2006). Land subsidence in Bangkok, Thailand. *Engineering Geology*, 82(4), 187-201.

Pierson, T. C., & Costa, J. E. (1987). A rheologic classification of subaerial sediment-water flows. *Reviews in Engineering Geology*, 7, 1-12.

Plank, S., Singer, J., Thuro, K. (2013). Assessment of number and distribution of persistent scatterers prior to radar acquisition using open access land cover and topographical data. *ISPRS Journal of Photogrammetry and Remote Sensing*, 85, 132-147.

Prati, C., Rocca, F., Guarnieri, A. M. (1989). Effects of speckle and additive noise on the altimetric resolution of interferometric SAR (ISAR) surveys. *Geoscience and Remote Sensing Symposium, 1989. IGARSS'89. 12th Canadian Symposium on Remote Sensing. 1989 International* 4, 2469-2472

Pratt, W. E., & Johnson, D. W. (1926). Local subsidence of the Goose Creek oil field. *The Journal of Geology*, 577-590.

Prokopovich, N. P. (1979). Genetic classification of land subsidence. *Evaluation and Prediction of Subsidence*, 389-399.

Proto, M., Bavusi, M., Bernini, R., Bigagli, L., Bost, M., Bourquin, F., Cottineau, L.-M., Cuomo, V., Vecchia, P.D., Dolce, M., Dumoulin, J., Eppelbaum, L., Fornaro, G., Gustafsson, M., Hugenschmidt, J., Kaspersen, P., Kim, H., Lapenna, V., Leggio, M., Loperte, A., Mazzetti, P., Moroni, C., Nativi, S., Nordebo S., Pacini F., Palombo, A., Pascucci, S., Perrone, A., Pignatti, S., Ponzo, F.C., Rizzo, E., Soldovieri, F., Taillade, F. (2010). Transport Infrastructure Surveillance and Monitoring by Electromagnetic Sensing: The ISTIMES Project. *Sensors*, 10, 10620-10639.

Razak, K.A., Straatsma, M.W., van Westen, C.J., Malet, J.-P., de Jong, S.M. (2011). Airborne laser scanning of forested landslides characterization: terrain model quality and visualization. *Geomorphology* 126, 186-200.

Revellino, P., Guerriero, L., Grelle, G., Hungr, O., Fiorillo, F., Esposito, L., Guadagno, F. M. (2013). Initiation and propagation of the 2005 debris avalanche at Nocera Inferiore (Southern Italy). *Italian Journal of Geosciences*, 132(3), 366-379.

Rib, H.T., Liang, T. (1978). Recognition and identification. In: Schuster, R.L., Krizek, R.J. (Eds.), *Landslide Analysis and Control*. Transportation Research Board Special Report, 176. National Academy of Sciences, Washington, 34-80.

Rockaway, J. D. (1976). The influence of map scale on engineering geologic mapping. *Bulletin of the International Association of Engineering Geology-Bulletin de l'Association Internationale de Géologie de l'Ingénieur*, 13(1), 119-122.

Roda, C. (1964). Distribuzione e facies dei sedimenti Neogenici nel Bacino Crotonese. *Geologica Romana*, 3, 319-366. (In Italian)

Roda, C., & Martelli, G. (2006). Il cammino di collasso del 25 aprile 1984 in territorio di Belvedere di Spinello (Crotone). *Giornale di Geologia Applicata*, 3, 237-248. (In Italian).

Rosen, P. A., Hensley, S., Zebker, H. A., Webb, F. H., Fielding, E. J. (1996). Surface deformation and coherence measurements of Kilauea Volcano, Hawaii, from SIR-C radar interferometry. *Journal of Geophysical Research: Planets*, 101(E10), 23109-23125.

Rosen, P.A., Hensley, S., Joughin, I.R., Li, F.K., Madsen, S.N., Rodriguez, E., Goldstein, R. (2000). Synthetic aperture radar interferometry, *IEEE Proceedings*, 88, 333- 376.

Rubin, A. M. (1992). Dike-induced faulting and graben subsidence in volcanic rift zones. *Journal of Geophysical Research: Solid Earth*, 97(B2), 1839-1858.

Sammarco, O. (2004). A tragic disaster caused by the failure of tailings dams leads to the formation of the Stava 1985 Foundation. *Mine Water and the Environment*, 23(2), 91-95.

Samsonov, S., d'Oreye, N. (2012). Multidimensional time-series analysis of ground deformation from multiple InSAR data sets applied to Virunga Volcanic Province. *Geophysical Journal International*, 191, 1095-1108.

Sartori, R. (2003). The Tyrrhenian back-arc basin and subduction of the Ionian lithosphere. *Episodes*, 26, 217-221.

Sauchyn, D.J., Trench, N.R. (1978). Landsat applied to landslide mapping. *Photogrammetric Engineering and Remote Sensing*, 44 (6), 735-741.

Scanvic, J.Y., Girault, F. (1989). Imagerie SPOT-1 et inventaire des mouvements de terrain: l'exemple de La Paz (Bolivie). *Photo Interpretation* 89 (2-1), 1-20 (in French).

Scanvic, J.Y., Rouzeau, O., Colleau, A. (1990). SPOT, outil d'aménagement exemple de realization par télédétection et analyse multicritère d'une cartographie des zones sensibles aux mouvements de terrain le site de La Paz — Bolivie. Bureau de Recherches Géologiques et Minières, Orléans, France. (In French).

Schulz, W.H. (2007). Landslide susceptibility revealed by LIDAR imagery and historical records, Seattle, Washington. *Engineering Geology*, 89, 67-87.

Scott, R.F. (1979). Subsidence - A review. En: Saxena, S.K. (ed.). *Evaluation and prediction of References 250 subsidence*. Proc. of the Int. Conf., Pensacola Beach, Florida, January 1978, Am. Soc. Civil Eng., New York, 1-25.

Scott, K. M., Vallance, J. W., Kerle, N., Luis Macías, J., Strauch, W., Devoli, G. (2005). Catastrophic precipitation-triggered lahar at Casita volcano, Nicaragua: occurrence, bulking and transformation. *Earth Surface Processes and Landforms*, 30(1), 59-79.

Seymour, M.S., Cumming, I.G., 1994. Maximum Likelihood Estimator for SAR Interferometry, in Proc. 1994 Int. Geosci. Remote Sensing Symp. IGARSS 94, Pasadena, USA, 1994, 2272-2275.2.5,6.2.

Shan, J., Toth, C.K. (2009). *Topographic Laser Ranging and Scanning: Principles and Processing*. CRC Press, Taylor and Francis Group, 590.

Sharpe, C. F. (1938). Landslides and related phenomena.

Soeters, R., van Westen, C.J. (1996). Slope instability recognition, analysis, and zonation. In: Turner, A.K., Schuster, R.L. (Eds.), *Landslides, Investigation and Mitigation*. National Academy Press, Washington, D.C.

Soldati, M. (2013). Deep-seated gravitational slope deformation. *Encyclopedia of Natural Hazards* 151-155. Springer Netherlands.

Sousa, J. J., & Bastos, L. (2013). Multi-temporal SAR interferometry reveals acceleration of bridge sinking before collapse. *Natural Hazards and Earth System Science*, 13(3), 659-667.

Sowter, A., Bateson, L., Strange, P., Ambrose, K., Syafudin, M.F. (2013). DInSAR estimation of land motion using intermittent coherence with application to the South Derbyshire and Leicestershire coalfields. *Remote Sensing Letters*, 4, 979-987.

Speight, J.G., (1977). Landform pattern description from aerial photographs. *Photogrammetry*, 32, 161-182.

Speranza, F., Macrì, P., Rio, D., Fornaciari, E., Consolaro, C. (2011). Paleomagnetic evidence for a post-1.2 Ma disruption of the Calabria terrane: consequences of slab breakoff on orogenic wedge tectonics. *Geological Society of America Bulletin*, 123, 925-933.

Squarzoni, C., Delacourt, C., Allemand, P. (2003). Nine years of spatial and temporal evolution of the La Valette landslide observed by SAR interferometry. *Engineering Geology*, 68(1), 53-66.

Stabile, T. A., Giocoli, A., Perrone, A., Palombo, A., Pascucci, S., Pignatti, S. (2012). A new joint application of non-invasive remote sensing techniques for structural health monitoring. *J. Geophys. Eng.*, 9, 53.

Stark, T. D., & Choi, H. (2008). Slope inclinometers for landslides. *Landslides*, 5(3), 339-350.

Stephens, P.R. (1988). Use of satellite data to map landslides. Proceeding ninth Asian Conference on Remote Sensing, Bangkok, Thailand, 11, 1-7.

Stramondo, S., Tesauro, M., Briole, P., Sansosti, E., Salvi, S., Lanari, R., Anzidei, M., Baldi, P., Fornaro, G., Avallone, A., Buongiorno, M. F., Franceschetti, G., Boschi, E. (1999). The September 26, 1997 Colfiorito, Italy, earthquakes: modeled coseismic surface displacement from SAR interferometry and GPS. *Geophysical Research Letters*, 26(7), 883-886.

Strozzi, T., Wegmüller, U., Tosi, L., Bitelli, G., and Spreckels, V. (2001). Land Subsidence Monitoring with Differential SAR Interferometry. *Photogrammetric Enginiry and Remote Sensing*, 67(11), 1261-1270.

Strozzi, T., Luckman, A., Murray, T., Wegmüller, U., Werner, C. L. (2002). Glacier motion estimation using SAR offset-tracking procedures. *IEEE Transaction on Geoscience Remote*, 40(11), 2384-2391.

Strozzi, T., Tosi, L., Wegmüller, U., Werner, C., Teatini, P., Carbognin, L. (2003). Land subsidence monitoring service in the lagoon of Venice. *Proc. IEEE Int. Geosci. Remote Sens. Symp. IGARSS 2003*, Toulouse, 21-25 July 1, 212 - 214.

Strozzi, T., Farina, P., Corsini, A., Ambrosi, C., Thüring, M., Zilger, J., Wiessman, A., Wegmüller, U., Werner, C. (2005). Survey and monitoring of landslide displacements by means of L-band satellite SAR interferometry. *Landslides*, 2(3), 193-201.

Strozzi, T., Wegmüller, U. (1999). Land subsidence in Mexico City Mapped by ERS Differential SAR Interferometry. *Proc. IEEE Int. Geosci. Remote Sens. Symp., IGARSS 1999*, Piscataway, New Jersey, 28 June-2 July, 4, 1940-1942.

Tandanand, S., & Powell, L. R. (1984). Influence of lithology on longwall mining subsidence. *Mining Engineering* (Littleton, Colo.), (United States), 36(12).

Tapete, D., Casagli, N., Fanti, R., Del Ventisette, C., Cecchi, R., Petrangeli, P. (2011). Satellite and ground-based radar interferometry for detection and monitoring of structural instability in archaeological sites. In *Geophysical research abstracts* (Vol. 13).

Tapete, D. & Cigna, F. (2012a). Site-Specific Analysis of Deformation Patterns on Archaeological Heritage by Satellite Radar Interferometry. *MRS Proceedings*, 1374, 283-295, Cambridge University Press.

Tapete, D. & Cigna, F. (2012b). Satellite-based preventive diagnosis: use of Persistent Scatterer Interferometry on cultural heritage sites in Italy. *RSPSoc 2012*, London, UK, 12-14 Sept 2012, 1-4.

Tarchi, D., Casagli, N., Fanti, R., Leva, D., Luzi, G., Pasuto, A., Pieraccini, M., Silvano, S. (2003). Landslide monitoring by using ground-based SAR interferometry: An example of application to the Tessina landslide in Italy. *Engineering Geology*, 68 (1-2), 15- 30.

Tarquini, S., Isola, I., Favalli, M., Mazzarini, F., Bisson, M., Pareschi, M.T., Boschi, E. (2007). TINITALY/01: a new Triangular Irregular Network of Italy, *Annals of Geophysics*, 50, 407-425.

Tarquini, S., Vinci, S., Favalli, M., Doumaz, F., Fornaciai, A., Nannipieri, L. (2012). Release of a 10-m-resolution DEM for the Italian territory: Comparison with global-coverage DEMs and anaglyph-mode exploration via the web, *Computers & Geosciences*, 38, 168-170.

Teatini, P., Ferronato, M., Gambolati, G., Bertoni, W., Gonella M. (2005a). A century of land subsidence in Ravenna, Italy. *Environmental Geology*, 47 (6), 831 - 846.

Teatini, P., Tosi, L., Strozzi T. (2011). Quantitative evidence that compaction of Holocene sediments drives the present land subsidence of the Po Delta, Italy. *Journal of Geophysical Research*, 116., B08407.

TELLUS (2006). <http://www.difesa.suolo.regione.campania.it/content/category/4/64/92/> [accessed on 7 September, 2015]

Terzaghi K. (1950). Mechanism of landslides, in Application of Geology to Engineering Practice, Berkey Vol., Geological Society of America, 83-123.

Tessitore, S., Fernández-Merodo, J. A., Herrera, G., Tomás, R., Ramondini, M., Sanabria, M., Duro, J., Mulas, J., Calcaterra, D. (2016). Comparison of water-level, extensometric, DInSAR and simulation data for quantification of subsidence in Murcia City (SE Spain). *Hydrogeology Journal*.

Tobita, M., Fujiwara, S., Ozawa, S., Rosen, P. A., Fielding, E. J., Werner, C. L., Murakami, M., Nakagawa, H., Nitta, K., Murakami, M. (1998). Deformation of the 1995 North Sakhalin earthquake detected by JERS-1/SAR interferometry. *Earth, planets and space*, 50(4), 313-325.

Tofani, V., Del Ventisette, C., Moretti, S., Casagli, N. (2014). Integration of remote sensing techniques for intensity zonation within a landslide area: A case study in the northern Apennines, Italy. *Remote Sensing*, 6(2), 907-924.

Tomás, R.; Márquez, Y.; López - Sánchez, J.M.; Delgado, J.; Blanco, P.; Mallorquí, J.J.; Martínez, M.; Herrera, G.; Mulas, J. (2005). Mapping ground subsidence induced by aquifer overexploitation using advanced Differential SAR Interferometry: Vega Media of the Segura River (SE Spain) case study. *Remote Sensing of Environment*, 98 (2005) 269 - 283.

Tomás, R.; Romero, R.; Mulas, J.; Marturia, J.; Mallorqui, J.; Lopez-Sanchez, J.M. ; Herrera, G.; Gutierrez, J.; González, P.J.; Fernandez, J.; Duque, S.; Concha-Dimas, A.; Cocksley, G.; Castaneda, C.; Carrasco, D. y Blanco, P. (2013). Radar interferometry techniques for the study of ground subsidence phenomena: a review of practical issues through cases in Spain". *Environmental Earth Sciences*. Received.

UNESCO (1984). Guidebook to studies of land subsidence due to ground-water withdrawal. Prepared for the International Hydrological Programme, working group 8.4. J.F. Poland (Ed.), USA.

Van Den Eeckhaut, M., Poesen, J., Verstraeten, G., Vanacker, V., Moeyersons, J., Nyssen, J., van Beek, L.P.H., Vandekerckhove, L. (2007). Use of LIDAR-derived images for mapping old landslides under forest. *Earth Surface Processes and Landforms* 32, 754-769.

Van Dijk, J.P. (1990). Sequence stratigraphy, kinematics and dynamic geohistory of the Crotone Basin (Calabria Arc, Central Mediterranean): an integrated approach. *Memorie della Società Geologica Italiana*, 44, 259-285.

Van Dijk, J.P. (1991). Basin dynamics and sequence stratigraphy in the Calabrian Arc (Central Mediterranean): records and pathways of the Crotone Basin. *Geologie en Mijnbouw*, 70, 187-201.

Van Dijk, J.P. (1994). Late Neogene kinematics of intra-arc oblique shear zones: the Petilia-Rizzuto Fault Zone (Calabrian Arc, Central Mediterranean). *Tectonics*, 13, 1201-1230.

Van Dijk, J.P. & Okkes, F.W.M. (1991). Neogene tectonostratigraphy and kinematics of Calabrian basins; implications for the geodynamics of the Central Mediterranean. *Tectonophysics*, 196, 23-60.

Van Zuidam, R.A. (1985). Aerial photo-interpretation in terrain analysis and geomorphologic mapping. International Institute for Aerospace Survey and Earth Sciences (ITC). Smits Publishers, The Hague. 442 pp.

Van Hasselt, J. P. (1992). Reservoir compaction and surface subsidence resulting from oil and gas-production-a review of theoretical and experimental research approaches. *Geologie en Mijnbouw*, 71(2), 107-118.

Vargas, G.C., 1992. Methodologie pour letablissement de cartes de sensibilité aux mouvements de terrain fonde sur l'utilisation d'un couple stéréographique SPOT XS/TM. Application à la région de Paz del Rio (Colombie): Proc. Ler Simposio International sobre Sensores Remotos y Sistemas de

Informacion Geografica (SIG) para el estudio de Riesgos Naturales, Bogotà, Colombia, 201-220. (In French).

Varnes, D.J. (1978). Slope movement types and processes. In Special Report 176. Landslides: Analysis and control (R.L. Schuster and R.J. Krizek, eds), TRB, NationalResearch Council, Washington, D.C., 11-33.

Varnes, D. J., IAEG (1984). Landslide Hazard Zonation - a review of principles and practice. Commission on Landslides. Paris, UNESCO, 60 pp.

Vasvári, V. (2005). Calibration of tipping bucket rain gauges in the Graz urban research area. Atmospheric research, 77(1), 18-28.

Vennari, C., Gariano, S. L., Antronico, L., Brunetti, M. T., Iovine, G., Peruccacci, S., Terranova, O., Guzzetti, F. (2014). Rainfall thresholds for shallow landslide occurrence in Calabria, southern Italy. Natyural Hazards of Earth Systems Science, 14(2), 317-330.

Waltham, T., Bell, F. G., Culshaw, M. (2007). Sinkholes and subsidence: karst and cavernous rocks in engineering and construction. Springer Science & Business Media.

Wasowski, J., & Bovenga, F. (2014). Investigating landslides and unstable slopes with satellite Multi Temporal Interferometry: Current issues and future perspectives. Engineering Geology, 174, 103-138.

Wegmuller, U., Werner, C., Strozzi, T. (1998) SAR interferometric and differential interferometric processing chain. International geoscience and remote sensing symposium. Vol. 2. Institute of electrical & electronics engineers, Inc (IEE).

Werner, C., Wegmüller, U., Strozzi, T., Wiesmann, A. (2000). Gamma SAR and interferometric processing software. In Proceedings of the ERS-ENVISAT symposium, Gothenburg, Sweden (Vol. 1620, p. 1620).

Werner, C., Wegmuller, U., Strozzi, T., Wiesmann, A. (2003). Interferometric point target analysis for deformation mapping. Proceeding of IEEE Geoscience and Remote Sensing Symposium. IGARSS, Toulouse, France, 7, 4362-4364.

Wieczorek, G.F. (1984). Preparing a detailed landslide-inventory map for hazard evaluation and reduction. Bulletin of the Association of Engineering Geologists 21, (3), 337-342.

Wieczorek, G.F., Snyder J.B. (2009). Monitoring slope movements. In Geological Monitoring. Geological Society of America, Boulder, 245-271.

WP/WLI (1990). International Geotechnical Societies' UNESCO Working Party on World Landslide Inventory. A suggested method for reporting a landslide. International Association Engineering Geology Bulletin 41, 5-12.

WP/WLI (1993). International Geotechnical Societies' UNESCO Working Party on World Landslide Inventory. A suggested method for describing the activity of a landslide. International Association Engineering Geology Bulletin 47, 53-57

Wright, T., Parsons, B., Fielding, E. (2001). Measurement of interseismic strain accumulation across the North Anatolian Fault by satellite radar interferometry. Geophysical Research Letters, 28 (10), 2117-2120.

- Xu, W., & Cumming, I. (1999). A region-growing algorithm for InSAR phase unwrapping. *Geoscience and Remote Sensing, IEEE Transactions on*, 37(1), 124-134.
- Yin, Y., Wang, F., Sun, P. (2009). Landslide hazards triggered by the 2008 Wenchuan earthquake, Sichuan, China. *Landslides*, 6(2), 139-152.
- Zanchetta, G., Sulpizio, R., Pareschi, M. T., Leoni, F. M., Santacroce, R. (2004). Characteristics of May 5-6, 1998 volcaniclastic debris flows in the Sarno area (Campania, southern Italy): relationships to structural damage and hazard zonation. *Journal of volcanology and geothermal research*, 133(1), 377-393.
- Zebker, H. A., & Goldstein, R. M. (1986). Topographic mapping from interferometric synthetic aperture radar observations. *Journal of Geophysical Research: Solid Earth*, 91(B5), 4993-4999.
- Zecchin, M. (2005). Relationships between fault-controlled subsidence and preservation of shallow-marine small-scale cycles: example from the lower Pliocene of the Crotone Basin (southern Italy). *Journal of Sedimentary Research*, 75, 300-312.
- Zecchin, M., Massari, F., Mellere, D., Prosser, G. (2003). Architectural styles of prograding wedges in a tectonically active setting, Crotone Basin, Southern Italy. *Journal of the Geological Society of London*, 160, 863-880.
- Zecchin, M., Massari, F., Mellere, D., Prosser, G. (2004a). Anatomy and evolution of a Mediterranean-type fault bounded basin: the Lower Pliocene of the northern Crotone Basin (Southern Italy). *Basin Research*, 16, 117-143.
- Zecchin, M., Mellere, D., Roda, C. (2006). Sequence stratigraphy and architectural variability in growth fault-bounded basin fills: a review of Plio-Pleistocene stratal units of the Crotone Basin, southern Italy. *Journal of the Geological Society of London*, 163, 471-486.
- Zecchin, M., Caffau, M., Civile, D., Critelli, S., Di Stefano, A., Maniscalco, R., Muto, F., Sturiale, G., Roda, C. (2012). The Plio-Pleistocene evolution of the Crotone Basin (southern Italy): interplay between sedimentation, tectonics and eustasy in the frame of Calabrian Arc migration. *Earth-Science Reviews*, 115(4), 273-303.
- Zeni, G., Bonano, M., Casu, F., Manunta, M., Manzo, M., Marsella, M., Pepe A., Lanari R. (2011) - Long-term deformation analysis of historical buildings through the advanced SBAS-DInSAR technique: The case study of the city of Rome, Italy. *Journal of Geophysics and Engineering*, 8 (3), 1-12.
- Zhou, X., Chang, N. B., Li, S. (2009). Applications of SAR interferometry in earth and environmental science research. *Sensors*, 9(3), 1876-1912.
- Zischinsky, U. (1966). On the deformation of high slopes. *Proceedings of the First Congress of the Int. Soc. Of Rock Mechanics, Lisboa*, 6/11, 179-185.

Acknowledgements

The list of people to whom saying thank you is very long, but I will try to be concise. First, I have to thank Professor Domenico Calcaterra, who believed in me and awarded me with this PhD project, even though he hardly knew me at that time. His remarks, his objective criticism, his encouragements and his advice were the main engine for my growth, as a research, but mostly as a man. Then I have to say thanks to my co-advisors, Prof. Massimo Ramondini and Prof. Kurosch Thuro, who helped and supported me during these three years of PhD project. Prof. Ramondini was a fundamental support for the geotechnical and engineering part of my thesis; Prof. Kurosch Thuro accepted and welcomed me in Munich, at the wonderful TUM (Technische Universität München), giving me the chance of working for the first time abroad: Collaborating with him has been an honour. I feel obligated to say thank you to two fundamental people who represented my light in my endless SAR problems and questions: Dott. Ing. Diego Di Martire and Dott. Simon Plank. Simply, without them, their time, their patience, their help, I would not be here, writing the acknowledgement, because there would not be a thesis at all. I will be grateful for life to them. Thanks are due to the PhD coordinator, Professor Fedi, who encouraged me for my international experience. I have to express my gratitude to Professor Günter Strunz, whose encouragements, whose enthusiasm towards my studies and my research, whose precious advice, represented a special boost to my scientific experience. Earth Observation Center of DLR (Deutsches zentrum für Luft- und Raumfahrt), in particular the Department of Geo-Risks and Civil Security is a great place to work, and I had the pleasure and the honour, thanks to Professor Strunz, to work there for 10 months. DLR time has represented one of the greatest experience that I have ever had in my life. The list of DLR people to whom aknowledge is too long. Anyone of them will read these few words will known that I am expressing my gratitude to them (the guys of the department, the guys of the basement, my roomates, the guys of the German class, the guys of the S-Bahn and of the bus, etc.). Without them, it would have not been the same. Then I would like to express my gratitude to my “UNINA” colleagues, Serena, Alessandro and Donato (my SAR group), Licia, Maria Teresa, Anna Claudia, Ferdinando, Francesco, Ahmed and in particular, at last, but not least, Gianfranco, whose friendship and time spend together are just unforgettable moments. It is such a great bunch of minds, which all deserve to be a scientist! I would like to say thank you to all my friends, who barely understood what I have done in these three years, but it does not matter, just thanks for being you. Thanks to those who came in Munich (my brotherly cousin Totore and his partner Ancela, Fulvio, the doctors, and bomber Roberto and his lovely wife Giusy), as well as to those of the high school (Vito and Vito, Lisa, Bert, Pasquale and Imma, Marco and Margherita, Mariano, Alfredo (a particular mention to him), it's hard to say, but yes, I missed you in the ten months abroad), those of the weekly football match (Pasquale,

Enzo, Nicola, Franco, Agostino, Mauro, etc.), those of Pomi/Tavernanova (Taccio and wife, SaRod), those of the university (Angie, Elena, Federica, Marianna, etc.) and those of the Circumvesuviana (Ida, Mario, Andrea, and Annarella too). Thanks to all of you, because, even in the hardest moment, I have never felt alone. Then I would like to say thank you to all the people that I met in Munich, it has been great time out there mostly thanks to you. Thanks to Marta and Francesca, who introduced me in the city, and thanks to Daniele and Alessio, always up for a beer or for a conversation. Thanks to the guys of Die Auswahl (in particular to coach Julian), it was a pleasure to play football with you and to spend my spare time with you. I will always remember the PIETROOO moments and the MIETTEEEEEE, LINKSSSS that I tried to say to you. If I will not succeed as a researcher, I can become your goalkeeper forever!

The biggest thanks goes to my family. Thanks for the sacrifices and for all. I just say that I love you.